

AFRL-ML-WP-TR-2001-4102

**FRACTURE BEHAVIOR OF A Si_3N_4 -BN
FIBROUS MONOLITH CERAMIC**



**J.L. PIERCE
UNIVERSITY OF DAYTON RESEARCH INSTITUTE
STRUCTURAL INTEGRITY DIVISION
DAYTON, OH 45411**

**L.P. ZAWADA
METALS, CERAMICS, AND NDE DIVISION
CERAMICS BRANCH
2230 10TH STREET
WRIGHT-PATTERSON AFB, OH 45433-7817**

**J.M. STAEHLER
SYSTRAN, INC.
2146 LINDEN AVENUE
DAYTON, OH 45410**

APRIL 2001

FINAL REPORT FOR PERIOD 01 OCTOBER 1999 - 01 APRIL 2001

Approved for public release; distribution is unlimited

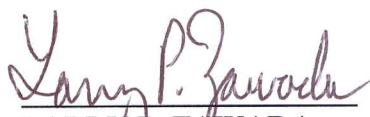
**MATERIALS AND MANUFACTURING DIRECTORATE
AIR FORCE RESEARCH LABORATORY
AIR FORCE MATERIEL COMMAND
WRIGHT-PATTERSON AIR FORCE BASE, OH 45433-7750**

NOTICE

WHEN GOVERNMENT DRAWINGS, SPECIFICATIONS, OR OTHER DATA ARE USED FOR ANY PURPOSE OTHER THAN IN CONNECTION WITH A DEFINITELY GOVERNMENT-RELATED PROCUREMENT, THE UNITED STATES GOVERNMENT INCURS NO RESPONSIBILITY OR ANY OBLIGATION WHATSOEVER. THE FACT THAT THE GOVERNMENT MAY HAVE FORMULATED OR IN ANY WAY SUPPLIED THE SAID DRAWINGS, SPECIFICATIONS, OR OTHER DATA, IS NOT TO BE REGARDED BY IMPLICATION OR OTHERWISE IN ANY MANNER CONSTRUED, AS LICENSING THE HOLDER OR ANY OTHER PERSON OR CORPORATION, OR AS CONVEYING ANY RIGHTS OR PERMISSION TO MANUFACTURE, USE, OR SELL ANY PATENTED INVENTION THAT MAY IN ANY WAY BE RELATED THERETO.

THIS REPORT IS RELEASABLE TO THE NATIONAL TECHNICAL INFORMATION SERVICE (NTIS). AT NTIS, IT WILL BE AVAILABLE TO THE GENERAL PUBLIC, INCLUDING FOREIGN NATIONS.

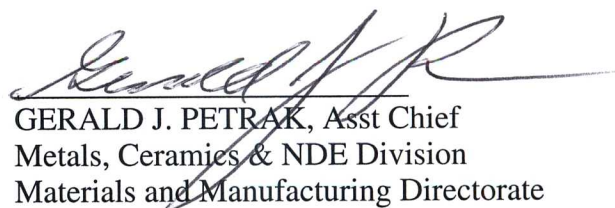
THIS TECHNICAL REPORT HAS BEEN REVIEWED AND IS APPROVED FOR PUBLICATION.



LARRY P. ZAWADA
Ceramics Branch
Metals, Ceramics & NDE Division



ALLAN P. KATZ, Chief
Ceramics Branch
Metals, Ceramics & NDE Division



GERALD J. PETRAK, Asst Chief
Metals, Ceramics & NDE Division
Materials and Manufacturing Directorate

IF YOUR ADDRESS HAS CHANGED, IF YOU WISH TO BE REMOVED FROM OUR MAILING LIST, OR IF THE ADDRESSEE IS NO LONGER EMPLOYED BY YOUR ORGANIZATION, PLEASE NOTIFY, AFRL/MLLN, WRIGHT-PATTERSON AFB OH 45433-7817 TO HELP US MAINTAIN A CURRENT MAILING LIST.

COPIES OF THIS REPORT SHOULD NOT BE RETURNED UNLESS RETURN IS REQUIRED BY SECURITY CONSIDERATIONS, CONTRACTUAL OBLIGATIONS, OR NOTICE ON A SPECIFIC DOCUMENT.

REPORT DOCUMENTATION PAGE			Form Approved OMB No. 074-0188	
Public reporting burden for this collection of information is estimated to average 1 hour per response, including the time for reviewing instructions, searching existing data sources, gathering and maintaining the data needed, and completing and reviewing this collection of information. Send comments regarding this burden estimate or any other aspect of this collection of information, including suggestions for reducing this burden to Washington Headquarters Services, Directorate for Information Operations and Reports, 1215 Jefferson Davis Highway, Suite 1204, Arlington, VA 22202-4302, and to the Office of Management and Budget, Paperwork Reduction Project (0704-0188), Washington, DC 20503				
1. AGENCY USE ONLY (Leave blank)	2. REPORT DATE April 2001	3. REPORT TYPE AND DATES COVERED Final 10/1/1999 - 04/01/2001		
4. TITLE AND SUBTITLE Fracture Behavior of a Si ₃ N ₄ -BN Fibrous Monolith Ceramic		5. FUNDING NUMBERS C N/A PE 61102F PR 2302 TA DW WU 1F		
6. AUTHOR(S) J.L. Pierce - University of Dayton Research Institute L.P. Zawada - Metals, Ceramics, and NDE Division J.M. Staehler - Systran, Inc.				
7. PERFORMING ORGANIZATION NAME(S) AND ADDRESS(ES) University of Dayton Research Institute Metals, Ceramics, and NDE Division Systran, Inc. Structural Integrity Division Ceramics Branch 2146 Linden Avenue Dayton, OH 45411 2230 10 TH Street Dayton, OH 45410 Wright-Patterson AFB, OH 45433-7817		8. PERFORMING ORGANIZATION REPORT NUMBER AFRL-ML-WP-TR-2001-4102		
9. SPONSORING / MONITORING AGENCY NAME(S) AND ADDRESS(ES) Materials and Manufacturing Directorate Air Force Research Laboratory Air Force Materiel Command Wright-Patterson Air Force Base, OH 45433-7750 POC: Larry P. Zawada, AFRL/MLLN, (937) 255-1352		10. SPONSORING / MONITORING AGENCY REPORT NUMBER AFRL-ML-WP-TR-2001-4102		
11. SUPPLEMENTARY NOTES This thesis was submitted in partial fulfillment of a Masters of Science degree in Materials Engineering at Wright State University.				
12a. DISTRIBUTION / AVAILABILITY STATEMENT Approved for public release; distribution is unlimited.			12b. DISTRIBUTION CODE	
13. ABSTRACT (Maximum 200 Words) The two different microstructures of Si ₃ N ₄ -BN fibrous monolith ceramic material were compared to each other and to monolithic Si ₃ N ₄ in order to evaluate the fracture behavior and effect of cell size on the mechanical performance of the material. The room temperature behavior was evaluated through fastfracture tensile testing of straight-sided, dogbone, and modified single-edge notched specimens with various notch lengths. Load-unload and cyclic fracture tests were performed along with several non-destructive evaluation (NDE) techniques including x-ray radiography, thermography, ultrasonic c-scanning, and acoustic emission to determine critical stages of damage evolution in each. The Si ₃ N ₄ -BN materials tested showed non-catastrophic fracture behavior compared to the monolithic Si ₃ N ₄ in tension and demonstrated to be insensitive to stress concentrations imparted by the notches. The influence of individual cell size on the fracture behavior of the FM materials was not evident as the cell bundles formed by the processing technique, not the individual cells, were the dominate microstructural feature. Cell bundle size in the materials tested was shown to influence the behavior as the displacements, extent of damage, and fracture energies were higher with larger cell bundles.				
14. SUBJECT TERMS, Ceramics, Fatigue Testing, Silicon Nitride			15. NUMBER OF PAGES 208	
			16. PRICE CODE	
17. SECURITY CLASSIFICATION OF REPORT Unclassified	18. SECURITY CLASSIFICATION OF THIS PAGE Unclassified	19. SECURITY CLASSIFICATION OF ABSTRACT Unclassified	20. LIMITATION OF ABSTRACT SAR	

NSN 7540-01-280-5500

Standard Form 298 (Rev. 2-89)
Prescribed by ANSI Std. Z39-18
298-102

TABLE OF CONTENTS

LIST OF FIGURES	v
LIST OF TABLES	xiii
FOREWORD	xiv
ACKNOWLEDGMENT	xv
INTRODUCTION	1
LITERATURE REVIEW: FIBROUS MONOLITHS	5
2.1 The Fibrous Monolith Concept.....	5
2.2 Processing Fibrous Monoliths	6
2.3 Mechanical Properties of Fibrous Monoliths	7
2.4 Literature Review Summary	23
TEXT MATRIX, MATERIAL DESCRIPTION, AND EXPERIMENTAL PROCEDURES	27
3.1 Test Matrix	27
3.2 Material Description	31
3.3 Experimental Procedures	35
TENSILE BEHAVIOR OF UNNOTCHED SPECIMENS	63
4.1 Monolithic Si_3N_4	63
4.2 Fibrous Monolith Material.....	64
4.3 Discussion	66
4.4 Summary	74
FAST FRACTURE OF MODIFIED SINGLE-EDGE NOTCH SPECIMENS ...	81
5.1 Fast Fracture of MSE(T) Specimens - $a_0/W = 0.3$	83
5.2 Fast Fracture of MSE(T) Specimens - Various Notch Lengths	90
5.3 Theoretical Prediction of Notch Length Effect	96
5.4 Fracture Energy	100
5.5 Summary	101

SINGLE LOAD-UNLOAD AND CYCLIC TESTING OF NOTCHED SPECIMENS	118
6.1 Single Load-Unload Testing	120
6.2 Cyclic Testing	124
6.3 Fracture Energy	126
6.4 Discussion	128
6.5 Summary	131
MICROSCOPIC INSPECTION	149
7.1 Procedure	149
7.2 Inspection Observations.....	150
7.3 Summary	154
SUMMARY AND CONCLUSIONS	164
8.1 Summary	164
8.2 Conclusions	169
REFERENCES	172
APPENDICES	177
A CALCULATION OF G FOR COMPLIANCE	177
B PREDICTION OF STRENGTH FOR Si_3N_4 -BN FM FROM LITERATURE VALUES	178
C PREDICTION OF STRENGTH FOR Si_3N_4 -BN FM FROM NEAT DATA ...	179
D HYPOTHESIS TEST OF VARIABILITY	180
E NOTCH SIZE EFFECT PREDICTION FOR NEAT Si_3N_4 USING LEFM	181
F NOTCH SIZE EFFECT PREDICTION FOR Si_3N_4 -BN FM USING LEFM ...	183
G CALCULATION OF FRACTURE ENERGY	185

LIST OF FIGURES

FIGURE	PAGE
1.1 Schematic representation of a single filament coextruded fibrous monolith	4
1.2 Schematic of structures with identical fractions of circles to total area. The circles in (a) are twice as large as those shown in (b). The area between the circles in (b) is thinner compared to (a).	4
2.1 Schematic representation of a multi-filament coextruded material.	26
3.1 Schematic illustrations showing processing route to fabricate fibrous monoliths using coextrusion methods ²² .	47
3.2 (a) Micrograph at 16x of Si_3N_4 -BN fibrous monolith [-45/0/+45]s with 125 μm cells (2-1 mm multi-filament strands).	48
3.2 (b) Micrograph at 16x of Si_3N_4 -BN fibrous monolith [-45/0/+45]s with 250 μm cells (2-2 mm multi-filament strands).	48
3.3 (a) Micrograph at 16x of Si_3N_4 -BN fibrous monolith showing a number of different processing defects.	49
3.3 (b) Micrograph at 320x of Si_3N_4 -BN fibrous monolith showing the jagged perimeter formed on the individual cells during multi-filament coextrusion.	50
3.3 (c) Micrograph at 2k x of Si_3N_4 -BN fibrous monolith showing the jagged perimeter formed on the individual cells during multi-filament coextrusion.	50
3.4 Schematic of the machining lay-out for each of the Si_3N_4 -BN FM plates.	51
3.5 (a) Photograph of the plate material illustrating the edge defects from processing.	52
3.5 (b) Micrograph at 10x of Si_3N_4 -BN fibrous monolith showing the microstructural defects created at the edge of the plate during hot-pressing.	52
3.6 Photograph of a specimen which came from the edge of a plate, the notch was machined on the edge which corresponded to the plate edge. The notch extends beyond the edge defects which can be identified visually.	53

3.7 (a) Schematic drawing of a straight-sided Si_3N_4 -BN FM tensile specimen with fiberglass tabs. (b) Schematic drawing of a dogbone Si_3N_4 -BN FM tensile specimen. (c) Schematic drawing of a neat Si_3N_4 dogbone tensile specimen in showing the dimensions tested. Not to scale.	54
3.8 Photograph of the wedge grips used to test the straight-sided Si_3N_4 -BN fibrous monolith specimens.	55
3.9 Schematic representation of the horizontal servo-hydraulic test system used for tensile testing the neat Si_3N_4 material as well as for all notched fracture testing.	55
3.10 Schematic illustration of the MSE(T) specimen geometry with the dimensions tested. Not to scale.	56
3.11 Photograph of the extensometer with the specially designed bent quartz rods for load-point displacement measurement.	56
3.12 Photograph of the set-up used for room temperature fast fracture testing of MSE(T) specimens.	57
3.13 Photograph of the set-up used for high temperature fast fracture testing of MSE(T) specimens.	57
3.14 Photograph illustrating the strain gage position with respect to the notch on the MSE(T) specimens.	58
3.15 Schematic representation of the x-ray radiography technique showing the method of sensing of an internal flaw.	58
3.16 (a) & (b) X-ray radiographs of representative plates of the Si_3N_4 -BN fibrous monolith and neat Si_3N_4 materials respectively. A large number of microstructural defects are detected and the radiograph of the FM material whereas the neat material appears to be uniformly dense except near the edges.	59
3.17 Schematic representation of the experimental apparatus used to obtain thermal images at Argonne National Laboratories ³⁸ .	60
3.18 Schematic representation of the experimental apparatus used to obtain ultrasonic C-scans.	61
3.19 Schematic representation of the acoustic emission test apparatus used during fracture testing.	62

4.1 Tensile plot showing typical stress versus strain behavior of monolithic Si_3N_4 .	76
4.2 Photograph of a fractured monolithic Si_3N_4 tensile specimen illustrating the brittle fracture.	76
4.3 (a) Tensile plot showing typical stress versus strain behavior of Si_3N_4 -BN FM material with a nominal cell size of $125\mu\text{m}$.	77
4.3 (b) Tensile plot showing typical stress versus strain behavior of Si_3N_4 -BN FM material with a nominal cell size of $250\mu\text{m}$.	77
4.4 Photographs of fractured straight-sided fibrous monolith tensile specimens.	78
4.5 (a) Tensile plot showing stress versus strain behavior of Si_3N_4 -BN FM material with a nominal cell size of $125\mu\text{m}$ and dogbone geometry.	79
4.5 (b) Tensile plot showing stress versus strain behavior of Si_3N_4 -BN FM material with a nominal cell size of $250\mu\text{m}$ and dogbone geometry.	79
4.6 Strength versus width for three differently processed FM materials. Results are inconclusive as to a width effect on the strength in the case for the straight-sided or the dogbone specimens.	80
4.7 Bar plot which shows that there may be an effect of the processing on the strength.	80
5.1 Results of fracture testing a FM specimen with the finer microstructure and an a_0/W of 0.3 at room temperature. (a) load or microstrain and AE count versus CMOD plot, (b) x-ray radiograph, (c) thermal diffusivity image, (d) ultrasonic c-scan, (e) acoustic emission histogram.	103
5.2 Results of fracture testing a FM specimen with the coarser microstructure and an a_0/W of 0.3 at room temperature. (a) load or microstrain and AE count versus CMOD plot, (b) x-ray radiograph, (c) thermal diffusivity image, (d) ultrasonic c-scan, (e) acoustic emission histogram.	104
5.3 Results of fracture testing a neat specimen with an a_0/W of 0.3 at room temperature. (a) load or microstrain and AE count versus CMOD plot, (b) photograph, (c) acoustic emission histogram.	105
5.4 Results of fracture testing the fibrous monolith and neat materials with a_0/W of 0.3 at 1150°C . (a) applied stress versus CMOD plot, (b) x-ray radiograph of FM with fine microstructure, (c) x-ray radiograph of FM with coarse microstructure, (d)	106

photograph of neat material

5.5 (a) Fracture behavior of Si_3N_4 -BN FM materials with an a_0/W of 0.3 as captured by an extensometer near the crack (notch) mouth opening.	107
5.5 (b) Fracture behavior of Si_3N_4 -BN FM materials with an a_0/W of 0.3 as captured by an extensometer near the point of loading.	107
5.6 Fracture surfaces (a) from a failed neat specimen and (b) from a failed fibrous monolith specimen, both with an a_0/W ratio of 0.3.	108
5.7 Photographs (a) and (b) are from the respective FM materials taken from the edge view opposite the notch after failure. The photographs show how the cracks initiate at the cell bundles in the 45° plies and how cracks are deflected along the cell bundles.	108
5.8 (a) Fracture behavior of Si_3N_4 -BN FM materials with an a_0/W of 0.1 as captured by an extensometer near the crack (notch) mouth opening.	109
5.8 (b) Fracture behavior of Si_3N_4 -BN FM materials with an a_0/W of 0.1 as captured by an extensometer near the point of loading.	109
5.9 (a) Fracture behavior of Si_3N_4 -BN FM materials with an a_0/W of 0.2 as captured by an extensometer near the crack (notch) mouth opening.	110
5.9 (b) Fracture behavior of Si_3N_4 -BN FM materials with an a_0/W of 0.2 as captured by an extensometer near the point of loading.	110
5.10 (a) Fracture behavior of Si_3N_4 -BN FM materials with an a_0/W of 0.5 as captured by an extensometer near the crack (notch) mouth opening.	111
5.10 (b) Fracture behavior of Si_3N_4 -BN FM materials with an a_0/W of 0.5 as captured by an extensometer near the point of loading.	111
5.11 Comparison of the behavior and fracture morphologies for specimens of the $125\mu\text{m}$ Si_3N_4 -BN fibrous monolith material with various notch lengths; (a) normalized load versus normalized CMOD plot, (b) through (e) x-ray radiographs of failed specimens with a_0/W 's = 0.1, 0.2, 0.3, and 0.5.	112
5.12 Comparison of the behavior and fracture morphologies for specimens of the $250\mu\text{m}$ Si_3N_4 -BN fibrous monolith material with various notch lengths; (a) normalized load versus normalized CMOD plot, (b) through (e) x-ray radiographs of failed specimens with a_0/W 's = 0.1, 0.2, 0.3, and 0.5.	113

5.13 Comparison of the behavior and fracture morphologies for specimens of the neat Si_3N_4 material with various notch lengths; (a) normalized load versus normalized CMOD plot, (b) through (d) x-ray radiographs of failed specimens with a_0/W 's = 0.1, 0.3, and 0.5.	114
5.14 Effect of notch size for the neat Si_3N_4 material.	115
5.15 Effect of notch size for the Si_3N_4 -BN materials.	115
5.16 Fracture surfaces: (a) neat Si_3N_4 , (b) [-45/0/+45] $^\circ$ s fibrous monolith, and (c) quasi-isotropic fibrous monolith.	116
5.17 Stress versus notch to width ratio showing the net-section stress predicted if the UTS = 144 MPa.	117
5.18 Total fracture energy per unit area as a function of notch size for the two fibrous monoliths and the neat materials.	117
6.1 Curve obtained from fast-fracture testing which shows the unloading strategy to be used to run single load-unload and cyclic tests.	133
6.2 Results of load-unload testing a FM specimen with the finer microstructure and an a_0/W of 0.3 at room temperature. (a) load versus displacement plot, (b) x-ray radiograph, (c) thermal diffusivity image, (d) ultrasonic c-scan, (e) acoustic emission histogram.	134
6.3 Results of load-unload testing a FM specimen with the coarser microstructure and an a_0/W of 0.3 at room temperature. (a) load versus displacement plot, (b) x-ray radiograph, (c) thermal diffusivity image, (d) ultrasonic c-scan, (e) acoustic emission histogram.	135
6.4 Results of load-unload testing a FM specimen with the finer microstructure and an a_0/W of 0.3 at room temperature. (a) load versus displacement plot, (b) x-ray radiograph, (c) thermal diffusivity image, (d) ultrasonic c-scan, (e) acoustic emission histogram.	136
6.5 Results of load-unload testing a FM specimen with the coarser microstructure and an a_0/W of 0.3 at room temperature. (a) load versus displacement plot, (b) x-ray radiograph, (c) thermal diffusivity image, (d) ultrasonic c-scan, (e) acoustic emission histogram.	137

6.6 Results of load-unload testing a FM specimen with the finer microstructure and an a_0/W of 0.3 at room temperature. (a) load versus displacement plot, (b) x-ray radiograph, (c) thermal diffusivity image, (d) ultrasonic c-scan, (e) acoustic emission histogram.	138
6.7 Results of load-unload testing a FM specimen with the coarser microstructure and an a_0/W of 0.3 at room temperature. (a) load versus displacement plot, (b) x-ray radiograph, (c) thermal diffusivity image, (d) ultrasonic c-scan, (e) acoustic emission histogram.	139
6.8 Results of load-unload testing a FM specimen with the finer microstructure and an a_0/W of 0.3 at room temperature. (a) load versus displacement plot, (b) x-ray radiograph, (c) thermal diffusivity image, (d) ultrasonic c-scan, (e) acoustic emission histogram.	140
6.9 Results of load-unload testing a FM specimen with the coarser microstructure and an a_0/W of 0.3 at room temperature. (a) load versus displacement plot, (b) x-ray radiograph, (c) thermal diffusivity image, (d) ultrasonic c-scan, (e) acoustic emission histogram.	141
6.10 (a) & (b) show the load-displacement data for the initial test and the restart data, respectively. The x-ray, thermal image and c-scan are shown in (c), (d), and (e). The thermal image and the c-scan show evidence of damage.	142
6.11 (a) shows the mechanical behavior for the initial test and the restart data. The x-ray, thermal image and the c-scan are shown in (b), (c), and (d).	143
6.12 Plot showing the total energy calculated from the area under the curve (loading portion) up to the failure load.	144
6.13 Plot showing the energy absorbed at various loads up to the fracture load which is the work of fracture.	144
6.14 (a) Plot showing the curve fit of the experimental compliance data used to predict the compliance at failure for the material with the smaller microstructural features.	145
6.14 (b) Plot showing the curve fit of the experimental compliance data used to predict the compliance at failure for the material with the smaller microstructural features.	145
6.15 (a) Plot illustrating how the estimated failure compliance was used to discount the	146

elastic energy at failure for the material with the smaller cell bundles.	
6.15 (b) Plot illustrating how the estimated failure compliance was used to discount the elastic energy at failure for the material with the larger cell bundles.	146
6.16 Qualitative representation of the results from the mechanical testing and the ultrasonic c-scanning for the specimens loaded to 35%, 65%, 77% and 86% of the estimated failure load for the material with the smaller microstructural features.	147
6.17 Qualitative representation of the results from mechanical testing and ultrasonic c-scanning for specimens loaded 25%, 50%, 77% and 94% of the estimated failure load for the material with the larger cell bundles.	148
7.1 Micrograph at 6.3x of Si_3N_4 -BN fibrous monolith [-45/0/+45] _s with 125 μm cells (2-1 mm multi-filament strands) showing crack with 45° orientation coming from the notch.	156
7.2 Schematic showing the strategy used for sectioning tested specimens.	156
7.3 (a) Micrograph at 32x of showing an example of the cracks found behind the notch in the case of each single load-unload test.	157
7.3 (b) Micrograph at 64x of illustrating how no cracks are found in untested notched specimens.	157
7.4 (a), (b), and (c) Shows a crack found in the BN around the notch found before polishing down to the notch tip.	158
7.5 Micrograph of 97-B49b section #1 after polishing down through the notch. There is a crack adjacent to the notch.	159
7.6 Micrograph of 97-B67c section #1 after polishing down through the notch. There is a crack adjacent to the notch and in the BN boundary near the notch.	159
7.7 Micrograph which demonstrates how fine the cracks in the BN are even when tested near failure.	160
7.8 (a), (b), and (c) Shows a crack which appears to have initiated at the surface in the BN and was deflected at the junction with the 0° ply.	161
7.9 Microscopic sections compared to the x-ray radiograph. Sketches from individual specimen sections were drawn from polished sections.	162

7.10 Micrograph illustrating that even in the presence of processing defects (skewed cell bundles) the preferred crack path is the cell bundles and at the defects formed presumably due to the impinged 0° cells	163
---	-----

LIST OF TABLES

TABLE	PAGE
2.1 Data reported by King ¹⁷ for Si_3N_4 -BN fibrous monolith materials in flexure.	13
2.2 Data reported by Staehler ³⁴ for various Si_3N_4 -BN fibrous monolith materials in tension, fatigue, and creep.	20
2.3 Data reported by ACR, Inc. ³⁵ for various Si_3N_4 -BN fibrous monolith materials in tension and fatigue.	22
3.1 Overview of the Test Matrix.	28
3.2 Overview of the analysis.	30
4.1 Tensile Test Data for Monolithic Si_3N_4 .	63
4.2 Tensile Test Data for Straight-Sided Fibrous Monoliths.	64
4.3 Tensile Test Data from Dogbone Fibrous Monoliths.	66
5.1 Results from fast-fracture testing Si_3N_4 -BN and monolithic Si_3N_4 materials.	82
6.1 Lists the data from the fast-fracture, the single load-unload, and the cyclic tests.	119
6.2 Lists the actual test loads in single load-unload testing.	121

FOREWORD

The research presented herein was part of a larger effort being conducted by the Materials & Manufacturing Directorate, Ceramic Development and Material Behavior Branch, at Wright-Patterson Air Force Base on the "Independent Testing and Verification of the Mechanical Properties of Fibrous Monoliths". Support for this work was provided under the U.S. Department of Energy (DOE) Interagency Agreement No. DE-AI02-96CH10871. This DOE agreement was an outgrowth of the Defense Advanced Research Project Agency's (DARPA) Advanced Ceramics Research Advanced Materials Partnership Program. The overall goal of this DARPA Partnership Program was to transition the newly developed processing technology used to fabricate fibrous monolithic ceramics into commercial application. The role of the Air Force under this program was to provide an objective evaluation of the fibrous monolithic materials developed under the Advanced Materials Partnership Program with a focus on the properties pertinent to aerospace application. The material examined herein was provided by the main subcontractor to the program, Advanced Ceramic Research, Inc. (ACR) of Tucson, Arizona.

ACKNOWLEDGMENT

The author gratefully acknowledges Mr. L. Zawada of the Air Force Research Laboratory and Dr. J. Staehler of Systran for the opportunity to work on this project and for their guidance and support. The author also wishes to acknowledge her thesis advisor, Dr. R. Srinivasan (Wright-State University), and the people of AFRL who gave their time, Dr. R. John, Dr. A. Rosenberger, Mr. D. Stubbs, Mr. K. Goecke, and Mr. A. Lackey. Individuals at Argonne National Laboratories are also recognized for coordinating and performing the thermal diffusivity imaging, Dr. W. Ellingson, Dr. J. G. Sun, and Mr. C. Deemer.

CHAPTER 1

INTRODUCTION

Fibrous monolith (FM) ceramics are an innovative class of materials that possess attractive qualities for aerospace and other high temperature applications. This material is designed to possess enhanced toughness over conventional monolithic ceramics through the addition of a weak interphase and is fabricated through cost-effective techniques. Fibrous monoliths are textured ceramics that contain “cells” of a strong phase which are separated by a weak “cell boundary” phase. A schematic representation of the cell and cell boundary structures of the FMs are shown in Figure 1.1. Coblenz¹ introduced the pioneering work on FMs in a patent in 1988. FM processing technology was later developed at the University of Michigan in the early 1990’s². Mature processes for commercial development of FMs were then optimized by the University of Michigan and Advanced Ceramics Research, Inc. under a DARPA Advanced Materials Processing initiative³⁻⁴.

The flexure behavior of FMs is well documented by tests conducted at the University of Michigan during the various stages of material development. Results of those studies qualitatively show that FMs exhibit "graceful" or non-catastrophic failure in bending⁵⁻¹⁸. However, design for potential aerospace applications will require a vast knowledge of the material properties with respect to the processing and microstructure. Material properties under other loading conditions such as tension, fatigue, and stress rupture will be required, and these properties will need to be measured for a range of temperatures. Information about the material

behavior in the presence of stress concentrators, similar to those in structural applications, at attachment points or at service damaged areas will also be required.

The cell size in the FM microstructure is also expected to influence the fracture resistance of fibrous monolith materials. When comparing two microstructures with differing cell sizes but identical volume fractions of the constituent phases, the material with the smaller cell size will, by necessity, contain more cells with thinner boundaries. See Figure 1.2 (a) and 1.2 (b) for schematic drawings that illustrate this concept using two different sized circles. The circles shown in (a) are twice the size of those in (b) but represent equivalent area fractions. The regions between the circles in 1.2 (b) are thinner compared to 1.2 (a).

Assuming that critical flaws scale with some aspect of the microstructure, such as grain size in a metal or monolithic ceramic, and fiber tow size or weave architecture in a composite, one would expect to achieve better mechanical properties with a finer structure. By analogy, one might expect the filament diameter or bundle size to play a dominant role in FMs. However, the processing of finer filaments using the current FM technology and standard ceramic powders can lead to rheology and handling problems not encountered with larger filaments. One manifestation of this are thin and/or discontinuous cell boundaries that can result from the fine orifices and multiple extrusions needed to produce FMs with finer filaments. Cell boundaries that are too thin, or discontinuous, could adversely affect the toughness leading to a cell size threshold for toughness^{5-8, 11, 14, 16-19}.

The intent of this program was to quantify the advantages of fibrous monoliths over monolithic ceramics, and to evaluate the effect of cell size on the mechanical performance. The material investigated was a Si_3N_4 -BN fibrous monolithic ceramic along with a monolithic or neat

Si_3N_4 ceramic. Two different microstructures of the Si_3N_4 -BN FM materials were tested, one with a 125 μm cell size and one with a 250 μm cell size. Mechanical testing, non-destructive evaluation, and analysis were used to meet the objectives of the research. Fast fracture tensile tests were performed on all test materials using both unnotched and modified single-edge notched specimens with various notch length-to-width ratios. Tests were performed either by continuous loading to failure, or by cyclic loading. A comparison of the fracture behavior for the different materials was made using work of fracture measurements and observations about the damage progression through nondestructive evaluation (NDE) techniques and microscopy. NDE techniques employed include x-ray radiography, infrared thermal imaging, c-scan ultrasonics, and acoustic emission. Microscopic observations were also made on polished sections to characterize the damage.

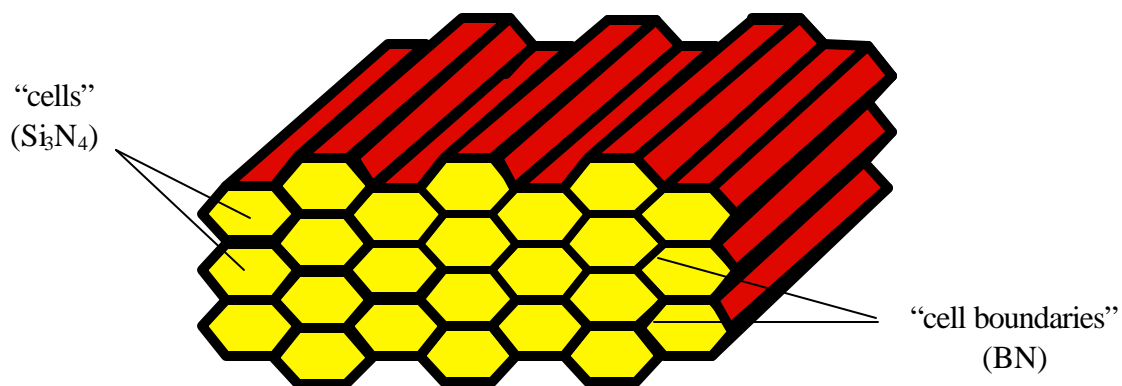


Figure 1.1 Schematic representation of a single filament coextruded fibrous monolith.

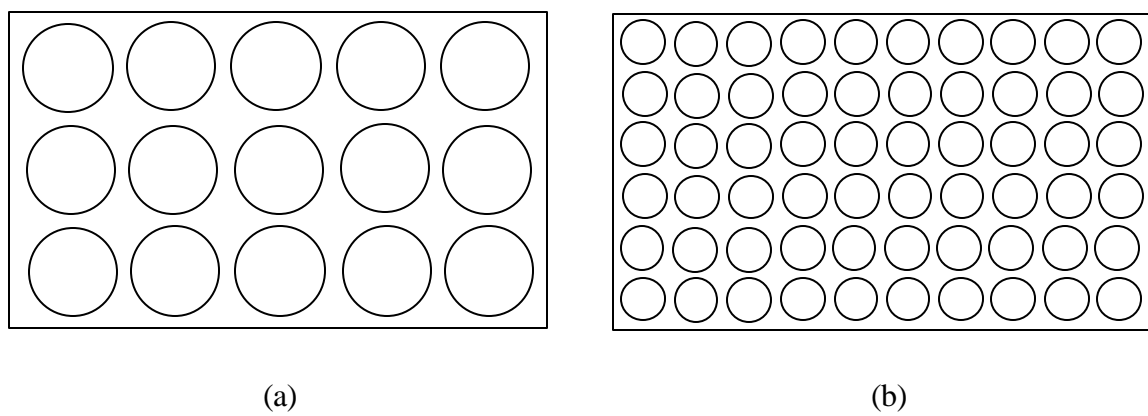


Figure 1.2 Schematic of structures with identical fractions of circles to total area. The circles in (a) are twice as large as those shown in (b). The area between the circles in (b) is thinner compared to (a).

CHAPTER 2

LITERATURE REVIEW: FIBROUS MONOLITHS

Ceramics have long been recognized as a class of materials with widespread potential for high-temperature applications. Modern structural ceramics combine the benefits of high specific properties and corrosion resistance at temperature but suffer from low toughness. Increased demands for performance improvements in aerospace applications and cost effective solutions in commercial applications will require the use of ceramics and their derivatives. Therefore, significant research has been directed at improving the toughness of ceramic materials through alterations in material processing and design of the microstructure.

2.1 The Fibrous Monolith Concept

The drive for better ceramic processing technology brought about a concept by Cook and Gordon²⁰ for a “fiber-less toughened” structural ceramic material which exploited weak interfaces to control crack deflection in brittle systems. More recent work has been done based on this concept by Coblenz¹ in 1988, who originated a method for fabricating a toughened, pressure-less, sinter-able, fibrous material, called a fibrous monolithic ceramic. Coblenz¹ made fibers through conventional powder techniques in which a cotton fiber was infiltrated with Al_2O_3 and subsequently coated with TiO_2 slurry. The fibers were then warm pressed into a ceramic preform and sintered. A similar approach to make a tough ceramic using a layered concept was demonstrated by Clegg, et. al.²¹ who coated SiC green sheets and used pressure-less sintering to make a tough SiC monolith with high strength.

Most recently, Halloran² of the University of Michigan, developed a processing technique to fabricate a similar material as was introduced by Coblenz¹. A number of different toughened materials with a similar fibrous texture as Coblenz have been made using green fiber extrusion techniques⁵. Thus the name "fibrous monolith ceramic" was adopted to refer to this material as well.

Modern fibrous monoliths are best described as textured ceramics since they contain "cells" of a strong phase which are separated by a weak "cell boundary" phase. The weak interface ideally allows for enhanced toughness, by absorbing crack energy and redirecting the crack path parallel to the reinforcing phase rather than through it^{5-6, 8-10, 17-18, 22}. A increase in toughness is usually made at the expense of strength and stiffness. Some examples of the cell and cell boundary materials that have been produced include SiC-BN, SiC-graphite, Si₃N₄-BN, ZrB₂-BN, HfB₂-BN, TiB₂-BN, Al₂O₃-Ni, Al₂O₃-Ni-2Cr, and Y-ZrO₂-Ni^{5-6, 8-10, 18}.

2.2 Processing Fibrous Monoliths

Several processing techniques have been developed at the University of Michigan to fabricate fibrous monolith ceramics. Ceramic powder of the primary constituent is first compounded with a thermoplastic polymer binder. The compounded mix is either dry-spun into green fibers or compression molded into a cylindrical feedrod which is extruded to form a green fiber. The cell boundary material is applied to the dry spun green fibers by dip-coating in a slurry^{5-9, 13}. For the feedrod technique, a cladding of the cell boundary material is applied to the feedrods and both materials are then coextruded^{10, 12, 14-15, 18, 22-23}.

The individual coated green filaments can then be laid-up in the desired architecture and warm pressed into a block. Alternatively, single coextruded filaments can be bundled together and then re-extruded to form a multi-filament coextruded structure²³. The schematic shown in Figure 2.1 represents the multi-filament coextruded structure. The cell bundles can be laid-up into various architectures as well. The warm pressed block undergoes a binder burnout process and is densified via sintering or hot pressing.

2.3 Mechanical Properties of Fibrous Monoliths

Preliminary studies at the University of Michigan on mechanical properties of fibrous monoliths have been performed^{5-16, 18-19, 22, 24-25}. These studies were limited to flexure on the most promising structural material, Si_3N_4 -BN.. The effects of constituent phase volume fraction, interfacial properties, submillimeter structure morphology, test conditions, and cell architecture, on the flexure behavior were investigated. Existing analytical models were used to describe the behavior and to predict the flexure properties of these materials. In addition, a limited study on the tensile, fatigue, and creep behavior was performed at Wright-Patterson Air Force Base under a DARPA initiative.

2.3.1 Flexure Behavior

Fibrous monolith (FM) materials exhibit non-catastrophic failure in flexure^{5-16, 18, 19, 22}. A typical load-displacement trace obtained for a unidirectional fibrous monolith material during flexure testing in displacement control exhibits linear-elastic behavior until an initial load drop, with subsequent peaks in load continuing out to large displacements. Such behavior demonstrates that fibrous monoliths have the ability of continued load-bearing capability after

failure is initiated. Failure of fibrous monoliths in flexure can be initiated by either tensile stresses or by shear stresses. The subsequent graceful failure of these materials is due to crack deflection at the cell/cell boundary interfaces and shear delamination of the cell boundaries. These mechanisms depend on the fraction and structure of the constituent phases (Si_3N_4 and BN), the test conditions, and the architecture of the material.

2.3.1.1 Flexure Behavior as a Function of Cell Fraction

A study of the apparent flexure strength of Si_3N_4 -BN FM as a function of cell fraction showed that the strength was increased while the work of fracture was decreased with an increased fraction of Si_3N_4 ¹². Thus, it was shown that the strength is dependent on the fraction of the continuous phase in the uniaxial direction. The work of fracture, however, did not show a linear trend with amounts of the weak BN phase. Instead, it was found to be greatest for the material consisting of 80% Si_3N_4 - 20% BN due to a combination of substantial strength and extensive crack deflection resulting in high fracture resistance. Based on various studies^{10, 12}, it was predicted that a ratio of approximately 85% Si_3N_4 to 15% BN would provide for the optimum balance of properties.

Studies have also been conducted to look at the effect of additions of Si_3N_4 to the BN boundary phase^{14, 18, 19}. The studies showed that addition of Si_3N_4 to the BN interphase increased the interfacial fracture strength of the material, but decreased the extent of crack deflection and delamination¹⁴. Specimens with pure BN in the interphase showed extensive crack deflection and splintering and retained a significant load following the initial load drop¹⁹. The specimens with up to 40% Si_3N_4 by volume in the interphase exhibited a slight increase in strength, yet a smaller retained load after the initial load drop and limited crack deflections. The

specimens with the largest fraction of Si_3N_4 in the interphase showed the highest strengths but showed little or no crack deflection.

Those results contradict the model of He and Hutchinson²⁶ that predicts the conditions for crack deflection at the interphase boundary. The basis for their prediction is the interfacial fracture resistance and the elastic mismatch of the reinforcing and interphase materials. Kovar et.al¹⁹ suggested that the discrepancy was due to crack deflection and propagation mechanisms occurring within the BN material and not at the Si_3N_4 -BN interface. Cracks were observed to grow into the BN phase, and then be deflected numerous times within the interphase boundary, while propagating parallel to the cells. Thus, the material property which governs crack deflection was found to be the fracture resistance of the BN both parallel and perpendicular to the cell boundary. A lower bound value of fracture resistance measured for BN perpendicular to the cell axis was approximately 120 J/m^2 compared to 30 J/m^2 for the direction parallel to the cell axis^{18,19}. That study by Kovar et. al.¹⁹ confirmed that the morphology of the BN on a submillimeter scale can also affect the extent of crack deflection and delamination cracking. The observation that crack deflection was retained within the BN boundary is indicative of the anisotropy in fracture resistance that exists as a result of the BN morphology. The BN has a plate-like structure (similar to graphite) which ideally becomes aligned parallel to the Si_3N_4 cells during coextrusion and/or during hot pressing. When the (0001) basal planes of the BN grains are aligned parallel to the cell wall, the greatest fracture resistance is in the [0001] direction. The degree to which this anisotropic structure forms is thought to be directly related to the processing^{18, 27, 28}.

It has also been suggested that defects which form as a result of processing can influence the alignment of the BN platelets and can alter the fracture deflection capability of the cell boundary phase^{17, 18, 27}. For example, rough or jagged Si_3N_4 cells, which are sometimes produced when fabricating multi-filament coextruded materials, can skew the orientation of the BN grains with respect to the cell. The flaws created by misalignment could allow a crack to kink out of the boundary and into the reinforcing cells. The worst case would be when the cell boundaries are thin or discontinuous. This type of defect can also be created due to flow instabilities during extrusion.

Another major feature of the submillimeter structure which affects the fracture resistance and the crack deflection within the BN interphase is the presence of microcracks. TEM studies by Trice and Halloran²⁷ revealed that the BN possesses extensive microcracks which separate the (0001) basal planes of the BN platelets into layers. The occurrence of microcracking during processing is attributed to the coefficient of thermal expansion (CTE) anisotropy in the directions parallel and perpendicular to the basal planes of the BN structure¹⁸. The presence of the microcracks are thought to allow for a propagation mechanism based on linkage of the pre-existing cracks and subsequent cleaving of the basal oriented BN grains about the uncracked ligaments²⁷.

The studies of Trice and Halloran²⁷ also showed that there exists an amorphous phase within both the Si_3N_4 cells and the BN cell boundary brought about by the use of sintering aids in the Si_3N_4 during processing²⁷⁻²⁹. The presence of the glassy phase effects the behavior by acting to bridge cracks in the cell boundaries and producing a toughening effect.

2.3.1.2 Flexure Behavior as a Function of Test Condition

Behavior of the Si_3N_4 -BN materials can be influenced by the test conditions. In flexure, the length between the loading pins of the testing apparatus compared to the thickness of the specimen can affect the ratio of tensile to shear stresses. In turn, this ratio dictates the failure as being tensile or shear. This phenomenon was demonstrated by Popovich et. al.¹¹ for fibrous monoliths. He showed that the failure mechanism changed from tensile to shear by changing span depth of the loading pins for a uniaxial SiC-graphite fibrous monolith material, and showed also showed that this change rarely occurs in the Si_3N_4 -BN materials.

The test temperature also has a large influence on the failure initiation and propagation mechanisms. Hilmas¹² showed that the apparent flexural strength of a uniaxial Si_3N_4 -BN with 20% BN was maintained from room temperature to 1000°C, but fell by about 40% at 1200°C. This observed drop in strength was attributed to the oxide sintering aids added to the Si_3N_4 material. During processing, an undesirable glassy phase forms in the grain boundaries, making them unstable at the higher test temperatures. These tests also showed an inverse relationship for work of fracture with increasing temperature.

Trice and Halloran²⁷⁻²⁹ compared the behavior of a uniaxial Si_3N_4 -BN FM over the temperature range from room temperature to 1400°C. The load-displacement behavior was shown to be linear-elastic up to the first load drop at test temperatures up to 1300°C. Values for work of fracture measured in this study were shown to increase slightly with increasing temperature up to 1000°C, but then decreased again up to 1400°C. They determined that the material exhibits a similar degree of crack deflection at 1000°C as seen for room temperature. However, the delamination distances were longer at 1000°C than at room temperature. It was

thought that softening of the oxide glassy phase present from the processing allowed for longer crack extension. It was also observed that the fracture morphologies changed from tensile stress initiated to shear stress initiated at 1100°C, as indicated by a change in compliance on the load-displacement curves. It was suggested that the observed behavior resulted from a decrease in strength of the BN at 1100°C.

2.3.1.3 Flexure Behavior as a Function of Architecture

The cell architecture in the Si_3N_4 -BN fibrous monolith material has also been shown to effect the fracture characteristics. Popovich et. al.¹⁵ showed that a relationship exists in flexure between strength and work of fracture with the amount of cell phase in the 0° direction in Si_3N_4 -BN FM's. They considered materials with a uniaxial and a biaxial multi-filament structure as well as materials with random chopped and woven mono-filaments. The woven material had 20% cells in the ± 45 direction. Uniaxial material was tested in both the 0° and 90° orientations.

The uniaxial material tested in the 0° direction, parallel to the tensile surface, had the highest strengths and largest work of fractures whereas the material tested 90° off-axis was the weakest and showed little fracture resistance. Strengths for the biaxial material, the chopped fiber, and the woven material were approximately the same at an intermediate value between the uniaxial on-axis and off-axis strengths. The work of fracture was greatest for the chopped fiber material and was approximately the same as for the on-axis uniaxial material. The woven material had the lowest work of fracture, followed by the uniaxial material tested 90° off-axis. The fracture resistance of the biaxial material fell in-between the highest and lowest values. It was concluded that in flexure there is a positive relationship to the fraction of cells parallel to the tensile surface and the properties obtained.

King¹⁷ also demonstrated the influence of cell architecture on the mechanical behavior of Si₃N₄-BN fibrous monoliths. He looked at uniaxial, biaxial, and several cross-ply architecture including [± 10], [$0/\pm 60$], and [$0/\pm 45/90$] in bending. He tested uniaxial material at various angles with respect to the tensile plane. The uniaxial material tested on-axis had the highest strength and modulus. At 10° off-axis, the results were similar. Between angles of 10° and 45° off-axis the strengths of the uniaxial material dropped off rapidly to a minimum value when tested 90° off-axis.

The strength, modulus, and work of fracture for the various architectures reported by King¹⁷ are shown in Table 2.1. This data show that the strength and work of fracture increases as the fraction of plies in the 0° direction is increased. The exception is the angle ply material with cells in the $\pm 10^\circ$ direction, which behaved similarly to the uniaxial material.

Architecture	E _x (GPa)	s (MPa)	WOF (J/m ²)	PL (MPa)
Unidirectional - (0°)	276 \pm 1	449 \pm 100	7340 \pm 1540	-
Cross-Ply - (0°/90°)	198 \pm 2	334 \pm 35	6390 \pm 930	- 180
Angle-Ply - ($\pm 10^\circ$)	262 \pm 2	434 \pm 82	8290 \pm 1060	-
Quasi-Isotropic - (0°/ $\pm 60^\circ$)	205 \pm 2	345 \pm 30	3200 \pm 440	- 140
Quasi-Isotropic - (0°/ $\pm 45^\circ/90^\circ$)	202 \pm 3	255 \pm 22	3800 \pm 770	- 140

Table 2.1 Data reported by King¹⁷ for Si₃N₄-BN fibrous monolith materials in flexure.

The uniaxial material tested by King¹⁷ exhibited linear behavior until the first load drop, followed by subsequent load peaks, out to large displacements associated with delamination cracking and pull-out of fractured cells. The fracture associated with the first load drop was

tensile initiated cell fracture. Failure of the cells occurs when the cell boundary material has a locally high fracture resistance compared to the cell material. The continued load-carrying capability shows that failure of individual cells does not preclude failure of the entire tensile surface as would be the case in monolithic or layered ceramics. Load transfer mechanisms usually described for fiber-reinforced composites³⁰⁻³³ are presumably allowing for continued load-carrying capability until the entire layer of cells fails. The cross-sectional area is then reduced, but continued crack deflection, shear delamination, and global load sharing allow for continued loading to large deflections until failure of the remaining plies.

The material with $\pm 10^\circ$ plies showed similar behavior and fracture characteristics to the uniaxial material. The load-deflection curve was linear-elastic to the peak load. At the peak load, failure of the cell boundary along the tensile surface was initiated. Tensile failure of the cell boundaries was shown to be typical in materials with off-axis oriented cells on the tensile surface. The strength of the ply is dictated by the strength of the relatively weak BN interphase. Failure of the specimen in this case occurred after extensive delamination cracking, resulting in high values for work of fracture.

The biaxial ([0/90]) material exhibited slight non-linearity prior to the peak load. Failure initiation occurred at the cell boundary between 0° and 90° layers followed by delamination between the ply layers. The multi-directional materials exhibited behavior close to that of the biaxial material. The material with the $[0/\pm 60]$ architecture exhibited an even greater degree of non-linearity before reaching the peak load. Fracture was initiated in the cell boundaries in the 60° plies below the tensile surface. Failure of the 0° plies occurred through the cells at a 60° angle.

The quasi-isotropic material with a $[0/\pm 45/90]$ architecture showed the most extreme case of non-linearity in the load-displacement trace. Like the $[0/\pm 60]$ material, the failure was found to have initiated at the BN boundary in the off-axis plies below and progressed along a line that was 45° to the axial direction. It was shown that when the material is multi-directional, having uniaxial and misaligned cells, tensile failure occurred by both cell boundary and cell fracture. When the material had cells oriented uniaxially on the tensile surface, the failure initiated in the cell boundaries and the ply failure was precluded by cell fracture along a line equal to the orientation of the cells below.

The non-linear behavior in the multi-directional fibrous monoliths measured by King¹⁷ was attributed to microcracking and failure of the BN cell boundaries in the off-axis plies well before failure of the uniaxially aligned plies. The quasi-isotropic material showed a greater extent of non-linearity as there is a greater number of off-axis plies than for the biaxial and $[0/\pm 60]$ architectures. In these materials, as well as in the $\pm 10^\circ$ material, a relatively high work of fracture was evident. It was suggested that the high fracture energies were possible, even with the premature failure of the off-axis plies, due to frictional sliding mechanisms^{17-19, 25}.

2.3.1.4 Modeling Flexure Behavior of Fibrous Monoliths

Application of existing models to predict the properties and to describe the behavior of the Si_3N_4 -BN fibrous monolith material in flexure has been considered. Work has been done to predict the elastic properties of unidirectional materials, and to extend those predictions to arbitrary microstructures. In addition, there has been some focus on modeling the mechanisms which govern energy absorption. So far no existing models accurately describe the dominant mechanisms of failure which are thought to include delamination cracking and frictional sliding.

King¹⁷ demonstrated the use of modified equations from laminate theory to predict the elastic properties of uniaxial Si_3N_4 -BN fibrous monolith material in flexure. He used a “brick model” to calculate the longitudinal and transverse elastic moduli for the uniaxial material. The model treats the cross-section as a grid of squares which combines the elastic elements in series and in parallel. The values predicted by this model were compared with the values of modulus measured experimentally by an ultrasonic impulse-excitation technique. The values of E_1 and E_2 were predicted within 3% of the experimental value in each case. In addition, King applied the Voigt and Reuss models from laminate theory for the longitudinal and transverse moduli. The Voigt model, or the rule-of-mixtures approach, also predicted the Young’s modulus within 3% of the experimental values. The Reuss model, in which uniform stress to elastic elements are connected in series only, underestimated the Young’s modulus but served as a lower bound for the transverse modulus.

Modified equations from laminate theory for prediction of Young’s modulus as a function of ply angle were applied for a uniaxially aligned architecture as well as for multiaxial architectures. The calculations were in terms of E_1 , E_2 , G_{12} , and ν_{12} , the values of which were predicted in the earlier described models. Results from the modulus predictions in terms of ply angle and multiaxial architectures showed good agreement, within 2.5%, of the experimentally measured values shown in Table 2.1.

The laminate theory models were taken a step further by King¹⁷ to predict the failure behavior of the multidirectional Si_3N_4 -BN fibrous monoliths. An upper bound calculation of the flexural strength was made using the Maximum Stress failure criterion assuming no loss in modulus prior to the peak load. The lower bound calculation used the same criterion but used

an iterative procedure to eliminate plies that exceeded the stress established by the Maximum Stress criteria. The apparent strength for the biaxial material was predicted adequately by the upper-bound technique. The results for the $[0/\pm 60]$ and the $[0/\pm 45/90]$ architectures were over predicted by the upper bound technique by 25-30% and the lower bound technique under predicted the apparent flexural strengths by nearly the same amount. The discrepancies for the quasi-isotropic materials, the $[0/\pm 60]$ and the $[0/\pm 45/90]$ architectures, were identified with the assumptions made about the damage accumulation. The experimental observations suggest that for those two materials, a large amount of microcracking in the off-axis layers occurs before the peak load, and therefore was not modeled correctly in either treatment.

Other attempts to predict the fracture behavior of the Si_3N_4 -BN fibrous monolith materials have been to describe the dissipative mechanisms of failure. The treatment of Folsom et. al.³¹ which calculates the energy absorption due to cracking for laminates were applied to fibrous monoliths. This approach incorporated the fracture energy of the reinforcement phase, the interfacial fracture energy and the cracked area created. Cracks in both the cells and the cell boundaries were taken into consideration by adding their contributions.

$$\begin{aligned} W_C &= W_L + W_i \\ &= \Gamma_L A_L + \Gamma_i A_i^{31} \end{aligned}$$

where

W_L = absorbed energy from cracking cells

W_i = absorbed from cracking in the cell boundaries

Γ_L = fracture resistance of the cells

Γ_i = fracture resistance of the cell boundaries

A_L = the cell area

A_i = the interfacial area

It was found using the cell and interfacial fracture energy values measured by Kovar et.al.¹⁹ and using the total possible crack area for a typical specimen size, the work of fracture predicted was 30% to 35% less than that measured by King¹⁷.

Two main discrepancies were found with this approach. One discrepancy is the implication that increasing the interfacial fracture resistance will increase the energy absorption capability. It was shown by Kovar et. al.¹⁹ that increasing the interfacial fracture of the BN phase decreases the delamination crack length. It has been suggested that the behavior seen by Kovar et. al.¹⁹ may be due to a mechanism termed crack kinking¹⁸. Delamination cracks are thought to kink out of the BN interphase into the cell phase if a flaw greater than a critical size is encountered in either. An increased interfacial fracture resistance in the BN could be considered such a flaw.

The other discrepancy in using this approach alone was that it severely underestimated the work of fracture. Kovar et. al.²⁵ suggested that in addition to crack area creation, energy absorption may also be due to the frictional sliding. After failure initiation, continued crack propagation dictates that remaining plies slide relative to one another. The energy due to sliding is then dependent on the number of plies or cells that are slipping, the distance slipped, and the frictional sliding resistance for cracked cell boundaries.

$$W_s = n\delta A_i \tau_b^{18, 25}$$

where

W_s = absorbed energy due to frictional sliding

n = the number of cell slipping

δ = the distance slipped

τ_b = the frictional sliding resistance for cracked cell boundaries

Using the assumption that the maximum number of cell boundaries are cracked, the results

indicated the energy due to sliding is similar to that due to the creation of crack area. Using the

contribution (Total energy = $W_C + W_S$) from both techniques, a more realistic work of fracture was predicted.

2.3.2 Tensile, Fatigue, and Creep Rupture Behavior

Knowledge of the behavior for the Si_3N_4 -BN fibrous monolith system is limited to flexure. Possible applications pertinent to the Air Force will, however, require a larger knowledge base of the mechanical properties of this material. Limited studies of the tensile, fatigue, and creep behavior of the Si_3N_4 -BN system have been performed by the Air Force and by the main manufacturer of the material, ACR Inc.

Staehler³⁴ performed a limited number of tests on several Si_3N_4 -BN materials in tension, fatigue and creep rupture. The materials tested included an uniaxial multi-filament, biaxial multi-filament, and a $[0/45/90/-45/0/45/90/-45/0/90]_s$ quasi-isotropic mono-filament material. Two different uniaxial multi-filament materials were tested; one fabricated with 1-1 mm strands for a nominal cell size of 50 μm , and the other with 2-1 mm strands for a cell size of 125 μm . The biaxial multi-filament material also had 2-1 mm strands with 125 μm cells. The quasi-isotropic mono-filament had a nominal cell size of 150-200 μm and had been hot-pressed at about half the pressure used to consolidate the uniaxial and the biaxial materials. All of the materials were manufactured to have a volume fraction of 85% Si_3N_4 and 15% BN.

Fast fracture tensile tests were performed at room temperature and 1150°C. Fatigue and creep rupture were performed at 1000°C and 1150°C. Nominal values reported by Staehler³⁴ for the various materials and test conditions are shown in Table 2.2.

Test Type	Architecture	Temp (C)	s (MPa)	E (GPa)	e (%)	t (h)	N
tension	[0], 1-1 mm	23	354	275	0.13		
tension	[0], 2-1 mm	23	496	283	0.18		
tension	[0], 2-1 mm	23	493	289	0.17		
tension	[0], 2-1 mm	1150	346	247	0.15		
tension	[0/90] 2-1 mm	23	151	213	0.1		
tension	[0/90] 2-1 mm	23	123	227	0.06		
tension	[0/90] 2-1 mm	1150	82	188	0.08		
tension	[0/90] 2-1 mm	1150	101	172	0.06		
tension	[Q-I]	23	119	151	0.1		
tension	[Q-I]	23	135	131	0.2		
tension	[Q-I]	23	141	168	0.13		
tension	[Q-I]	23	158	188	0.1		
tension	[Q-I]	1150	100	131	0.1		
tension	[Q-I]	1150	83	116	0.1		
fat T-T	[0], 2-1	1000	150	248-280			160
fat T-T	[0], 2-1	1000	120	220-290			301,725
fat T-T	[0], 2-1	1150	120				37,315
fat T-T	[0/90], 2-1	1000	40				180,000
fat T-T	[0/90], 2-1	1150	40				37,315
fat T-T	[2-I]	1150	40				16,605
creep	[0], 1-1	1000	150	210		100	
creep	[0], 2-1	1150	120			1.9	
creep	[0], 2-1	1150	130			4.9	
creep	[0/90], 2-1	1000	40			50	
creep	[0/90], 2-1	1150	40			19	
creep	[Q-1]	1150	40			9.7	
creep	[Q-1]	1150	60			2.08E-03	
creep	[Q-1]	1150	80			2.64E-03	

Table 2.2 Data reported by Staehler³⁴ for various Si₃N₄-BN fibrous monolith materials in tension, fatigue, and creep.

The fast-fracture tension tests at room temperature in displacement control showed linear behavior in both uniaxial materials. It was also found that the material with the larger microstructural features had a higher strength, by nearly 28%, over the material with the smaller features. The increase in modulus and strain at failure was not considered significant. The difference in properties between the two materials was attributed to a large number of microstructural defects found in the material with the small cells. The defects found were thought to be a direct result of the multi-filament coextrusion process and the anomalies that arise trying to process smaller cell sizes.

The room temperature results for the materials with the different cell architectures showed that as the fraction of Si_3N_4 in the loading direction decreases, so does the strength. A drop in strength by approximately 73% was measured for the biaxial materials compared to the uniaxial material with the same nominal cell size. A simple correction for the fraction of cells in the loading direction indicated that the loss in strength due to architecture should have only been around 50%. Staehler³⁴ suggested that differences between measured and predicted can be attributed, at least in part, to the presence of the cross-ply. Plys in the loading direction can become impinged and damaged due to the cross-plys during processing. The quasi-isotropic material was comprised of single-filaments. The average room temperature strength of this material was around 138 MPa.

Strength data were obtained at 1150°C for only the multi-filament materials with the larger cell size and for the quasi-isotropic material. When comparing the data to room temperature, all materials suffered about a 30% loss in strength. This is compared to the 50% loss in strength measured in flexure at the University of Michigan at 1100°C.

A limited number of fatigue and creep rupture tests were performed at 1000°C and 1150°C by Staehler³⁴ for the [0] and [0/90] materials and the quasi-isotropic material. The results indicated that 1000°C may be the upper-bound use temperature for optimum fatigue and creep rupture properties for all materials investigated. At 1150°C these materials suffer from creep, but remain fairly resistant to oxidation ingress. The resistance to oxidation was documented by SEM inspection. Of the materials tested, the uniaxial material showed the greatest fatigue and creep resistance under the conditions tested.

Advanced Ceramics Research³⁵ has also reported preliminary tensile, fatigue and creep rupture results for Si₃N₄-BN in several lay-ups. The data are shown in Table 2.3. ACR also showed that properties are dependent on the fraction of plies in the 0° direction. The room temperature tensile strengths of approximately 379 MPa for unidirectional multi-filament material reported by ACR are on similar to the values reported by Staehler for the material with the smaller nominal cell size. Similarly to Staehler, the biaxial strength is less than 50% of uniaxial strength. The single filament quasi-isotropic material was reported as having a room temperature strength of 119 MPa.

Architecture	Fast Fracture Room Temperature s, MPa [ksi]	Fast Fracture 1150 °C s, MPa [ksi]	Low Cycle Fatigue 1 Hz, 120 MPa, R=0.1 1000°C
Quasi-isotropic Single Filament	119 [17]	100 [14.5]	n/a
Uniaxial Multifilament	379 [55]	n/a	302,000 cycles (run out)
Biaxial Multifilament	150 [22]	82 [12]	n/a

Table 2.3 Data reported by ACR, Inc.³⁵ for various Si₃N₄-BN fibrous monolith materials in tension and fatigue.

At 1150°C, the biaxial material suffered the largest loss in strength. This material lost 45% while the quasi-isotropic material suffered a 15% loss. Fatigue and creep data were only measured at 1000°C on uniaxial materials. In fatigue the material reached run-out at 120 MPa, while run-out in creep was 150 MPa. Retained properties after creep testing showed the material suffered no loss in strength.

2.4 Literature Review Summary

The need for tough ceramics has led to the development of a fiber-less textured ceramic known as a fibrous monolith. Fabrication of fibrous monolith material consists of traditional powder ceramic processes, relying heavily on coextrusion techniques and hot-pressing. Of the materials which can be processed, the Si_3N_4 -BN system shows the greatest potential for structural application. The majority of the work done to characterize this material's mechanical behavior has been in flexure.

It was shown that the apparent flexural strength was dependent on the fraction of Si_3N_4 in the loading direction, whereas the energy absorbing capability rose with BN content to a threshold near 20% BN by volume. The role of the structure and orientation of the BN interphase was also discussed in terms of the dissipative mechanisms of failure in this material.

The test conditions such as specimen geometry and test temperature were shown to effect the failure mode. The length to thickness of a flexure test specimen was shown to change the failure initiation mechanism from tensile to shear. The apparent strength of the material decreased with temperature due to an amorphous phase that forms during processing as a result of additive sintering aids. This glassy phase was also shown to effect the BN boundaries as an apparent change in failure mode from tensile to shear occurs above 1100°C.

The strength was shown to be dependent on the volume fraction of Si_3N_4 cells oriented along the loading direction. The failure mechanisms which drive the failure of the ply on the tensile surface, and which dictate the subsequent crack deflection and delamination, change with architecture. Failure can occur from tensile stresses by cell fracture, by cell boundary fracture,

by both cell and boundary fracture, or alternatively by shear stresses. Tensile failure initiation was observed on the surface of the specimen when the cell boundary material had a high fracture resistance relative to the cell material, the length to thickness ratio was high, or the test temperature was low. Failure initiation due to shear at the midsection of the specimen was observed when the boundary material was comparatively weak, the length to thickness ratio was low, or the test temperature was high.

Available laminate theory could be applied to the fibrous monolith material to predict the elastic properties as a function of ply angle. However, since other mechanisms such as global load sharing and microcracking take place, models from laminate theory which predict failure strength and work of fracture did not readily apply. Other types of models that account for these and other failure mechanisms, such as frictional sliding, might better approximate failure of the fibrous monoliths.

Limited preliminary data in tension, fatigue, and creep show that properties are dominated by the fraction of plies in the loading direction. Tensile results revealed that there may be effects of processing which dictate a cell size and architecture effect. Elevated temperature testing showed that no loss in durability when tested at 1000°C. However, 1150°C may be beyond the useful temperature range for this material. Limitations at elevated temperatures were presumably due to creep mechanisms and not oxidation.

Review of the literature for Si_3N_4 -BN FMs shows a deficiency in the knowledge base for behavior under tensile loading conditions. In addition, limited direct measurement has been made to address cell size issues and little information has been gathered to study the material behavior in the presence of stress concentrations. Therefore, the study herein was proposed to

address these issues through the use of mechanical, non-destructive testing, and existing methods. The goal was to quantify the mechanical behavior in terms of notch sensitivity, or energy absorption capability, for materials with different cell sizes and in the presence of machined notches.

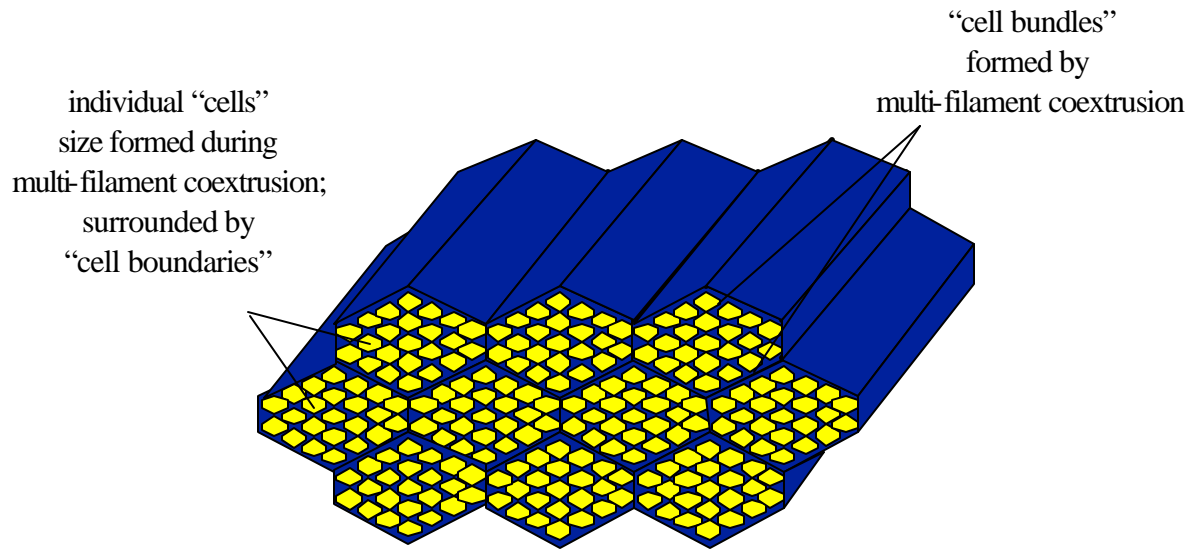


Figure 2.1 Schematic representation of a multi-filament coextruded material.

CHAPTER 3

TEST MATRIX, MATERIAL DESCRIPTION, AND EXPERIMENTAL PROCEDURES

A description of the test matrix, the materials, and the experimental procedures are described in the following chapter. The first section defines the test matrix. The next section describes the test materials and the specimen geometry's tested. The last section describes the procedures used in performing both the destructive and non-destructive tests.

3.1 Test Matrix

The mechanical performance of two Si_3N_4 -BN fibrous monolith systems, one with a cell size of $125\text{ }\mu\text{m}$ and the other with a cell size of $250\text{ }\mu\text{m}$, were compared to each other and to monolithic Si_3N_4 . The mechanical behavior was evaluated through fast-fracture tensile testing straight-sided, dogbone, and modified single-edge notched specimens of each of the materials. Loading conditions including continuous loading to failure, load-unload, and cyclic loading. A limited number of tests were also run at elevated temperature. See Table 3.1 and the included schematics for an overview of the test matrix and of the different loading conditions.

Fast-fracture tests were run continuously to failure on straight-sided and dogbone specimens in order to obtain a base-line strength for the materials. The same loading

Test Temp (°C)	Loading (0.001 mm/s)	Specimen Geometry	Number of Specimens		
			Fibrous Monolith		Neat Si ₃ N ₄
			125 µm	250 µm	
23	¹ continuous to failure	SS	4	4	---
		DB	2	2	2
		MSE(T) a ₀ /W = 0.3	3	2	2
		MSE(T) a ₀ /W = 0.1	1	1	1
		MSE(T) a ₀ /W = 0.2	1	1	---
		MSE(T) a ₀ /W = 0.5	1	1	1
	² single load-unload	MSE(T) a ₀ /W = 0.3	4	4	---
	³ cyclic	MSE(T) a ₀ /W = 0.3	1	1	---
1150	¹ continuous	MSE(T) a ₀ /W = 0.3	1	1	1

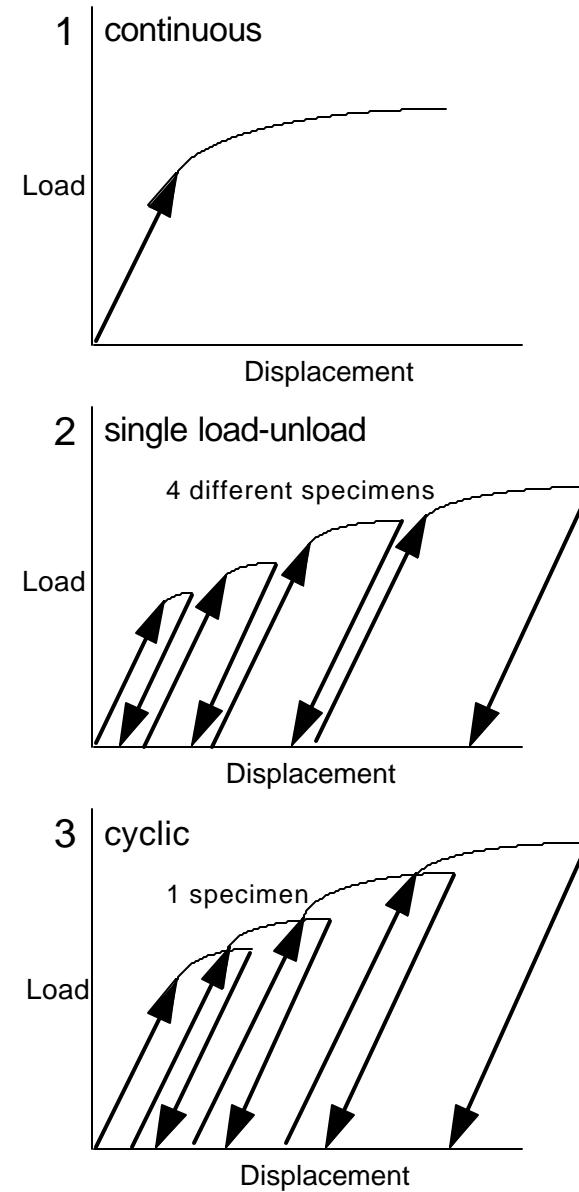


Table 3.1 Overview of the Test Matrix.

conditions were used to test notched specimens at room temperature. The notched specimens had one of four notch length-to-width ratios (a_0/W), 0.1, 0.2, 0.3, and 0.5. Different notch lengths were used to observe notch sensitivity. A specimen with an a_0/W ratio of 0.3 from each material was tested at 1150°C to look at temperature effects. In addition to the fast-fracture tests, a number of load-unload and cyclic fracture tests were performed at room temperature. These tests were performed in conjunction with several non-destructive evaluation (NDE) techniques including x-ray radiography, infrared imaging, ultrasonic c-scanning, and acoustic emission to determine the critical stages of damage evolution.

Results from testing the various a_0/W ratios were used to quantify the notch sensitivity of the material. The applicability of two different approaches to describe the notched behavior of the materials were considered: a Linear-Elastic Fracture Mechanics (LEFM) approach, and a net-section stress approach. Ultimately, a comparison of the fracture behavior had to be made using work of fracture measurements and observations of damage progression made through NDE and microscopic inspections. See Table 3.2 for an overview of the analysis outlined above, showing the physical meaning of the terminology associated with the analyses and the equations used.

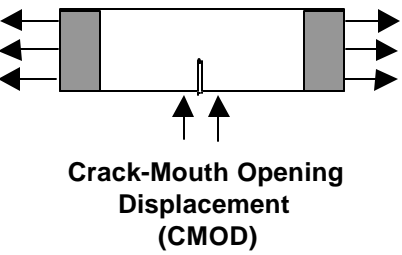
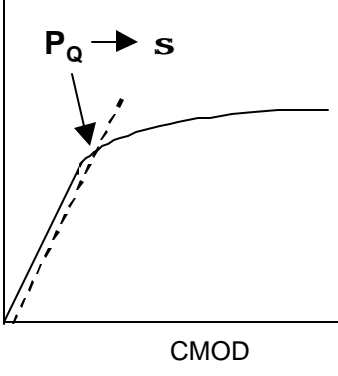
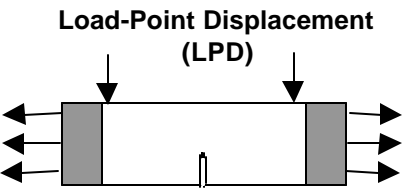
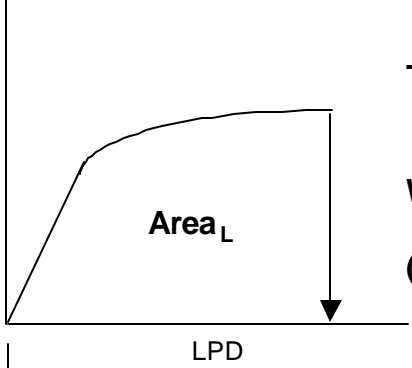
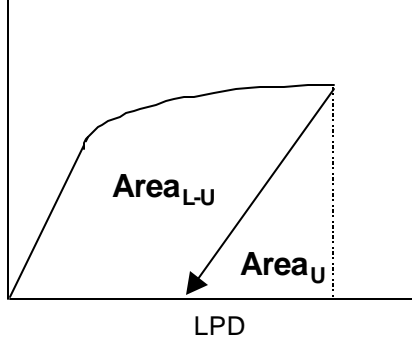
<p>Notched Behavior in Terms of Linear-Elastic Fracture Mechanics (LEFM)</p>	 <p>Crack-Mouth Opening Displacement (CMOD)</p>  <p>Where,</p> <p>Effective Stress Intensity Factor, K_Q</p> $K_Q \approx s \sqrt{\pi a_0} * F(a_0/W)$
<p>Fracture Behavior in Terms of Energy Absorption or WOF (Work of Fracture)</p>	 <p>Load-Point Displacement (LPD)</p>  <p>Total Work of Fracture, WOF_T</p> <p>$WOF_T = \text{Area}_L / \text{Cross-sectional area (elastic + "plastic")}$</p>  <p>Work of Fracture, WOF</p> <p>$WOF = \text{Area}_{L-U} / \text{Cross-sectional area ("plastic" only)}$</p>

Table 3.2 Overview of the analysis.

3.2 Material Description

The materials tested in this study included a Si_3N_4 -BN fibrous monolith system and a monolithic Si_3N_4 material. Two different microstructures of the Si_3N_4 -BN were tested, each with a multi-filament coextruded structure. Both fibrous monolith materials had the same cell bundle volume fraction, bulk density, and cell architecture. All test materials were produced by Advanced Ceramics Research, Inc. (ACR), Tucson Arizona, using multi-filament coextrusion techniques.

3.2.1 Fibrous Monolith Material

Ten 114 mm x 76 mm (4.5"x3") plates of Si_3N_4 -BN fibrous monolith material were produced using multi-filament coextrusion techniques for this study. Five plates were manufactured to have individual cell sizes of 125 μm within 1 mm cell bundles and the other five were made with 250 μm cells within 2 mm cell bundles. The cell bundles are formed because of the coextrusion process. The coextrusion processing steps are illustrated in Figure 3.1 which include: 1) ceramic/polymer preparation, 2) feedrod formation, 3) coextrusion, 4) green body structure formation and compaction, 5) binder removal, and 6) densification^{17,23}. Initial coextrusion of the feed rod was through a spinneret of 2 mm diameter. The resulting filaments were bundled together and co-extruded a second time to form multi-filament bundles. The 125 μm and 250 μm cells were formed this second extrusion using 1 mm and 2 mm spinnerets, respectively.

Sintering aids were used in fabrication to aid in consolidation. These sintering aids were approximately 6 wt% Y_2O_3 and 2 wt% Al_2O_3 . The target Si_3N_4 to BN ratio for both materials was 85% to 15%.

The FM lay-ups were formed by stacking sheets of uniaxially aligned multi-filament strands. The finer celled material originally supplied by ACR had 16 sheets stacked in a [0/0/-45/0/+45/-45/0/+45]_s sequence with an as-fabricated thickness of approximately 7.6 mm (0.3"). The material with the larger filaments had 8 sheets stacked in a [0/-45/0/+45]_s sequence and was 6.5 mm thick.

Since the materials were not fabricated with identical multi-filament lay-ups and had thickness' that were too large to test, each was machined such that the resultant lay-up was [-45/0/+45]_s. In machining the plates with the 125 μm cells, more material was removed from one surface than from the other. The micrograph in Figure 3.2 (a) shows a cross section from a plate of the finer microstructure with more plies removed on one surface. Figure 3.2 (b) shows how the machining on the plates of material with the larger cells was symmetric.

Both microstructures were found to contain a nominal 75 vol.% of cells and a 25 vol.% of cell boundaries. Each had an average bulk density pycnometry reading of 3.06 g/cc. The plates with the fine cells were machined down to approximately 2.9 mm thick and the plates with the large cells were approximately 4.3 mm thick, both with the [-45/0/+45]_s cell bundle architecture as described above.

Optical inspection of the as-received fibrous monolith materials found a number of microstructural abnormalities that were presumably caused during processing. Looking parallel to the tensile direction as in Figures 3.2 (a) and 3.2 (b), the 45° cells impinge upon the 0° plies. In turn, this displaces the 0° cell bundles and causes the displaced material to form points between the 45° bundles.

The cell bundles in the 45° plies can become distorted as well. Distorted cell bundles may be a result of alignment and impingement of the 0° and 45° plies. Kinks also form in the 0° plies during the extrusion process. Other types of defects observed, which were also a direct result of the multi-filament coextrusion processing, include jagged cell edges and inconsistent cell sizes within the cell bundles.

All the defects described above are shown in the micrographs in Figures 3.3 (a), (b), and (c). Figure 3.3 (a) illustrates the impinged, distorted, and kinked cells as described above. This figure also shows how the multi-filament coextrusion process can produce variations in the individual cell size contained within a bundle. Figure 3.3 (b) shows rough or jagged cells formed within the cell boundaries due to the multi-filament coextrusion processing. Rough or jagged cell surfaces are thought to adversely affect the orientation and the properties of the BN interphase structure. The micrograph in Figure 3.3 (c) shows a crack within the BN interphase which exemplifies how the jagged cells can effect the orientation of the BN structure.

3.2.2 Monolithic Si_3N_4

Two 114 mm x 76 mm plates of the monolithic Si_3N_4 material were processed for this study using identical powder stock, sintering aids, and processing steps as was used to fabricate the fibrous monolith material. The only difference in the processing was the absence of the BN cladding. It was desired to have neat material that was processed in the same manner as the FMs for direct comparison. Therefore, feedrods of the Si_3N_4 were formed and extruded into Si_3N_4 strands. The strands were then made into laminate sheet, laid-up uniaxially, and then consolidated the same as for the FMs. The average pycnometer bulk density measured for the neat materials was 3.31 g/cc.

3.2.3 Machining Layout

Each FM plate was machined into four straight-sided specimens; three of which were 19 mm (3/4") wide for notched fracture testing while the fourth was 12.5 mm (1/2") wide for tensile testing. The machining lay-out for the specimens is shown in Figure 3.4. In each case, the 12.5 mm tensile specimen was machined from the interior of the plate to avoid any possible edge effects. The machining lay-out for the Si_3N_4 material was identical to that for the fibrous monolith material, except that the tensile specimens had a dogbone geometry. Specimens were machined from the plates using a diamond saw blade. Final grinding of the specimen surfaces was done using a 320 grit wheel at a removal rate of 0.05 mils per pass.

Tensile specimens were machined from the plate interior because all of the plates appeared to have edge defects formed during hot-pressing. The defects were evidenced visually by a white residue in the material within a region around the edge of the plates. Figure 3.5 (a) is a photograph taken of an as-received plate showing the region of affected material.

King¹⁷ showed that material in the outer edge of the plate typically contains a significant amount of α -SiC in addition to the β - Si_3N_4 and BN. The interior material was not shown to contain SiC but was found to contain β - Si_3N_4 and non-transformed α - Si_3N_4 in addition to the BN. He suggested that this was caused by a significant thermal gradient across the billets during hot-pressing. The outer edges were hotter and caused a reaction with the graphite dies whereas the center was cooler. Within the region of affected material at the edge, filaments can become displaced from alignment with the plies in the interior. It is suggested that these displaced and distorted ply ends result from a combination of extreme heat at the edge during hot pressing and flow of the material as it fills in gaps at the edges that occurred during the lay-up process. Figure

3.5 (b) is a micrograph of the cross-section of material at the edge of a plate showing the displaced and distorted cells.

The presence of edge defects were not as critical for the fracture specimens since a single-edge notch was machined into these specimens on the plate-edge-side, and the machined notch extended well beyond the distorted edge region. The failure initiation point was then expected to be dominated by the stress concentration due to the notch and not the plate defects at the edges. Refer to Figure 3.4 for the illustration of the orientation of the notches with respect to the plate edges. The notch lengths were longer than the zone that contained the edge defects. See the photograph in the Figure 3.6 for an example of a specimen with a single edge notch of a length equivalent to $a_0/W = 0.3$.

3.3 Experimental Procedures

3.3.1 Tension Test Procedures

Tension tests on the 12.5 mm straight-sided fibrous monolith specimens and on the monolithic Si_3N_4 dogbone specimens provided base-line properties for these materials; namely elastic modulus, strength, and work of fracture, and plate to plate variability. The base-line moduli were utilized as a reference check during the fracture testing.

3.3.1.1 Specimen Geometry

In addition to the straight-sided tensile specimens, two dogbone specimens from each microstructure of the fibrous monolith material were tested to look at geometry effects. The fibrous monolith dogbone specimens were machined from fracture specimens, had a gage width of 12.5 mm, and had a 30% reduction from tab width to gage width. The monolithic Si_3N_4

tensile specimens had a dogbone geometry with a 30% reduction from tab width to gage width as well. The gage width for these specimens was 6 mm. Figures 3.7 (a), 3.7(b), and 3.7 (c), show schematics of the respective test specimens for the fibrous monolith and neat materials along with their dimensions. The schematic of the straight-sided specimen includes the fiberglass tabs used for gripping. The use of the fiberglass tabs is discussed in section 3.3.1.3.

3.3.1.2 Testing Apparatus

The apparatus used for tensile testing included a MTS^{*} vertical servo-hydraulic test machine, a data acquisition computer, and a clip gage extensometer. The test system was equipped with wedge grips fitted with serrated grip inserts. Use of both DC and AC controllers allowed for tests to be conducted in load, strain, or stroke control. Specialized software was used to command the controllers to run the test and to acquire data through a 12-bit digitizer. See Figure 3.8 for a photograph the test frame with the wedge grips and wedge inserts. A calibrated clip gage extensometer was used to measure strain.

Tensile specimens of the neat Si_3N_4 material were tested on a similar MTS servo-hydraulic test system with a horizontal load frame and rigid clamping grips. See Figure 3.9 for a schematic representation of the horizontal load frame. Rigid clamping grips allow for a higher degree of alignment, which was desirable in testing the brittle monolithic material. These tests were also run using the same system software and the data in this case were collected through a 16-bit digitizer. A clip gage type extensometer was used for strain measurement.

3.3.1.3 General Procedures

^{*} MTS is a registered trademark of the MTS Corporation

The fibrous monolith tensile specimens were prepared for testing by adhering fiberglass tabs at each end.. The use of tabbed specimens in the wedge grips for tensile testing the fibrous monolith material minimized the stress concentration imparted by the grips on the straight-sided geometry. All tests, including the neat material, were run at room temperature and with a constant stroke rate of 0.001 mm/s.

3.3.2 Fracture Test Procedures

Fracture testing of both fibrous monolith materials and neat Si_3N_4 material was performed using the horizontal load frame with rigid clamping grips. Tests were run continuously to failure (fast fracture), in a single load-unload regime, or with cyclic loading at room temperature using modified single edge-notched specimens. The specimens tested had one of four notch length to width (a_0/W) ratios; 0.1, 0.2, 0.3, or 0.5. The load-unload and cyclic fracture tests were performed on specimens with an a_0/W ratio of 0.3 and were used in conjunction with several non-destructive evaluation techniques to study damage progression. Additional fracture tests were performed on each material at 1150° with an a_0/W ratio of 0.3.

3.3.2.1 Specimen Geometry

The modified single-edge notched MSE(T) specimen geometry is described by the height (H) or the distance between the grips, the width (W), and the initial notch length (a_0). All of the specimens tested were 19 mm wide and were tested with a H/W ratio of 4.3. The majority of the specimens tested had an a_0/W ratio of 0.3, however, specimens with ratios of 0.1, 0.2, and 0.5 were tested as well. See Figure 3.10 for a schematic representation of the MSE(T) specimen.

Each notch was machined using a table saw. The table saw has a stage with motorized travel in the x-direction and manual travel in the y-direction. The specimens were prepared for machining by sandwiching them between two pieces of fiberglass to protect them from burring. Each specimen was leveled and aligned perpendicular to the blade using a dial indicator. The cut was made using a high concentration diamond blade that was approximately 0.15 mm (0.006") thick. The notch was made by removing 0.0254 mm (0.001") per pass. The dimensions of the notches made using this procedure were all within 2% of the target length and were no more than one half of the notch width out-of plane.

3.3.2.2 Testing Apparatus

Two different extensometers were used during each fracture test. One extensometer was used to measure the crack-mouth opening displacement (CMOD) while the other measured displacement at the points of loading. Several different types of extensometers, including a high-temperature style alumina rod extensometer and various clip gage types were used to measure the CMOD on different tests. In general, the clip gage extensometers were preferred to measure CMOD as they have higher resolution and are capable of better repeatability. A high-temperature style extensometer with bent quartz rods specifically designed for these tests measured the load-point displacement (LPD). A photograph of the modified extensometer used for load-point displacement measurement is shown in Figure 3.11. The data, including the load, stroke, CMOD displacement, and the load-point displacement, were collected by the computer. Both filtered and unfiltered data were collected and stored. A photograph of the room temperature test set-up is shown in Figure 3.12. The photo shows the

specimen instrumented with a high-temperature extensometer for CMOD measurement and the bent rod extensometer for load-point displacement measurement.

For elevated temperature testing, an induction heated furnace system was added to the test frame. A photograph of the elevated temperature test set-up is shown in Figure 3.13.

3.3.2.3 General Procedures

Prior to fracture testing, a series of modulus checks on each specimen were performed to verify that the MSE(T) specimens were aligned. A specimen was considered to be aligned when the elastic modulus was within 10% of the Young's modulus for the material. Before machining the notches, each specimen was loaded and unloaded a number of times under very small loads (loads equal to a stress of 5 MPa). An average modulus was determined for each specimen from the stress versus strain data acquired in the un-notched condition. Once each specimen was notched, it was cycled to the same low net section loads. The unloading data from each cycle was used to obtain an average compliance and modulus using linear-elastic relationships. Those equations used are as follows:

$$C = d / P \text{ (experimental)}$$
$$C = 2G a_0 / EBW \text{ (theoretical)}$$

where

C = compliance

d = the crack mouth opening displacement (CMOD)

P = load

G = elastic energy release rate

a_0 = initial notch length

E = elastic modulus

B = specimen thickness

W = specimen width

The modulus was determined when the theoretical value of compliance was equal to the experimental value measured. The constants used to calculate G for the MSE(T) specimen geometry with clamped ends were developed by John and Rigling³⁶. The modulus results were then compared with the average Young's modulus obtained from the pre-notched and tensile specimens.

Fracture tests specimens were not only instrumented with two extensometers, but were also instrumented with two strain gages and two acoustic emission transducers to aid in identifying critical loads that result in damage progression. One strain gage was added on either side of the notch. For reference in later discussions of the data, the strain gage that was positioned on the load cell side of the specimen notch (the right -side of the specimen notch as shown in all subsequent photographs) is referred to as strain gage number 1. The strain gage that was positioned on the actuator side of the specimen notch (the left-side of the specimen notch as shown in subsequent photographs) is referred to as strain gage number 2. The gages were offset from the notch by approximately one to two millimeters with the center of each gage level with the notch tip. See Figure 3.14 for a photograph of the strain gage set-up. The position of the AE transducers is discussed in section 3.3.3.4.

A triangular waveform profiler was used to produce an actuator displacement rate of 0.001 mm/s in stroke control. For the tests run continuously to failure, only half of the triangular waveform was used. The single load-unload tests utilized the entire waveform. Filtered data recorded from each test included; load, CMOD, load-point displacement, and stroke.

3.3.3 Non-Destructive Evaluation Procedures

Non-destructive evaluation (NDE) techniques were utilized to characterize the fibrous monolith material without altering its structure or properties. Details surrounding the use of and the techniques associated with non-destructive evaluation are given elsewhere³⁷. Due to the potential insight NDE may provide in characterizing the damage progression of the fibrous monolithic material, a number of NDE techniques were implemented before, during, and after fracture testing.

Several different NDE techniques were considered for damage evaluation of the fibrous monolith material. Techniques used include visual inspection, x-ray radiography, infrared thermal diffusivity imaging (or thermography), ultrasonic c-scanning, and acoustic emission detection. Each of the techniques performed are suited for detection of specific types of anomalies using different physical principles. It was proposed that the different techniques used in combination with one another would then provide a comprehensive evaluation of the condition of the fibrous monolith material.

Visual inspection with the aid of low magnification ($<32\times$) was used in the case of each specimen to identify gross surface changes. X-ray radiography was used to identify through-the-thickness type cracks with high resolution. Thermography and ultrasonic c-scanning were used to detect interlaminar type cracks found to occur in the fibrous monolith material. Acoustic emission detection was to identify stress levels critical to damage progression as well as location of damage. Since none of these techniques had been performed on fibrous monolith material before, the final step in the overall characterization of the material was to verify the NDE results by sectioning, polishing, and inspecting suspected damaged regions under magnification.

3.3.3.1 X-ray Radiography

The system used to obtain x-ray radiographs is located at Wright-Patterson Air Force base, Ohio and is a Philips minifocus x-ray tube that is rated for 160 kVp (kilo-volt potential) and 25 mA. The focal spot size of the beam for this tube is 0.4 mm which is related to the resolution of the system. Energies used to inspect the FM and the neat material were 60 to 80 KeV with 5 mA current. Kodak type M high resolution film was the sensing material employed. The distance between the x-ray source and the film was approximately 40 inches. To obtain the images, the test materials were placed flat directly on the film which produced a 1:1 image. Exposure time required to obtain the image was approximately one to two minutes. A contact print or positive was made from the film for viewing. A schematic representation of the x-ray system used in this study is shown in Figure 3.16.

X-ray radiography was used in this study to identify as-processed anomalies prior to testing. The FM and neat test materials in the as-received plate form were inspected via this technique. Figures 3.16 (a) and 3.16 (b) contain radiographic images from representative plates of the FM and neat materials, respectively. All of the FM plates were shown to contain a significant amount of irregular dark features which can be seen in Figure 3.16 (a). The defects are areas of high density compared to the surrounding material. Microscopic investigation performed on the test material discussed earlier showed that the material contains a number of defects, some of which can be described as skewed cell bundles or kinked bundles. Skewed cell bundles, presumably caused during hot pressing due to alignment and impingement of the 0° and 45° plies, allows for a change in the x-ray attenuation. The exact mechanism that allows for

these denser strips to appear so clearly on the x-ray has not been identified. The radiograph of the neat material shows it to be uniformly dense except around the edges.

In addition to using x-ray radiography for as-received material, the technique was used to detect through-the-thickness type cracks that developed during mechanical testing.

Radiographs were obtained on all MSE(T) specimens both before and after continuous fracture testing and load-unload testing.

3.3.3.2 Infrared Thermal Imaging

Infrared thermal imaging was performed at Argonne National Laboratory in Argonne, Illinois. The thermal imaging apparatus is comprised of a flash lamp system, an infrared camera, and a computer for data acquisition and processing. More information on this system can be found elsewhere³⁸. The flash lamp system uses two standard photographic xenon flash-lamps to generate the thermal pulse. The infrared sensing camera was a Galileo model IR video camera made by the Amber Engineering Company. The IR camera uses a focal plane array of InSb detectors capable of 256 x 256 pixels. The camera is interfaced with a function generator and a dual timing trigger. A digital frame grabber acquires images from the camera, and these images are further processed on the computer. See Figure 3.17 for a schematic drawing of the rapid infrared thermal imaging apparatus used at Argonne³⁸.

Rapid infrared thermal imaging was employed to document the damage induced from the load-unload testing. This technique better lends itself to the detection of interlaminar defects than does the radiography technique. Only the MSE(T) specimens with an a_0/W ratio of 0.3 were inspected via this technique. Specimens were inspected both before and after testing.

All of the fibrous monolith specimens that were tested via the load-unload procedures, and designated specimens tested continuously to failure, were sent to Argonne Labs to undergo thermal imaging. The MSE(T) specimens that were cyclically loaded underwent thermal imaging before testing to obtain a reference thermal diffusivity value and heat flow pattern. Following testing, the specimens were sent back to be evaluated by both the thermal imaging and by time domain techniques. Designated specimens with an a_0/W ratio of 0.3 that were tested continuously to failure were also inspected by these methods following mechanical testing. An average pre-test diffusivity from the cyclically loaded specimens were used as a reference for all post processing and analysis.

3.3.3.3 Ultrasonic C-scanning

Reflector plate type c-scan images were obtained using immersion scanning equipment at the University of Dayton Research Institute. The major components of the scanning system include a large open water tank, a motorized x-y scanner with a manual z control, a broadband ultrasonic transducer, a JSR-PR35 signal pulser/receiver, and a computer equipped with SONIX™ operating and data acquisition software. See Figure 3.18 for a schematic illustration of the ultrasonic scanning system. The transducer used was a KB Aerotech 10 MHz focused transducer, which had a 12.5 mm diameter and a 75 mm focal length. The scanning step size of the transducer or correspondingly the image pixel size was set to be 0.25 mm.

Reflector plate type ultrasonic c-scans were also obtained for interlaminar delaminations detection. Before scanning the fibrous monolith specimens, a calibration of the system was performed using a reference block according to standards in the literature³⁹. Calibration, in this

case, refers to the method of setting and documenting the gain of the system so a scan can be reproduced or compared to others.

Only the MSE(T) specimens which had undergone testing were scanned and therefore no pre-test scan was obtained for comparison. The c-scanning technique was only considered for use in this study after the thermal imaging technique was shown to lack in resolution needed to detect evolving damage in the fibrous monolith materials. Although it was known to have better resolution, immersion ultrasonic c-scanning was not originally proposed in the experimental plan since extended periods of exposure to water has been shown to degrade the mechanical properties of materials containing boron nitride.

3.3.3.4 Acoustic Emission Inspection

The equipment used to obtain the acoustic emission information was from the Digital Wave Corporation. The main components of the system included: two broadband contact transducers, two broadband preamplifiers, a signal conditioner, and a signal analysis processor. The transducers were set on the fibrous monolith test specimens approximately 70 mm apart, centered about the middle of the specimen. A schematic in Figure 3.19 illustrates the components of the AE test system. The transducers were held in contact with the specimen during the test by using vacuum grease and spring clips. Data acquisition and final analysis was performed using a computer equipped with Digital Wave's Fracture Wave Detector (FWD) software. Parametric information for load and crack-mouth opening displacement in volts was also obtained by the signal analysis processor through a connection to the MTS controller.

Acoustic emission (AE) detection methods were used to identify stress levels critical to the damage initiation and evolution in the fibrous monolith material during fracture testing. AE

data from specimens tested to failure were used to determine appropriate unload points for the single load-unload testing. In addition to providing a relationship with stress-CMOD information, the information obtained from the AE was used to provide another source for damage location identification. This information was compared to the output obtained from the other NDE techniques on the same single load-unload specimens.

Before running each fracture test, the sound wave velocity in the material was determined for use in the source location detection. The velocity was found by conducting a “lead-break” test. The time of flight associated with breaking a pencil lead on the specimen in front of each transducer was used along with the distance between the transducers to obtain velocity.

The data from the fracture tests along with the velocity of sound estimation were reduced through the FWD software which uses cross-correlation techniques for source location detection. The output from the source location module was given in terms of event number, time, location, and parametrics. The location data were then made into a histogram and plotted along the length of the specimen. The parametrics data were converted from voltage to load and CMOD and plotted against the data obtained from the CMOD extensometer.

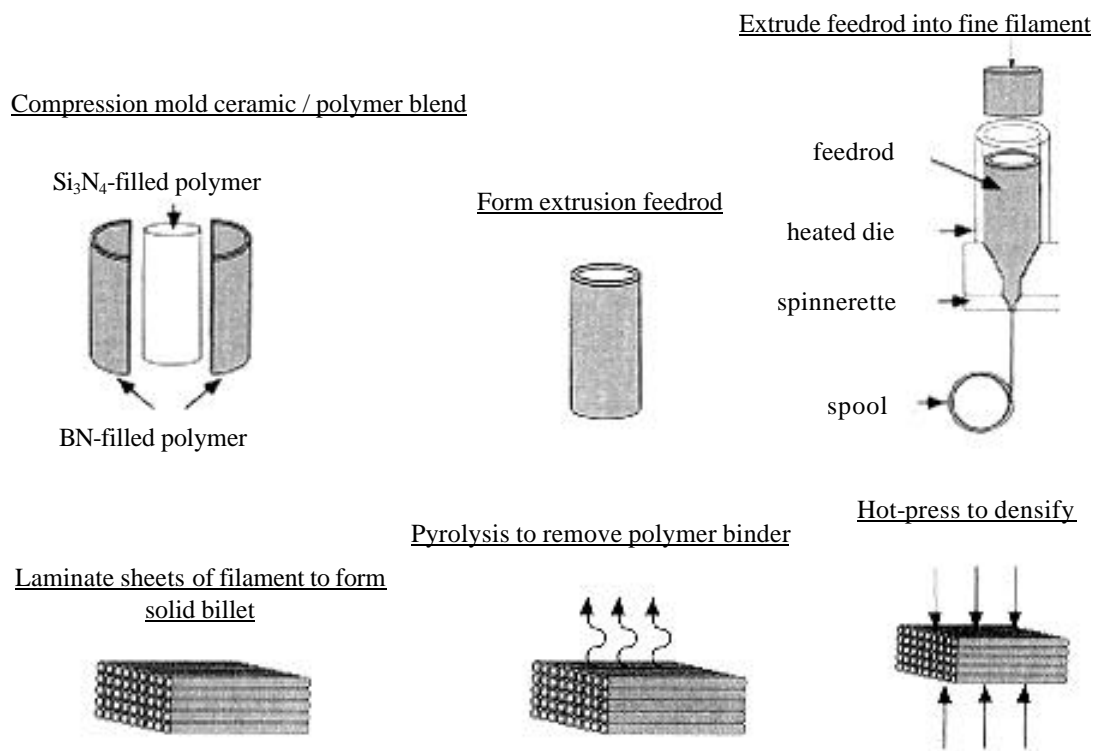


Figure 3.1 Schematic illustrations showing processing route to fabricate fibrous monoliths using coextrusion methods²².

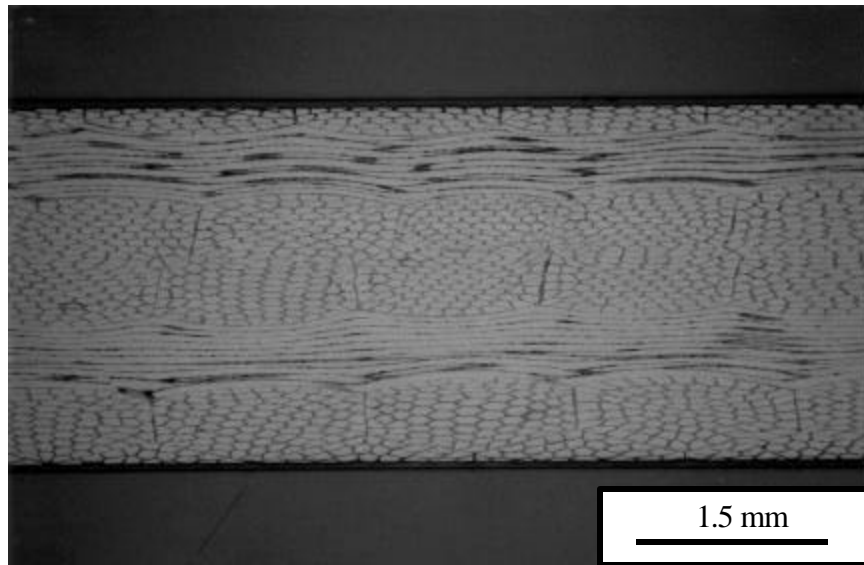


Figure 3.2 (a) Micrograph at 16x of Si_3N_4 -BN fibrous monolith [-45/0/+45]_s with 125 μm cells (2-1 mm multi-filament strands).

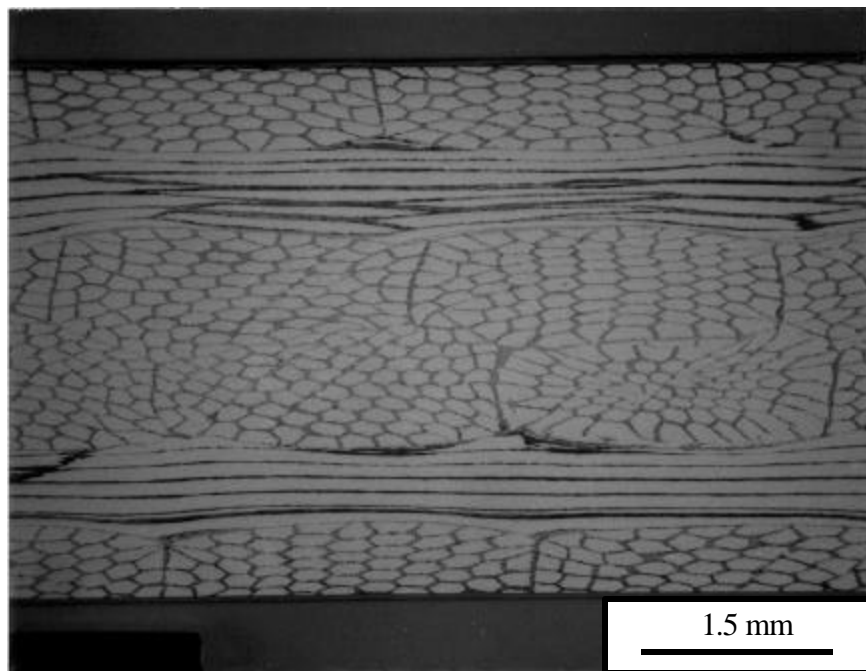


Figure 3.2 (b) Micrograph at 16x of Si_3N_4 -BN fibrous monolith [-45/0/+45]_s with 250 μm cells (2-2 mm multi-filament strands).

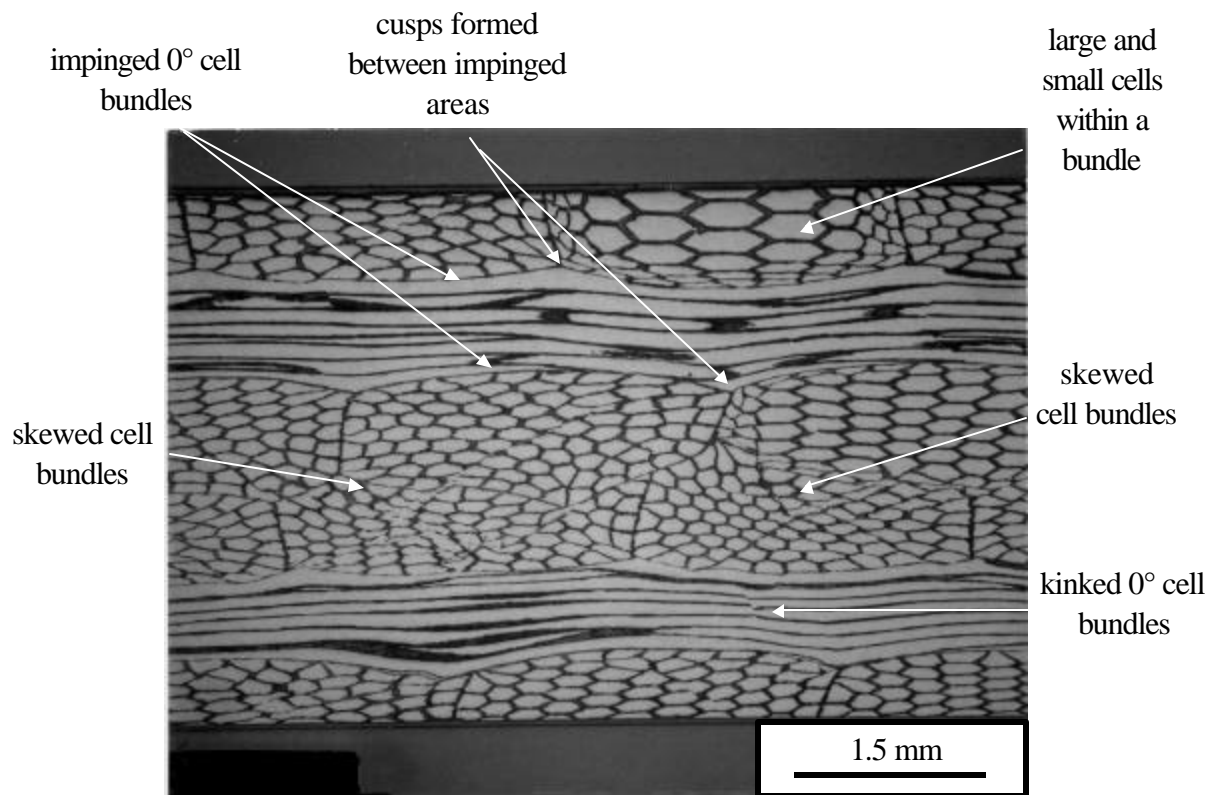


Figure 3.3 (a) Micrograph at 16x of Si_3N_4 -BN fibrous monolith showing a number of different processing defects.

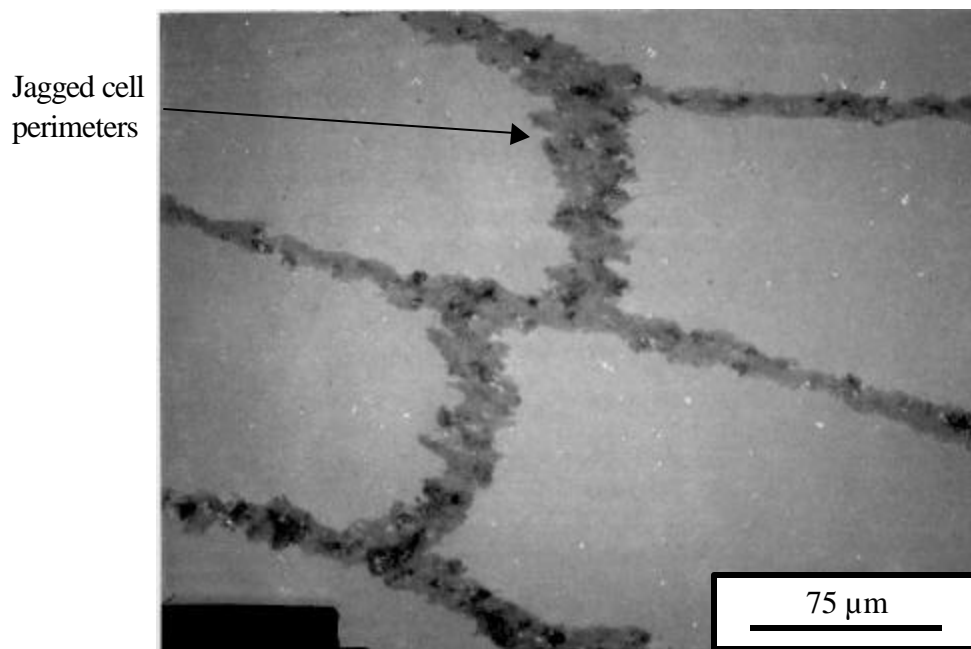


Figure 3.3 (b) Micrograph at 320x of Si_3N_4 -BN fibrous monolith showing the jagged perimeter formed on the individual cells during multi-filament coextrusion.

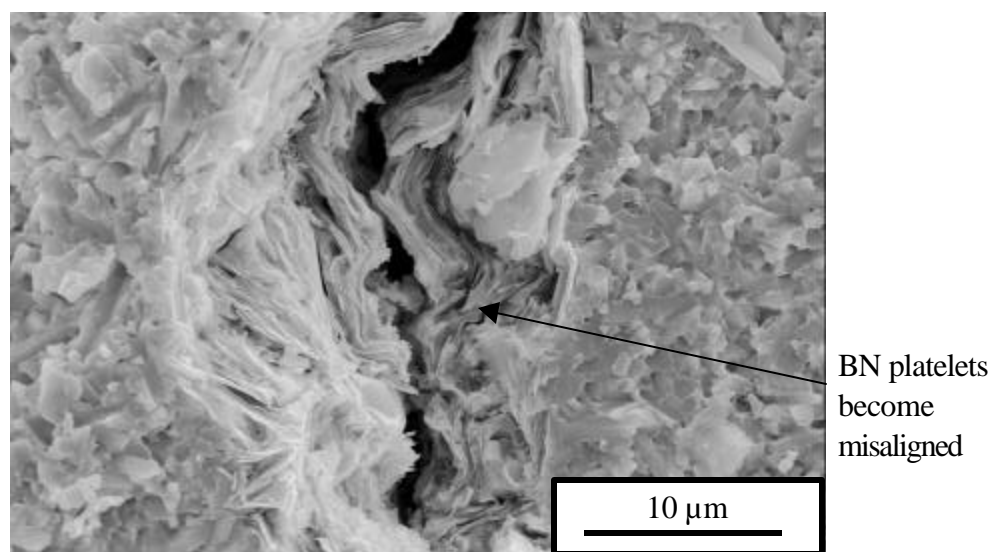


Figure 3.3 (c) Micrograph at 2k x of Si_3N_4 -BN fibrous monolith showing the jagged perimeter formed on the individual cells during multi-filament coextrusion.

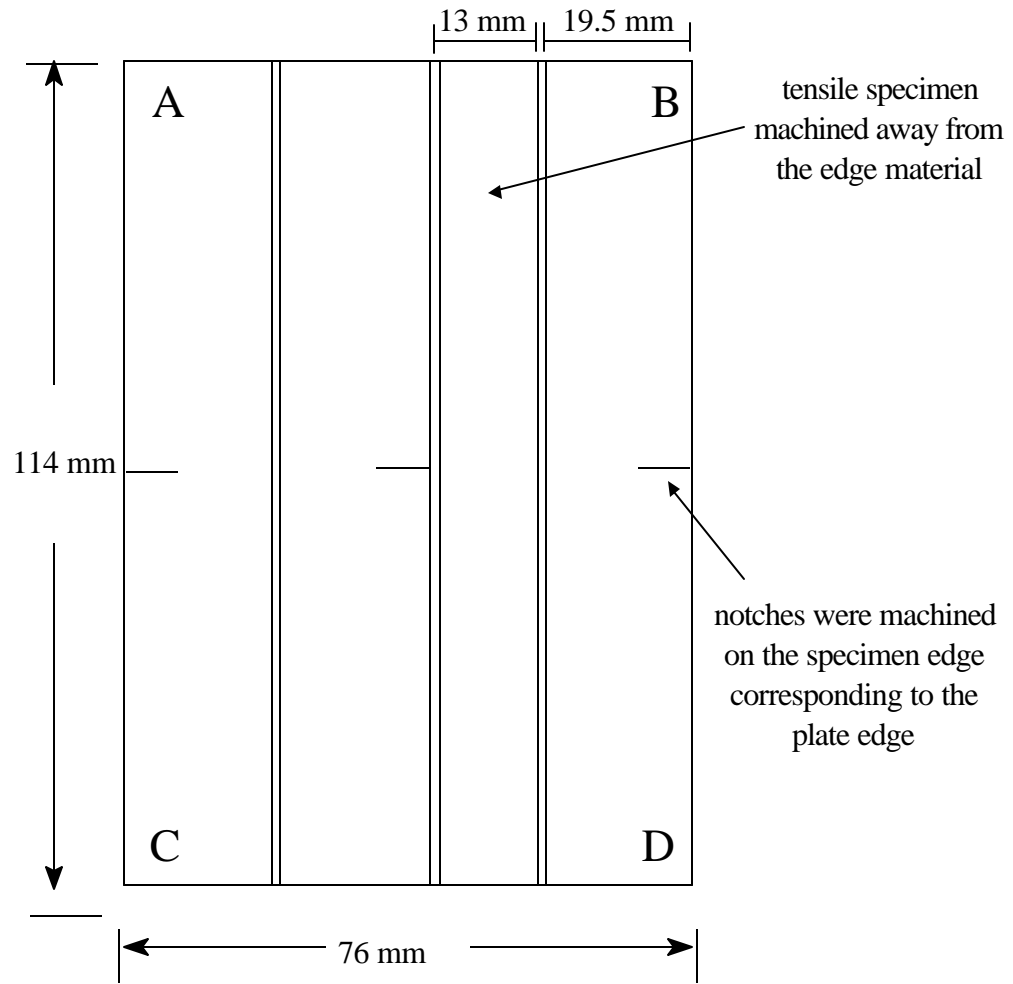


Figure 3.4 Schematic of the machining lay-out for each of the Si_3N_4 -BN FM plates.

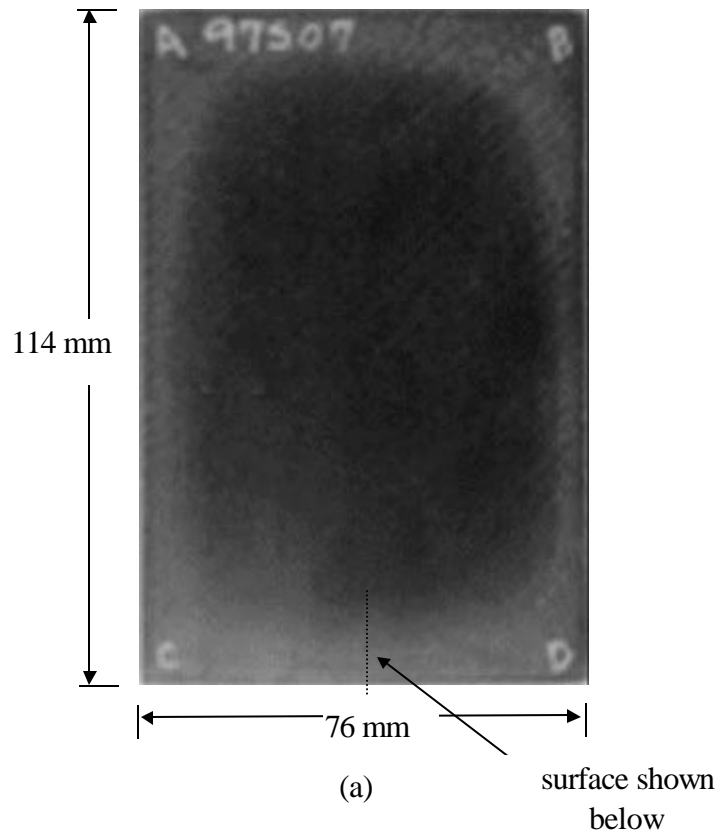
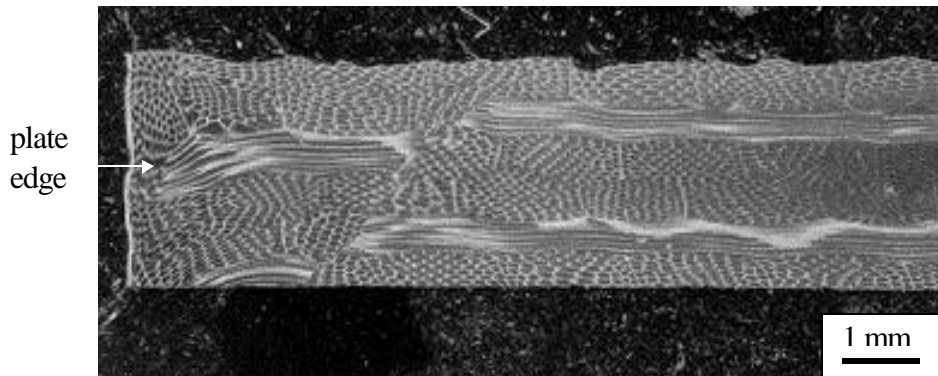


Figure 3.5 (a) Photograph of the plate material illustrating the edge defects from processing.



(b)

Figure 3.5 (b) Micrograph at 10x of Si_3N_4 -BN fibrous monolith showing the microstructural defects created at the edge of the plate during hot-pressing.

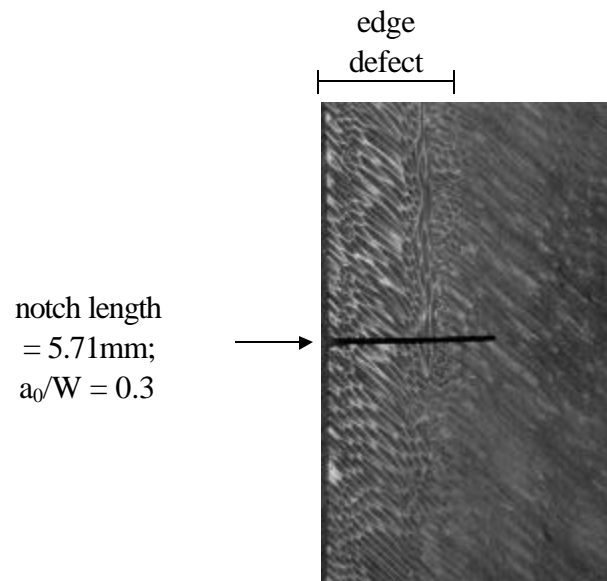
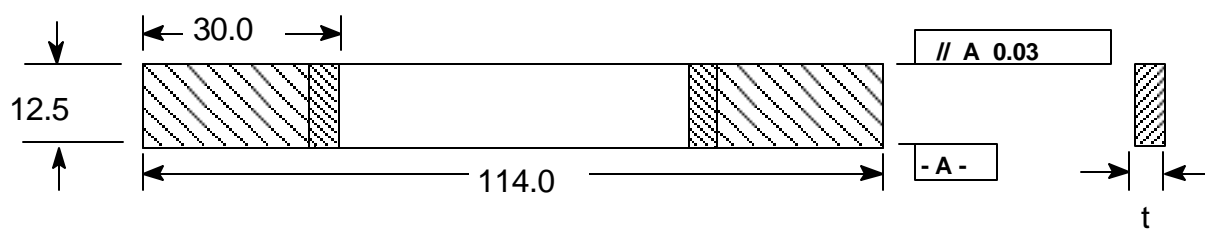
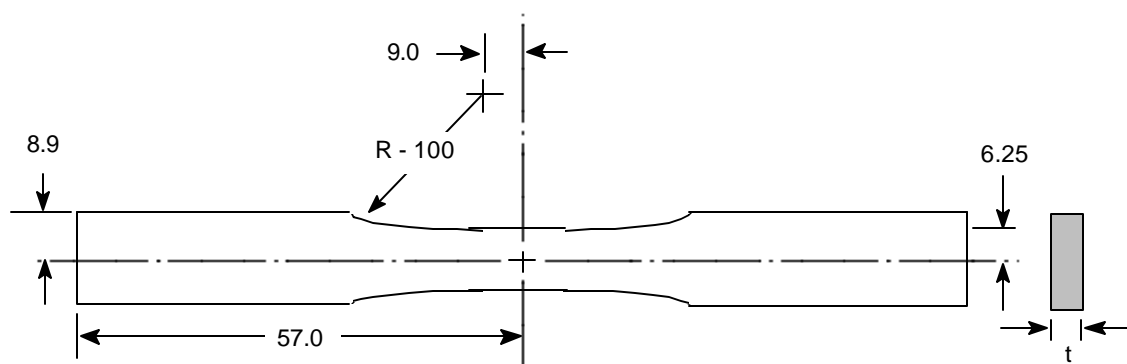


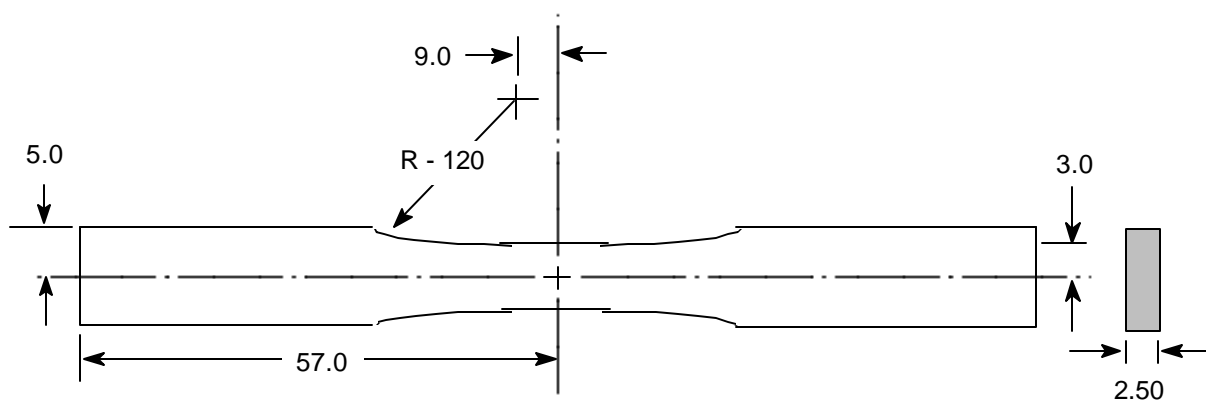
Figure 3.6 Photograph of a specimen which came from the edge of a plate, the notch was machined on the edge which corresponded to the plate edge. The notch extends beyond the edge defects which can be identified visually.



(a)



(b)



(c)

Figure 3.7 (a) Schematic drawing of a straight-sided Si_3N_4 -BN FM tensile specimen with fiberglass tabs. (b) Schematic drawing of a dogbone Si_3N_4 -BN FM tensile specimen. (c) Schematic drawing of a neat Si_3N_4 dogbone tensile specimen in showing the dimensions tested. Not to scale.



Figure 3.8 Photograph of the wedge grips used to test the straight-sided Si_3N_4 -BN fibrous monolith specimens.

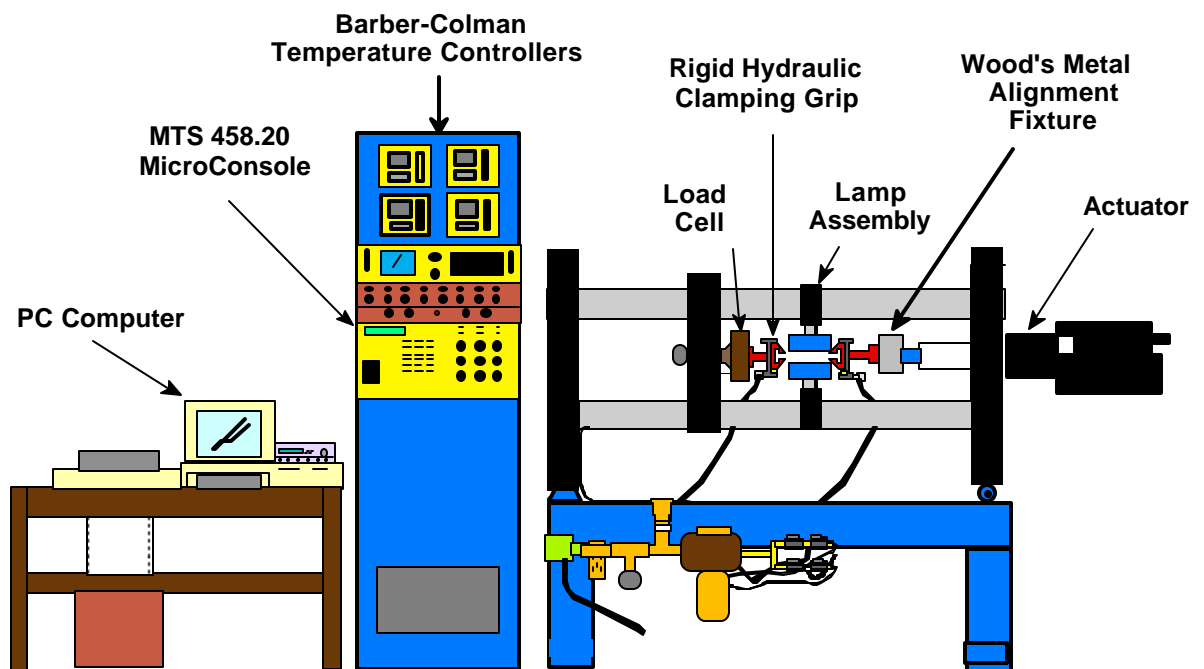


Figure 3.9 Schematic representation of the horizontal servo-hydraulic test system used for tensile testing the neat Si_3N_4 material as well as for all notched fracture testing.

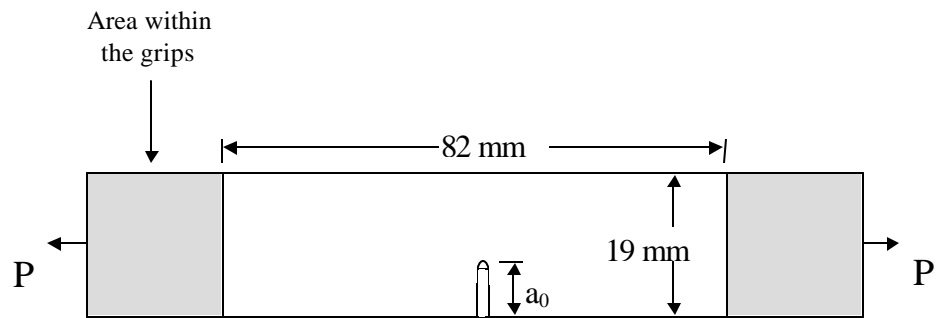


Figure 3.10 Schematic illustration of the MSE(T) specimen geometry with the dimensions tested. Not to scale.

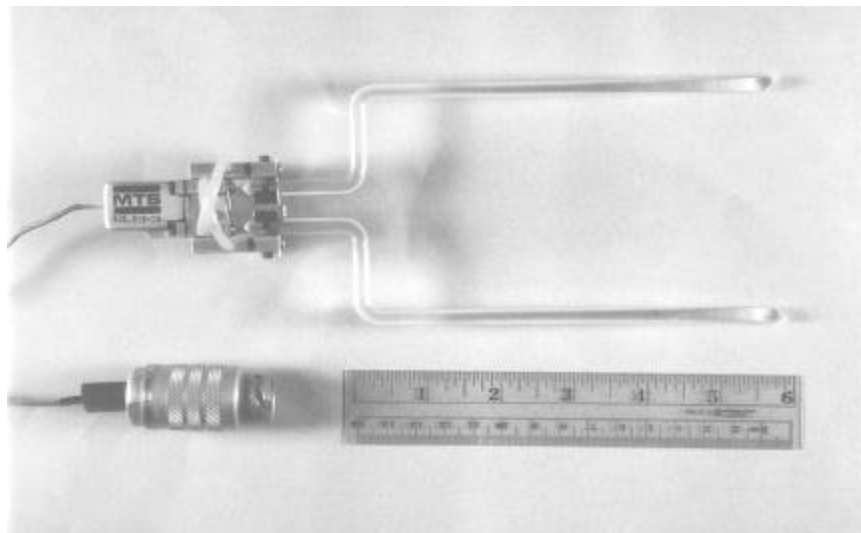


Figure 3.11 Photograph of the extensometer with the specially designed bent quartz rods for load-point displacement measurement.

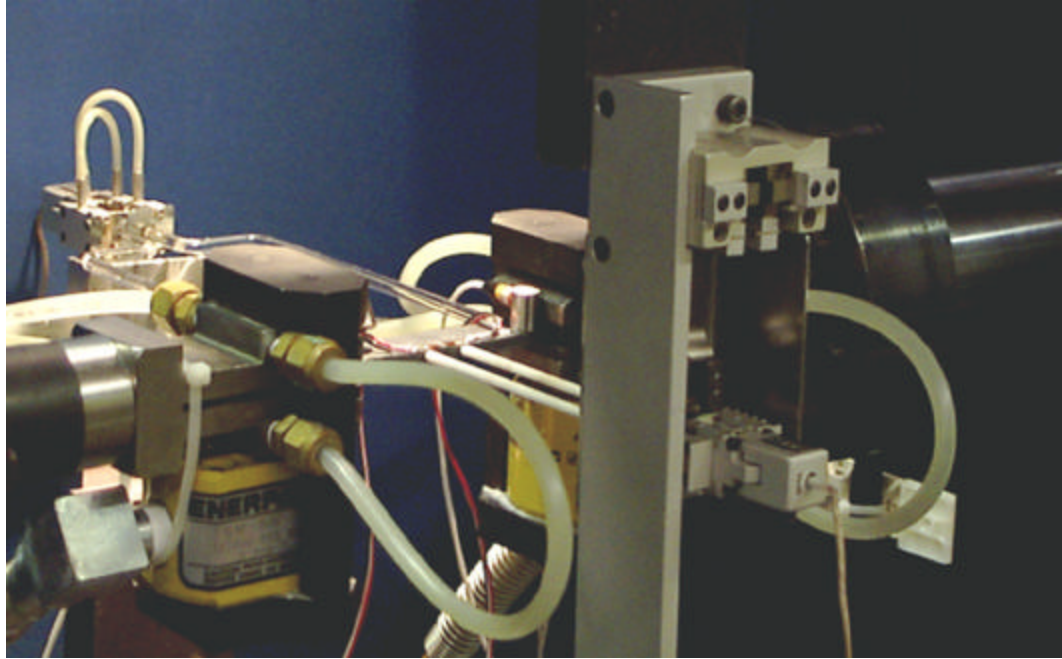


Figure 3.12 Photograph of the set-up used for room temperature fast fracture testing of MSE(T) specimens.

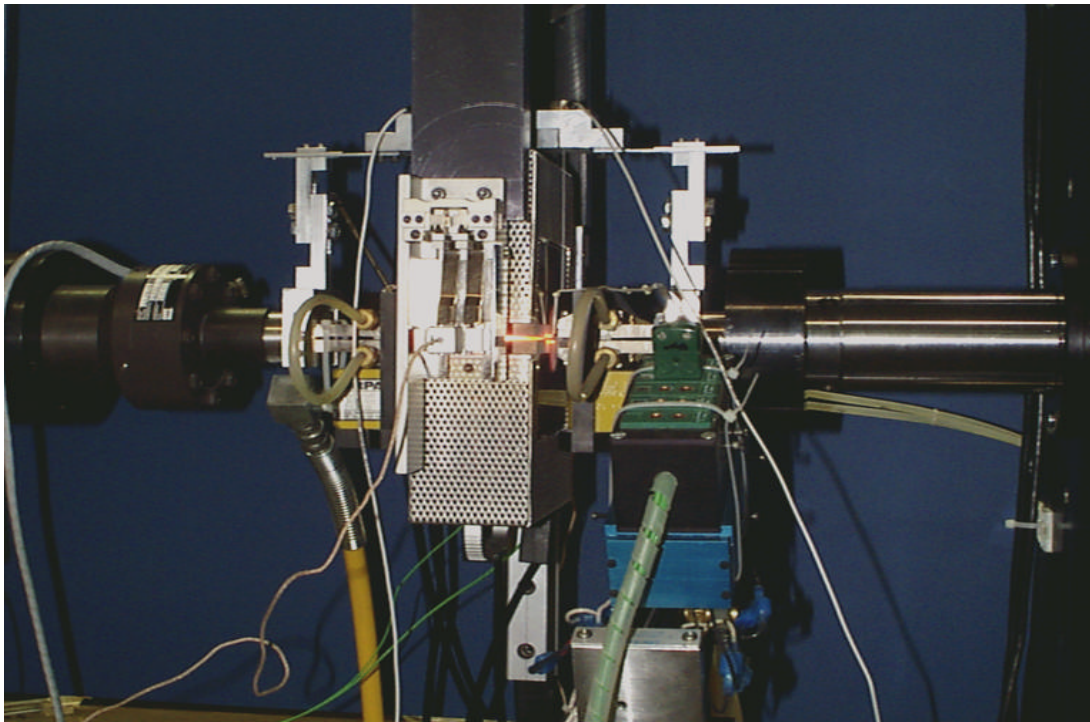


Figure 3.13 Photograph of the set-up used for high temperature fast fracture testing of MSE(T) specimens.

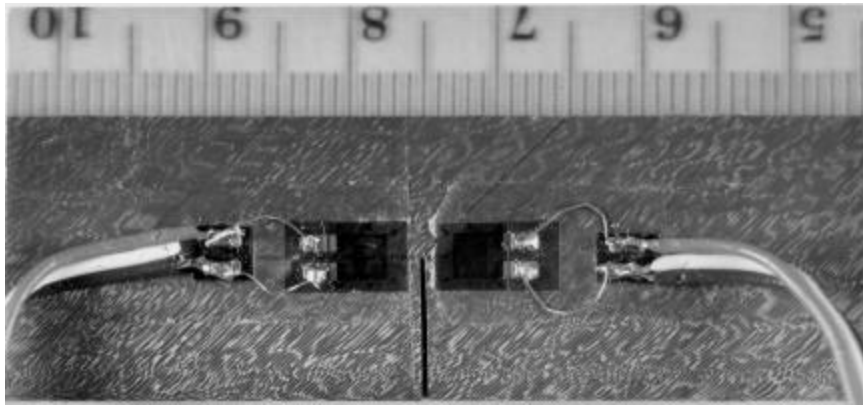


Figure 3.14 Photograph illustrating the strain gage position with respect to the notch on the MSE(T) specimens.

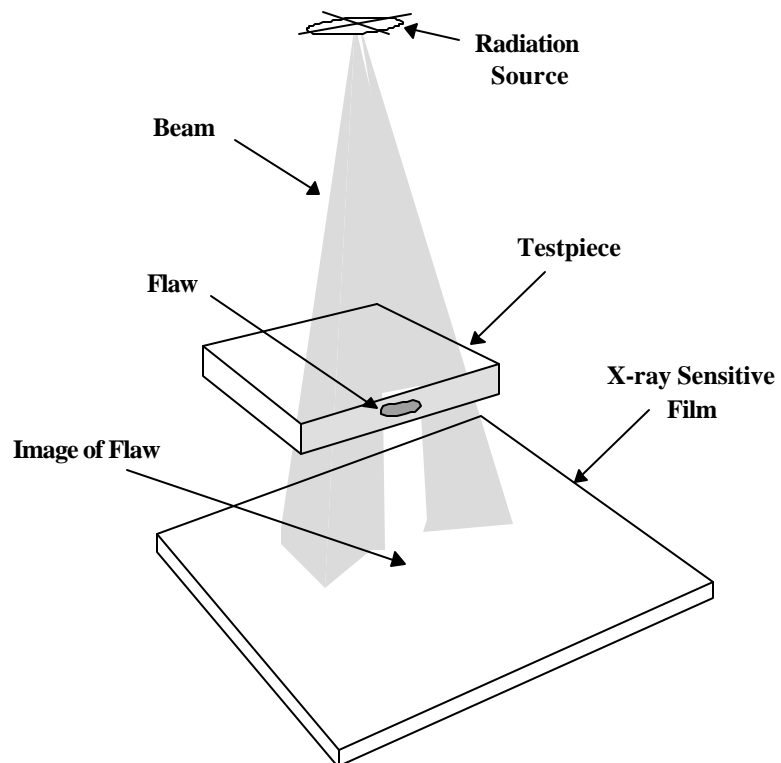


Figure 3.15 Schematic representation of the x-ray radiography technique showing the method of sensing of an internal flaw.

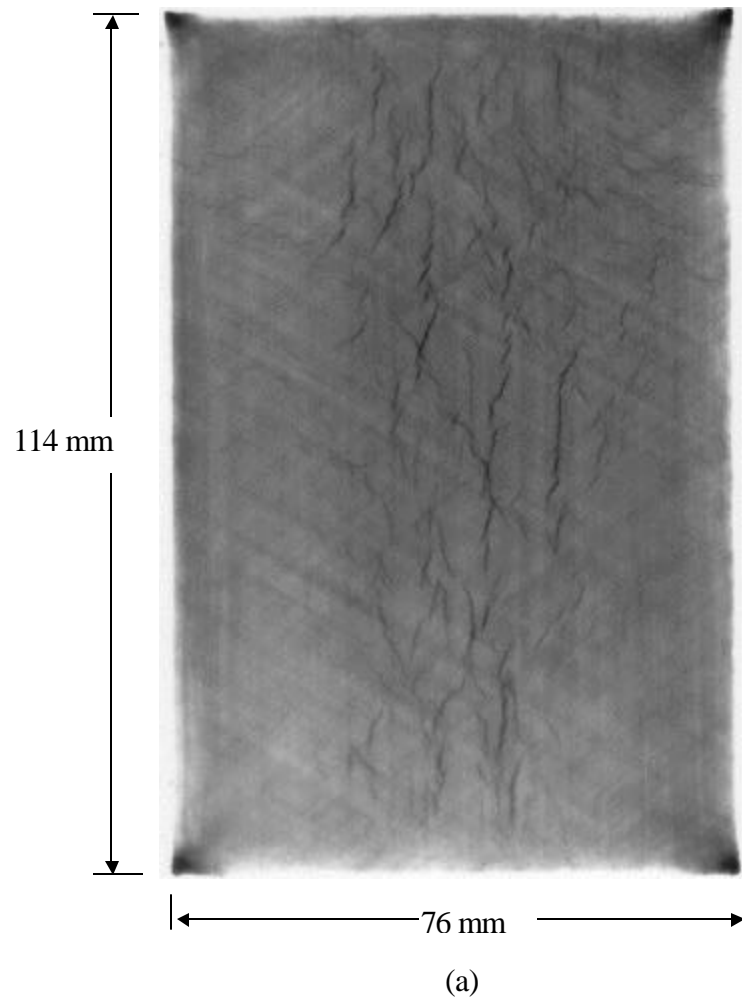


Figure 3.16 (a) & (b) X-ray radiographs of representative plates of the Si_3N_4 -BN fibrous monolith and neat Si_3N_4 materials respectively. A large number of microstructural defects are detected and the radiograph of the FM material whereas the neat material appears to be uniformly dense except near the edges.

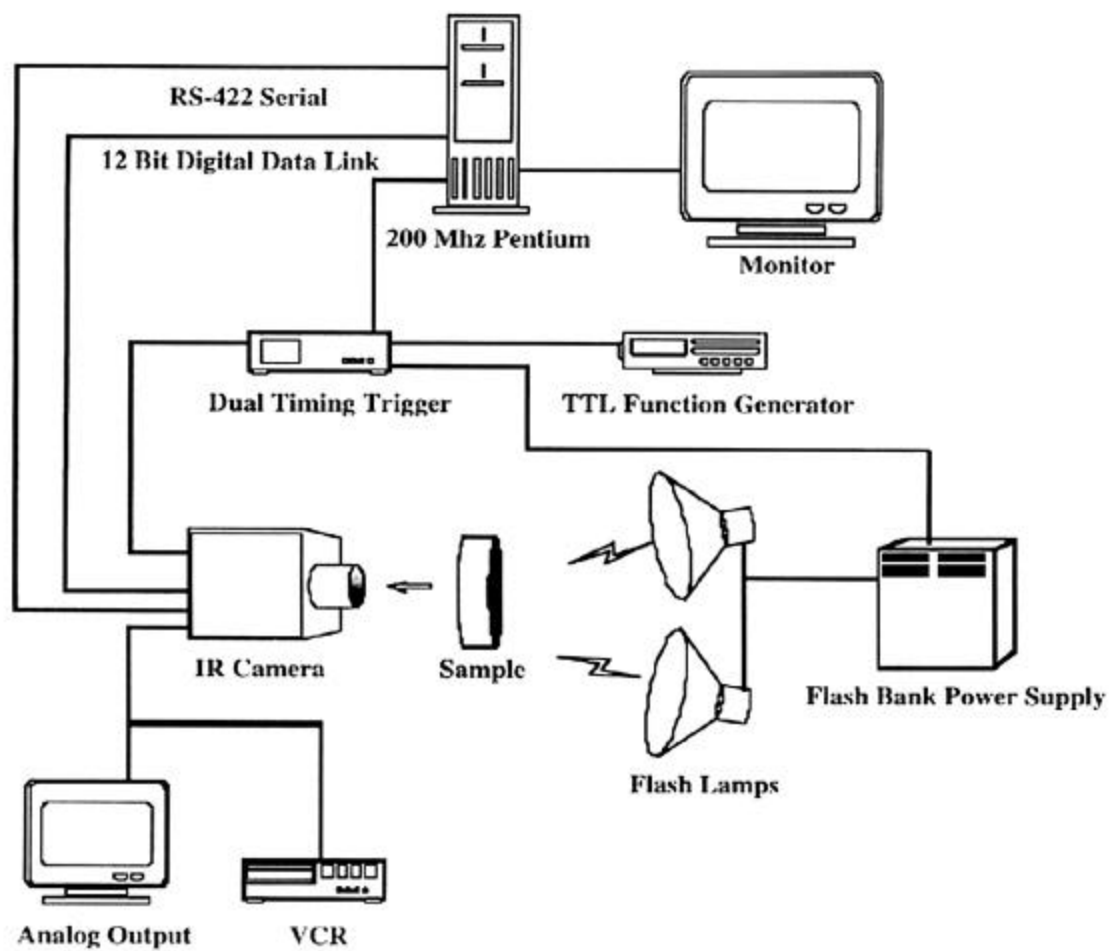


Figure 3.17 Schematic representation of the experimental apparatus used to obtain thermal images at Argonne National Laboratories³⁸.

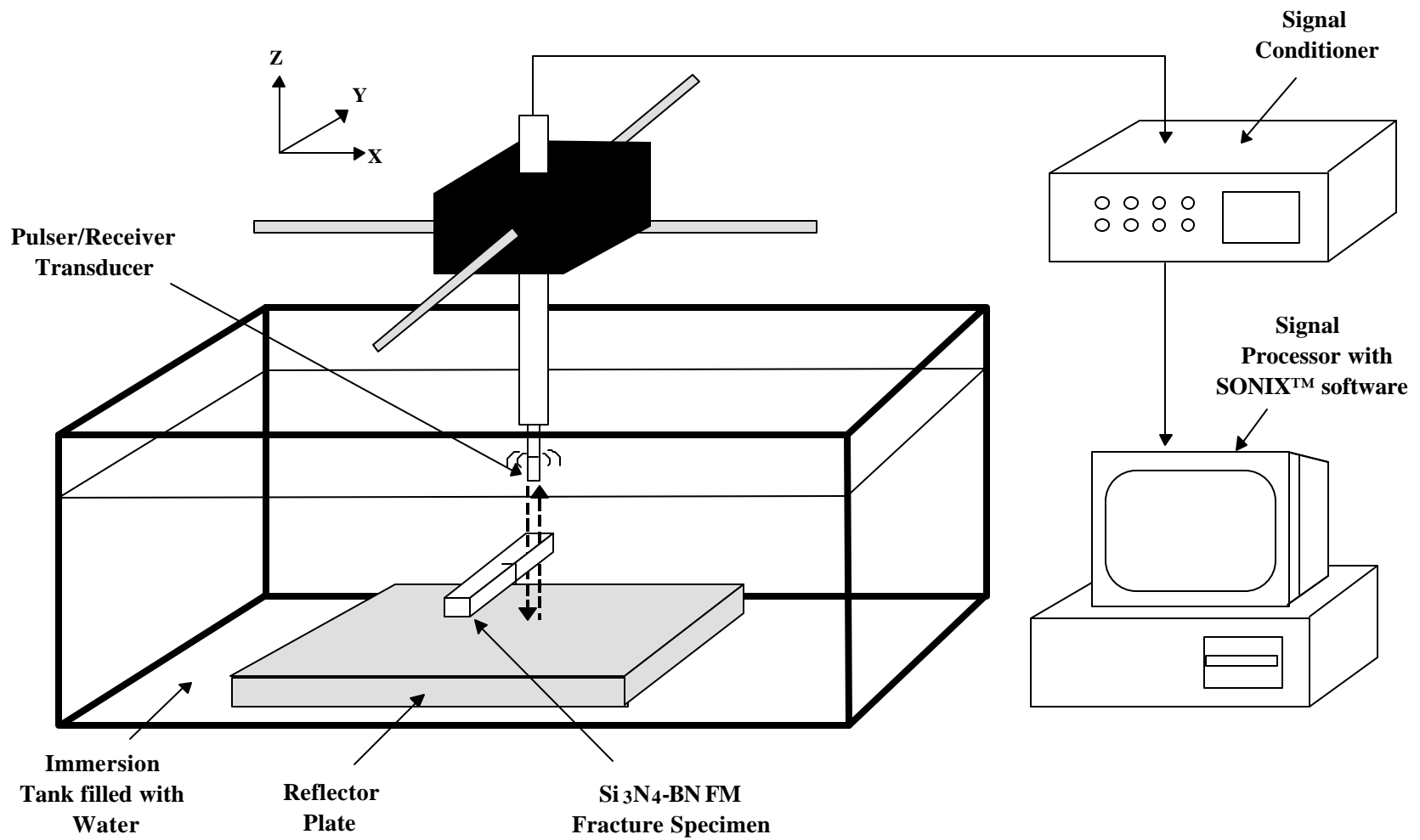


Figure 3.18 Schematic representation of the experimental apparatus used to obtain ultrasonic C-scans.

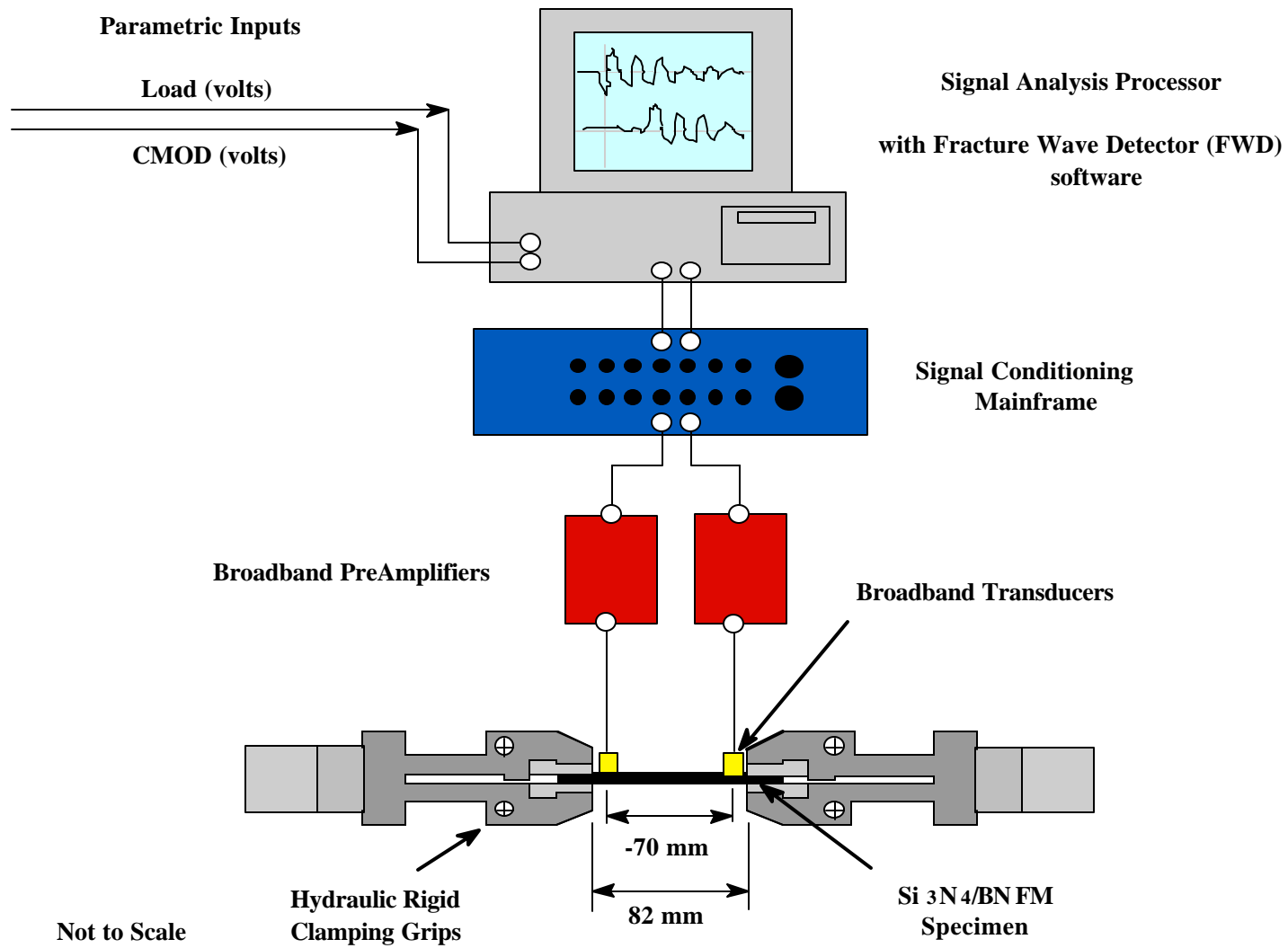


Figure 3.19 Schematic representation of the acoustic emission test apparatus used during fracture testing.

CHAPTER 4

TENSILE BEHAVIOR OF UNNOTCHED SPECIMENS

The following chapter presents the tension data generated on unnotched specimens.

The tensile behavior is discussed in terms of fraction of Si_3N_4 phase, microstructural feature size, and specimen geometry.

4.1 Monolithic Si_3N_4

Two monolithic Si_3N_4 dogbone specimens were tension tested. The data are listed in Table 4.1. Specimen 97-K34 was found to have a strength of 480 MPa and stiffness of 286 GPa. The other specimen, 97-K38, failed at 527 MPa and had a modulus of 274 GPa. The average strength measured for this material was approximately 504 MPa, the average modulus was 280 GPa, and the strain at failure was only 0.17%. A representative stress-strain trace shown in Figure 4.1 depicts the linear behavior to failure for this material.

Specimen #	Plate #	Cell Size	Strength (MPa)	Modulus (GPa)	Strain at Failure (%)	Work Of Fracture (J/m^2)
97-K34	P97017	neat	480	286	0.16	58395
97-K38	P97018	neat	527	274	0.18	43424
avg:			503.5	280	0.17	
std dev:			33.2	8	0.01	

Table 4.1 Tensile Test Data for Monolithic Si_3N_4 .

The fracture surfaces were flat and brittle in nature, as shown in Figure 4.2. The failure initiation site in the case of specimen 97-K34 was located on the surface of the

specimen and therefore may have been a result a machining flaw. The crack in specimen 97-K38 initiated at a dark inclusion within the material and did not seem to occur as a result of the machining or the test machine grips. It is suspected that the lower strength value measured for specimen 97-K34 may have resulted from a machining defect. Despite the difference in strength, both specimens had approximately the same strain at failure.

Specimen #	Plate #	Cell Size	Strength (MPa)	Modulus (GPa)	Work of Fracture (J/m ²)
97-B44	97S01	125 μ m	127	213	59771
97-B48	97S02	125 μ m	na	na	na
97-B52	97S03	125 μ m	96	200	222754
97-B56	97S04	125 μ m	114	180	371037
97-B60	97S05	125 μ m	115	212	44614
avg:			113	201	
std dev:			13	15	

Specimen #	Plate #	Cell Size	Strength (MPa)	Modulus (GPa)	Work of Fracture (J/m ²)
97-B64	97S06	250 μ m	126	191	608179
97-B68	97S07	250 μ m	132	183	284521
97-B72	97S08	250 μ m	na	na	na
97-B76	97S09	250 μ m	124	215	570114
97-B80	97S10	250 μ m	122	210	na
avg:			126	200	
std dev:			4	15	

both cell sizes		avg:	120	201	
straight-sided		std dev:	11	14	

Table 4.2 Tensile Test Data for Straight-Sided Fibrous Monoliths.

4.2 Fibrous Monolith Material

Data obtained from tensile testing straight-sided specimens of the fine celled and coarse celled fibrous monolith materials are presented in Table 4.2. Nominal strain values are not reported as the damage observed for the failures was outside the gage length of the extensometer used. The strength values for the material with the finer cell structure ranged from

96 MPa to 127 MPa, with a mean strength of 113 MPa and a standard deviation of 13 MPa. The strengths measured for the material with the larger cell structure ranged from 122 MPa to 132 MPa with a mean of 126 MPa and standard deviation of 4 MPa. The mean value of modulus for both materials was found to be approximately 200 GPa with a standard deviation in each case of 15 GPa.

Figures 4.3 (a) and 4.3 (b) illustrate the representative behaviors of the fibrous monolith materials. The plots illustrate that both materials behave elastically at low loads and then exhibit large displacements near failure.

In both materials, the damage included widespread inter-ply delamination and failure of the 0° plies. A photograph of a representative straight-sided tensile specimen from each microstructure is shown in Figure 4.4. In each case the specimens remained essentially intact even though the load dropped to zero. The specimens shown in the figure were pulled apart in the test machine after the failure, which resulted in a large amount of pull-out of the cell bundles. It was observed that the cracks progressed around as well as in-between cell bundles instead of the path around single cells within the bundles. This was interesting, as the shortest distance between opposite sides of a bundle would be a straight line through the bundle middle, i.e. along single cell boundaries.

In addition to tensile testing the straight-sided specimens, two dogbone specimens from each microstructure were also tested to measure the effects of geometry on the strength. The data are listed in Table 4.3. The strengths measured for the material with the 125 μm cells were 127 and 98 MPa and the strengths measured for the material with the 250 μm cells were 106 and 114 MPa. Modulus values for the materials were approximately 250 GPa and 175 GPa,

respectively. Representative stress-strain curves are shown in Figure 4.5 (a) and 4.5 (b). The damage induced in these specimens was also widespread, extending outside the gage length. Therefore, the nominal strains at failure depicted by the plots are not accurate. Again, it was observed that cracks were directed around the cell bundles and not the individual cells.

Specimen #	Plate #	Cell Size	Strength (MPa)	Modulus (GPa)	Work of Fracture (J/m ²)
97-B45	97S01	125 μ m	121	286	6225
97-B51	97S02	125 μ m	98	213	4476
avg:			109.5	249.5	
std dev:			16.3	51.6	

Specimen #	Plate #	Cell Size	Strength (MPa)	Modulus (GPa)	Work of Fracture (J/m ²)
97-B71	97S07	250 μ m	106	na	6291
97-B74	97S08	250 μ m	114	175	8373
avg:			110	175	
std dev:			5.7		
both cell sizes			avg:	109.8	224.7
dogbone			std dev:	9.9	56.4

all FM data			avg:	116.3	207.1
both geometries			std dev:	11.4	30.1

Table 4.3 Tensile Test Data from Dogbone Fibrous Monoliths.

4.3 Discussion

4.3.1 Tensile Results

Experimental data were compared to tensile data found in the literature. Limited data have been reported for the tensile strength of monolithic Si_3N_4 . Due to the difficulties in testing ceramics in tension, flexure testing is the commonly used characterization method. The approximate tensile strength for a hot-pressed Si_3N_4 material with an α/β ratio of 60:40 was found to be 547 MPa⁴⁰⁻⁴¹. The strength of the neat Si_3N_4 material tested in this study was measured to be about 8% lower at 504 MPa. Differences in processing, constituent phases,

and machining of the Si_3N_4 materials used in this study versus that reported in the literature may account for the small discrepancy in strength since scatter in properties of ceramics results from differences in flaw distribution.

No data have been reported in the literature for fibrous monolith material with the same microstructures and architectures as being tested in this study. However, fast fracture tensile data was reported by Staehler³⁴ and Advanced Ceramic Research Corporation³⁵ for unidirectional multi-filament coextruded Si_3N_4 -BN material. As presented in Chapter 2, Staehler showed a strength value of 495 MPa for material with a reported nominal cell size of 125 μm (2:1 mm strands) and an 85% volume fraction of Si_3N_4 . ACR measured a value of 379 MPa for uniaxial multi-filament material with an unreported cell size and 80% volume fraction of Si_3N_4 .

A comparison between the reported strengths and those measured in this study is possible if the values obtained from the literature are normalized to account for differences in volume fraction of the Si_3N_4 phase and in the fraction of cells in the axial direction. To do so, the assumption is made that the 45° plies in the materials tested in this study do not carry any of the tensile load. The test materials have two out of six plies in the axial (0°) direction ($\approx 33\%$), whereas the materials in the literature had 100% of the plies in the axial direction. After normalizing, the strengths calculated from the data reported by Staehler³⁴ and ACR³⁵, respectively, are 144 MPa and 117 MPa. See Appendix B for the calculations of normalized strength using values from the literature.

The normalized value obtained from Staehler's data is about 12.5% to 17% higher than the average strength obtained from the two FM materials tested in this study. The normalized

value from ACR's data falls between the strengths measured for the two fibrous monolith materials. This strength prediction discounts any effect of the 45° plies. The data from Staehler indicates that the 45° plies may hinder the strength of the material. A negative effect on strength by the addition of cross-ply in the material tested by Staehler was also speculated. It was thought that the 0° plies may become damaged by the addition of the cross-ply during hot-pressing. Evidence of impingement and other abnormalities, presumed to be a result of processing, were observed in the materials tested in this study and are clearly identified in Figure 3.3 (a).

4.3.2 Tensile Behavior of Fibrous Monolith versus Monolithic Si_3N_4

A comparison of the Si_3N_4 -BN fibrous monolith materials with the monolithic Si_3N_4 , shows that the fibrous monolith material sacrifices strength and stiffness for apparent toughness. In tension, the fibrous monolith materials exhibited non-linear behavior and torturous fracture. In contrast, the monolithic Si_3N_4 ceramic showed linear elastic behavior and catastrophic failure with a relatively flat fracture surface.

Although the behaviors are quite different, a direct comparison of the strengths of the different materials is possible by normalizing the monolithic strength using a pseudo rule-of-mixtures approach. If the average strength measured for the neat material is multiplied by the area percent of Si_3N_4 cells in the axial direction, and it is assumed that the tensile strength contribution of the BN is negligible, then the predicted strength of the neat material is approximately 125 MPa. This value falls in the range of the strengths measured for the two fibrous monolith materials. See Appendix C for the calculation.

In stiffness, both of the fibrous monolith materials showed about a 29% decrease compared to the neat material. An approach which can be used to predict the Young's modulus of a fibrous monolith material with a $[-45/0/+45]_s$ lay-up is by using equations from laminate theory. King¹⁷ showed good agreement in predictions made for the elastic properties in multidirectional fibrous monoliths. Although that analysis was not repeated for this study, a comparison of the Young's modulus measured by King¹⁷ for materials with $[0/\pm 60]$ and $[0/\pm 45/90]$ architectures with those measured for the $[-45/0/+45]_s$ shows the moduli to be comparable at 205 ± 7 GPa, 202 ± 3 GPa, and 201 ± 14 GPa, respectively.

The greatest advantage fibrous monolith materials with multi-axial architectures have over monolithic materials in tension is expected to be toughness. The extensometer (strain) measurements were not able to capture the complete deformation history of the fibrous monolith materials. However, a relative comparison of the total work of fracture (WOF_T) for the fibrous monolith materials and the monolithic material was possible using stroke measurements. In addition to extensometer data, stroke data off the MTS actuator was recorded in each test by a LVDT (linear variable differential transducer). The area under the load versus stroke curve provides an estimate of WOF_T .

The work of fracture defined in this manner is the total fracture energy including elastic energy and an unknown contribution from the test system. The results are listed in Tables 4.1 through 4.3 for the neat and fibrous monolith materials. The WOF_T was calculated by dividing the area under the curve by the cross-sectional area of the specimen. The neat material had an average WOF_T on the order of $50,000 \text{ J/m}^2$. The WOF_T for the fibrous monolith material in the straight-sided geometry showed large discrepancies from specimen to specimen, which ranged

from 44,614 J/m² to 608,179 J/m². The average WOF_T for the fibrous monolith material in the dogbone geometry was an order of magnitude smaller compared to the neat material and straight-sided fibrous monolith specimens at 6000 J/m².

Discrepancies in the WOF_T and thus the stroke data may in part be attributed to the resolution of the measurement device. The LVDT is not accurate enough to measure the small load-point displacements being tested. This issue was addressed in later testing of the notched specimens. In these later tests, a second extensometer was designed and implemented for more accurate measurement of displacement at the point of loading for work of fracture determination.

4.3.3 Tensile Behavior of Fibrous Monoliths as a Function of Cell Size

The data presented in Table 4.2 and Table 4.3 for both the straight-sided and dogbone specimens do not illustrate that there is a significant difference in behavior when comparing the fibrous monolith material with the 125 μm cells to that with the 250 μm cells. Comparison of the two materials in the straight-sided geometry and the dogbone specimens separately, it is shown that they fall within each other's range. A test of hypothesis for the means on the limited data sets show that there is no significance difference in strength between the two materials. See Appendix D for the hypothesis test calculation.

The data show that for both specimen geometries, there is a larger variability for the material with the smaller cells than for the material with the larger cells. The variability may result from the differences in material processing and the machining. Recall from Chapter 3 that the fibrous monolith material with the smaller cell size had more distorted cells and more defects

such as kinks and distorted cell boundaries. It is suggested that this increased occurrence of defects most likely contributed to the increased variability.

In addition, the plates of materials for the two microstructures were originally fabricated with a different number of plies. The plates of material with the smaller cells were fabricated with a total of 16 plies and were approximately 7.6 mm thick after hot-pressing. The plates of material with the larger cells were fabricated with 8 plies and were 6.5 mm thick after hot-pressing. It is possible that the extra material being pressed, in the case of the smaller microstructure, allowed for inconsistencies in consolidation and structure of the resultant cell bundles as a result of more movement of the constituent material as the tile condensed.

Also recall from Chapter 3 that several of the outer plies had to be removed from each plate to make the architectures similar and test coupons thin enough to test. Unfortunately, that machining was not done symmetrically for the plates of material with the 125 μm cells. More material was removed from one surface than from the other. Refer to Figure 3.2 (a) and 3.2 (b) for micrographs of the two test materials. This inconsistency in the machining of two different sets of plate material may also contribute to the variability in the data.

The data in Table 4.2 and 4.3 also show the trends in moduli for the fine and coarse microstructures. For the straight-sided and the dogbone specimens, the mean value of modulus is the same for both microstructures but there is some variability. Variability in the modulus can be attributed to the sensitivity of this measurement with slight differences in specimen alignment within the test machine, and the use of a 12-bit (low resolution) digitizer in the test apparatus.

From a strength and stiffness perspective, one might not expect there to be a difference between the materials, as they contain the same volume fraction of the reinforcing phase. The

cell size in the fibrous monolith microstructure is, however, expected to influence the fracture resistance. What was found, however, is that individual cell size does not influence behavior of the material being investigated in this study. The largest microstructural feature in the material is what dominates fracture behavior, and for the multi-filament coextruded fibrous monolith materials those are the cell bundles. The materials being studied herein have two different cell bundle sizes. Recall from Chapter 3 that the material with the 125 μm cells had multi-filament strands which were 1 mm after coextrusion and the material with the 250 μm cells had 2 mm strands. Therefore, comparisons of the data for the fibrous monolith materials being studied should be made in terms of cell bundle size and not individual cell size.

Assessment of the toughness in terms of cell bundle size for the straight-sided specimens was not possible for a majority of the data due to invalid strain and a large variability in the stroke data. The limited tests on the dogbone specimens may show that the material with the larger cell bundles absorbs slightly more energy upon fracture. The average WOF_T 's for the fine and coarse celled materials were 5351 J/m^2 and 7332 J/m^2 , respectively.

4.3.4 Tensile Behavior as a Function of Specimen Geometry

Dogbone specimens from each microstructure were tested as well as the straight-sided specimens to obtain the base-line strength of the materials. When testing straight-sided specimens it is a concern that the stress concentration at the point of gripping may initiate failure and affect the strength results. Normalized strength estimates from the results in the literature and from the experimental results on the monolithic Si_3N_4 material showed that the average strengths from the straight-sided specimens may be low.

A comparison of the straight-sided versus dogbone specimens tested in this study showed different results depending on the microstructure. For the material with the smaller cell bundles, the geometry did not seem to have an effect on the average strength. For the material with the coarser microstructure, the average strength for the dogbone specimens is lower than for the straight-sided. This is opposite to the trend that would be expected if gripping was an issue. However, since there is no effect of individual cell size and no significant effect of cell bundle size on the strength and stiffness, one can say that the results are within the scatter of the entire data set.

Another issue to consider with specimen geometry is the effect of specimen width on the properties of the material. Generally, there exists an edge effect when testing laminated composites of finite width that is associated with a triaxial state of stress near free edges (or other geometric discontinuities), where stress transfer is mostly by interlaminar stresses⁴²⁻⁴³. The presence of interlaminar shear stresses in the region effected can influence the failure mode and properties. The magnitude of these stresses, and thus the width of the effected zone away from the edge, are a function of the elastic properties, ply angles, stacking sequence, and ply thickness⁴²⁻⁴⁵. Anomalies at the edges associated with hot-pressing or machining can also influence the stress-state at the edges. A simple estimate of the boundary layer for edge effects is anywhere from one to two times the laminate thickness⁴²⁻⁴³.

To determine if the specimen width has influenced the tensile strength measured in this study, an experiment was performed on both straight-sided and dogbone specimens with different test widths. Three different specimen widths were considered for each geometry: 19mm, 16 mm, and 12.5 mm. The materials used for this side experiment were fabricated

differently than the test material. The straight-sided specimens came from material with a different binder system and the dogbone specimens came from material with the same binder system as the original materials being tested in this study, but had a slower binder burnout schedule. Due to the differences in material processing, the idea of this aside was not to compare nominal values of strength, but to look at trends in behavior with respect to specimen width.

The strength data from the fast fracture tests performed as a function of width are shown in Figure 4.6. The results do not show conclusively that there is an effect of specimen width on the tensile strength. A larger number of tests and a wider range of specimen widths should be tested to address this issue.

This plot does show, however, a large difference in strengths measured for the differently processed materials. There is a large drop in strength shown for the dogbone specimens compared to the straight-sided specimens which is believed to be due to processing differences and not due to specimen geometry. If the strengths for a specimen width of 12.5 mm are plotted for each material as in Figure 4.7, one might conclude that the new binder system enhances strength while a slow binder burnout schedule adversely affects strength. With this result it should be concluded that binders and processing schedules significantly influence behavior and should therefore be reported with any mechanical behavior data generated on fibrous monolith materials.

4.4 Summary

Fast-fracture tensile testing of unnotched specimens showed that the properties of the fibrous monolith materials are directly related to the reinforcing phase in the axial direction and

that the [-45/0/+45]_s architecture being tested in this study may not provide for optimum fracture resistance compared to neat Si₃N₄ material as illustrated by the large range in the WOF_T results.

Fracture surfaces of the fibrous monolith tensile coupons show that fracture is influenced by the largest microstructural feature which is the cell bundles in multi-filament coextruded materials and not the individual cells. The two materials tested herein not only had differing individual cell sizes but also different cell bundle sizes due to the processing technique. A comparison of the results obtained by testing straight-sided specimens from the two different fibrous monolith materials showed that there is statistically no significant difference in the strength. However, a larger variability in strength from plate to plate was observed for the material with the finer microstructural features, which was attributed to processing and machining. Total work of fractures based on actuator stroke implies that the material with the larger cell bundles may have increased energy absorption capacity.

Tensile data were generated for dogbone specimens from both microstructures of the fibrous monolith materials to address specimen geometry issues. The results of the strength comparison for the two specimen geometry's were inconclusive. Other fibrous monolith materials were used to address the effect of specimen width on the strength. The outcome of this experiment was also inconclusive due to the limited number of data obtained. These data show that a significant difference in material properties can result with changes in binder systems and burnout schedules and it was verified that pedigree of the fibrous monolith materials should be considered when comparing data.

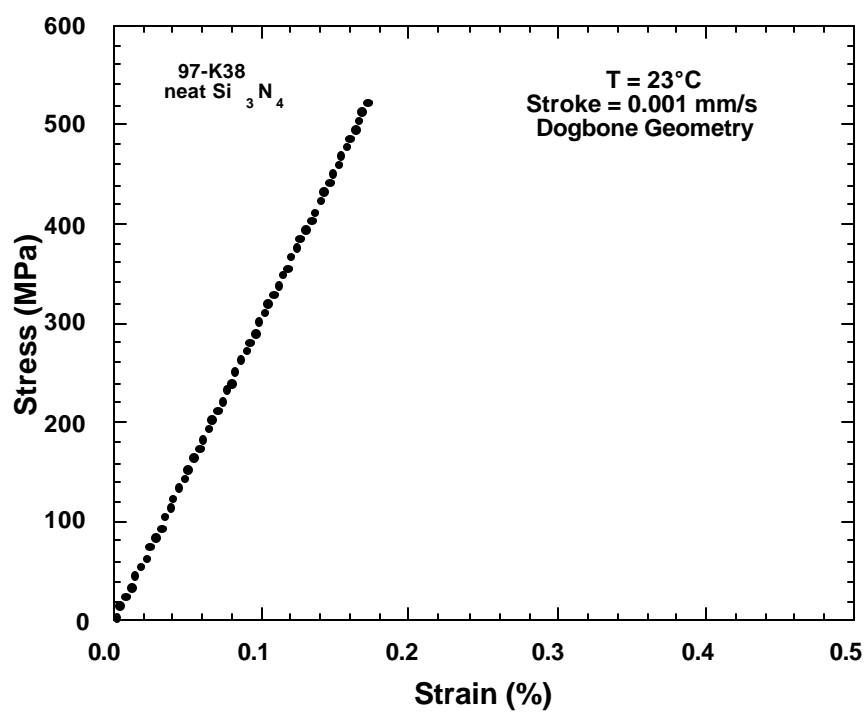


Figure 4.1 Tensile plot showing typical stress versus strain behavior of monolithic Si_3N_4 .



Figure 4.2 Photograph of a fractured monolithic Si_3N_4 tensile specimen illustrating the brittle fracture.

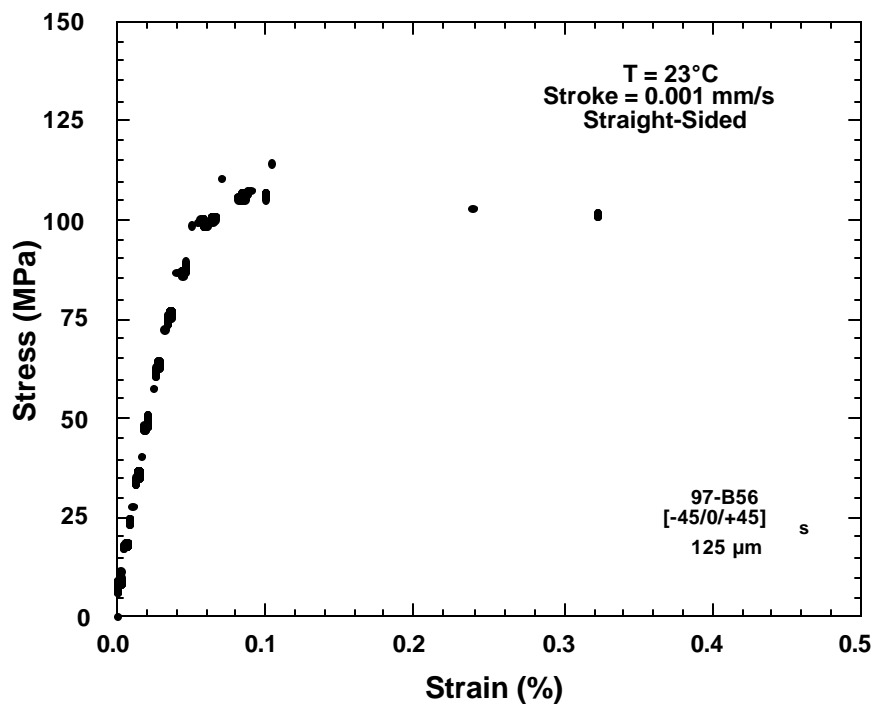


Figure 4.3 (a) Tensile plot showing typical stress versus strain behavior of Si_3N_4 -BN FM material with a nominal cell size of 125μm.

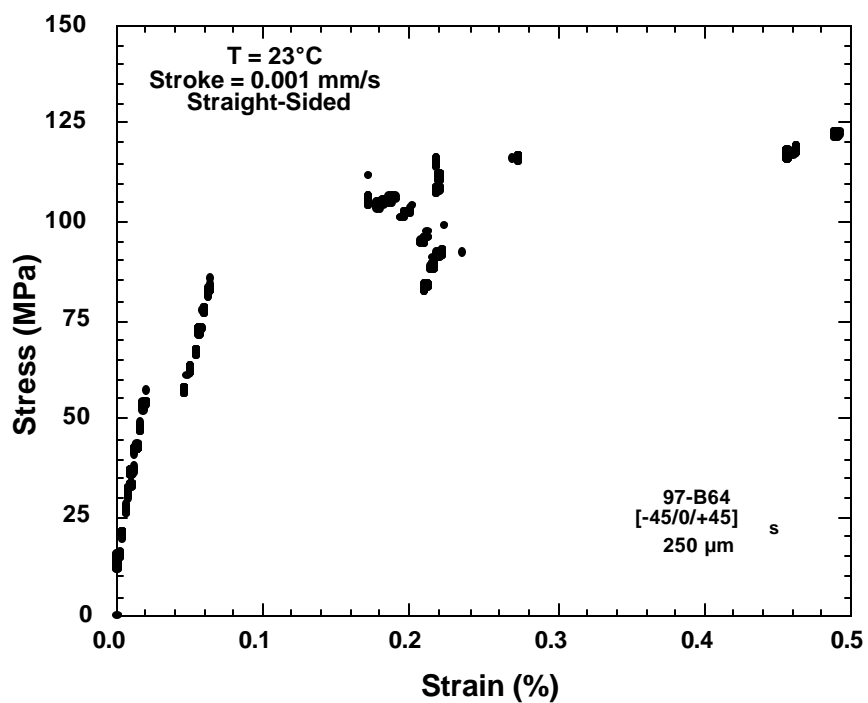


Figure 4.3 (b) Tensile plot showing typical stress versus strain behavior of Si_3N_4 -BN FM material with a nominal cell size of 250μm.



125 μm cells



250 μm cells

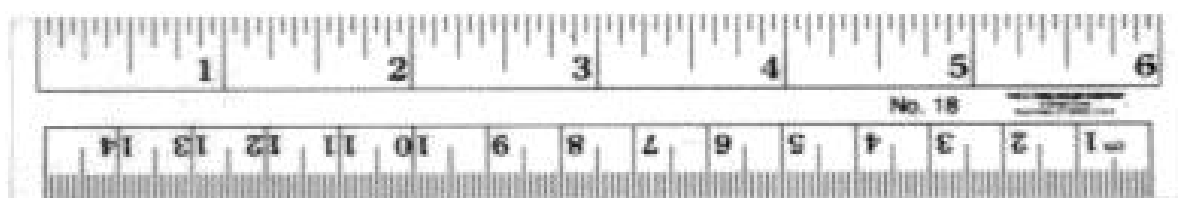


Figure 4.4 Photographs of fractured straight-sided fibrous monolith tensile specimens.

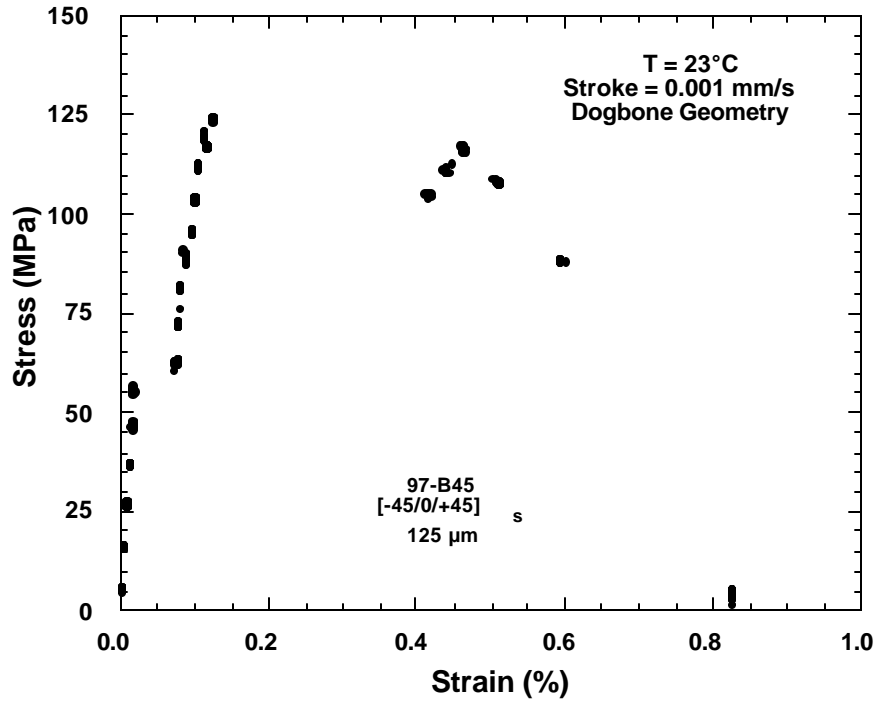


Figure 4.5 (a) Tensile plot showing stress versus strain behavior of Si_3N_4 -BN FM material with a nominal cell size of 125μm and dogbone geometry.

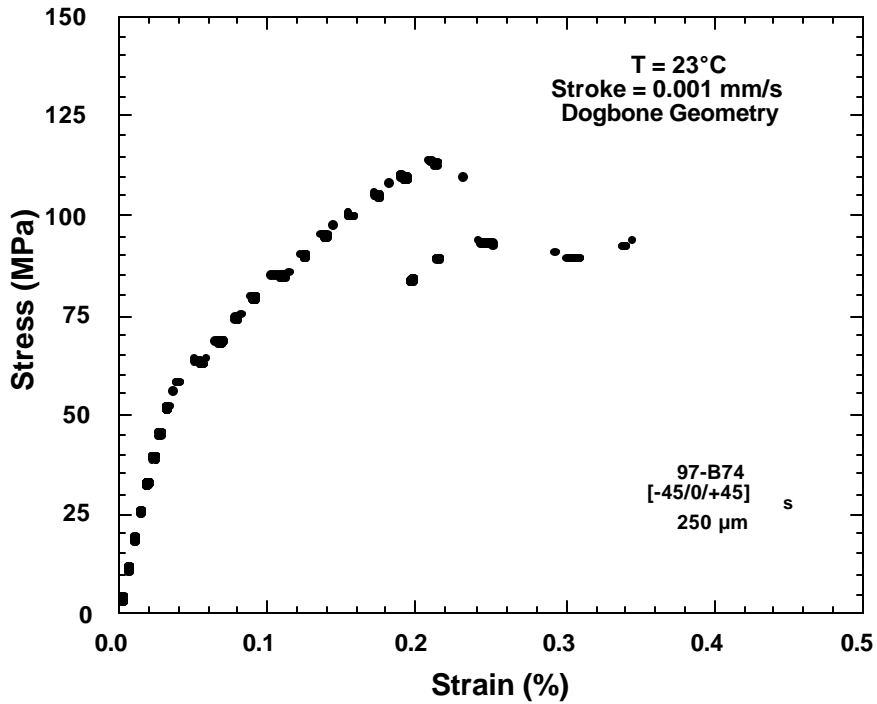


Figure 4.5 (b) Tensile plot showing stress versus strain behavior of Si_3N_4 -BN FM material with a nominal cell size of 250μm and dogbone geometry.

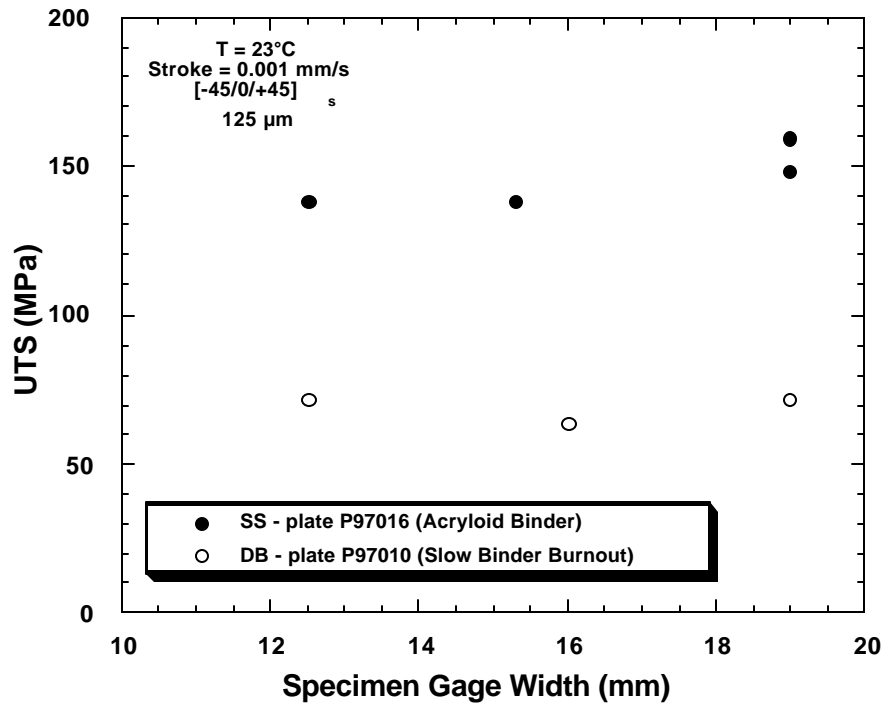


Figure 4.6 Strength versus width for three differently processed FM materials. Results are inconclusive as to a width effect on the strength in the case for the straight-sided or the dogbone specimens.

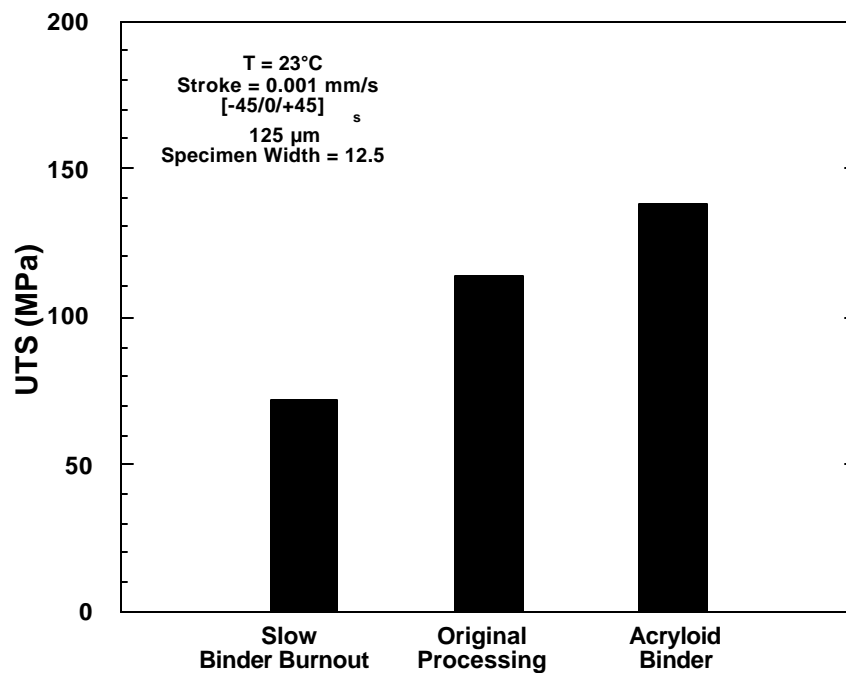


Figure 4.7 Bar plot which shows that there may be an effect of the processing on the strength.

CHAPTER 5

FAST FRACTURE OF MODIFIED SINGLE-EDGE NOTCH SPECIMENS

The following chapter presents and compares the data generated through fast-fracture testing modified single-edge notch specimens of the different test materials. The first section reviews the results for both the monolithic and the fibrous monolith materials obtained using MSE(T) specimens with a notch-to-width ratio of 0.3. Included in this section are data generated for specimens tested at both room temperature and at 1150°C. The second section presents the results of testing MSE(T) specimens with various notch lengths. The applicability of two different approaches to describe the material behavior were evaluated: a Linear-Elastic Fracture Mechanics (LEFM) approach, and a net-section stress approach. A comparison of the fracture behaviors was ultimately made using work of fracture measurements and observations made about the damage progression through NDE. All data generated through fast-fracture testing MSE(T) specimens are presented in Table 5.1.

Test Temp (°C)	Notch Size a_0/W	Microstructure	ID #	Initial E (CMOD) (GPa)	Initial Compl (CMOD) (m/N)	Max Load (kN)	CMOD @ max load	load pt d @ max load	Net Section Stress (MPa)	$K_{I, (app)}$ (MPa√m)	$K_{I, (initial)}$ (MPa√m)	$K_{II, (initial)}$ (MPa√m)	WOF Total - LPd (J/m ²)
23	0.1	125 μm	97-B58 failed in grip	---	---	6.9614	0.015469	0.058381	- 140	na	5.29	7.03	3874
		250 μm	97-B78 did not fail	---	---	9.0926	0.011403	0.045703	- 122	na	8.58	9.73	2765
		Neat	97-K37	268	0.898	4.1036	0.0036818	0.052943	96	7.66	---	---	233
	0.2	125 μm	97-B55	211	2.19	6.815	0.034482 0.035487	0.054661 0.056092	154	16.91	7.69	9.93	3946
		250 μm	97-B70	203	1.53	8.817	0.033409 0.051945	0.051226 0.064105	133	14.68	7.49	11.65	4253
	0.3	125 μm	97-B43	215	3.57	5.4714	0.039594	---	141	18.20	6.32	10.81	---
			97-B47	---	---	4.916	0.034498	0.047506	127	16.36	6.66	9.98	1909
			97-B57	224	3.48	4.983	0.034665	0.04804	129	16.75	5.88	10.76	2158
		250 μm	97-B65	---	---	8.02	0.048321	0.045217	149	18.12	5.08	9.04	2600
			97-B75	206	2.5	7.6881	0.046468	---	134	16.95	7.16	10.58	---
		Neat	97-K32	287	3.13	1.9932	0.0062799	0.011087	60	7.72	---	---	225
			97-K36	289	3.13	2.088	0.0065094	0.012878	62	8.07	---	---	285
	0.5	125 μm	97-B46	---	---	3.307	0.046849	0.031766	119	17.86	8.10	10.80	1052
		250 μm	97-B62	---	---	5.062	0.056684	0.10173	122	18.35	5.44	9.06	1454
		Neat	97-K33	262	8.06	1.1065	0.0090101	0.0057235	46	6.96	---	---	48

Table 5.1 Results from fast-fracture testing Si₃N₄-BN and monolithic Si₃N₄ materials.

5.1 Fast Fracture of MSE(T) Specimens - $a_0/W = 0.3$

This section reviews the data for fast-fracture tests run continuously to failure on the neat and the fibrous monolith materials using MSE(T) specimens with an a_0/W ratio of 0.3. Refer to Figure 3.10 for an illustration of the MSE(T) specimen geometry. An a_0/W of 0.3 was chosen for the majority of the tests as it allowed for a sufficient number of cell bundles on either side of the notch and was thought to be outside the boundary layer for interference due to edge effects. In the material with the largest cell bundles, a notch length of 5.71 mm allowed for 60% of the 2 mm cell bundles to remain in front of the notch. The notch length was also larger than the material thickness (which was 4.3 mm for the thickest material). A notch length larger than the material thickness, conceivably insures that the test would not be affected by interlaminar shear stresses at the composite edges. With the chosen notch length, the edge defects identified due to processing were also not considered an issue as illustrated in Figure 3.6.

5.1.1 Room Temperature Behavior

At room temperature, tests on MSE(T) specimens of all materials were performed with strain gages and acoustic emission transducers implemented on either side of the notch in order to capture information about the onset and progression of damage from the notch tip. In addition, certain specimens were inspected both prior to and following testing using several non-destructive techniques in order to better characterize the damage.

Representative data from a fibrous monolith specimen with the smaller microstructure, 97-B47, are given in Figures 5.1 (a) through Figure 5.1 (e). Figure 5.1 (a) shows the load versus displacement trace that contains data obtained by the CMOD extensometer, two strain gages, and the AE transducers. The loading data are non-linear to failure and show a number of

discontinuities where relative changes in CMOD are detected with little increase in load. These discontinuities are associated with the progression of damage. Specimen failure occurred at a load of approximately 4.9 kN and crack mouth opening displacement of 0.04 mm.

The microstrain data recorded shows a change in linearity near where the first AE events are detected. The maximum microstrain occurs after the on-set of non-linearity in the loading data. The traces for strain gages number one and number two are of differing magnitude. The reason being that they are on 45° plies and will not necessarily see the same strain on either side of the notch. This response is consistent for specimens of both the fibrous monolith materials with an a_0/W of 0.3 and therefore is useful in detecting initial and later stages of damage.

The plot in Figure 5.1 (a) also illustrates that acoustic emission events are first detected at fairly small displacements. The load that corresponds to the first AE events, and conceivably the onset of damage, is approximately 2 kN. Perhaps other critical stages in the load-CMOD trace for damage progression are portrayed by rapid increases in AE detections with small changes in CMOD. It is observed that steep increases in the number of events occur at displacements which correspond to those discontinuities in the load-CMOD trace and therefore may also indicate that damage is rapidly progressing at those conditions.

Data from the NDE techniques, are shown in Figures 5.1 (b), (c), (d), and (e). The damage induced is widespread and is not contained directly behind the notch. From the radiograph in Figure 5.1 (b), pronounced cracks can be seen along the +45° and -45° directions corresponding to cracking along the cell bundles in those orientations. Cracks can also be detected both between and through the 0° bundles. There may also be evidence of

delamination in the radiograph as the texture on the surface of the layer below the delaminated layer can be seen. The dark features in the radiograph, which correspond to the processing flaws (identified in Chapter 3), do not appear to have any influence on the failure mode.

The thermal image and the c-scan in Figures 5.1 (c) and 5.1 (d), respectively, clearly show evidence that there are delaminated plies behind the notch. Although both images outline the same damage zone, the thermal image shows greater resolution. The through-ply cracks running along the 45° direction are depicted in this image whereas they are not in the c-scan, and the intensity of the thermal image suggests that the damage exists on different levels within the test specimen. The c-scan, on the other hand, detects some of the differences in density due to the processing flaws which can also be seen in the radiograph.

The histogram in Figure 5.1 (e) shows the number of AE events detected at various locations along the length of the specimen. AE events were detected in a large range around the notch. The location of the AE events identifies that there is distributed damage ahead of the crack tip.

Similar information for a representative specimen with the coarser microstructure, 97-B65, is presented in Figure 5.2 (a) through 5.2(e). The behavior is similar to the material with the smaller cell bundles, the load-CMOD trace is essentially non-linear to failure. This specimen failed around 8 kN after a displacement of 0.048 mm. The large difference in load carrying capability between the two materials is due to the difference in cross-sectional areas.

As before, there are changes in the slope of the microstrain traces for both gage one and gage two which correspond to the first AE events at a load of 2 kN. The maximums for gage number one and gage number two coincide with loads of 7 and 6 kN, respectively. At

approximately 6 kN there is also a noticeable bend in the load-displacement trace and a rapid increase in the number of AE events detected. This may indicate that 6 kN is a critical load for damage progression.

The NDE data from test specimen 97-B65 are shown in Figure 5.2 (b), (c), (d), and (e). The damage zone detected using NDE for this test specimen was larger than was detected for the material with the finer microstructure. This is consistent with the displacement measured for this specimen. In the x-ray radiograph in Figure 5.2 (b), again pronounced cracks can be seen along the + and - 45° directions corresponding to cracking between cell bundles in those orientations. Cracks can also be detected across the 0° cell bundles and along on the axial direction between cell bundles.

The thermal and c-scan images shown in Figures 5.2 (c) and (d), respectively, illustrate that the cracks seen in the radiograph outline a large delaminated zone behind the notch. The AE histogram in Figure 5.2 (e) does not depict the extent of the damage zone as well as for the specimen discussed earlier. It does show that a larger number of events were detected on the load cell side of the notch, yet adjacent to the notch. AE events on the actuator side of the notch were located significantly further away from the plane of the notch.

Data shown in Figures 5.3 (a) through 5.3 (c) is for specimen 97-K32, a monolithic Si_3N_4 fracture specimen. The behavior shown here is linear, and failure occurred at a load of 2 kN. The strain behavior was linear to failure. The strain gages on either side of the notch measured identical values indicating the fracture bisected them. Only one acoustic emission event was detected during the test and is associated with the CMOD at the point of failure. Although no NDE data were taken on the neat Si_3N_4 material, a photograph of the failed

specimen is shown in Figure 5.3 (b). The photograph shows the characteristic brittle nature of the fracture. One crack grew in the plane of the notch until failure. The histogram in Figure 5.3 (c) depicts the one acoustic emission event as being detected in the center of the specimen at the notch.

5.1.2 Elevated Temperature Behavior

Results from testing both of the fibrous monolith materials and the neat material at 1150°C are given in Figures 5.4 (a) through 5.4 (d). Figure 5.4 (a) is a plot of stress versus displacement measured by the CMOD extensometer. The data are shown in terms of applied stress as the materials have different cross-sectional areas. The behavior of the two fibrous monolith materials is identical. The behavior is linear at low loads followed by rapid displacements out to failure. The neat material shows linear behavior. The data for all three tests shows a significant amount of noise that is attributed to linear expansion of the extensometer rods, and therefore the data for the neat material is represented with a dashed line on the plot.

Damage from testing is depicted for each material by x-ray radiographs shown in Figures 5.4 (b), (c), and (d), respectively. The damage detected in both fibrous monolith materials show similar widespread damage as seen at room temperature. Damage features such as cracks along the cell boundaries in the 45° and 0° plies as well as delamination and cell bundle fractures can be identified. The neat material shows a single brittle failure in the same plane as the notch.

5.1.3 Discussion

5.1.3.1 Behavior of Fibrous Monolith versus Monolithic

Figure 5.5 shows applied stress (far-field stress) versus displacement curves for the two fibrous monolith materials and the monolithic material. The plot in 5.5 (a) shows the relationship between applied stress and the displacement measured by the extensometer near the crack mouth opening while 5.5 (b) shows stress versus displacement measured at the point of loading. Both plots illustrate that the fibrous monolith materials can withstand higher applied stresses and show enhanced toughness over the stiffer neat material in the presence of a notch. This data documents the enhanced toughness of fibrous monolith ceramics over monolith ceramics.

There is a distinct difference in the nature of the fracture between the neat and in the fibrous monolith materials. Fibrous monoliths show evidence of extended failure by widespread delamination, whereas the neat material fails with a single catastrophic crack. Figure 5.6 illustrates further the difference between the fractures obtained for the fibrous monolith and neat materials with a notch. The neat fracture in 5.6 (a) looks flat and smooth to the right of the notch. The fibrous monolith specimen in 5.6 (b) has a large amount of cell bundle pull-out which outlines the comparatively torturous crack path.

5.1.3.2 Fracture Behavior as a Function of Microstructure

The plots in 5.5 (a) and 5.5 (b) illustrate that the two fibrous monolith materials show nearly identical behavior. The material with the 2 mm cell bundles (250 μm cells) appears to have gone to a slightly higher stress and displacement to failure. Consistent with that result, it was demonstrated through the NDE results that the material with the coarser microstructure fractures with a more widespread damage zone and with significantly more AE events detected.

The damage in both of the fibrous monolith materials was similar in nature as illustrated in Figures 5.7 (a) and 5.7 (b). The figures show the fine and coarse microstructure, respectively, taken from the edge view on the opposite side of the notch of failed specimens. In both cases the failure probably initiated in the cell boundary material between cell bundles of the 45° surface layers. These cracks are deflected at the underlying 0° plies and then run in the axial direction between the surface 45° ply and the 0° ply until they hit a “weak” spot in the 0° ply and can cut through. This phenomenon is similar to that observed by King¹⁷ and Kover et. al.¹⁸.

5.1.3.3 Fracture Behavior - Room versus Elevated Temperature

In comparing the behavior at 1150°C for the fibrous monolith materials with that at room temperature, there is approximately a 50% loss in strength. The neat material exhibited approximately a 24% loss in strength. Refer to Figures 5.4 and 5.5 (a) for a comparison of the elevated temperature and room temperature behaviors shown in terms of applied stress versus CMOD. It is suspected that the decrease in strength at high temperature for these fibrous monolith materials may be the result of glassy phases in the BN phase, which weakens the BN at 1150°C. Both of the fibrous monolith materials did experience slightly larger displacements to failure at elevated temperature than at room temperature.

The overall changes in behavior for the fibrous monoliths are similar to that observed in flexure above 1100°C. The drop in strength observed in flexure was attributed to the existence of an amorphous phase in the grain boundaries of both the Si₃N₄ and the BN phases from processing^{13, 18, 27, 29}. The amorphous phase softens significantly at temperatures above 1100°C and reduces strength. Although analytical microscopy of the fractured specimens tested at

1150°C in this study was not performed to document the existence of the amorphous phase, it is assumed that the same phenomenon has occurred.

Similar to the results for flexure, there was a small decrease in the overall work of fracture from room to elevated temperature. Results from a study by Trice^{27, 29} indicated that the lengths of the delamination type cracks were longer than those after room-temperature testing. Trice also observed a change in the fracture initiation from tensile to shear at 1100°C due to the weakened BN phase. In this case, displacements measured were longer which is consistent with a greater amount of cracking before failure. The x-ray radiographs do not show any noticeable differences in the fracture morphologies between room and elevated temperatures in this study.

5.2 Fast Fracture of MSE(T) Specimens with Various Notch Lengths

This section reviews the results from testing the various materials using notch-to-width ratios of 0.1, 0.2, and 0.5. Specimens from both fibrous monolith microstructures were tested with the various notch lengths. The Si_3N_4 neat material was only tested with the smallest and the largest notch lengths.

5.2.1 Fast-Fracture Behavior - $a_0/W = 0.1$

Figures 5.8 (a) and 5.8 (b) compare the two fibrous monolith materials and the neat material with an a_0/W of 0.1. These plots show the relationship between applied stress and the displacement measured by the CMOD extensometer and the LPD extensometer, respectively. Notch lengths as small as 1.9 mm demonstrate how the monolithic Si_3N_4 material suffers compared to the fibrous monolith materials.

Although the data from the fibrous monoliths are shown in the figures for comparison to the neat material, no comparison can be made between the two fibrous monolith materials as neither one had a failure that initiated at the notch. The material with the finer microstructure did not fail within the gage length of the specimen. This behavior suggests that the inherent flaws in the microstructure are greater in size than the machined notch. The material with the coarser cell structure did not fail because the load limit of the test machine was reached. The unloading data for this specimen are shown in the plots as well.

When comparing the data obtained from the CMOD and load-point extensometers, the latter measures larger displacements to failure. Similar differences in displacements were observed with the neat material.

5.2.2. Fast-Fracture Behavior - $a_0/W = 0.2$

The plots given in Figures 5.9 (a) and 5.9 (b) compare the two fibrous monolith materials with an a_0/W of 0.2. The neat material was not tested with this notch length. Unlike for the a_0/W ratio of 0.3, the finer microstructure withstands a higher stress than does the coarse material. However, the difference in strength values lies within the scatter for strength. Displacement data taken near the notch opening suggests that the coarser microstructure appears to exhibit slightly more displacement than the fine grain material. This is consistent with the results from the fibrous monolith specimens tested with an a_0/W of 0.3. The displacements measured near the notch opening are approaching those measured by the load-point extensometer. The applied stresses and load-point displacements measured for both of the fibrous monolith materials are larger than those measured for the specimens with the a_0/W of 0.3 (Figure 5.5).

5.2.3 Fast-Fracture Behavior - $a_0/W = 0.5$

The data from specimens tested with the longest notch length (9.5 mm) are given in Figures 5.10 (a) and 5.10 (b). All of the materials show a decreased in strength. The fibrous monolith materials show greater retained strength compared to the neat Si_3N_4 material in the presence of the notch. In comparing the two fibrous monolith materials, again the coarser microstructure appears to show slightly larger displacements to failure. One distinct difference is that both fibrous monolith materials exhibited substantially more displacement for a given stress level when measured near the crack mouth opening. For this notch length it was also observed that the overall displacements are now larger near the notch than at the grips and that the overall displacements at the point of loading are smaller than for the shorter notch lengths. This shift in behavior suggests that there has been a significant change in how damage occurs in the specimen and in the constraints to bending and rotation of the specimen. The neat material does not show a significant difference in behavior between the displacement measured near the notch opening or at the point of gripping.

5.2.4 Discussion

5.2.4.1 Notched Behavior - CMOD versus LPD

Differences seen in the data from the fibrous monoliths depicted by the CMOD extensometer compared to the LPD extensometer are what might be expected for a composite material tested in the single-edge notch geometry with clamped ends. For the shortest notch size, the displacement at the load point is larger than that measured at the notch opening. For the largest notch size, the displacement at the notch opening is larger. When the notch size is small, the entire specimen experiences deformation and therefore the global displacement (as

measured at the load point) is greater. When the notch size is large, the average stress level is small and therefore most of the specimen does not deform.

One interesting observation is that for all four notch length tested, the load point CMOD versus stress traces have nearly the same slope. However, for the CMOD measurements near the crack mouth opening, the largest crack length investigated exhibited a more gradual slope on the stress versus CMOD trace. This suggests that there is a change in the fracture process for this crack length. It is suggested that this change is most likely driven by rotation and bending in the specimen as a result of the long notch length. In addition, the fracture zone was confined to a narrow region ahead of the notch.

5.2.4.2 Notched Behavior- Fracture Morphology

The effect of the notch length on the behavior may best be studied along with the corresponding NDE of the fracture. Figures 5.11 (a) through 5.11 (e) contains both destructive and nondestructive data from the material with the 1 mm cell bundles (125 micron cells). The plot in 5.11 (a) shows the normalized load versus the normalized CMOD data for each notch length. The figure does not include a_0/W of 0.1 since the failure did not occur at the notch for that specimen. The plot shows that there is a notch length effect. As the notch gets longer, the relationship between normalized load and normalized displacement becomes more linear. One way of interpreting this behavior would be that there is a decrease in the distributed damage zone created ahead of the notch.

Radiographs from each specimen for the finer microstructure are shown in 5.11 (b), (c), (d), and (e). The radiograph for the specimen tested with an a_0/W of 0.1 in Figure 5.11 (b)

shows how the only damage occurred within the gripped area which was the cause failure.

Given the precise alignment of the test frame, a failure in the grips suggests that the stress concentration at the clamping grip combined with naturally occurring defects within the fibrous monolith material have more of an effect than the small machined notch. Therefore, the material is insensitive to the notch.

The specimen with an a_0/W ratio of 0.2 in Figure 5.11 (c) shows a large damage zone away from the notch. There is evidence of widespread delamination and through ply cracking. There is a crack in a 45° ply and in a 0° ply which emanates from the notch, but there are additional cracks in the $+$ and $- 45^\circ$ plies and delamination type cracks which extend across the width of the specimen.

It is suggested that cracks away from the notch were initiated by shear stresses that resulted during the failure process. The higher loads required to fail the net-cross section of the specimen with an a_0/W of 0.2 may have allowed for this larger damage zone area.

In comparison, the specimen with the notch length of 5.71 mm (a_0/W of 0.3) shows that the damage is contained within about a 12 mm zone on either side of the notch and originates from the notch tip. The damage seen in this radiograph was described in an earlier section. Finally, the longest notch length has the smallest damage zone, with all of the damage emanating from the notch tip.

The normalized plot and the radiographs for the material with the $250\text{ }\mu\text{m}$ cells are shown in Figure 5.12 (a) through 5.12 (e). The cross-sectional area of the specimen with the smallest notch resulted in a required maximum load that was too large to fail the specimen in the test system. Therefore, the data from this specimen are not shown in 5.12 (a). The data for the

other specimens show the same trend as for the material with the smaller cell bundles. As the notch length increases, the load versus displacement relationship becomes slightly more linear. In this case the data for an a_0/W of 0.2 and 0.3 show the same behavior until reaching about 75% of the peak load (50% of the peak CMOD). At that point the material with the longer notch length experiences larger displacements at the notch opening with increasing loads.

The radiograph for the specimen with an a_0/W of 0.1 is shown in Figure 5.12 (b). Due to the small notch size and large specimen geometry, it was not possible to load this specimen to failure. The lack of damage suggests that no large stress concentration existed at the notch tip. The specimen with the a_0/W of 0.2 in Figure 5.12 (c) shows widespread delamination similar to that observed in the material with the finer microstructure. There are delamination and through-thickness cracks that run along cell bundle boundaries in the ± 45 directions from the notch as well as in other places along the edge. The relatively light area in the radiograph is an area where the surface layer of the material is missing.

The damage in the specimen tested with an a_0/W ratio of 0.3 in Figure 5.12 (d) was described earlier. However, unlike the finer material, there is some cracking away from the notch. This material is thicker and has thicker plies whose stacking could have influenced the material farther away from the edges compared to the thinner material. The thicker material requires higher loads to fail the specimen which also may have allowed for the differences in failure morphology.

The specimen with the longest notch is shown in Figure 5.12 (e). The radiograph in this case shows damage which is more localized behind the notch. The cracks all appear to be influenced by the presence of the notch.

The normalized plot and photographs taken of the failed neat samples with a_0/W ratios of 0.1, 0.3, and 0.5 are shown in Figures 5.13 (a) through 5.13 (d). The three traces exhibited in Figure 5.13 (a) shows that for all three notch lengths the behavior was identical to failure, with no apparent notch length effect. Each curve shows an identical linear relationship between normalized load and CMOD. It has been suggested in the literature⁴⁶ that notch length effects as seen in fiber-reinforced composites also exist in brittle materials. However, the notch length effect is only evident at notch lengths which are small (<0.0254 mm) where the stress intensity is negligible and therefore are typically not recognized. The photos show that the specimen fracture morphology does not appear to be altered by the notch length. Catastrophic failure characterized by a single crack in the plane of the notch is observed for each.

5.3 Theoretical Prediction of Notch Length Effect

The trend in applied stress with notch length is shown in Figures 5.14 and 5.15 for the neat and fibrous monolith materials, respectively. On those plots, the theoretical predictions for strength with notch size using equations from linear-elastic fracture mechanics (LEFM) and using net section stress are shown.

5.3.1 Notch Size Effect - Monolithic Si_3N_4

Figure 5.14 shows that the strength of the neat material follows a trend with a_0/W ratio that can be accurately described in terms of stress intensity predicted by equations from LEFM. The prediction using LEFM principles says that the applied stress is equal to the stress intensity factor, K , divided by the square root of the notch length and a constant, which is a function of specimen geometry⁴⁷⁻⁴⁸. The value of K in this case is defined as the effective toughness of the

material, K_Q . The value of K_Q approaches the critical stress intensity factor, K_C , as the specimen size increases (plane strain conditions)⁴⁷⁻⁴⁸. See Appendix E for the development of the predicted behavior of the neat material in terms of effective toughness. The value for effective toughness obtained using this methodology was around 8 MPa√m, which agrees with values of fracture toughness found in the literature for Si₃N₄ materials⁴¹. The net-section stress calculation severely overestimates the strength as it does not take into account the stress intensity at the notch.

5.3.2 Notch Size Effect - Fibrous Monoliths

The plot in Figure 5.15 shows the same LEFM and net-section stress predictions for the fibrous monolith materials. The value of K used in this case to predict the notch effect in terms of LEFM equations was calculated using the initial notch length and the load at the onset of non-linearity in the load-displacement trace. The calculations for this prediction are given in Appendix F.

K_Q in this case is smaller than for the neat material at approximately 7 MPa√m and so the LEFM prediction overestimates the effect of the notch. The prediction for notch size effect in terms of the net-section strength was calculated using the average tensile strengths from the straight-sided tensile coupons for both the fine and coarse microstructures combined (120 MPa). The net-section stress prediction in this case was slightly lower than the actual test data. The most likely explanation for this result was an underestimate of the true tensile behavior of the fibrous monolith. The net-section stress prediction in Figure 5.15 was based on the average tensile strength collected earlier on test coupons taken from each fibrous monolith plate, as

described in the tension test result section earlier. Given the scatter in the tensile data, the net section results fall very close to the scatter band.

5.3.3 Discussion - LEFM vs. Net-Section Stress

The applicability of LEFM analysis and the meaning of K in terms of toughness calculated in this manner for the fibrous monolith materials is limited due to the assumptions made about material isotropy, specimen size, damage zone size and morphology. In addition, the original notch tip stress distribution is altered at the onset of damage and can no longer be modeled by LEFM principles.

Perhaps a more correct comparison of fracture toughness per se could be made for the fibrous monolith materials versus the neat material using these equations if the laminate lay-up included 90° plies as well. These materials exhibit quasi-isotropic behavior and preliminary testing on a quasi-isotropic fibrous monolith specimen showed that the nature of the fracture in a global sense may be more applicable to this analysis. A quasi-isotropic specimen that was 19 mm wide with an a_0/W of 0.3 was tested as a preliminary check on the methodology. A comparison of the fracture surfaces for neat material, fibrous monolith material with a $[-45/0/+45]_s$ lay-up and a fibrous monolith material with a quasi-isotropic architecture is shown in Figure 5.16 (a), (b), and (c), respectively. Although the failure surface of the quasi-isotropic specimen still shows some evidence of axial splitting and cracking in the 45° plies out of plane, the global failure occurred in the plane of the notch unlike for the material with the $[-45/0/+45]_s$ architecture.

The use of LEFM equations on quasi-isotropic fibrous monolith materials could be further substantiated using specimens with widths much larger than were considered in this

study. Wider specimens would be necessary to accommodate flaw sizes large enough to insure that the value of K_Q being measured approaches K_C . The notch length effect shown by the fibrous monolith materials is similar to that seen in polymer matrix fiber-reinforced composites. Data reduction techniques to describe the crack (or notch) size effect in fiber-reinforced laminate composites described by Sendeckyj⁴⁶ identifies that K_Q asymptotically approaches K_C as the flaw size approaches about 25.4 mm for typical polymer matrix composites. A wider specimen would also allow for a globally small damage zone in which there would still be a region where elastic stress field equations are applicable.

Ultimately, the net-section stress prediction in Figure 5.15 is a more applicable description of the notched behavior. The discrepancy between net-section stress and notched strength was most likely due to an underestimate of the materials true tensile strength. The apparent lack of notch sensitivity in FMs may be aided by pre-existing damage in the form of microcracks in the BN from processing. Other researchers²⁷⁻²⁹ have speculated that such flaws act to further lower the notch sensitivity of the material by disrupting the stress field near the notch tip.

If it is assumed that the ultimate tensile strength measured was low and that the actual strength of the material should be closer to that estimated for the test material using Staehler's³⁴ unidirectional data (144 MPa), then the net-section stress would more closely approximate the behavior measured in this investigation. See Figure 5.17 for the applied stress versus a_0/W data plotted against a net-section stress prediction using an UTS of 144 MPa. As stated earlier, accounting for the inherent scatter in the tensile data results in all of the data falling within or very near the net section values.

5.4 Fracture Energy

It was shown that the notched behavior of the fibrous monoliths tested in this study cannot accurately be modeled using LEFM. It was also shown that the net-section stress prediction of the behavior was influenced by the limited tensile data available. Perhaps, a better description of the toughness and notch size effect of the fibrous monoliths compared to the neat material comes from the fracture energy. The fracture energy is the total work done due to testing. The total work of fracture per unit area (WOF_T) includes the elastic energy contribution and was calculated for each specimen using the area under the load-point displacement curve. It was shown through tensile testing that a high-resolution measurement of this displacement was needed for an accurate calculation. The results in terms of total work of fracture for the materials are shown in Figure 5.18 and in Table 5.1.

Figure 5.18 shows the WOF_T versus notch-to-width ratio for the three test materials. The work of fracture measurements for the fibrous monoliths with an a_0/W of zero came from specimens with the dogbone geometry. From Chapter 4, the values from the dogbone specimens were the only data taken during tension testing that were deemed valid for this measurement. The plot shows that the fibrous monolith materials require a much higher total work of fracture to failure than the neat material, even at the smallest notch lengths. The data for the fibrous monolith materials show a definite trend with a_0/W ratio and the material with larger cells shows a slightly higher WOF_T at each notch length. The data for the neat material do not show a discernible trend with notch length.

Ideally, one could model the effect of the notch size on the behavior of these fibrous monolith materials in terms of the failure mechanisms and the fracture energy trend. A greater understanding of the complexities surrounding the cell architecture, the BN structure, and the damage progression is needed for this loading condition and specimen geometry. Such analysis is beyond the scope of this research, however, further experiments presented in the next chapter were aimed at a greater understanding of the damage progression of the material to aid in future efforts.

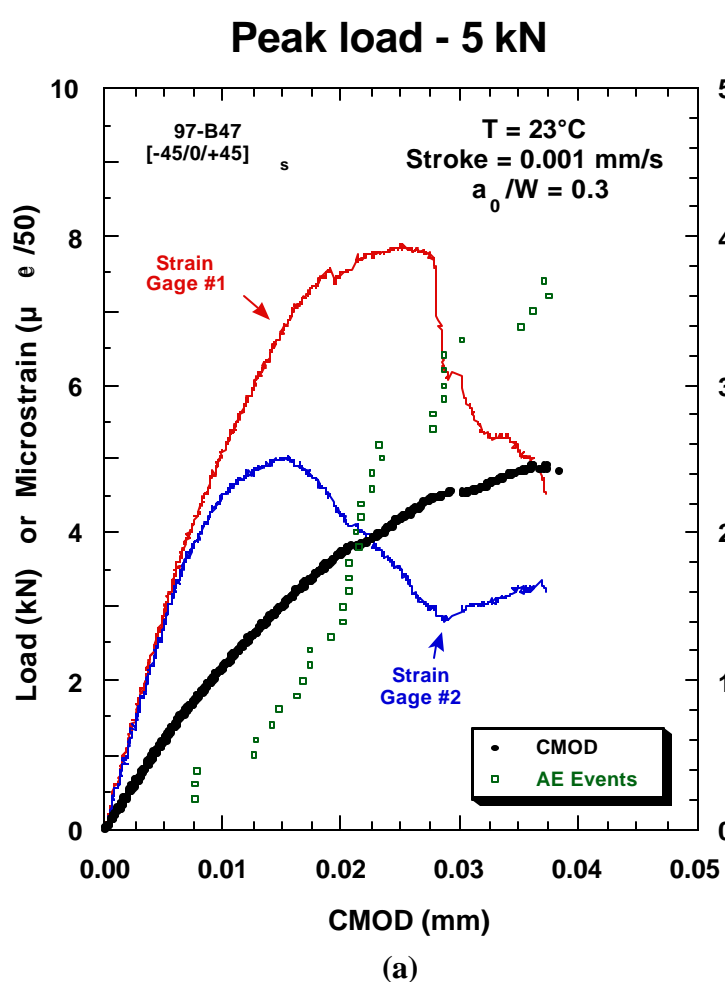
5.5 Summary

The mechanical behavior of the fibrous monolith materials show advantages in both strength and toughness over the neat material in the presence of the various stress concentrations tested. In general, the two fibrous monolith materials showed nearly the same behavior for a given notch length. Slightly higher failure loads, displacements, damage zone sizes, and total work of fractures were detected in the material with the larger microstructural features.

For a given notch length, except for that with an a_0/W of 0.3, differences were seen in the displacements for the fibrous monolith materials when measured near the notch opening versus at the point of gripping. When comparing the behavior and fractures for the various notch lengths and materials, it was found that the fibrous monolith materials exhibit behavior which is altered by the length of the notch while the neat materials exhibit behavior which is altered by the stress concentration at the notch. The neat material showed identical fracture morphologies for the various notch lengths and the behavior could be modeled by LEFM

relationships. LEFM relationships do not correctly model the notch size effect in the case of the fibrous monolith materials. The net-section stress is a more accurate prediction of the behavior if the correct tensile strength of the material is considered to be higher.

The total work of fractures for the fibrous monolith materials are higher compared to the neat material. The WOF_T data plotted in terms of a_0/W ratio for the FM materials shows a trend which could be described by damage initiation and progression mechanisms with further understanding of the tensile failure behavior.



125 μ m cells / 2-1mm strands

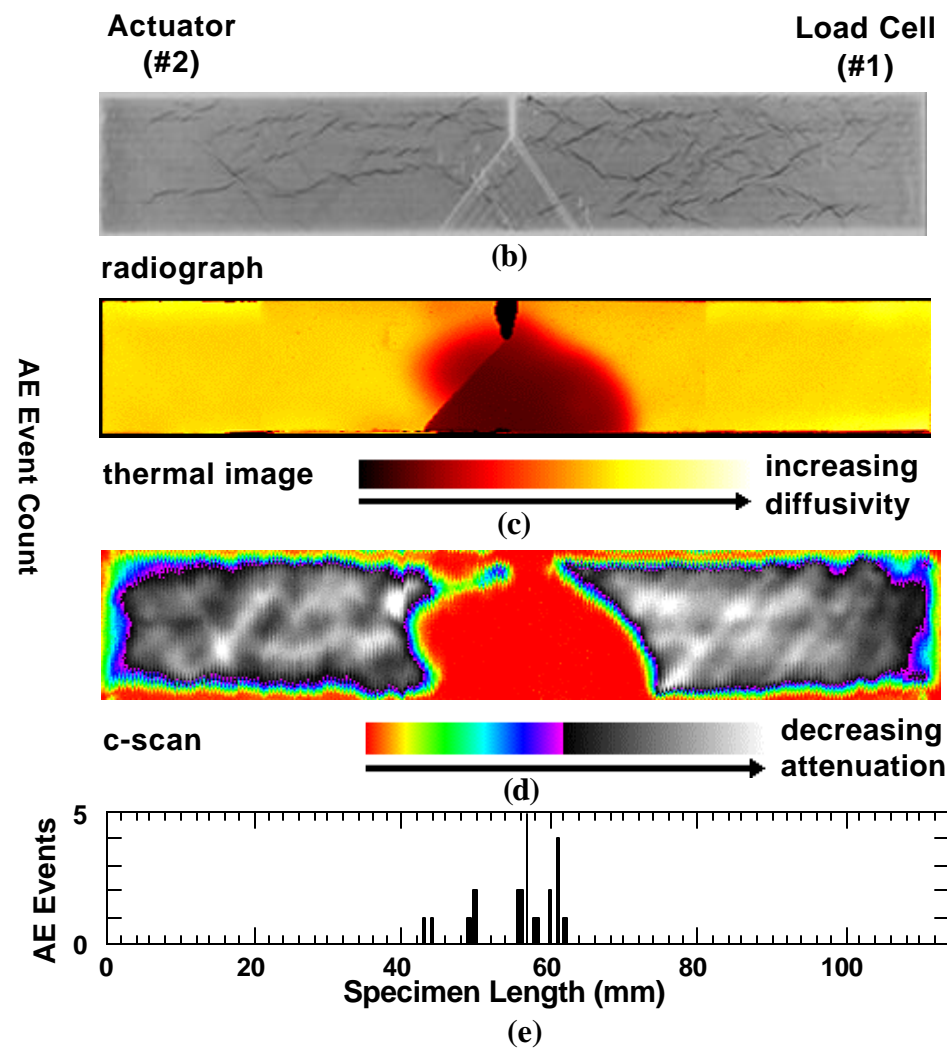


Figure 5.1 Results of fracture testing a FM specimen with the finer microstructure and an a_0/W of 0.3 at room temperature. (a) load or microstrain and AE count versus CMOD plot, (b) x-ray radiograph, (c) thermal diffusivity image, (d) ultrasonic c-scan, (e) acoustic emission histogram.

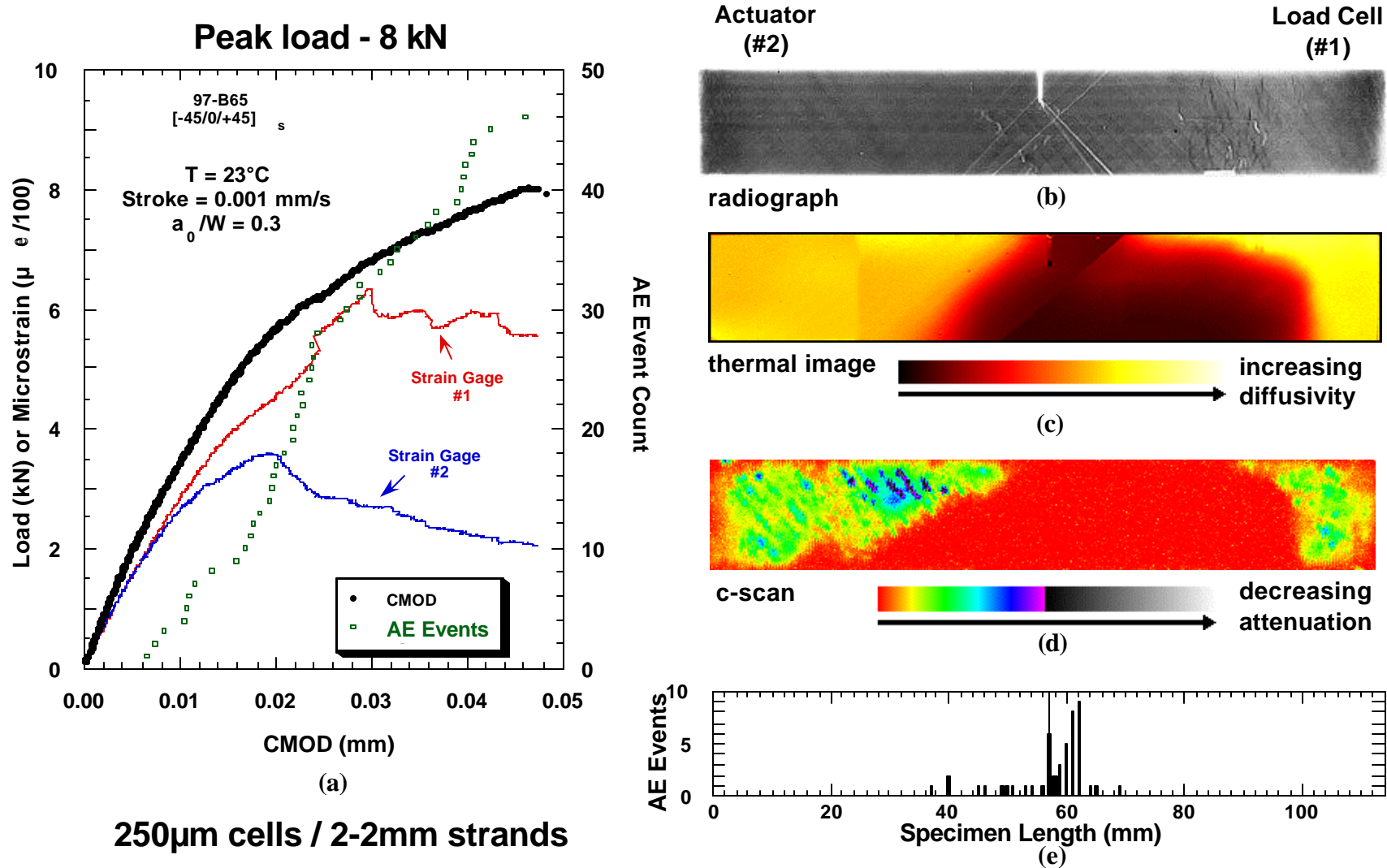


Figure 5.2 Results of fracture testing a FM specimen with the coarser microstructure and an a_0/W of 0.3 at room temperature. (a) load or microstrain and AE count versus CMOD plot, (b) x-ray radiograph, (c) thermal diffusivity image, (d) ultrasonic c-scan, (e) acoustic emission histogram.

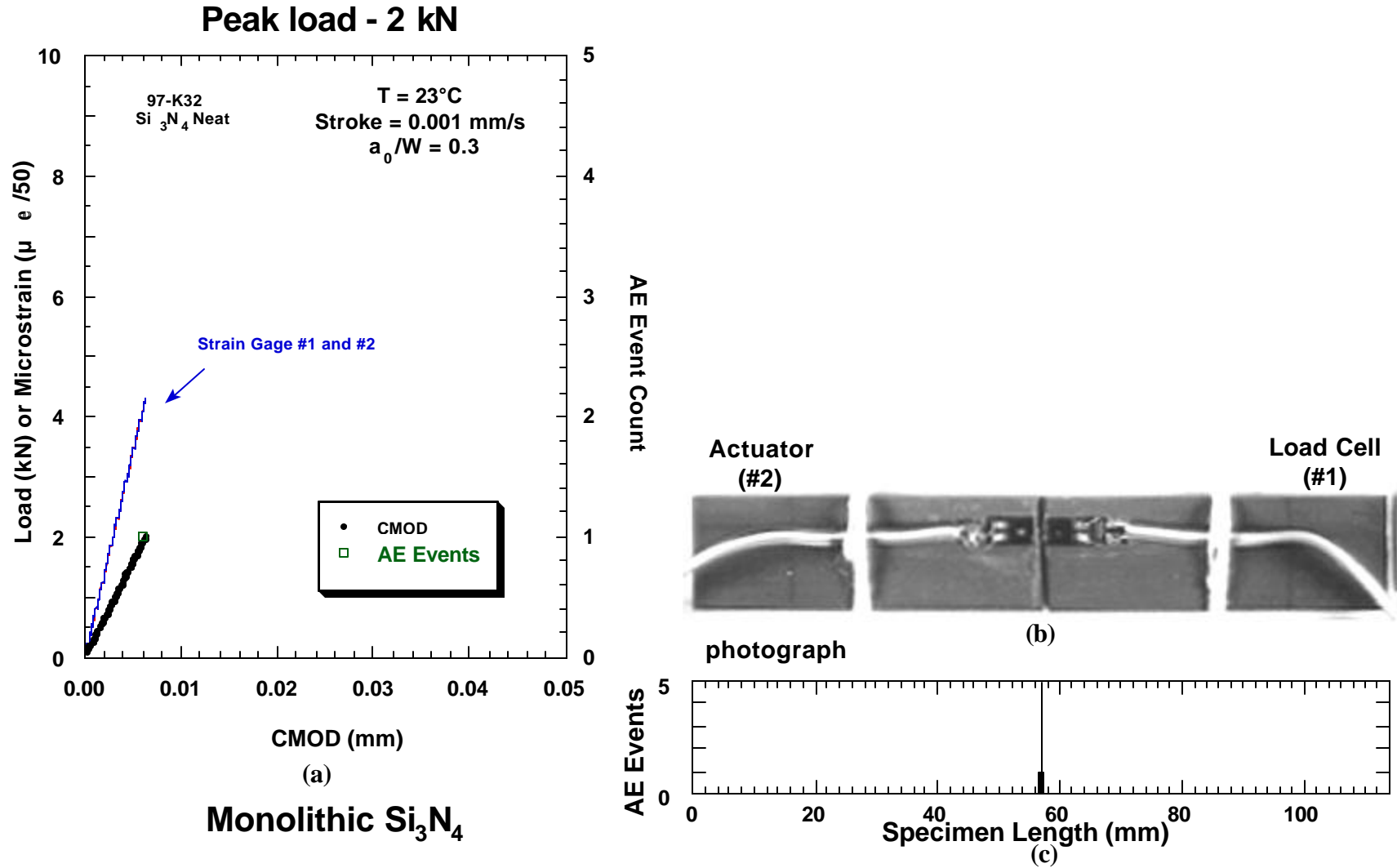
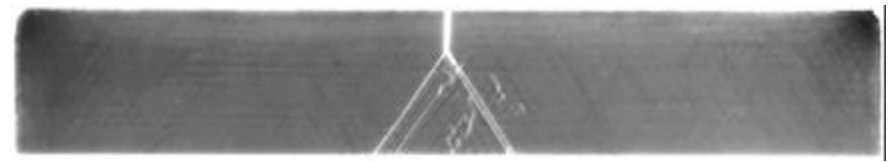
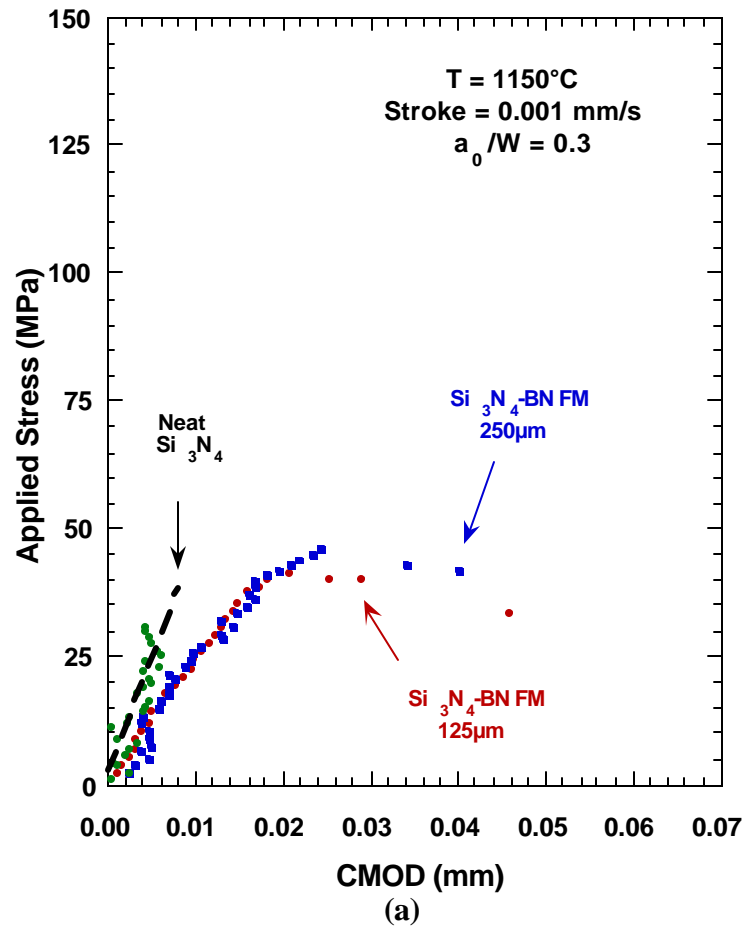
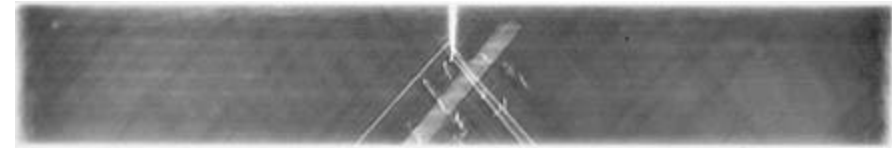


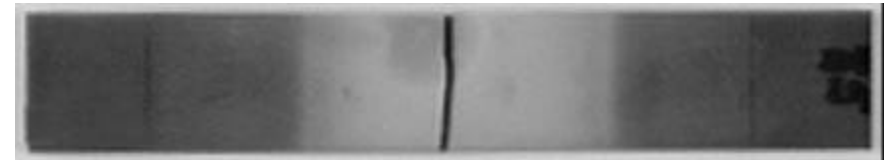
Figure 5.3 Results of fracture testing a neat specimen with an a_0/W of 0.3 at room temperature. (a) load or microstrain and AE count versus CMOD plot, (b) photograph, (c) acoustic emission histogram.



125 μm Si_3N_4 -BN FM
(b)



250 μm Si_3N_4 -BN FM
(c)



Neat Si_3N_4
(d)

Figure 5.4 Results of fracture testing the fibrous monolith and neat materials with a_0/W of 0.3 at 1150°C . (a) applied stress versus CMOD plot, (b) x-ray radiograph of FM with fine microstructure, (c) x-ray radiograph of FM with coarse microstructure, (d) photograph of neat material

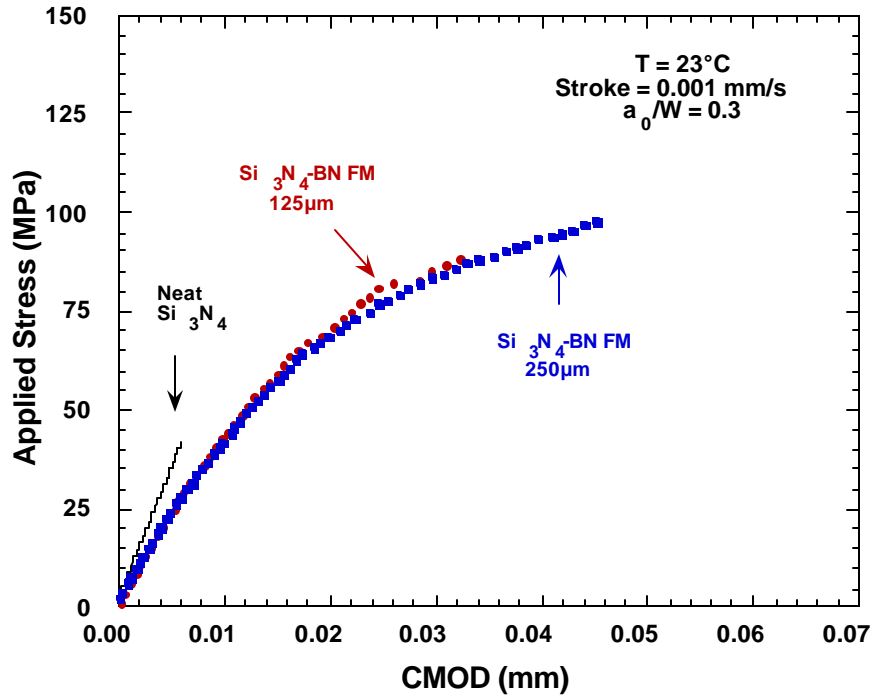


Figure 5.5 (a) Fracture behavior of Si_3N_4 -BN FM materials with an a_0/W of 0.3 as captured by an extensometer near the crack (notch) mouth opening.

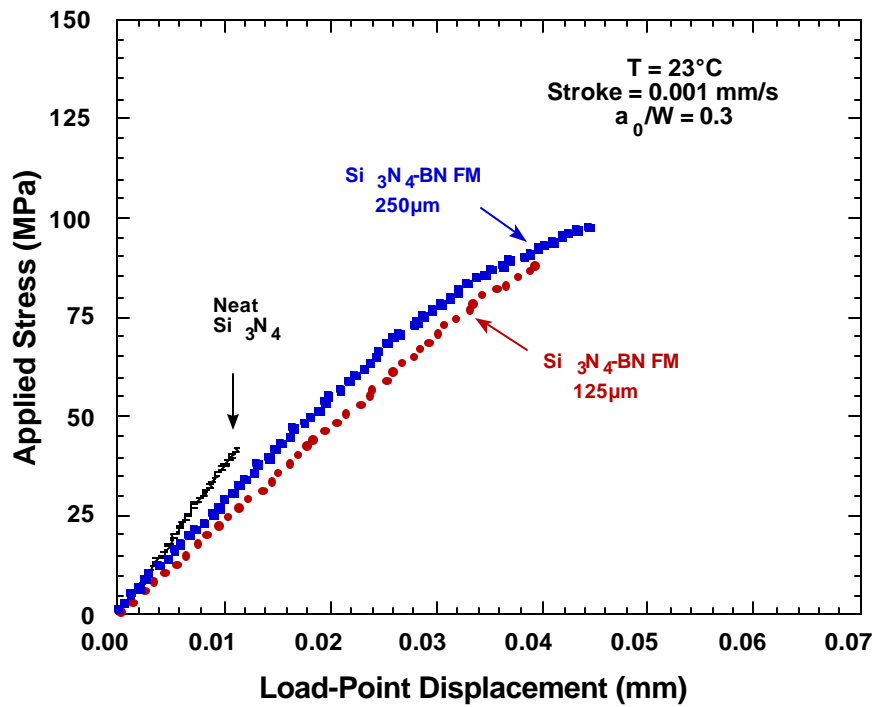


Figure 5.5 (b) Fracture behavior of Si_3N_4 -BN FM materials with an a_0/W of 0.3 as captured by an extensometer near the point of loading.

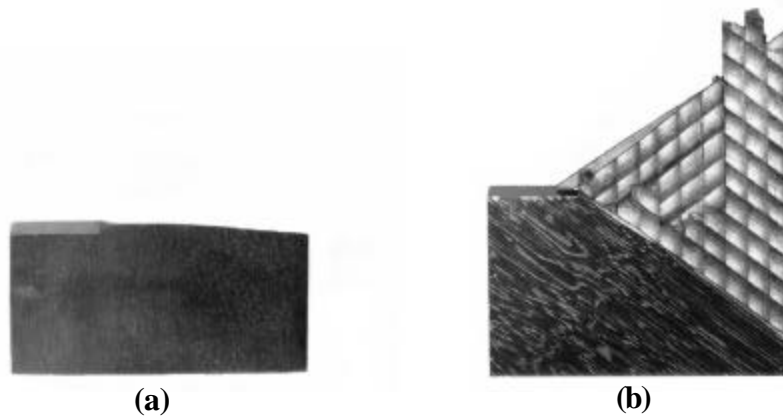
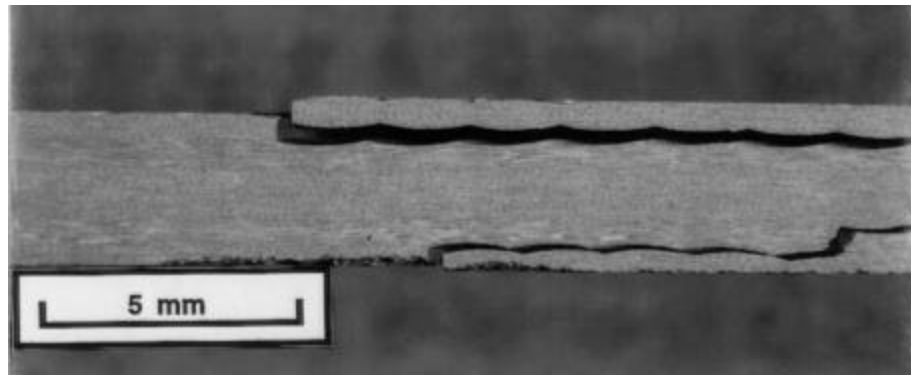
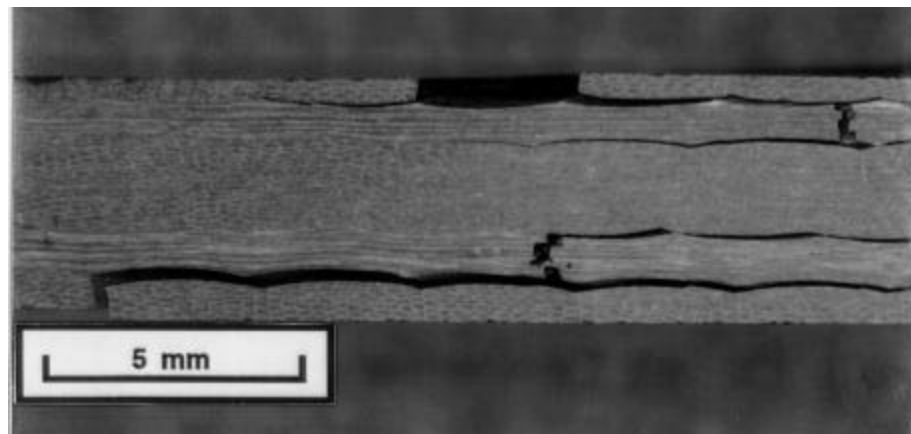


Figure 5.6 Fracture surfaces (a) from a failed neat specimen and (b) from a failed fibrous monolith specimen, both with an a_0/W ratio of 0.3.



(a)



(b)

Figure 5.7 Photographs (a) and (b) are from the respective FM materials taken from the edge view opposite the notch after failure. The photographs show how the cracks initiate at the cell bundles in the 45° plies and how cracks are deflected along the cell bundles.

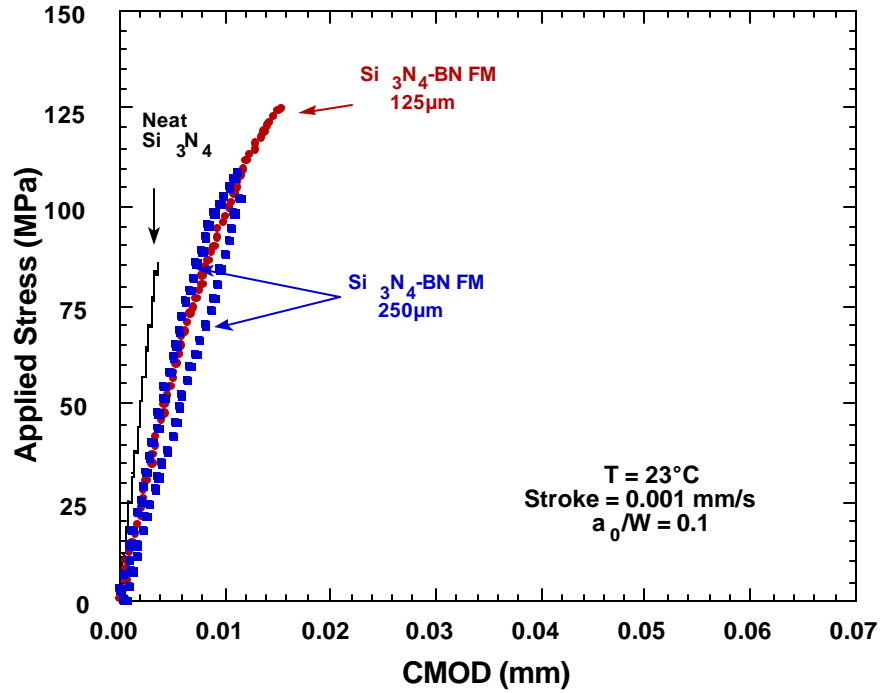


Figure 5.8 (a) Fracture behavior of Si_3N_4 -BN FM materials with an a_0/W of 0.1 as captured by an extensometer near the crack (notch) mouth opening.

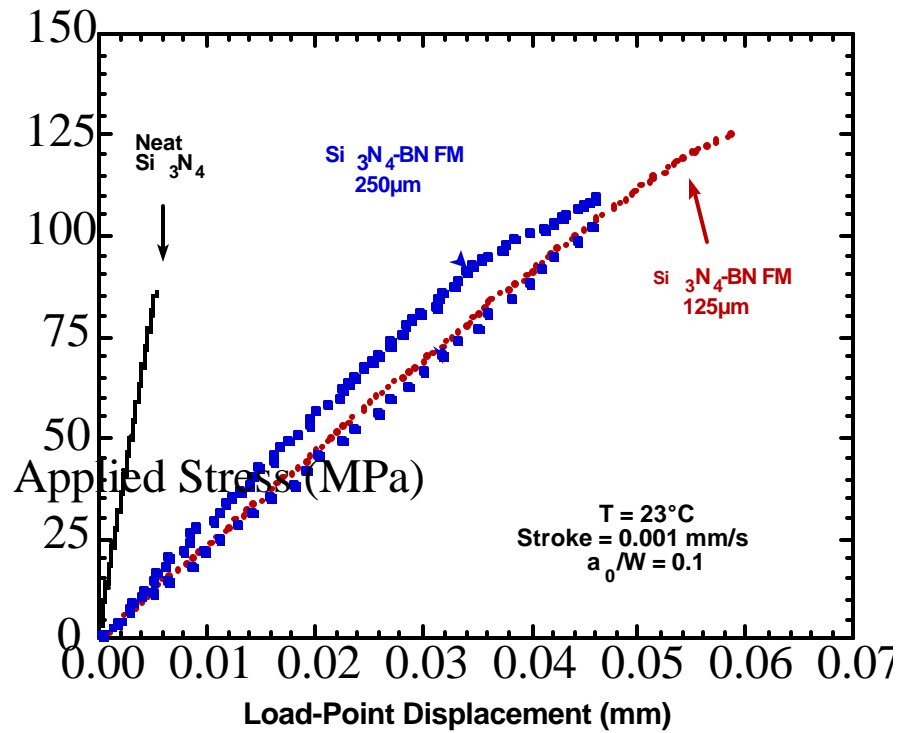


Figure 5.8 (b) Fracture behavior of Si_3N_4 -BN FM materials with an a_0/W of 0.1 as captured by an extensometer near the point of loading.

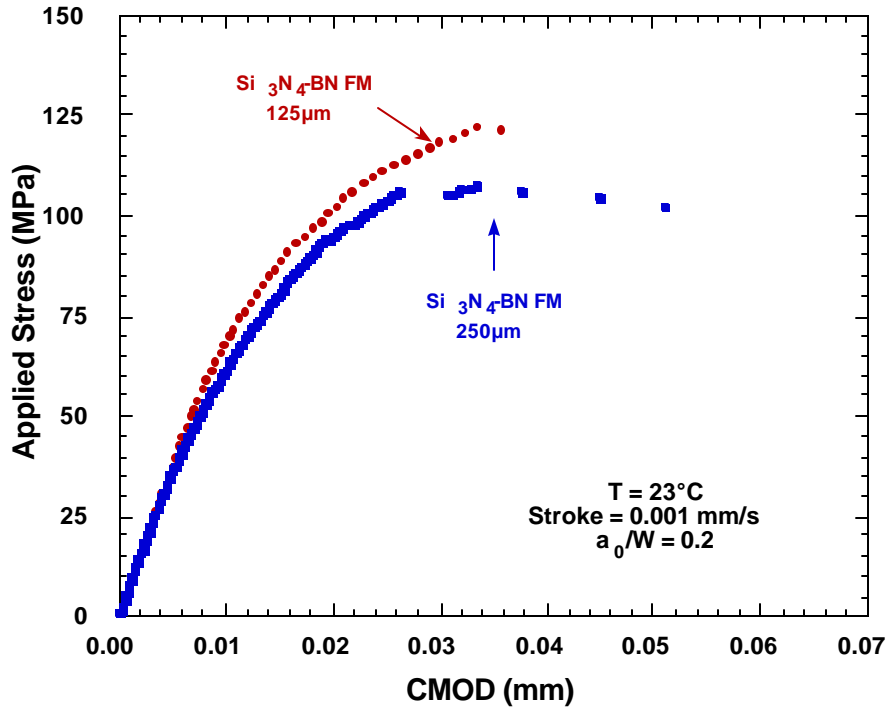


Figure 5.9 (a) Fracture behavior of Si₃N₄-BN FM materials with an a_0/W of 0.2 as captured by an extensometer near the crack (notch) mouth opening.

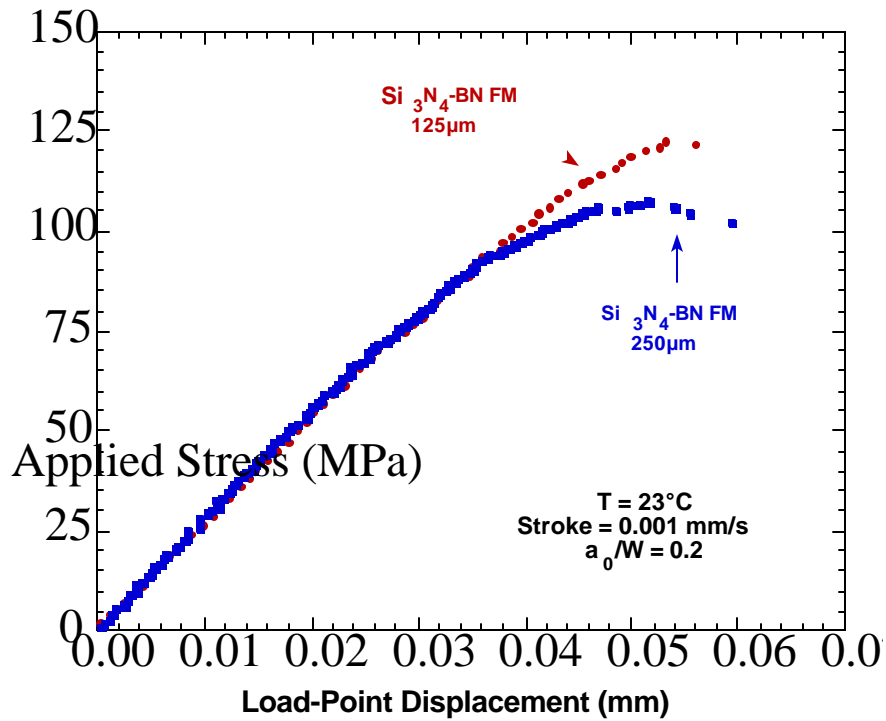


Figure 5.9 (b) Fracture behavior of Si₃N₄-BN FM materials with an a_0/W of 0.2 as captured by an extensometer near the point of loading.

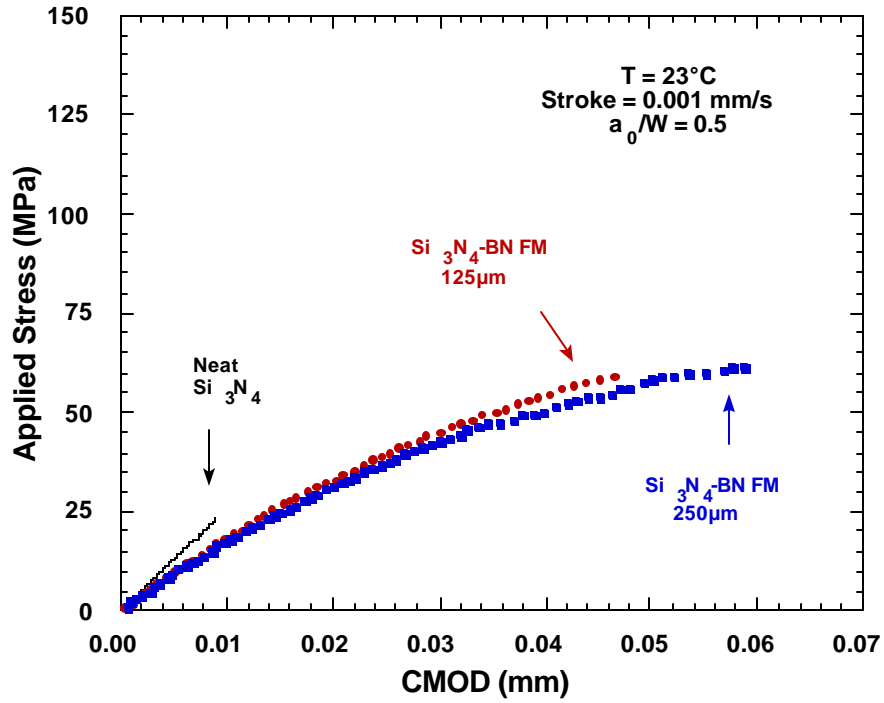


Figure 5.10 (a) Fracture behavior of Si_3N_4 -BN FM materials with an a_0/W of 0.5 as captured by an extensometer near the crack (notch) mouth opening.

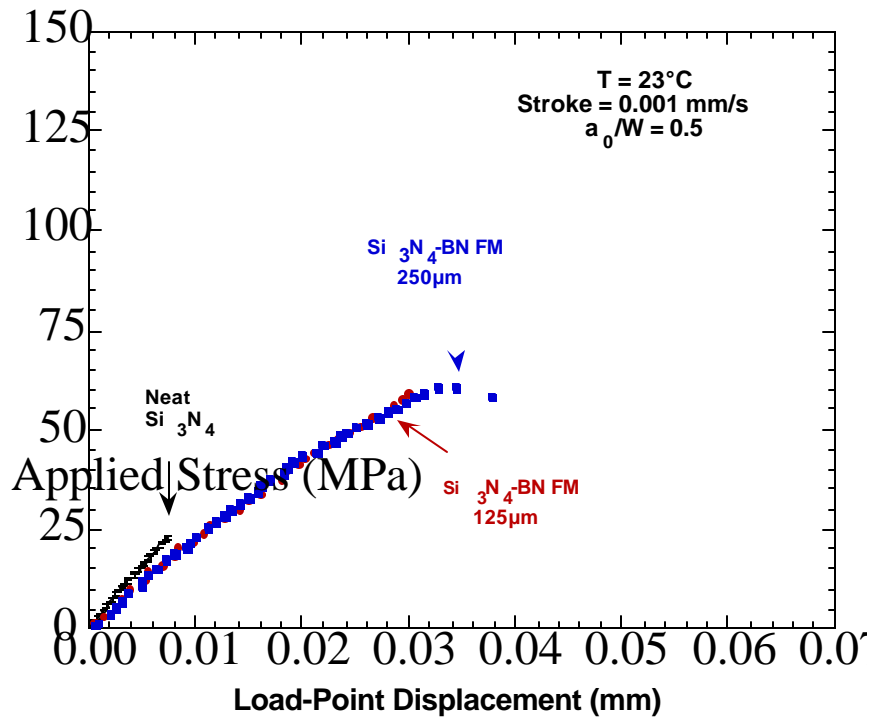


Figure 5.10 (b) Fracture behavior of Si_3N_4 -BN FM materials with an a_0/W of 0.5 as captured by an extensometer near the point of loading.

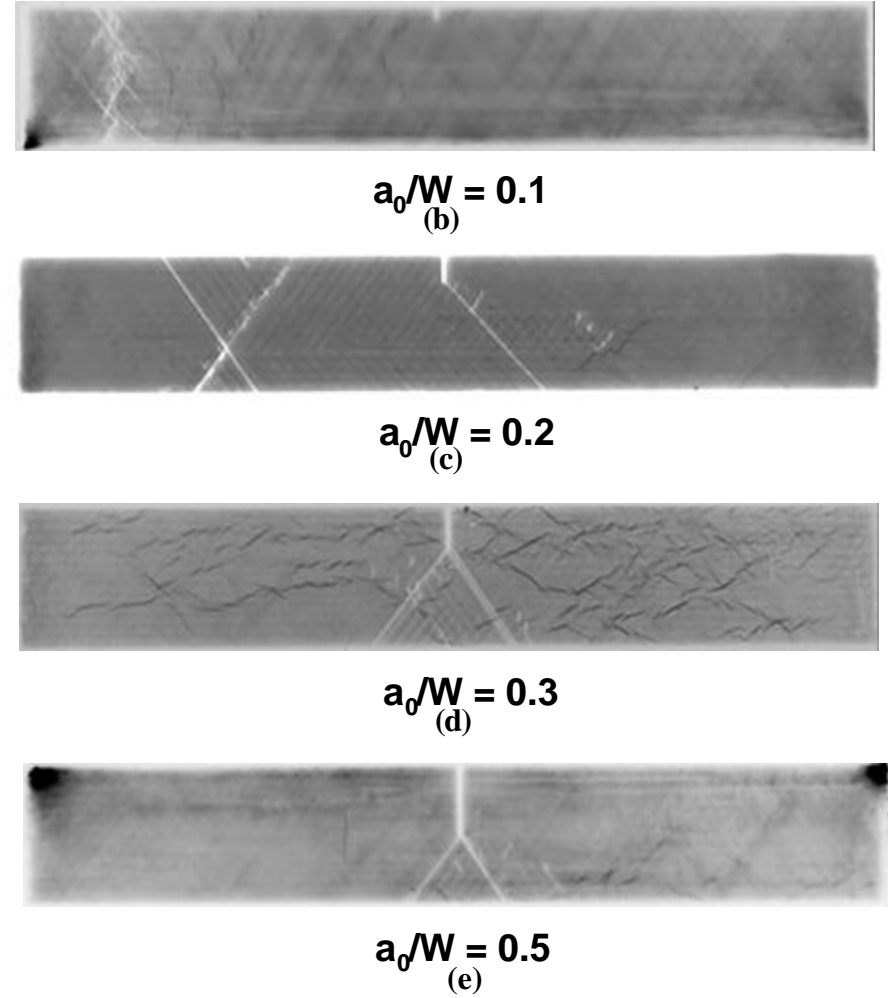
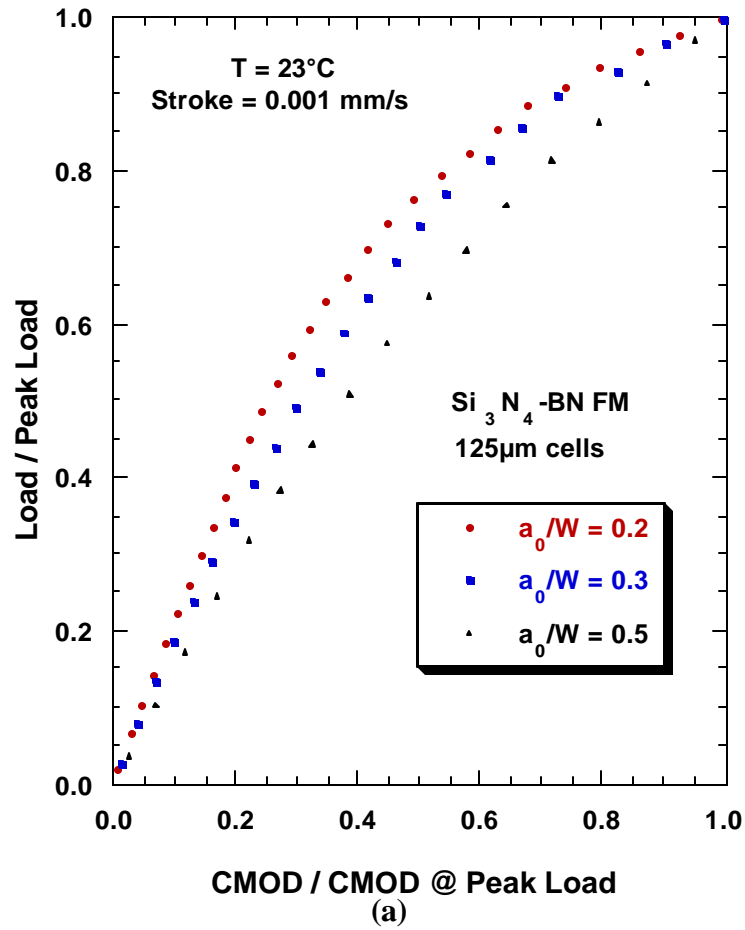


Figure 5.11 Comparison of the behavior and fracture morphologies for specimens of the 125 μm $\text{Si}_3\text{N}_4\text{-BN}$ fibrous monolith material with various notch lengths; (a) normalized load versus normalized CMOD plot, (b) through (e) x-ray radiographs of failed specimens with a_0/W 's = 0.1, 0.2, 0.3, and 0.5.

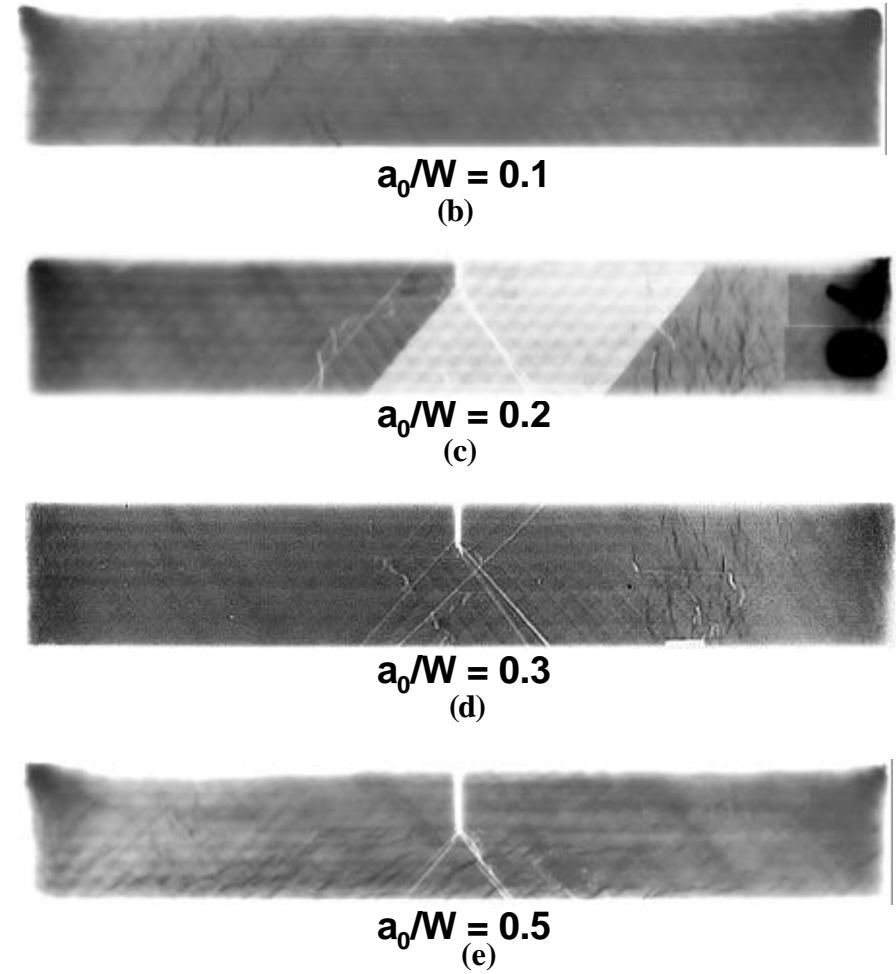
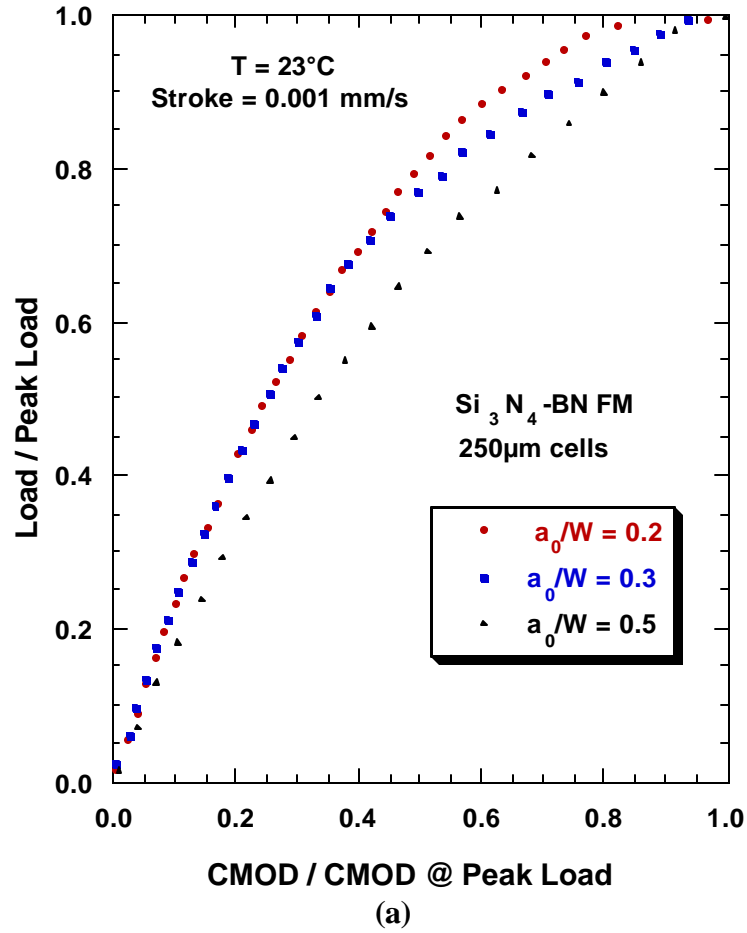


Figure 5.12 Comparison of the behavior and fracture morphologies for specimens of the 250 μm $\text{Si}_3\text{N}_4\text{-BN}$ fibrous monolith material with various notch lengths; (a) normalized load versus normalized CMOD plot, (b) through (e) x-ray radiographs of failed specimens with a_0/W 's = 0.1, 0.2, 0.3, and 0.5.

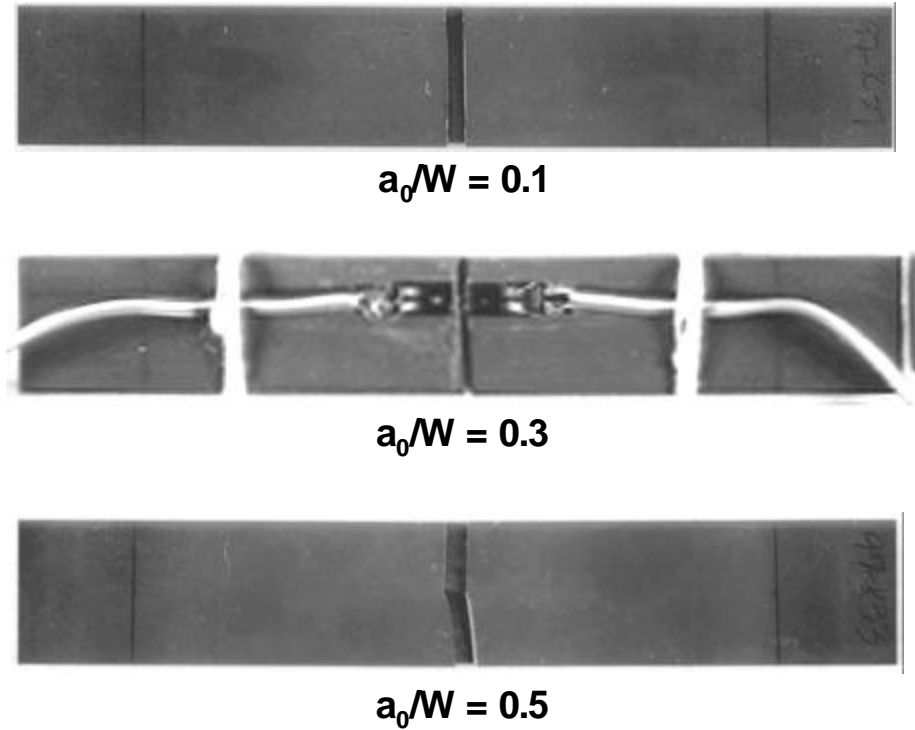
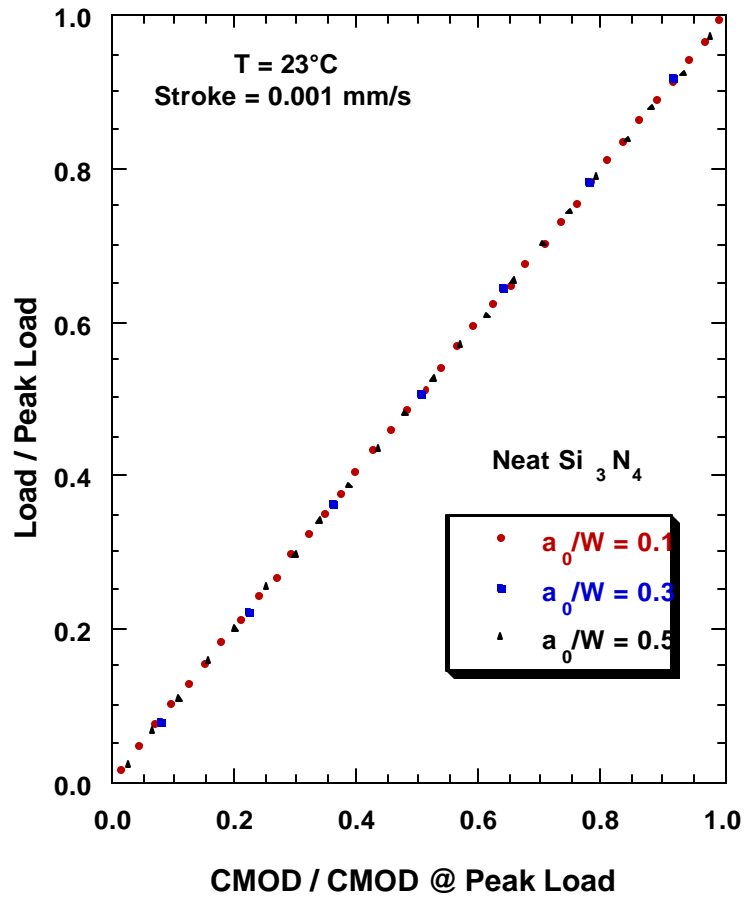


Figure 5.13 Comparison of the behavior and fracture morphologies for specimens of the neat Si_3N_4 material with various notch lengths; (a) normalized load versus normalized CMOD plot, (b) through (d) x-ray radiographs of failed specimens with a_0/W 's = 0.1, 0.3, and 0.5.

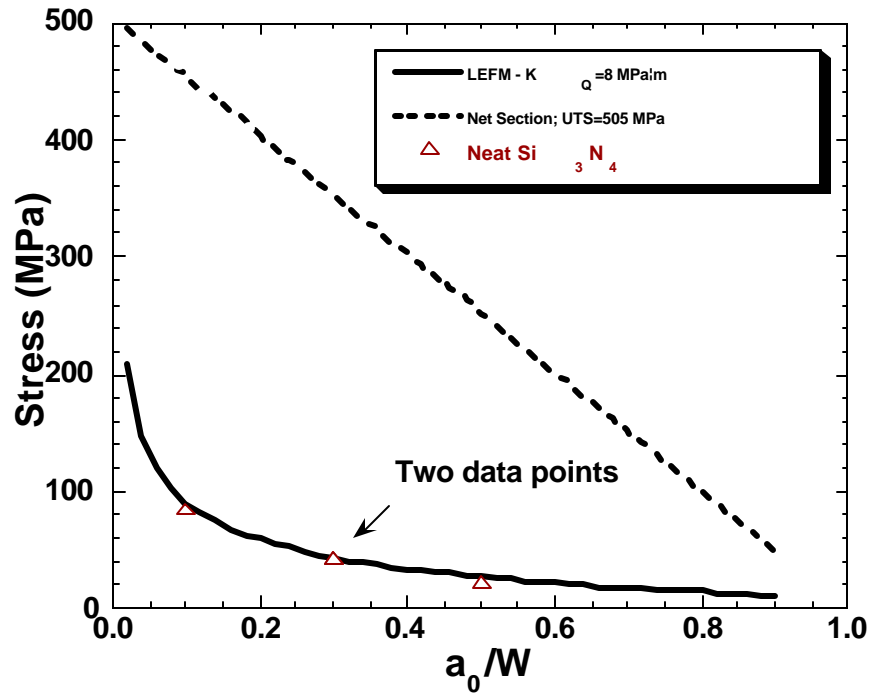


Figure 5.14 Effect of notch size for the neat Si_3N_4 material.

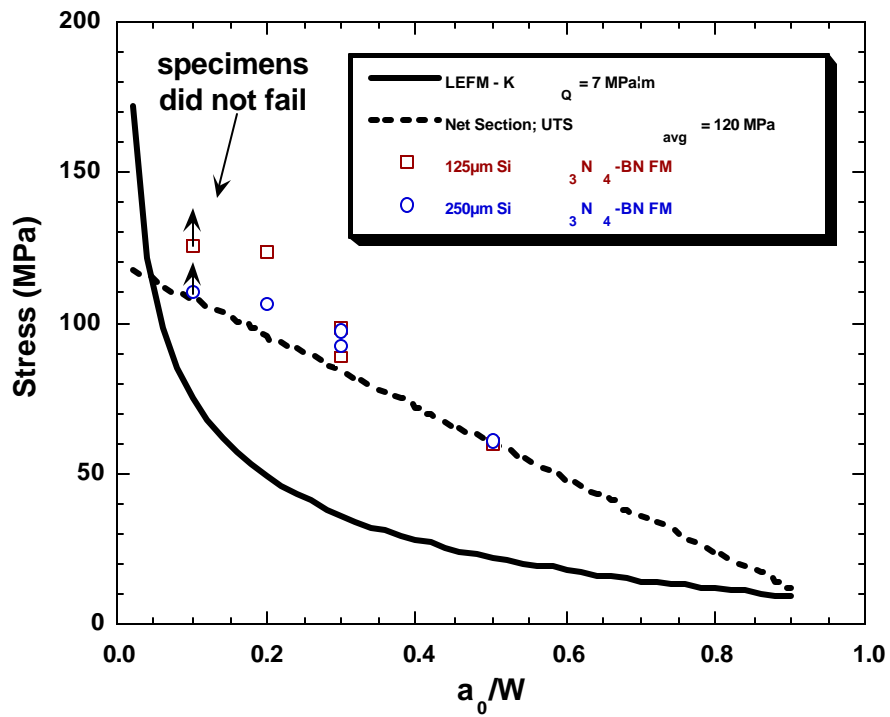


Figure 5.15 Effect of notch size for the Si_3N_4 -BN materials.

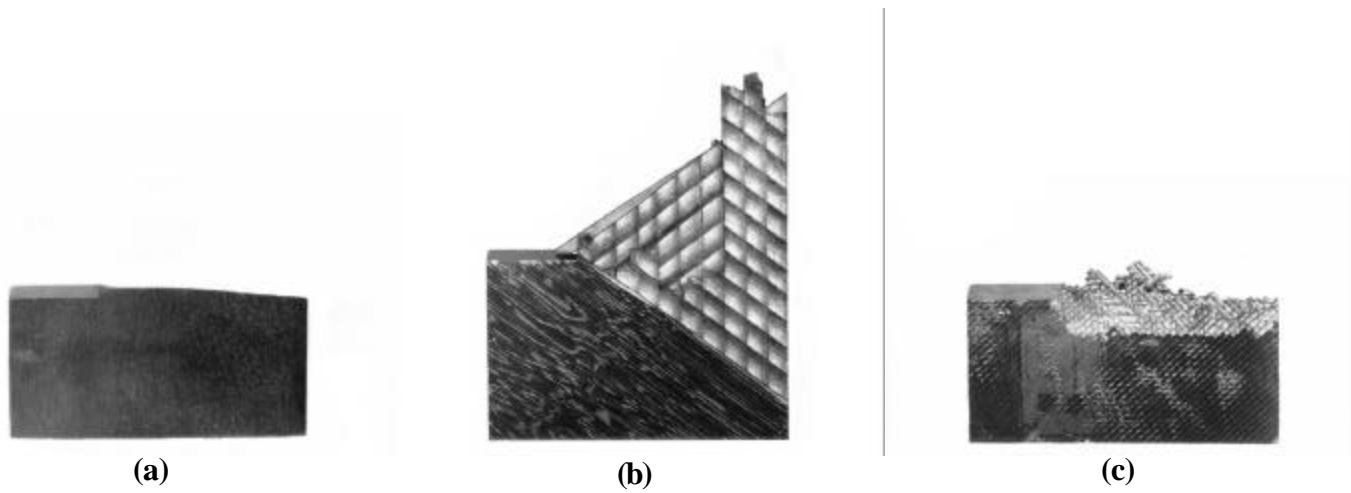


Figure 5.16 Fracture surfaces: (a) neat Si_3N_4 , (b) $[-45/0/+45]_s$ fibrous monolith, and (c) quasi-isotropic fibrous monolith.

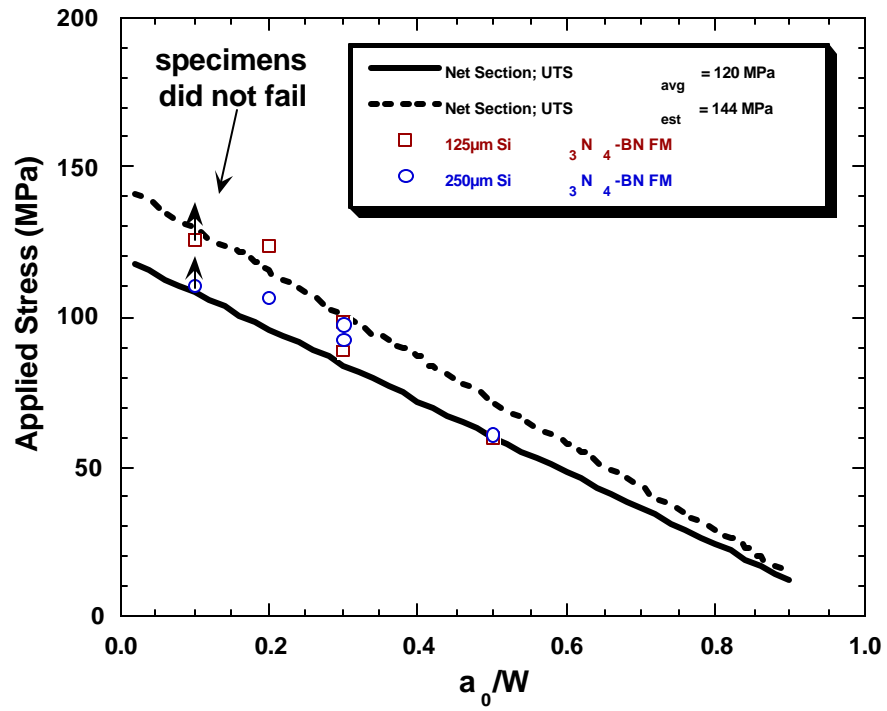


Figure 5.17 Stress versus notch to width ratio showing the net-section stress predicted if the UTS = 144 MPa.

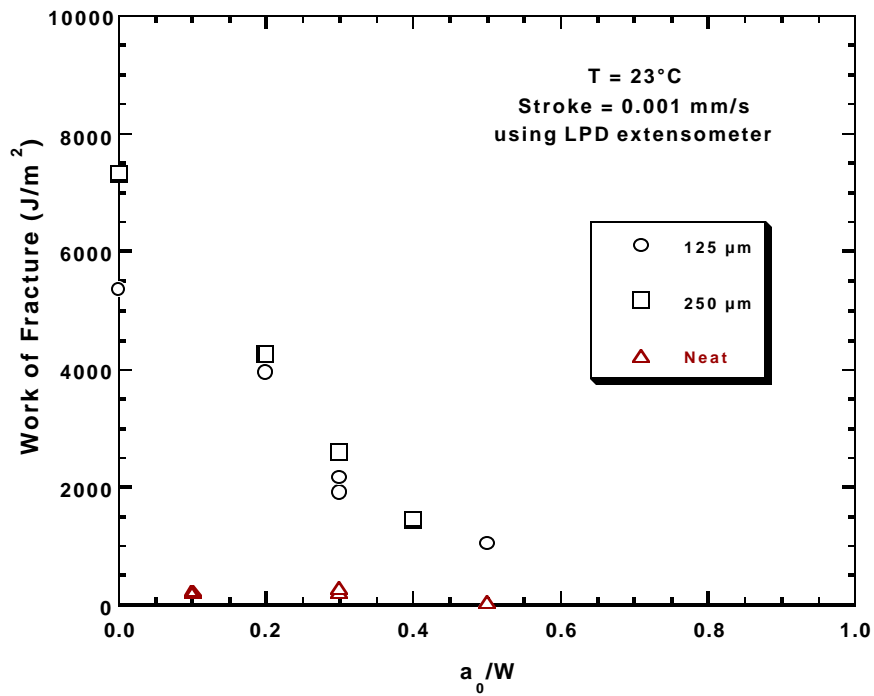


Figure 5.18 Total fracture energy per unit area as a function of notch size for the two fibrous monoliths and the neat materials.

CHAPTER 6

SINGLE LOAD-UNLOAD AND CYCLIC TESTING OF NOTCHED SPECIMENS

The results from single load-unload and cyclic testing of fibrous monoliths are presented and discussed in this section. Specimens from each microstructure were tested to various load levels and unloaded for evaluation using x-ray radiography, thermal imaging, and ultrasound. The first two sections present the mechanical test data, including the acoustic emission data, as well as the results from the NDE obtained from single load-unload tests and from cyclic loading tests. The last section discusses the results in terms of total work of fracture and absorbed energy of fracture or the work of fracture. The results from the load-unload testing, combined with the data for the notched fast-fracture tests, are given in Table 6.1.

Test Temp (°C)	Notch Size a/W	Microstructure	ID #	Initial E (CMOD) (GPa)	Initial Compl (CMOD) (m/N)	Initial Compl (L-pt Δ) (m/N)	Max Load (kN)	unloading Compliance (CMOD)	CMOD @ max load	unloading Compliance (L-pt Δ)	load pt d @ max load	Net Section Stress (MPa)	$K_{I(EP)}$ (MPa \sqrt{m})	$K_{I(peak)}$ (MPa \sqrt{m})	$K_{II(peak)}$ (MPa \sqrt{m})	WOF $T_{max} \cdot L \cdot P_d$ (kN \sqrt{mm})(mm $\sqrt{2}$)	estimated Compliance at failure - LPd	Fracture Energy plastic only LPd
23	0.1	125 μ m	97-B68 tailed in grip	---	---	---	6.9614	---	0.015469	---	0.058381	- 140	na	5.29	7.03	3873.68	---	---
		250 μ m	97-B78 did not fail	---	---	---	9.0926	---	0.011403	---	0.045703	- 122	na	8.58	9.73	2764.84	---	---
		Neat	97-K37	268	0.898		4.1036	---	0.0036818	---	0.052943	95.5	7.66	---	---	233.24	---	---
	0.2	125 μ m	97-B55	211	2.19		6.815	---	0.034482 0.035487	---	0.054661 0.056092	154.15	16.91	7.69	9.93	3945.65	---	---
		250 μ m	97-B70	203	1.53		8.817	---	0.033409 0.033179	---	0.051226 0.051126	133.79	14.68	7.49	11.65	4252.57	---	---
	0.3	125 μ m	97-B43	215	3.57	---	5.4714	---	0.039594	---	---	141.88	18.20	6.32	10.81	---	---	---
			97-B47	---	---	12.15	4.916	---	0.034498	---	0.047506	126.49	16.36	6.66	9.98	1908.86	7.32	362.70
			97-B57	224	3.48	10.76	4.983	---	0.034665	---	0.04804	129.28	16.75	5.88	10.76	2157.84	7.32	647.93
			97-B49a (load unload)	214	3.65	6.83	1.68	3.81	0.0065116	6.8	0.011161	na	na			176.60	---	7.27
			97-B53 (load unload)	214	3.62	7.5	3.29	4.4	0.015968	7.61	0.027187	na	na			819.64	---	83.32
			97-B42 (load unload)	254	3.56	6.71	3.85	5.19	0.022196	7.02	0.028046	na	na			1014.29	---	100.21
			97-B49b (load unload)	213	3.68	6.67	4.32	4.95	0.022539	7.01	0.030908	na	na			1254.59	---	86.66
			97-B59 (cyclic)				1.9968 3.0349 3.5173 4.0059 3.5357 3.8593	0.00416684 0.004652678 0.004995255 0.005670542 0.005671828 0.015679634	0.0088011 0.015305 0.019222 0.025274 0.022697 0.025734	0.006829202 0.006970098 0.007076139 0.00725058 0.007248478 satulated	0.013164 0.021177 0.024898 0.029763 0.036631 0.039207	na na na na na na	na na na na na na			253.36 608.09 800.69 1114.91 805.60 992.57 1151.05	---	11.59 33.39 12.32 85.59 ---
		250 μ m	97-B65	---	---	4.28	8.02	---	0.048321	---	0.045217	139.68	18.12	5.08	9.04	2600.06	4.70	884.60
			97-B75	206	2.5	---	7.6881	---	0.046468	---	---	133.5	16.95	7.16	10.58	---	---	---
			97-B67a&b (load unload)	214	2.4	4.38	1.12	2.42	0.0027806	4.3	0.004865	na	na			33.74	---	1.68
			97-B73 (load unload)	214	2.4	4.55	2	2.47	0.005851	4.27	0.0093104	na	na			---	---	---
			97-B81 (load unload)	206	2.53	4.5	4.006	2.98	0.012155	4.63	0.01946	na	na			494.67	---	34.93
			97-B67c (load unload)	200	2.6	4.5	6.15	3.87	0.026692	4.68	0.029706	na	na			1155.22	---	94.91
			97-B69 (load unload)	209	2.45	4.31	7.54	3.94	0.032352	4.67	0.036418	na	na			1679.73	---	144.57
			97-B69 (load unload)				2.0335 3.9998 5.0134 6.0027 6.5034 7.0103 7.5171	0.002543623 0.002826855 0.003009148 0.003246121 0.003414834 0.003619254 0.003870868	0.0053445 0.011914 0.015799 0.020153 0.02302 0.026175 0.029877	0.004407422 0.004369674 0.004457122 0.00448109 0.004533503 0.004617871 0.004712313	0.008872 0.018029 0.023181 0.027759 0.030621 0.033483 0.036917	na na na na na na na	na na na na na na na			116.88 444.59 712.94 1002.52 1194.46 1403.45 1630.21 1785.78	---	10.64 23.28 41.50 15.39 37.58 46.77 15.84
			Neat	97-K32	287	3.13	1.9932	---	0.0062799	---	0.011087	59.87	7.72	---	---	225.41	---	---
			97-K36	289	3.13		2.088	---	0.0065094	---	0.012878	62.45	8.07	---	---	284.90	---	---
	0.5	125 μ m	97-B46	---	---	---	3.307	---	0.046849	---	0.031766	118.96	17.86	8.10	10.80	1051.59	---	---
		250 μ m	97-B62	---	---	---	5.062	---	0.056684	---	0.10173	122.17	18.35	5.44	9.06	1453.52	---	---
		Neat	97-K33	262	8.06		1.1065	---	0.0090101	---	0.0057235	46.36	6.96	---	---	48.07	---	---

Table 6.1 Lists the data from the fast-fracture, the single load-unload, and the cyclic tests.

6.1 Single Load-Unload Testing

Single load-unload tests were performed on the two fibrous monolith materials using notched specimens with an a_0/W ratio of 0.3. Three specimens from each microstructure were loaded to different stress levels, unloaded, removed from the test frame, and inspected using various NDE techniques. The first specimen from each microstructure was loaded until the first AE event was detected. The second and third specimens from each FM material were loaded to two progressively higher levels above the first AE event but below the failure stresses. Upon completion of the NDE, the specimens unloaded at the onset of AE were reloaded to 85-95% of each material's suspected failure stress and unloaded. They were then re-evaluated a second time via NDE.

Target loads for single load-unload testing were chosen based on events in the load versus crack mouth opening displacement traces, the microstrain data, and the acoustic emission data observed during fast-fracture testing. An illustration of this strategy is given in Figure 6.1. Shown in the figure are the fracture data obtained from specimen 97-B47. Lines have been added to indicate the target test loads.

The average failure loads from fast-fracture tests on the fine and coarse microstructures were 5 kN and 8 kN, respectively. The first AE events, and conceivably the onset of damage, corresponded to about 2 kN for both fibrous monolith materials. This was about 40% of the failure load in the fine microstructure and about 25% in the coarse microstructure. The target loads for the two intermediate-load level specimens of the finer microstructure were 60% and 80% of the failure load, or 3 and 4 kN, respectively. The corresponding stress levels were 54 MPa and 72 MPa. For the coarse microstructure, the target load levels were 50 and 75% of

the ultimate, or 4 and 6 kN. The corresponding stresses in this case were about 48 and 73 MPa, similar to those used for the fine structure. Table 6.2 gives a summary of the actual loads (and stresses) achieved in each test.

Microstructure	Specimen ID#	Max Test Load (kN)	Max Stress (MPa)	Percent of Max Failure Load
125	97-B49a	1.68	30	34
	97-B53	3.29	59	66
	97-B42	3.85	69	77
	97-B49b	4.32	78	86
250	97-B67a	1.12	13	14
	97-B67b	2.00	24	25
	97-B73	4.01	49	50
	97-B81	6.15	75	77
	97-B67c	7.54	91	94

Table 6.2 Lists the actual test loads in single load-unload testing.

The results from testing to a peak load of 2 kN on the fine celled material (97-B49) and the coarse celled material (97-B67) are shown in Figures 6.2 (a) through (e) and in 6.3 (a) through (e), respectively. Figures 6.2 (a) and 6.3 (a) show the load-displacement traces obtained by both the CMOD and LPD extensometers as well as the number of AE events collected. The NDE results, including an x-ray radiograph, a thermal diffusivity image, an ultrasonic c-scan, and a AE data location histogram are given in (b) through (e). The load-displacement traces for the respective materials are shown to be linear with no discernable hysteresis, and although a few AE hits were detected, the NDE techniques provided no

evidence of damage. The x-ray radiographs and the IR images are identical to the pre-test images. No pre-test c-scan was obtained for comparison in either case.

The data obtained for the specimen with the coarser microstructure, 97-B67, requires some explanation. This specimen was unloaded around 1 kN after an AE event was detected. This was believed to be within the elastic response region of the material and the decision was made to reload the specimen to the original target load of 2 kN. Based on the similarity of the reloading curve, the 1 kN load excursion appears to have had no effect upon the subsequent reloading. During the second load excursion, the data acquisition system failed and thus the dashed line indicates the assumed behavior to the peak test load. Both traces are linear with no hysteresis, suggesting that there was no damage to the specimen. The c-scan, on the other hand, shows a large region with signal attenuation. This, however, seemed inconsistent with the low loads and linear load-displacement traces, suggesting a possible problem with the scan itself.

Results for specimens 97-B53 and 97-B73, which were run to 3.29 kN and 4.01 kN respectively, are beginning to show hysteresis and permanent offset. However, while a significant number of acoustic emission events were detected, there was no indication of damage on the radiographs or the IR image. The c-scan probably does not show any change as well, however, the interpretation is not definitive without a pre-test scan. See Figures 6.4 and 6.5 for the results from specimens 97-B53 and 97-B73, respectively.

Specimens 97-B42 and 97-B81 which, were tested to higher loads yet, show even more hysteresis in the load-displacement traces and permanent offset in the displacement. The data for these specimens are shown in Figures 6.6 and 6.7, respectively. In both materials, a

significantly larger number of acoustic emission hits were also detected. The radiographs and thermal images look identical to the pre-test scans. The c-scans on the other hand, hint that there is evidence of damage.

The c-scan for specimen 97-B42 may show a small growth of the attenuated area in the vicinity of the notch. There is also a strip of attenuated area on the scan that corresponds to the specimen edge. The signal attenuation in this case is attributed to plate edge defects in the material. This specimen came from a plate edge and the notch was machined on that outer plate edge as explained in Chapter 3. The c-scan for specimen 97-B81 also may show a small growth of the attenuated area right behind the notch. The AE location data seems to verify that there may be some form of damage right behind the notch.

Specimens 97-B49 and 97-B67, which had already been tested to 2 kN and unloaded, were re-tested close to the measured failure loads. The specimen with the smaller cells is labeled "97-B49b" as this test was the second load-unload cycle and specimen 97-B67 is labeled as "97-B67c" as this test was actually the third load excursion for this specimen. The respective test loads for the two specimens were 4.32 kN and 7.54 kN. See Figures 6.8 and 6.9 for the load-displacement traces and the corresponding NDE images.

The data in each case showed hysteresis and a large number of AE hits. A fewer number of AE hits and a smaller displacement were captured for 97-B49b than for specimen 97-B42 which was tested to a lower load. This may be attributed to specimen-to-specimen variability or possibly due to the previous loading cycle in specimen 97-B49b. The specimen

with the larger cells, 97-B67c, showed a large permanent offset and a large number of AE hits over any of the previous tested specimens from that material.

In the case of specimen 97-B49b, the c-scan and AE event history show evidence of damage. The c-scan shows an attenuated area behind the notch off to the left side. The acoustic emission location plot also shows a larger number of events on the left side of the notch. For specimen 97-B67c, the thermal image, c-scan, and AE all show evidence of damage in the vicinity of the notch. Both specimens were c-scanned following the first load-unload cycles so there are pre-test scans which can be compared. However, as explained earlier, the c-scan done on specimen 97-B67 after the first load-unload cycles may not have been done according to the calibration procedures. It is still believed, however, that a change in shape of the attenuated area behind the notch is evidence of a change in the structure and not from differences in scanning procedures.

6.2 Cyclic Testing

In addition to the single load-unload tests, a cyclic test was run on a single notched specimen from each microstructure. For the cyclic tests, the specimens were loaded and unloaded near the same stress levels as the previous single load-unload tests, but without being removed from the test machine. This test was to provide information about the energy being absorbed and compliance at the various load levels using a single specimen instead of using different specimens. The specimens that were cyclically loaded were also inspected using the various NDE techniques, but only after the final load cycle.

Specimen 97-B59 was loaded and unloaded several times up to a maximum load of around 4 kN. The load-displacement data are shown in Figure 6.10 (a) and 6.10 (b). This test was prematurely stopped due to a load limit being reached, and then restarted. The data obtained after the test was restarted are shown in Figure 6.10 (b). The load-displacement traces from this specimen before the restart show increasing permanent offset as the load increases. Upon re-start, it was attempted to repeat the last two cycles but a large change in the CMOD, presumably due to damage, prompted the unload. The specimen was subsequently reloaded to a small load, which showed that the specimen still had load-carrying capability.

For this specimen, there is no detectable damage seen in the x-ray radiograph but there is a damage zone behind the notch as detected using the thermal and ultrasonic techniques. The specimen itself showed no damage detectable by eye, therefore, it is presumed that the damage shown includes cracks emanating $\pm 45^\circ$ from the notch which outline an area of interply delamination. Delamination type cracks are not readily detected using x-rays unless there is an appropriate aspect ratio to the defects allowing for more x-rays to penetrate the specimen and expose the film.

The specimen with the larger cells, 97-B69, was loaded and unloaded up to a maximum of 7.5 kN. The load-displacement data again show that permanent damage is being induced through the formation of hysteresis loops with increased load. None of the NDE techniques applied in this case show any conclusive evidence of damage. See Figures 6.11 (a) through 6.11 (d) for the data from this specimen.

6.3 Fracture Energy

The total energy and the absorbed energy were calculated for each single load-unload and cyclic test using the load versus displacement data obtained from the load-point displacement extensometer. The total energy, or total work of fracture (WOF_T), was calculated using only the loading portion of the traces for both the single load-unload and cyclic loading tests and the cross-sectional areas of the specimen in each case. The absorbed energy, or work of fracture (WOF), was measured using the nominal area of the loops formed by each load-unload cycle. These values are per unit area. Refer to Table 3.2 for the definitions and physical meanings for total work of fracture versus work of fracture.

WOF_T for each material are plotted in Figure 6.12 against normalized load. The normalized load is the test load divided by the failure load measured during fracture testing. Included on this plot is the total work of fracture measured for the fast-fracture test specimens with an a_0/W of 0.3, including the neat material specimen. As was shown in the WOF_T versus a_0/W plot in Figure 5.18, the material with the coarser microstructure has a higher total fracture energy than the material with the smaller microstructural features. Prior to the failure point, however, the data from the two fibrous monolith materials are grouped tightly together and are nearly identical, with no abrupt changes in the data. For this crack length the fibrous monolith materials demonstrate a substantially greater energy absorbing ability over the monolithic material.

The WOF is plotted against normalized load for the fibrous monolith specimens only in Figure 6.13. Work of fracture was also calculated for the fibrous monolith specimens tested to failure and are included in the plot. The work of fracture for the fractured specimens was

calculated using an estimated compliance at fracture that was extrapolated from the load-unload and cyclic test data.

To estimate the compliance at failure for each material, an average compliance was found over the entire unloading curve for each load-unload excursion. The average compliance was plotted against normalized load. A curve was fit to the data and a compliance value corresponding to the failure load was extrapolated. Plots showing the compliance predictions for the respective fibrous monolith materials are provided in Figures 6.14 (a) and 6.14 (b). A threshold value is shown on each plot that corresponds to the lowest compliance value measured for each material during the modulus determination portion of each test. The modulus determination procedure was described in Chapter 3. The average compliance at failure was found to be 7.32×10^{-9} m/N for the fine microstructure and 4.7×10^{-9} for the coarse microstructure.

The compliance estimates were then used to calculate the plastic contribution of the failure energy by subtracting the elastic portion (the area under the curve generated by the compliance) from the total area under the fast-fracture loading curves. An example of the compliance curves generated for the fractured specimens are shown for the fibrous monolith materials in Figures 6.15 (a) and 6.15 (b). The initial loading portion of the data for specimen 97-B47 were not recorded due to problems with the LPD extensometer and have been extrapolated. The corresponding portion of the compliance curve for 97-B47 is shown by a dashed line. The compliance curves for both specimens are shown to follow the slope of the initial loading curves well and are thus thought to be reasonable estimates.

The plot of work of fracture versus normalized load in Figure 6.13 shows that the majority of the energy absorbed is a result of mechanisms that occur near material failure. Around 75% of the total energy absorbed occurs after testing to a load which is 90% of the failure load or greater. Both materials show a similar magnitude of absorbed energy until failure, where the material with the larger cell bundles shows a higher work of fracture. Nominally the values of work of fracture for the two fibrous monolith materials were approximately 648 J/m^2 and 885 J/m^2 , respectively.

6.4 Discussion

6.4.1 Discrepancies in NDE results

The load-displacement (with AE) data presented in sections 6.1 and 6.2 show that permanent damage is being induced progressively with increasing load through measurable permanent offset in displacement for both fibrous monolith materials. This is shown qualitatively by the load-unload traces in Figures 6.16 and 6.17 for the fibrous monolith material with the finer microstructure and coarser microstructure, respectively. However, none of the imaging NDE techniques, except possibly the ultrasonics, identifies any damage at those loads.

The corresponding ultrasonic c-scans around the notched area are shown along with the single load-unload curves for both materials in Figures 6.16 and 6.17. From Figure 6.16, it is apparent that the ultrasonic technique has identified a damage zone behind the notch in 97-B49b compared to 97-B49a. The same may be said for specimen 97-B67c in Figure 6.18, however, the scans are not directly comparable as explained earlier.

The other imaging NDE techniques did not show the same results due to the nature of the damage experienced by these materials. The physical size and morphology of the damage may be finer than that which is resolvable by the methods used in this study. Thermography did show evidence of damage compared to the as-received image on specimen 97-B59 as shown in Figure 6.10 (c) and possibly for 97-B67c in Figure 6.9 (c). The radiography technique did not detect the damage in either case. It is suggested that this was because the damage was interlaminar. Although the radiography did show the ability to discern interply cracking in the case of the fast-fracture tests given in Chapter 5, the technique is not very well suited for that type of damage detection unless there is a large enough aspect ratio to the anomalies.

6.4.2 Behavior in Terms of Energy

The trends in total and absorbed energy per unit area show that the two fibrous monolith materials behave similarly except near the failure loads, where the material with the larger cell bundles demonstrated a higher work of fracture. The differences in work of fracture between the two materials are thought to be due to the effect of the cell bundle size on the fracture mechanisms. Estimates of the work of fracture for both materials using concepts of Kovar and Thouless^{18, 19, 25, 49} predict a similar difference in work of fracture between the materials as was measured in this study.

Kovar and Thouless^{18, 19, 25, 49} studied the work of fracture of fibrous monolith in bending. They described work of fracture in terms of two mechanisms: delamination (or interfacial cracking) and frictional sliding due to crack kinking. The equations and variables used by Kovar and Thouless to describe the crack area creation and the frictional sliding mechanisms were described in section 2.3.1.4 of this text and are shown below.

$$(1) W_C = W_L + W_i$$

$$= \Gamma_L A_L + \Gamma_i A_i$$

and

$$(2) W_S = n \delta A_i \tau_s$$

where

$$W_T = W_C + W_S$$

Using this analysis, they were able to predict a nominal work of fracture in bending accurately compared to that measured by King¹⁷. Nominal predictions for work of fracture using the above analysis in this study are not accurate due to the test conditions and material architectures. However, the above equations are used for a relative comparison between the two different microstructures.

Several assumptions are made to complete the analysis. First it is assumed that there is no contribution to absorbed energy by the 45° plies. Since the dominate microstructural feature was shown to be the cell bundles and not the individual cells, the equivalent area of cell bundles in the axial direction are used in place of the cell area in equation 1 above. The calculation of the uniaxial cell bundle area excludes the area of the BN phase between the individual cells. A second assumption is that values measured by Kovar and Thouless^{18, 19, 25, 49} for interfacial fracture energies, cell slip distance, and frictional sliding resistance are applicable. It is also assumed that all of the cell bundles and all of the cell bundle boundaries fracture. See Appendix G for the calculations.

A comparison of the W_T 's calculated for each microstructure show that the material with the larger cell bundles should dissipate about 31% more energy upon fracture than the material with the smaller bundles. A comparison of the WOF values from Figure 6.13 for the

respective materials shows that the material with the larger cell bundles absorbs about 27% more energy. Since the percent difference in energy predicted and measured are nearly identical, it is concluded that the dominate fracture mechanisms are the same in tension and as in bending and that there is probably no contribution to the absorbed energy by the 45° plies.

Before reaching fracture, absorbed energies are identical for the two materials.

Therefore, it is assumed that the dominant mechanisms for energy absorption are not effected by the cell size. Trice²⁷ has considered other deformation models based on the crack progression of pre-existing microcracks in the BN and the peeling or cleaving of the boron nitride. His description of sub-microscopic damage may be consistent with the results of this study where damage was evident by the load-displacement traces and AE events but was too small to be detected using conventional NDE imaging techniques. It may be shown with further studies that energy absorption models should include contribution of microcracking on the sub-microscopic level as well.

6.5 Summary

Fibrous monolith specimens from both the coarse and fine microstructures were tested to various load levels and unloaded for evaluation using non-destructive techniques and absorbed energy calculations. It was found that for the higher loads, permanent damage was being accumulated as evidenced by hysteresis and permanent offset in strain. However, the damage is thought to be associated with interfacial delamination that is too small to be detectable with the NDE techniques used. The WOF associated with absorbed energy shows that the two materials behave similarly until fracture, where the dominant energy absorbing

mechanisms are associated with large delamination crack area creation and frictional sliding.

Energy absorption based on these mechanisms shows an effect of the cell bundle size when identical volume fractions of cell bundles are tested.

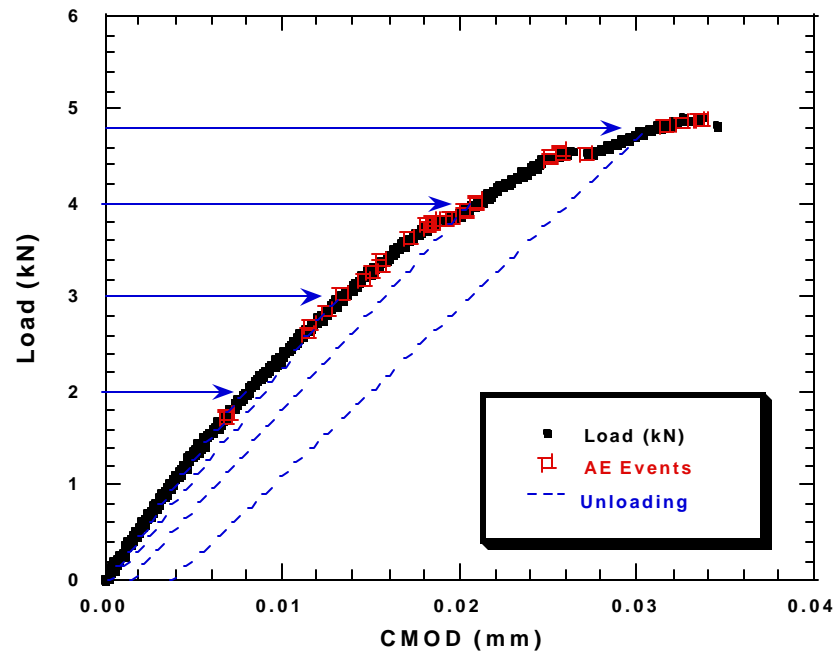


Figure 6.1 Curve obtained from fast-fracture testing which shows the unloading strategy to be used to run single load-unload and cyclic tests.

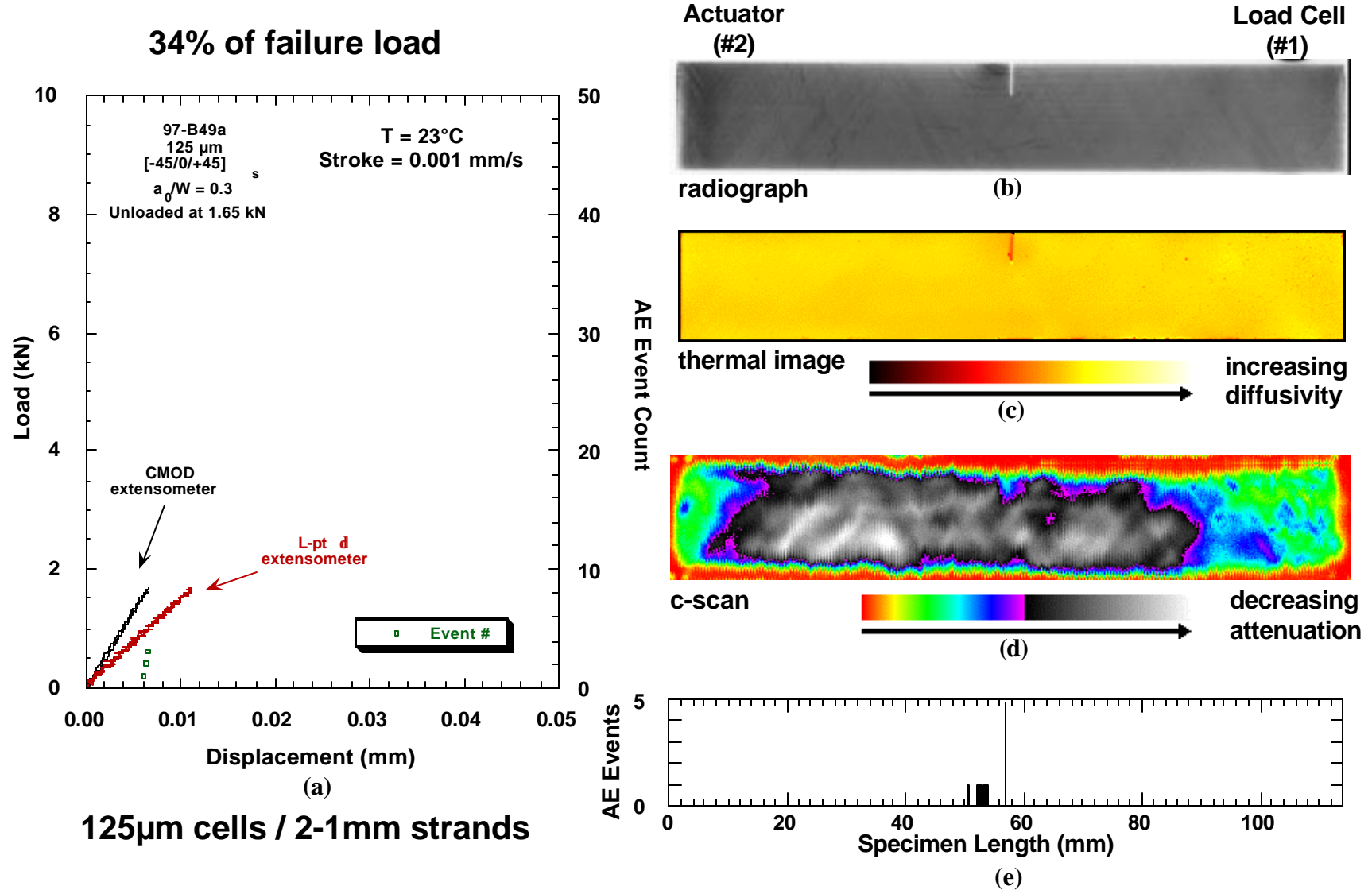


Figure 6.2 Results of load-unload testing a FM specimen with the finer microstructure and an a_0/W of 0.3 at room temperature. (a) load versus displacement plot, (b) x-ray radiograph, (c) thermal diffusivity image, (d) ultrasonic c-scan, (e) acoustic emission histogram.

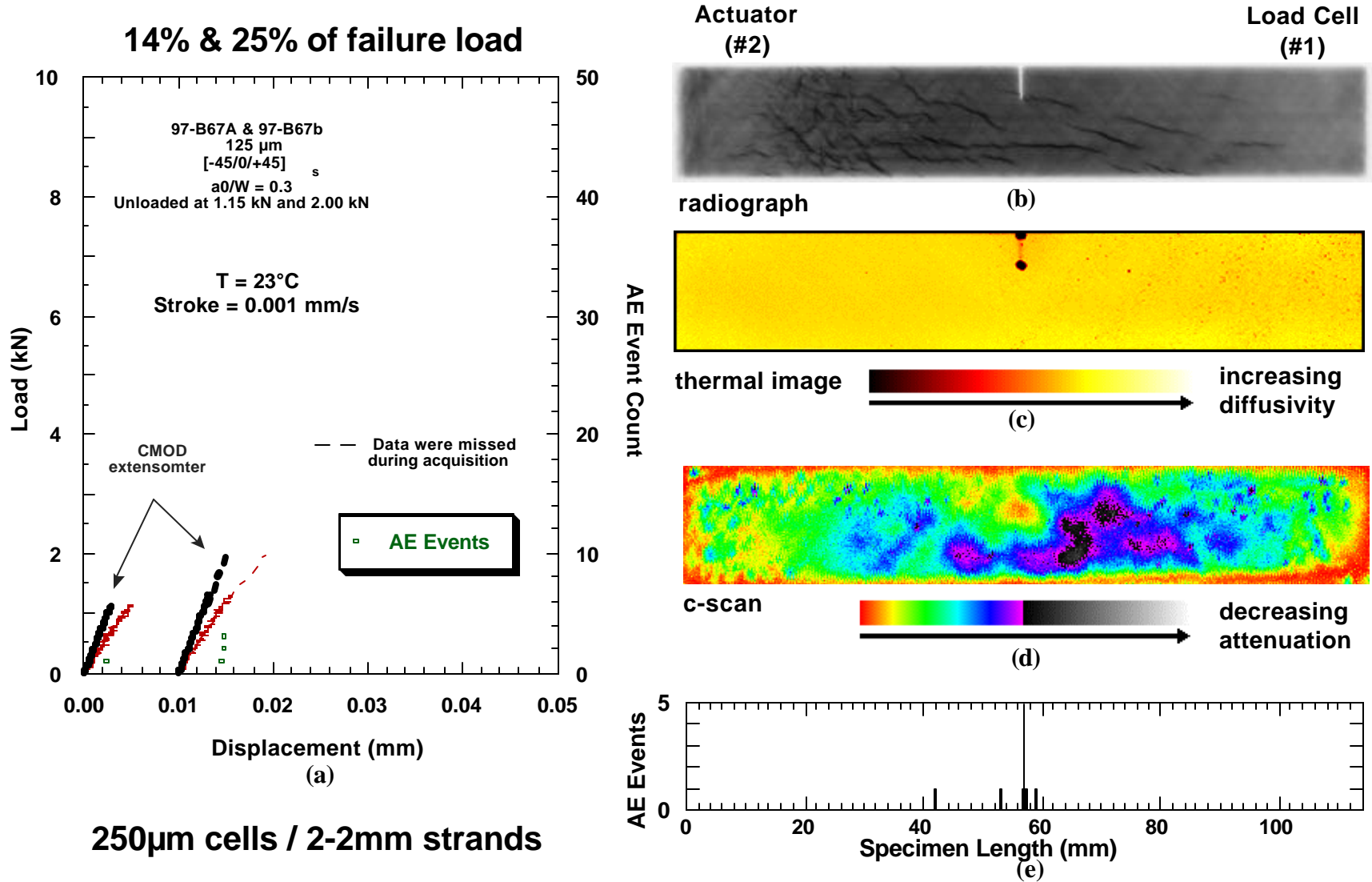


Figure 6.3 Results of load-unload testing a FM specimen with the coarser microstructure and an a_0/W of 0.3 at room temperature. (a) load versus displacement plot, (b) x-ray radiograph, (c) thermal diffusivity image, (d) ultrasonic c-scan, (e) acoustic emission histogram.

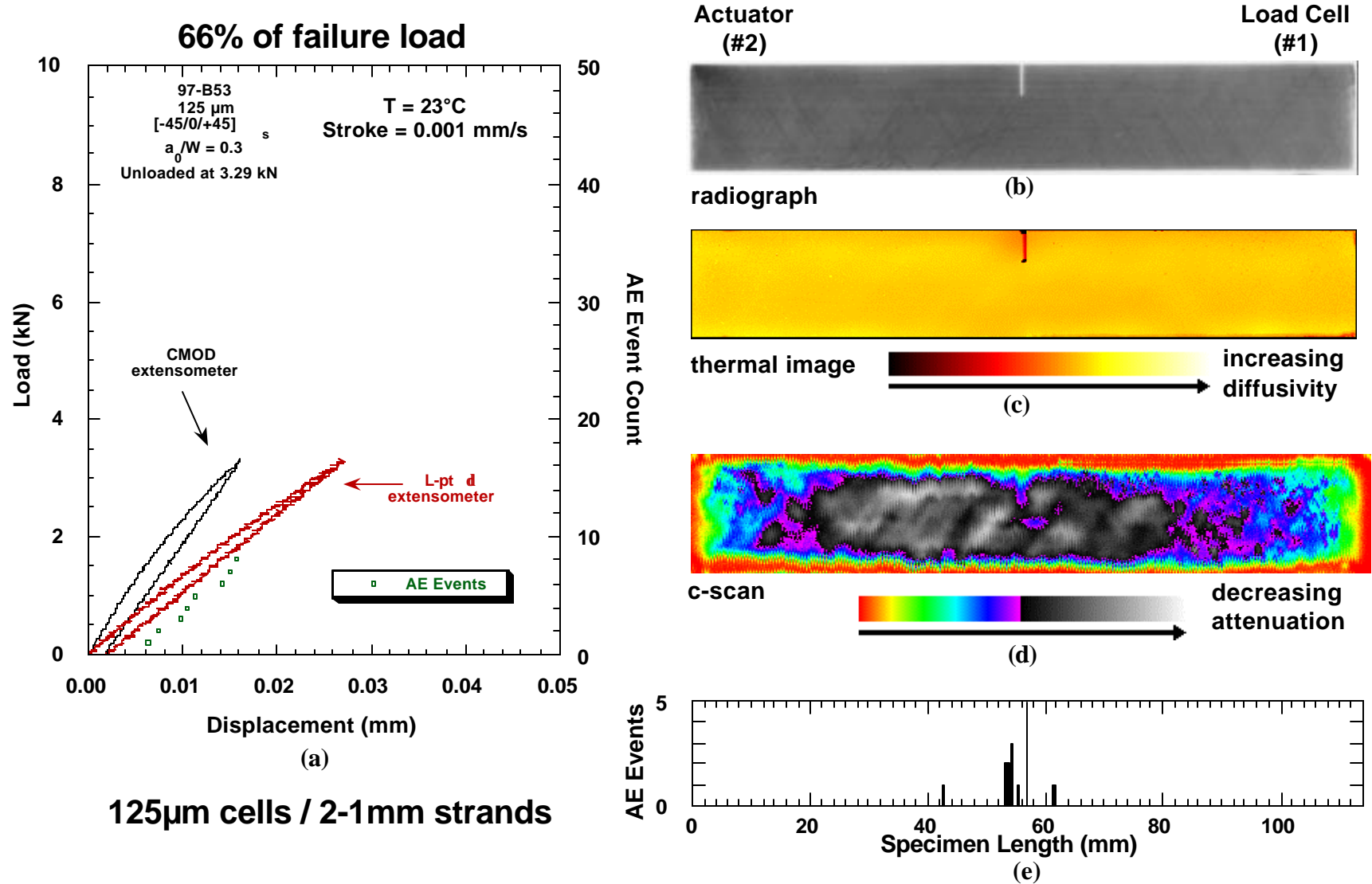


Figure 6.4 Results of load-unload testing a FM specimen with the finer microstructure and an a_0/W of 0.3 at room temperature. (a) load versus displacement plot, (b) x-ray radiograph, (c) thermal diffusivity image, (d) ultrasonic c-scan, (e) acoustic emission histogram.

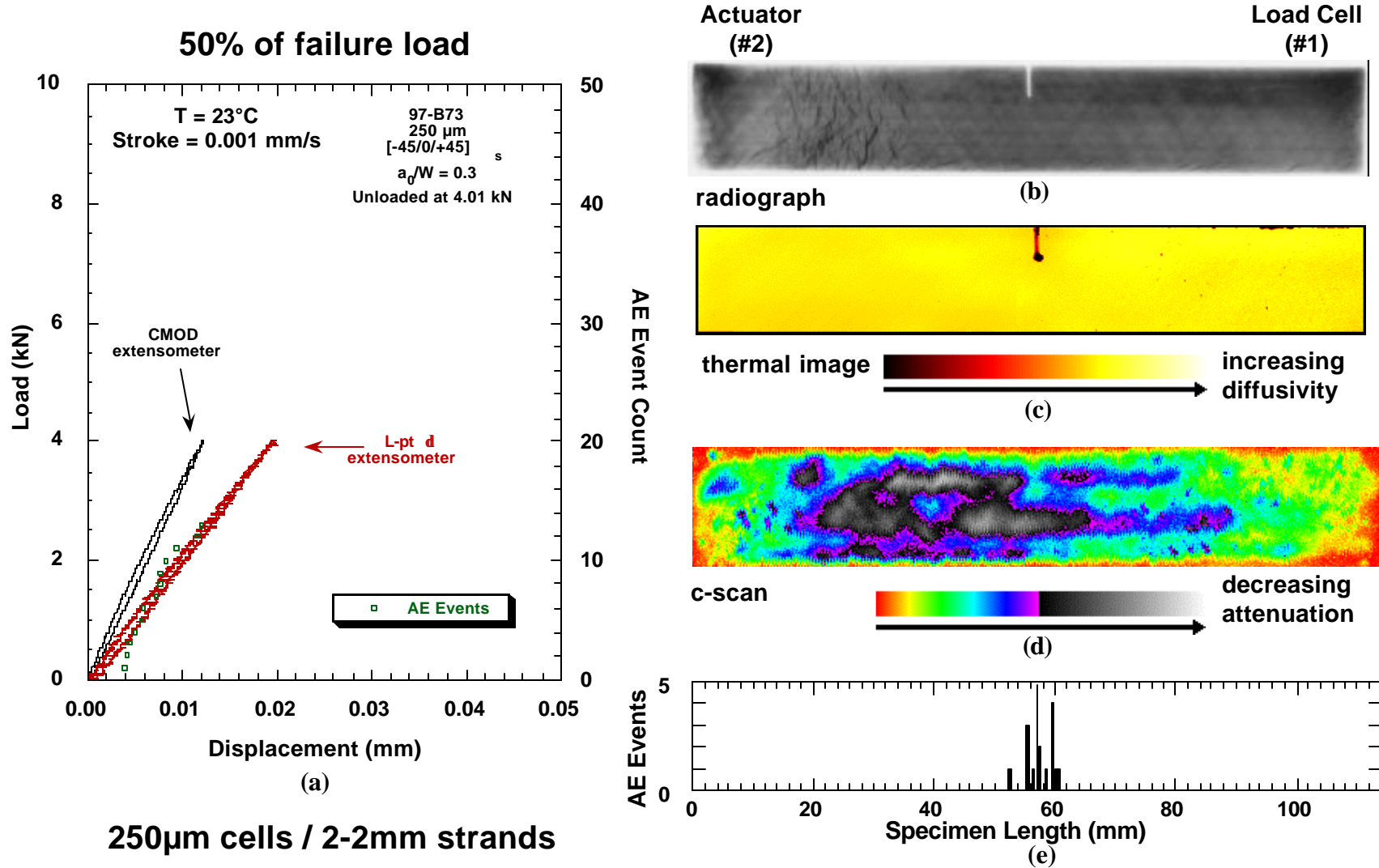
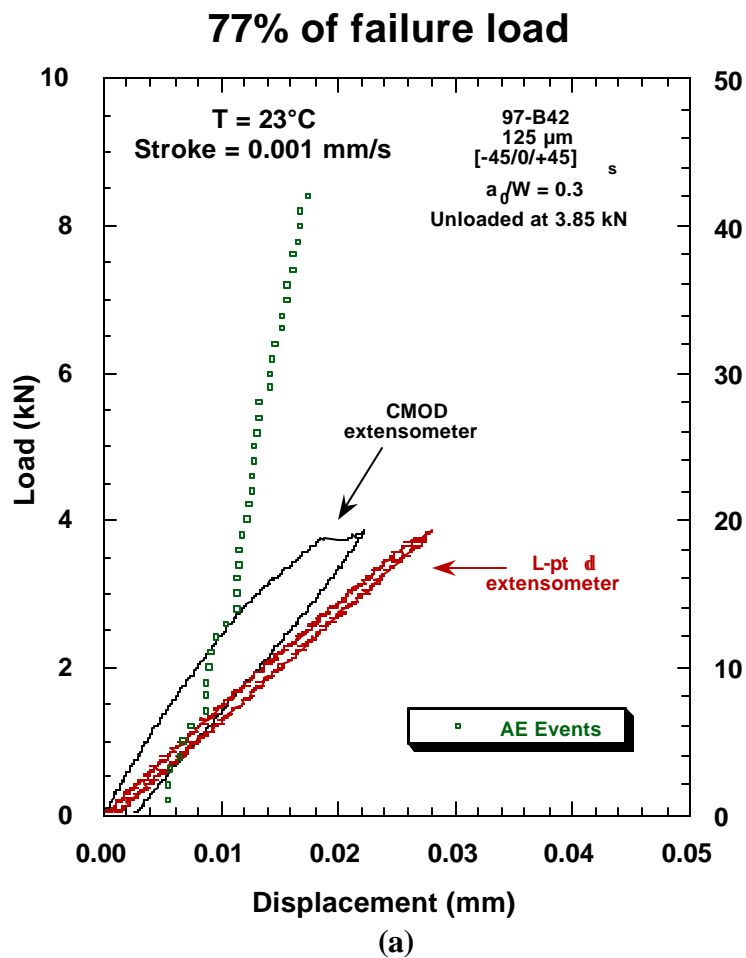


Figure 6.5 Results of load-unload testing a FM specimen with the coarser microstructure and an a_0/W of 0.3 at room temperature. (a) load versus displacement plot, (b) x-ray radiograph, (c) thermal diffusivity image, (d) ultrasonic c-scan, (e) acoustic emission histogram.



125μm cells / 2-1mm strands

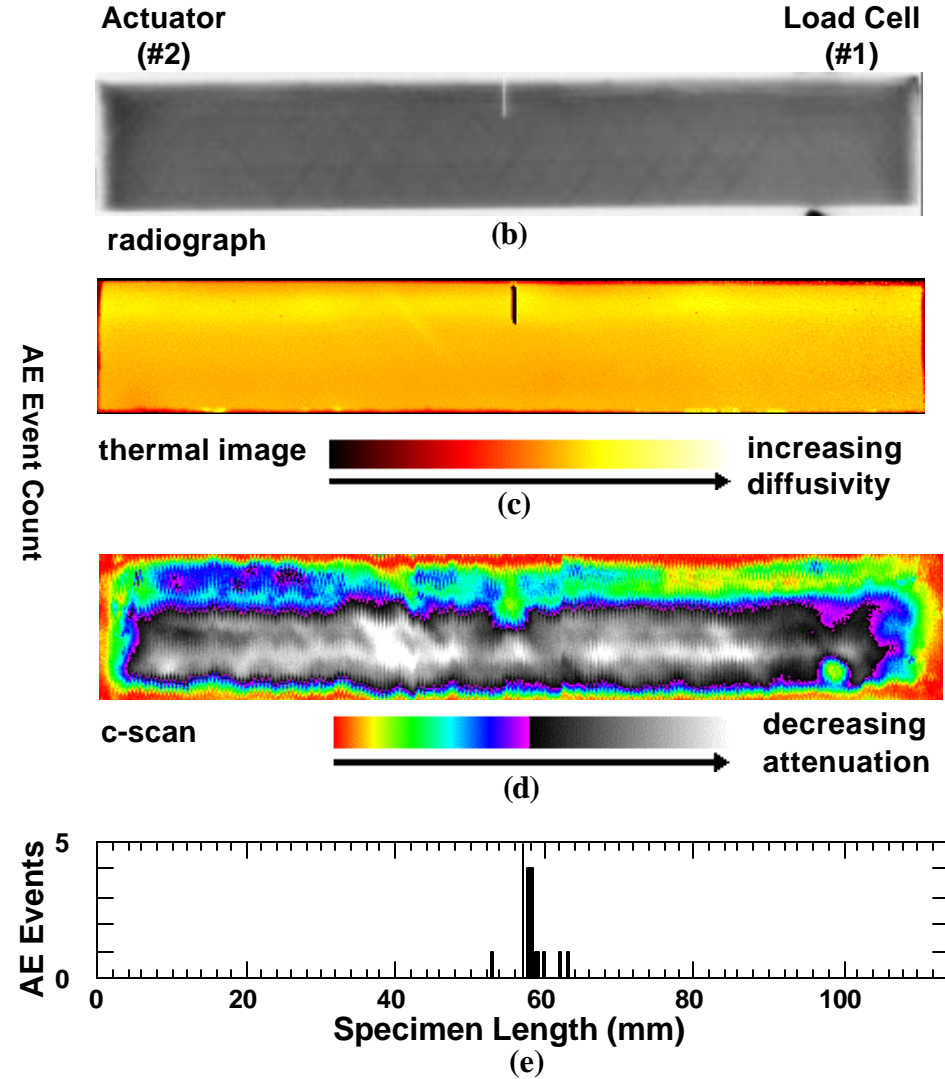


Figure 6.6 Results of load-unload testing a FM specimen with the finer microstructure and an a_0/W of 0.3 at room temperature. (a) load versus displacement plot, (b) x-ray radiograph, (c) thermal diffusivity image, (d) ultrasonic c-scan, (e) acoustic emission histogram.

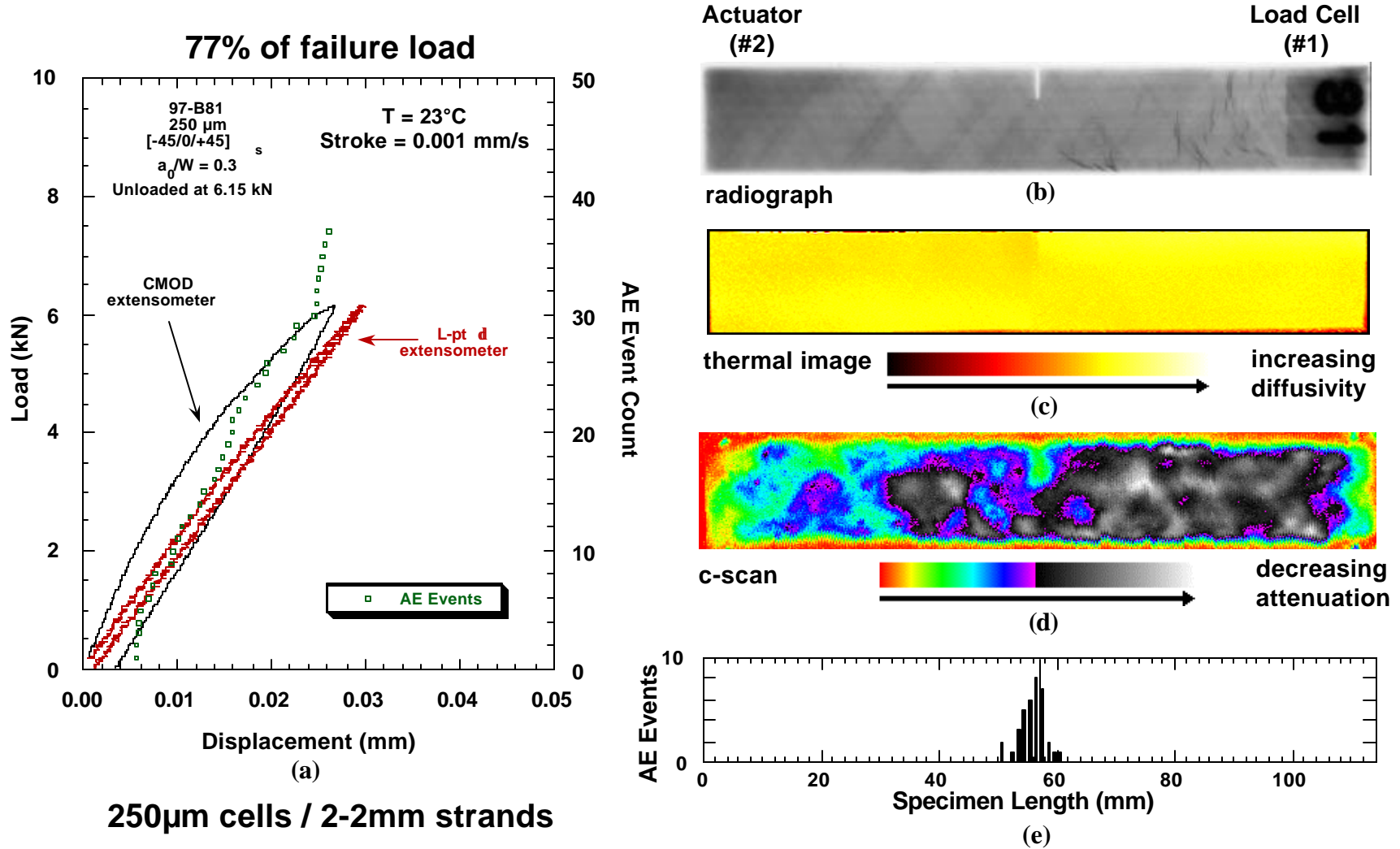
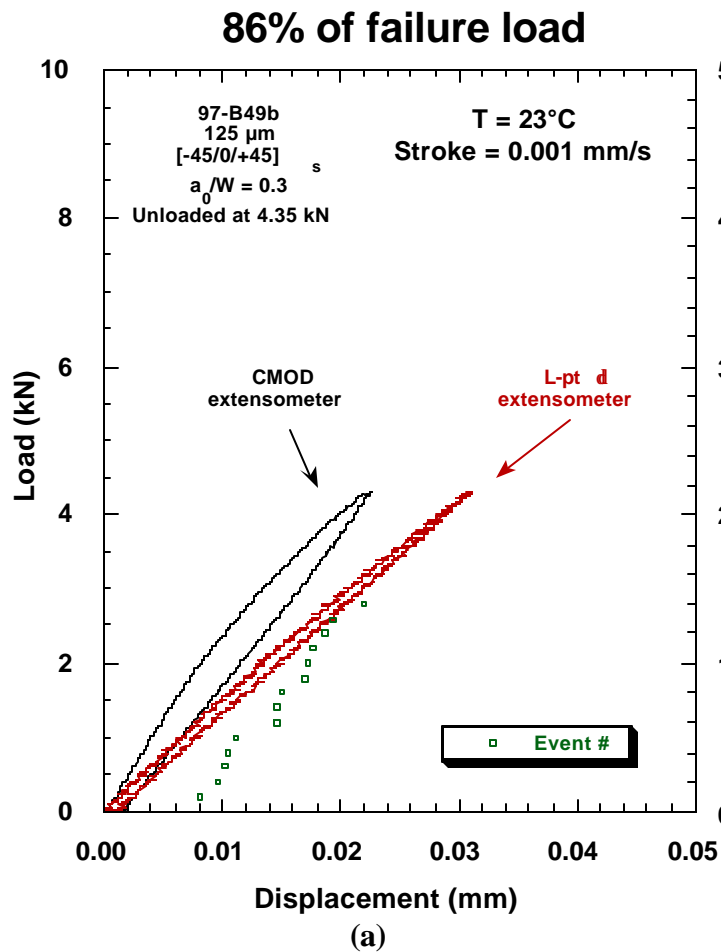


Figure 6.7 Results of load-unload testing a FM specimen with the coarser microstructure and an a_0/W of 0.3 at room temperature. (a) load versus displacement plot, (b) x-ray radiograph, (c) thermal diffusivity image, (d) ultrasonic c-scan, (e) acoustic emission histogram.



125 μm cells / 2-1mm strands

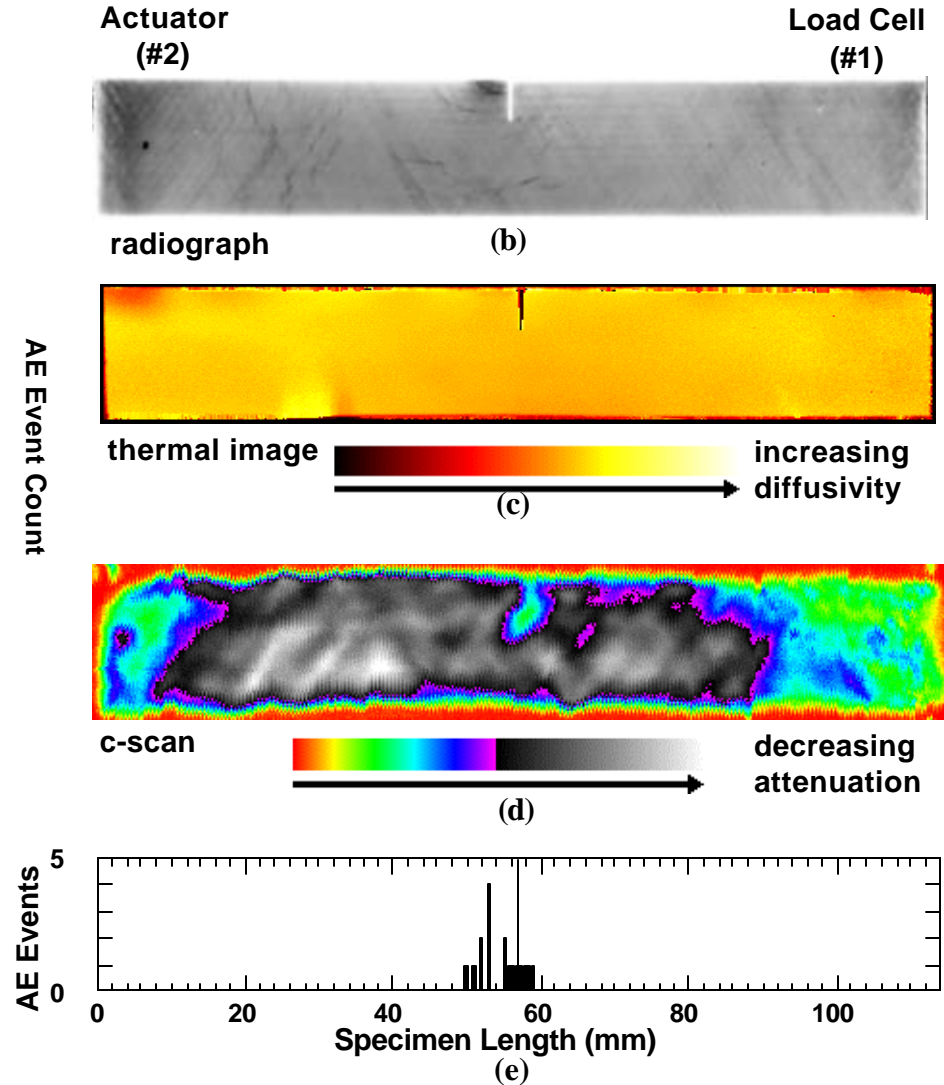
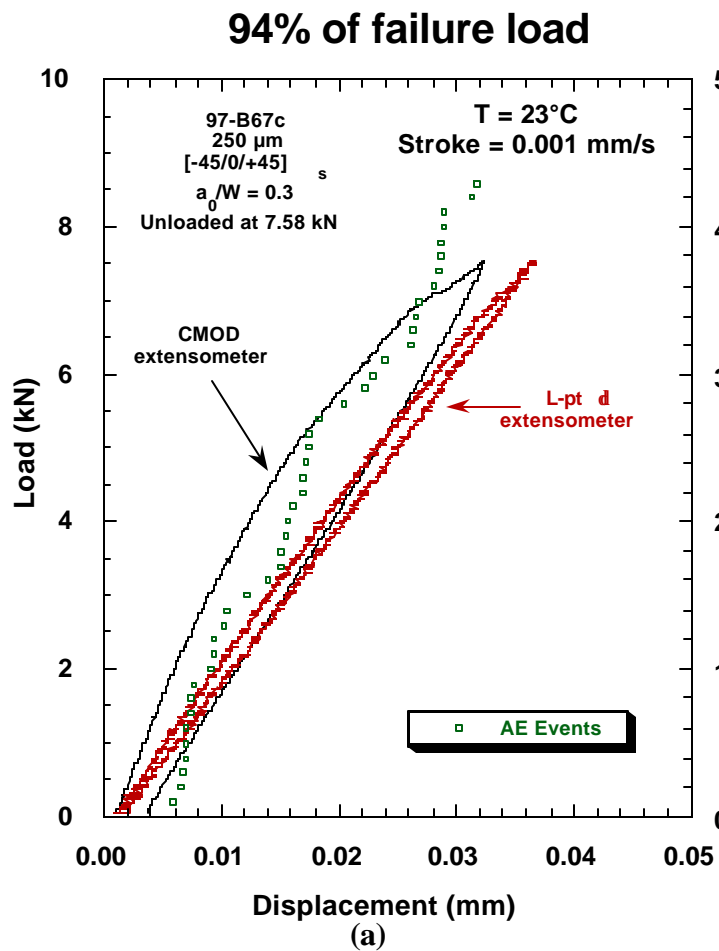


Figure 6.8 Results of load-unload testing a FM specimen with the finer microstructure and an a_0/W of 0.3 at room temperature. (a) load versus displacement plot, (b) x-ray radiograph, (c) thermal diffusivity image, (d) ultrasonic c-scan, (e) acoustic emission histogram.



250 μm cells / 2-2mm strands

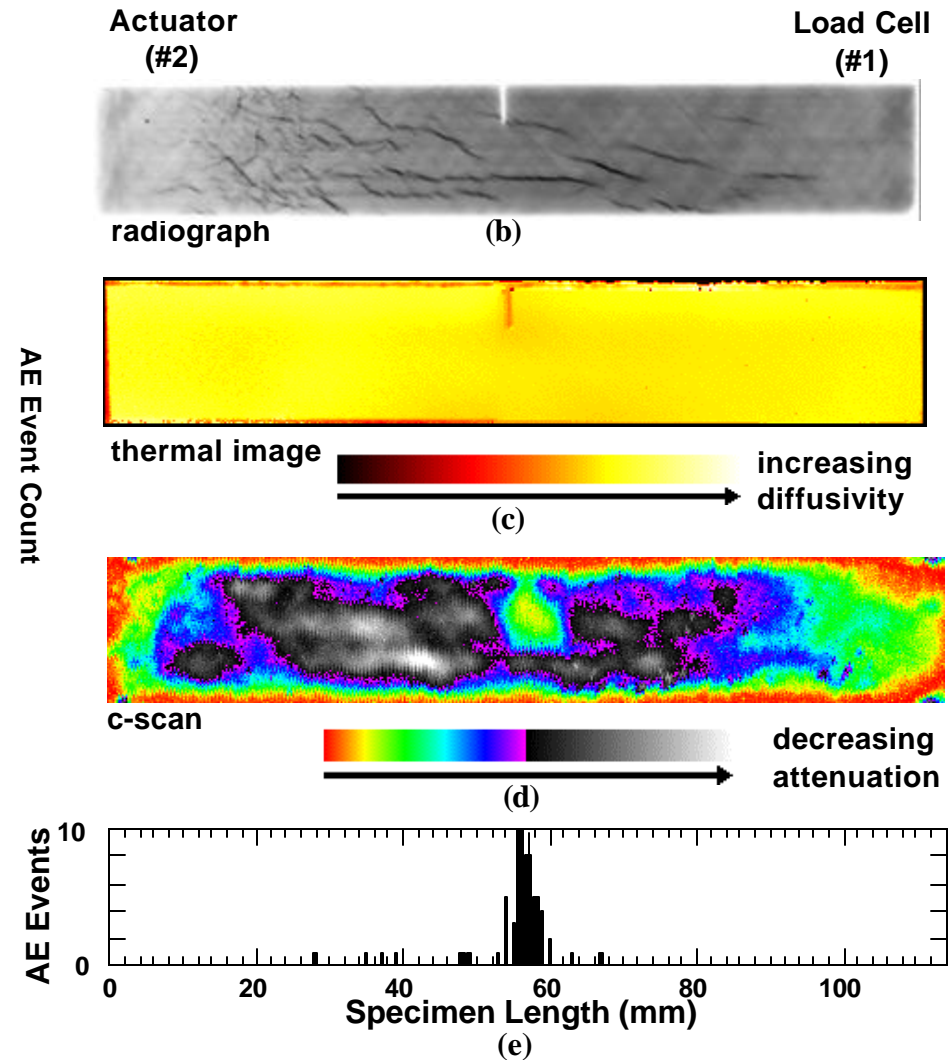
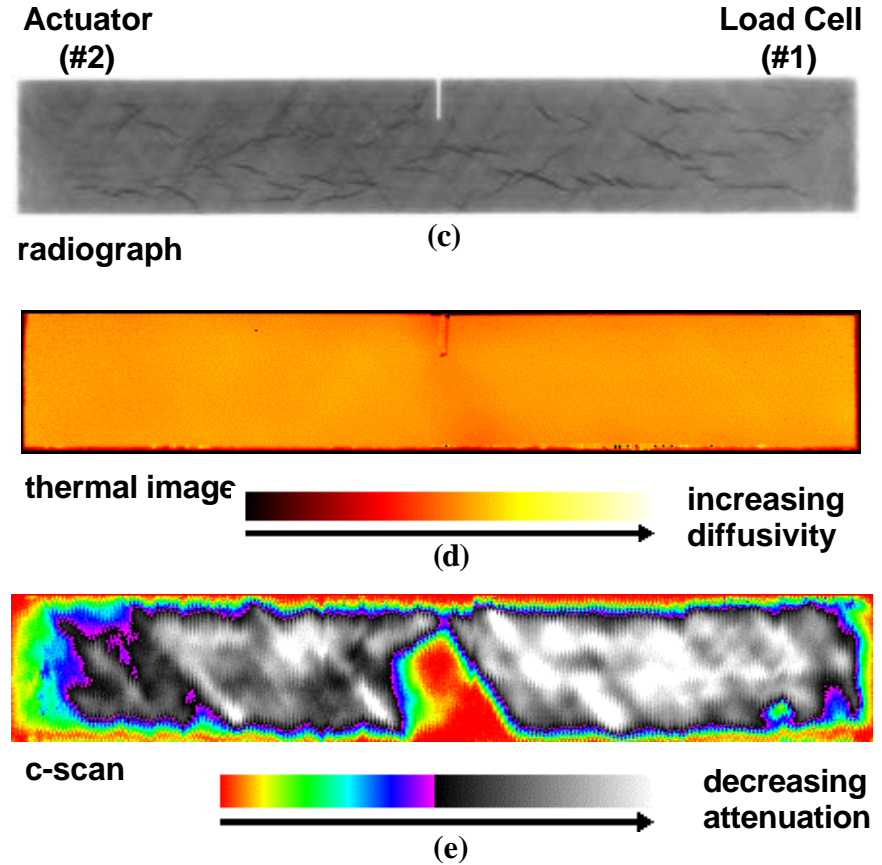
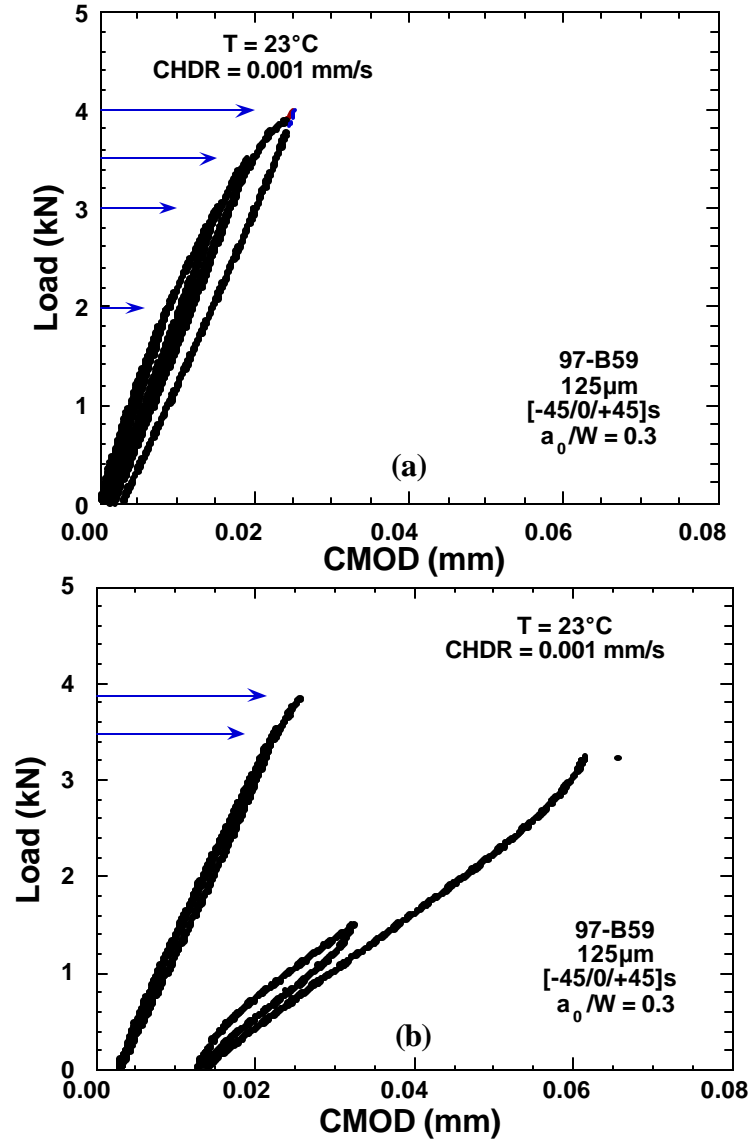
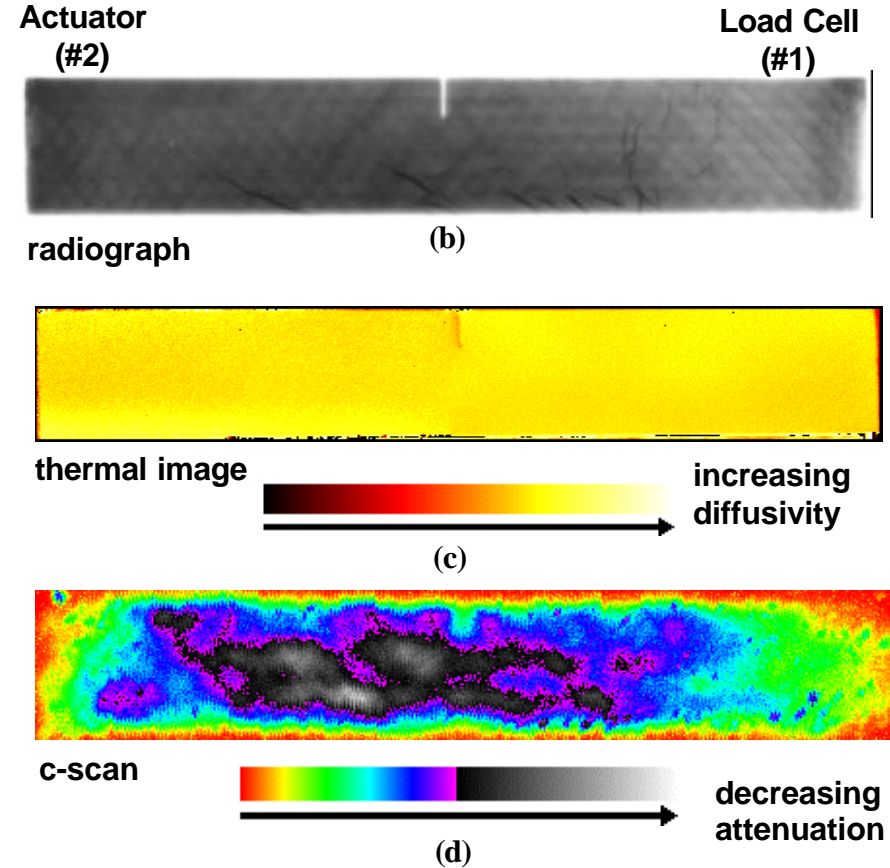
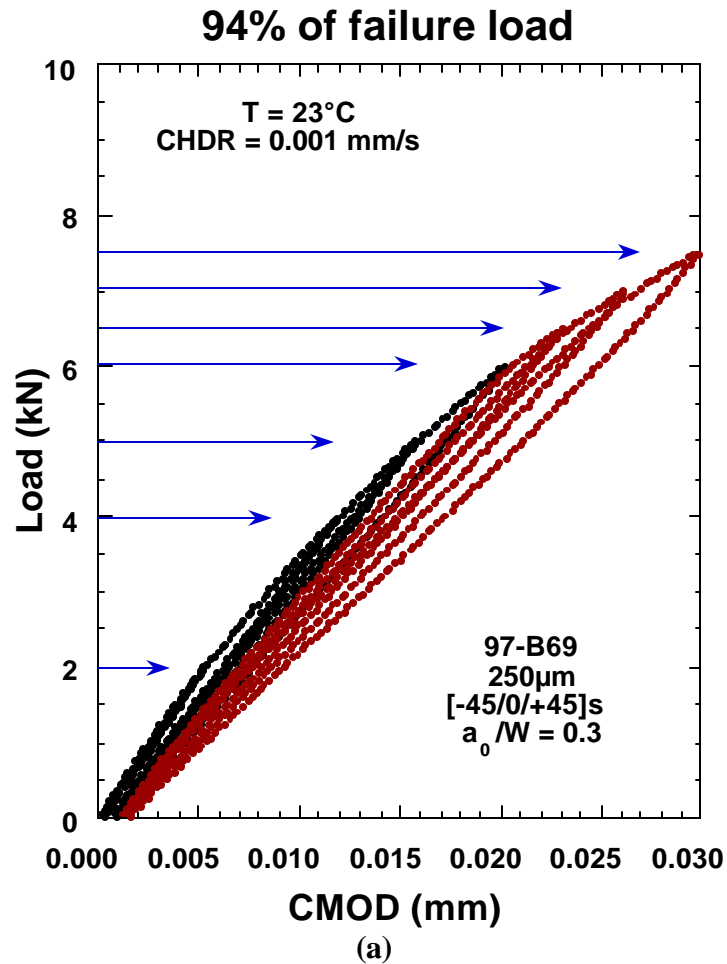


Figure 6.9 Results of load-unload testing a FM specimen with the coarser microstructure and an a_0/W of 0.3 at room temperature. (a) load versus displacement plot, (b) x-ray radiograph, (c) thermal diffusivity image, (d) ultrasonic c-scan, (e) acoustic emission histogram.



125μm cells / 2-1mm strands

Figure 6.10 (a) & (b) show the load-displacement data for the initial test and the restart data, respectively. The x-ray, thermal image and c-scan are shown in (c), (d), and (e). The thermal image and the c-scan show evidence of damage.



250µm cells / 2-2mm strands

Figure 6.11 (a) shows the mechanical behavior for the initial test and the restart data. The x-ray, thermal image and the c-scan are shown in (b), (c), and (d).

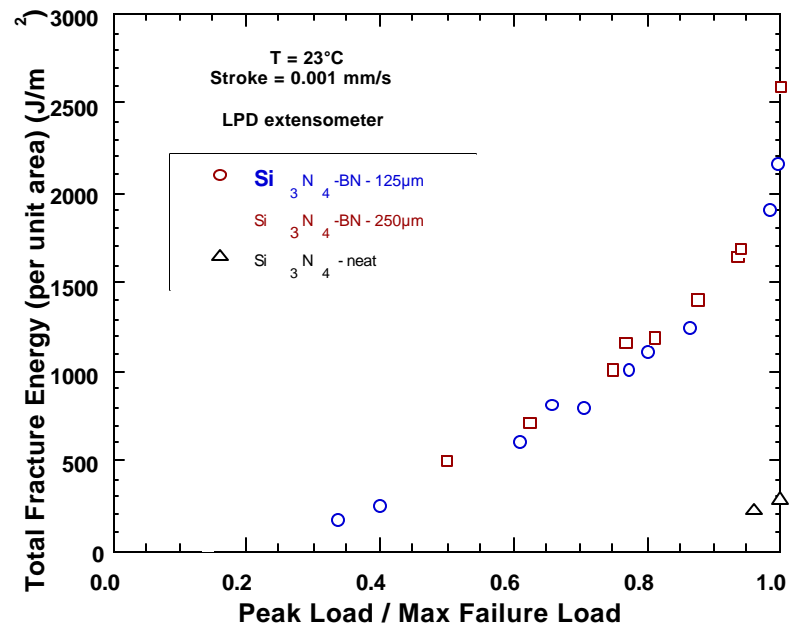


Figure 6.12 Plot showing the total energy calculated from the area under the curve (loading portion) up to the failure load.

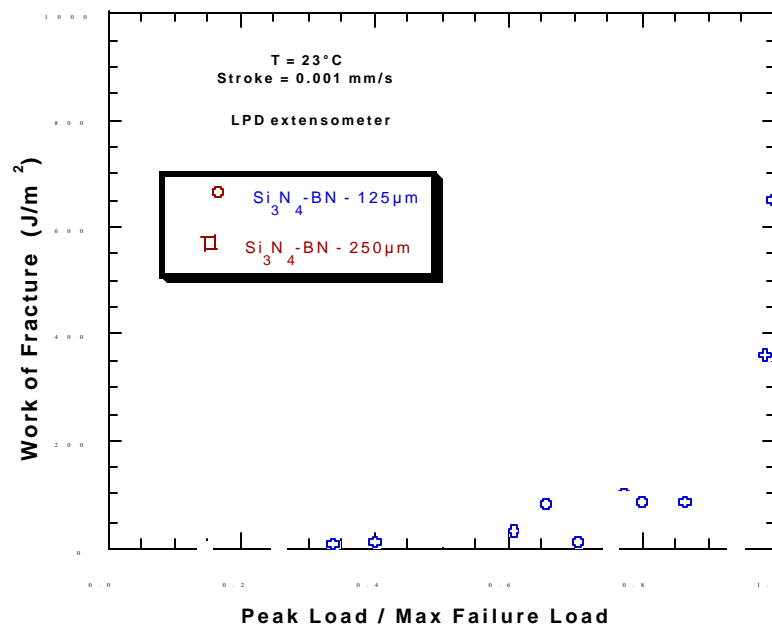


Figure 6.13 Plot showing the energy absorbed at various loads up to the fracture load which is the work of fracture.

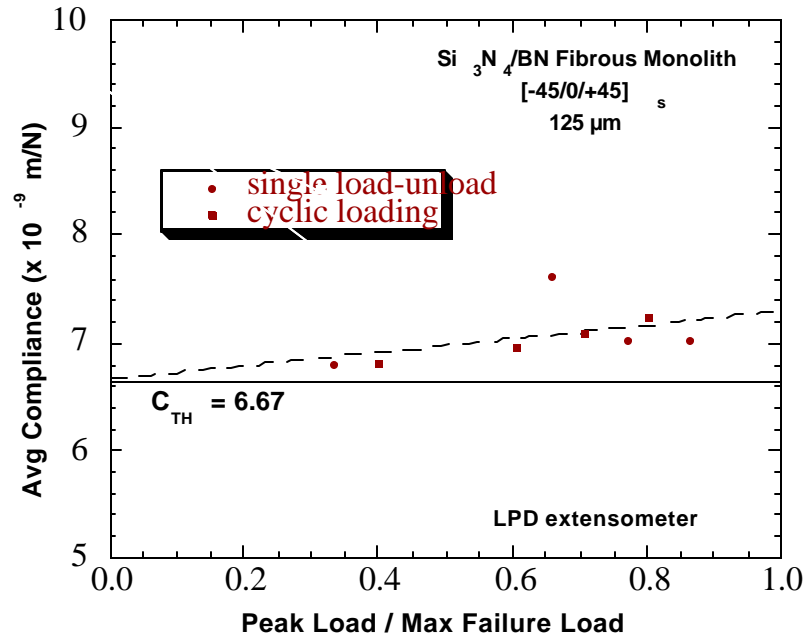


Figure 6.14 (a) Plot showing the curve fit of the experimental compliance data used to predict the compliance at failure for the material with the smaller microstructural features.

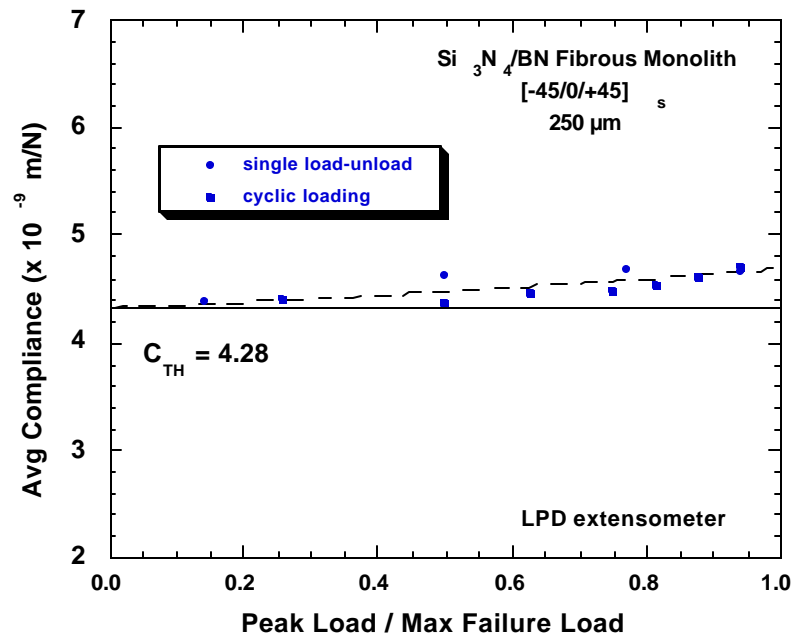


Figure 6.14 (b) Plot showing the curve fit of the experimental compliance data used to predict the compliance at failure for the material with the smaller microstructural features.

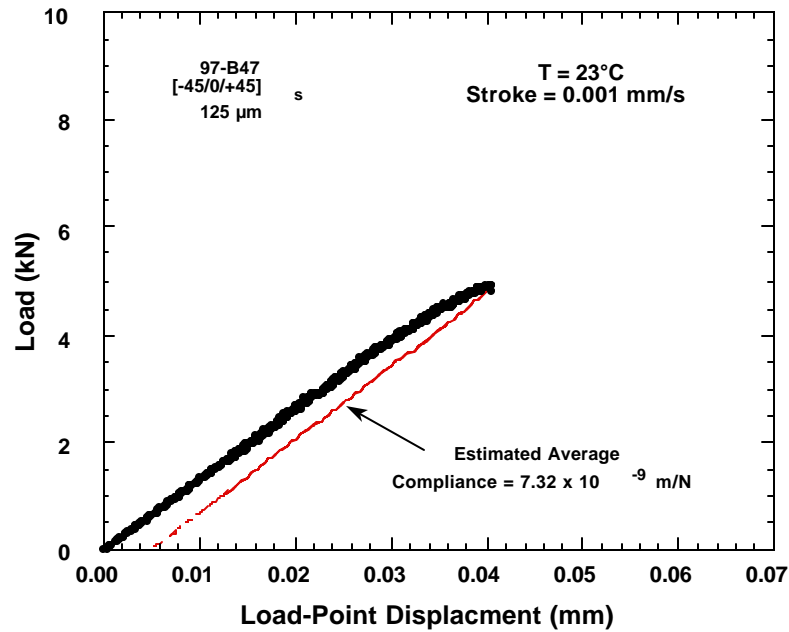


Figure 6.15 (a) Plot illustrating how the estimated failure compliance was used to discount the elastic energy at failure for the material with the smaller cell bundles.

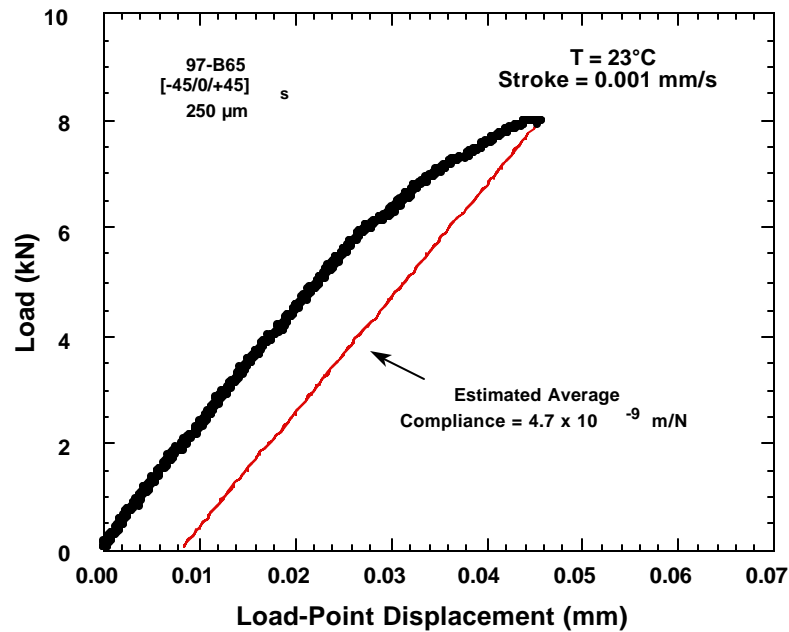


Figure 6.15 (b) Plot illustrating how the estimated failure compliance was used to discount the elastic energy at failure for the material with the larger cell bundles.

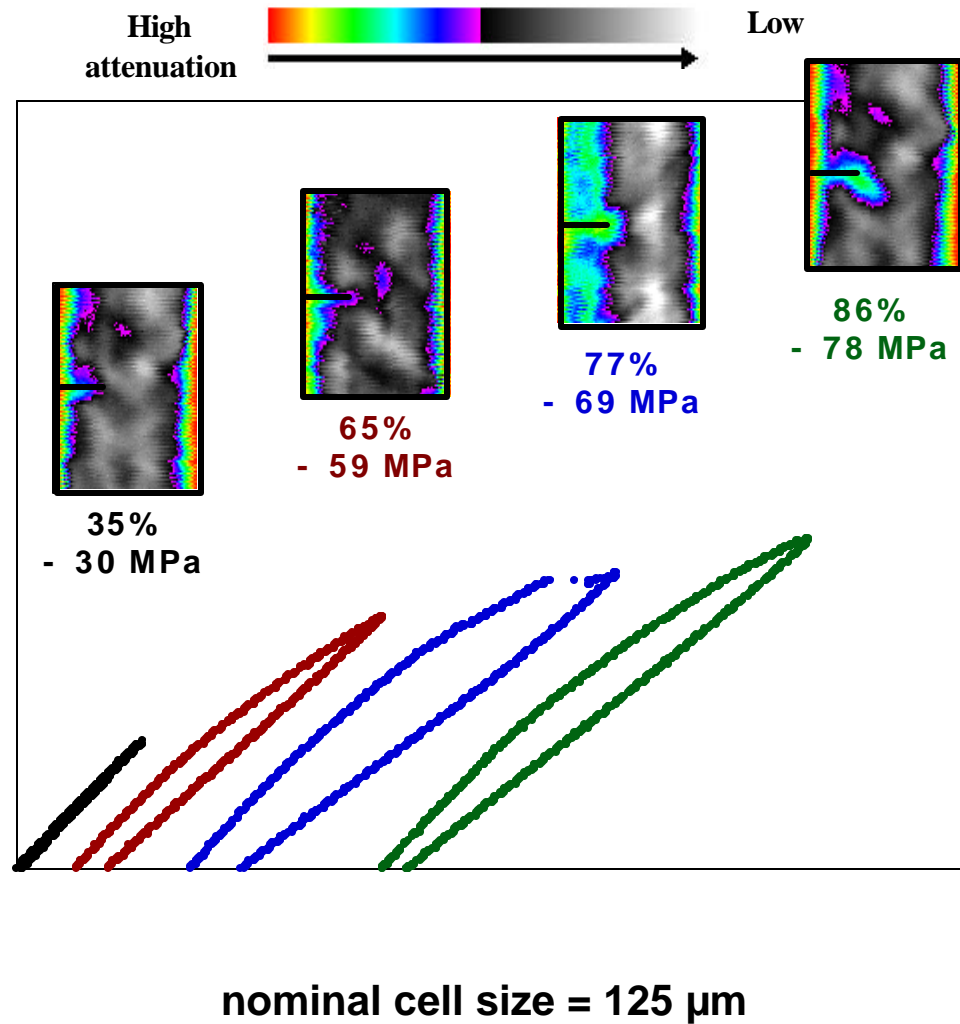


Figure 6.16 Qualitative representation of the results from the mechanical testing and the ultrasonic c-scanning for the specimens loaded to 35%, 65%, 77% and 86% of the estimated failure load for the material with the smaller microstructural features.

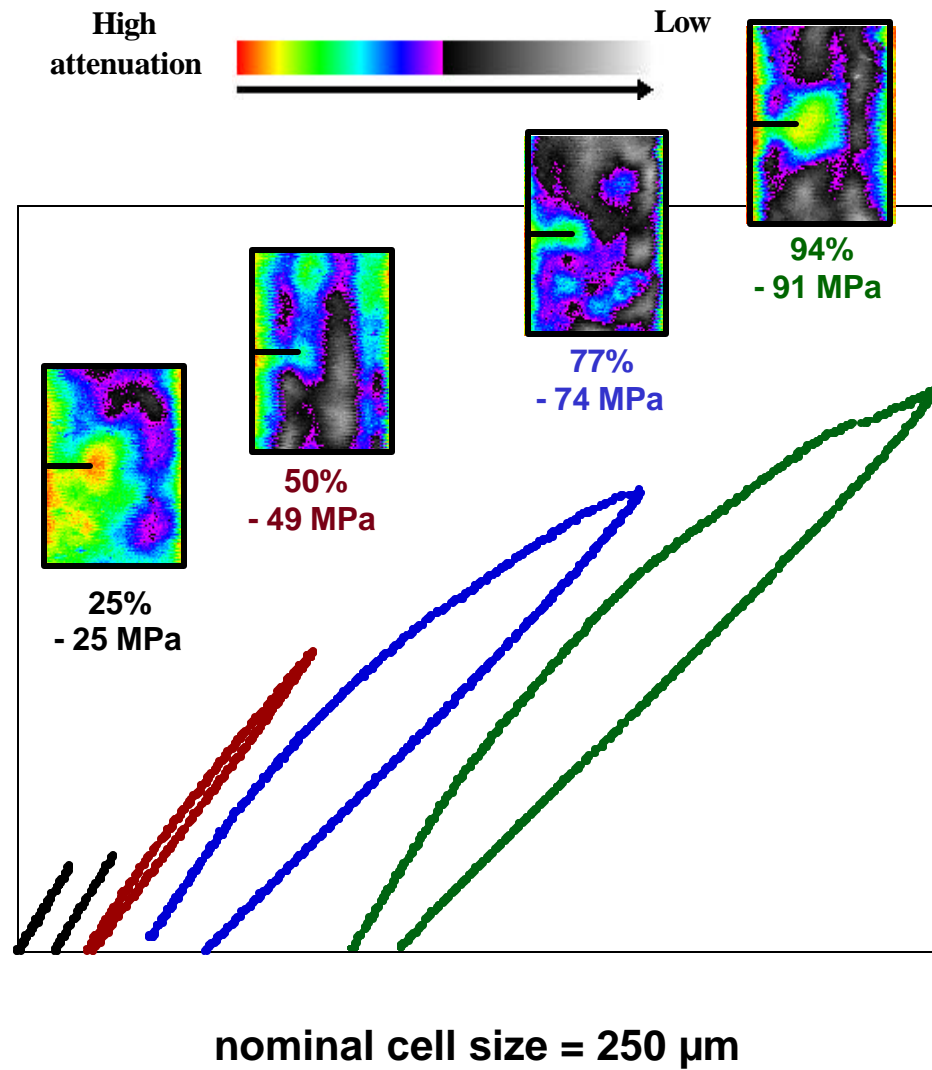


Figure 6.17 Qualitative representation of the results from mechanical testing and ultrasonic c-scanning for specimens loaded 25%, 50%, 77% and 94% of the estimated failure load for the material with the larger cell bundles.

CHAPTER 7

MICROSCOPIC INSPECTION

Selected fibrous monolith MSE(T) specimens were sectioned and polished for microscopic inspection following mechanical testing. The type and extent of damage developed from testing to the various load levels were documented using optical microscopy.

7.1 Procedure

The specimens inspected were those with an a_0/W of 0.3 that were tested under the load-unload regime and those that were fracture tested from each microstructure. The surfaces and edges of all specimens were first inspected under low magnification ($<32\times$) before they were sectioned. None of the specimens tested under the load-unload regime showed any surface damage detectable at low magnification. Damage was visible on the surfaces of the fractured specimens. Cracks could be seen in the 45° surface plies as shown in Figure 7.1.

Next, the specimens were sectioned and polished. Each specimen was sandwiched between two pieces of glass to protect the surfaces from burring and shear lips while sectioning. Several 24 mm x 5 mm sections were cut from the middle of each specimen, centered on the notch plane, such that the inspection surfaces were perpendicular to the notch plane (parallel to the tensile direction). See Figure 7.2 for a schematic drawing which illustrates how the tested MSE(T) specimens were sectioned for inspection. The inspection sections were labeled as #1, #2, and #3, with #1 being the section right behind the notch tip as shown on the figure.

The cut sections were mounted in a colored epoxy using vacuum infiltration. The mounted samples were polished using an automatic polisher on perforated textmet and diamond suspension. The coarsest diamond used was 15 μ m and the smallest was 1 μ m. The samples were examined using a high powered optical microscope.

7.2 Inspection Observations

7.2.1. Single load-Unload Specimens

All specimens from both microstructures were examined except for the specimens tested to the lowest loads. These specimens were re-tested to loads near the expected failure loads and were not sectioned until after the last load-unload cycle. The #1 inspection sections showed a through- thickness type crack behind the notch of each specimen examined. An example of the cracks seen in the vicinity of the notch tip are shown in Figure 7.3 (a). The micrograph shown in Figure 7.3 (a) shows evidence of the notch being polished away with the crack to the left of the notch's wake. For comparison, an as-received specimen was notched, sectioned, and polished in a similar manner. The micrograph for the as-received specimens is

shown in Figure 7.3 (b). It was found that no such cracks existed in the as-received material and therefore it was determined that the damage seen in Figure 7.3 (a) was due to testing and not from the notching procedure.

Cracks were also found in BN cell boundaries in the vicinity of the notch in both microstructures. The two specimens showing evidence of this were both tested to the highest loads before unloading. An example of the cracks found in the BN is shown in Figures 7.4 (a), (b), and (c) at three different magnifications. The figure is of inspection section 97-B49b-#1 after being lightly polished. At the highest magnification, one can see that the crack has a torturous path, but it stays within the cell boundary. This type of crack morphology is consistent with observations reported by studies at the University of Michigan^{17-19, 27}.

Specimen 97-B49b-#1 was polished further to determine if there were other cracks behind the notch similar to those in Figure 7.3 (a). The same type of through-thickness crack was found adjacent to the notch. See Figure 7.5 for a micrograph of the damage observed upon further polishing. The crack location seems to be consistent with the ultrasonic c-scan of 97-B49b that shows an attenuated area off to one side of the notch.

The #1 inspection section from the specimen with the coarser microstructure, 97-B67c, also showed evidence of both through-the-thickness types cracks and cracks in the BN interphase material. This section is shown in Figure 7.6. The damage found is also thought to be evident on the corresponding ultrasonic c-scan and possibly in the thermal diffusivity image.

In the inspection sections located further away from the notch, #2-#4, no cracks were identified except in specimen 97-B67c. Again, specimen 97-B67c had the coarser microstructure and was tested to the highest load level. A limited number of hairline cracks in

the BN cell boundaries between the 0° plies and both the adjacent 45° plies were indentified. See Figure 7.7 for an example of how fine the cracks appear. The cracks identified were about the length of a cell bundle (2mm) and had a stand-off of about 1 μ m in magnitude. One of the cracks identified within inspection section #2 is shown in Figures 7.8 (a), (b), and (c) at three different magnifications. The crack shown is in-between two of the 45° oriented cell bundles on the specimen surface. The crack extends inward to the 0° ply. At the interface of the 45° surface ply and the 0° ply within the BN boundary, the crack is deflected in both directions and runs parallel to the 0° ply.

The type of hairline cracks observed in the BN interphase of specimen 97-B67c were not identified in any of the other specimens except what has already been discussed for specimen 97-B49b-#1. This is consistent with the fact that damage was not positively detected by the NDE techniques for the other specimens. However, difficulties associated with polishing this material may hinder optical verification. The graphitic structure of the BN material and the existence of microcracking allows for pull-out when polishing. As a result, spotty areas in the BN make fine hairline cracks difficult to discern. Successful polishing procedures were found to include using low weight and minimal polishing fluids.

7.2.2 Fast-Fracture Specimens

One specimen from each microstructure that had been fracture tested was also sectioned and polished for inspection. Observations made from these specimens showed good correlation to the NDE images. In these specimens, a larger stand-off of the cracks make them easily detectable by the NDE, especially in the x-ray radiographs. An example of this is given in Figure 7.9 for specimen 97-B59, which has the finer microstructure.

Pictured in this figure are the radiography image and schematic drawings of the damage found on four different polished surfaces. Interlaminar delaminations and through-thickness type cracks could be identified in the successive cross-sections. The interlaminar cracks are shown to run left and right whereas the intralaminar cracks are shown to run up and down on the schematic drawings. Each section, except for #1, contained both an interlaminar crack between the -45° front surface ply and the neighboring 0° ply as well as a through-thickness type intralaminar crack within the -45° surface ply on the right side of the notch. The interlaminar crack identified between the surface plies was observed to get longer with each successive section. It was also observed that with each successive section the through-thickness type crack in the -45° surface ply appears farther away from the center notch plane. This observation was consistent with the "fanning out" of the damage zone in the -45 direction on the right side of the notch detected by the x-ray radiograph.

On the left side of the notch, both delamination and through-thickness type cracks were identified between the inner plies of the specimen. Cracks appeared to get farther away from the center in sections #2 and #3 as they followed the $+45^\circ$ angle of the cell bundles. The same damage identified in sections #2 and #3 did not appear in section #4. In section #4 a crack at the front surface, which is an extension of the delamination from the right side of the center notch plane, was identified. In the x-ray, the damage zone to the left of the notch was not observed to continue "fanning" across the width of the specimen. Accordingly, damage appeared more extensive in sections closest to the notch tip (sections #2 and #3) on the left side of the notch.

Observations made of polished cross-sections of the inspection samples from the failed fibrous monolith specimens verified that almost all cracking occurs along the perimeter of the cell

bundles within the BN interphase boundaries. Only a few instances were documented where the cell bundles failed. In addition, it was found that the cusps formed in-between the impinged areas along the 0° plies seem to influence damage. Cracks are observed to occur in the 0° plies at those points or cusps. The sharp points must act as flaws which allows for crack kinking out of the cell boundary into the 0° ply.

Other types of defects identified in the microstructures include jagged cell edges, skewed cell bundles, and kinked 0° plies. None of these defects seem to influence the crack path. See the micrograph in Figure 7.10 for an illustration of how the cracks are influenced by the defects inherent to the multi-filament cross-ply architecture and not other types of defects named above.

7.3 Summary

Observations made from optical inspection are consistent with the WOF and NDE results which show that damage is not accumulated on a macroscopic scale until near failure. Cracks directly behind the notch tip are evident in both materials at each loading condition inspected. Only the materials tested to the highest loads considered in this study show evidence of cracking within the BN boundaries. A greater extent of fine cracks within the BN boundaries were found in the material with the larger cells. Cracks were seen in-between adjacent 45° cell bundles and in between the 0° and the 45° plies. These cracks tended to be about a cell boundary in length. Other observations include the occurrence of large displacements between plies in the composite upon fracture. This may explain the large increase in the WOF behavior at loads near 90% of the failure load. Also, it was determined that the defects created by the cross-ply architecture may adversely influence the fracture behavior, and the other defects

associated with multi-filament coextruded microstructure did not noticeably influence the fracture morphology.

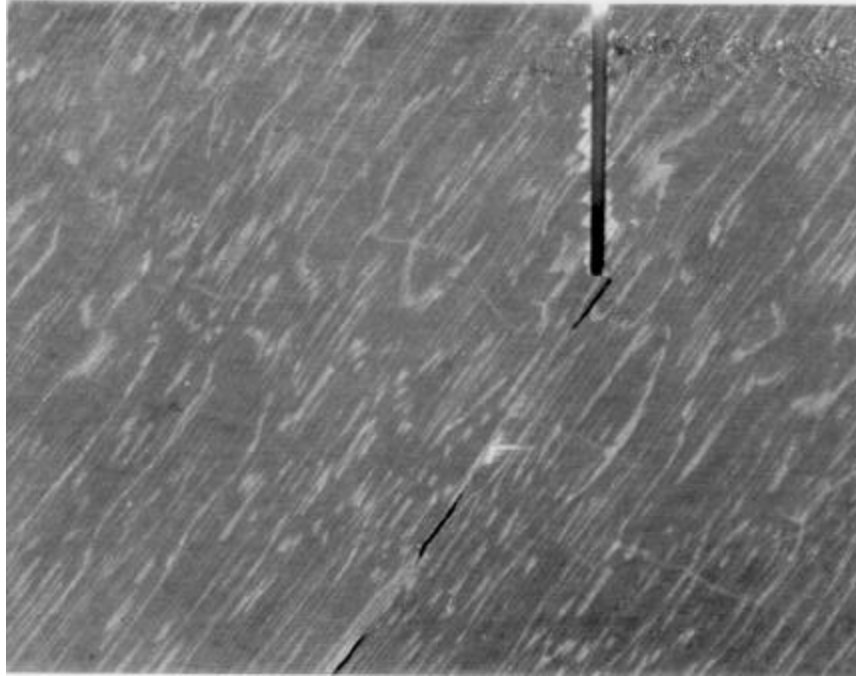


Figure 7.1 Micrograph at 6.3x of Si_3N_4 -BN fibrous monolith [-45/0/+45]_s with 125 μm cells (2-1 mm multi-filament strands) showing crack with 45° orientation coming from the notch.

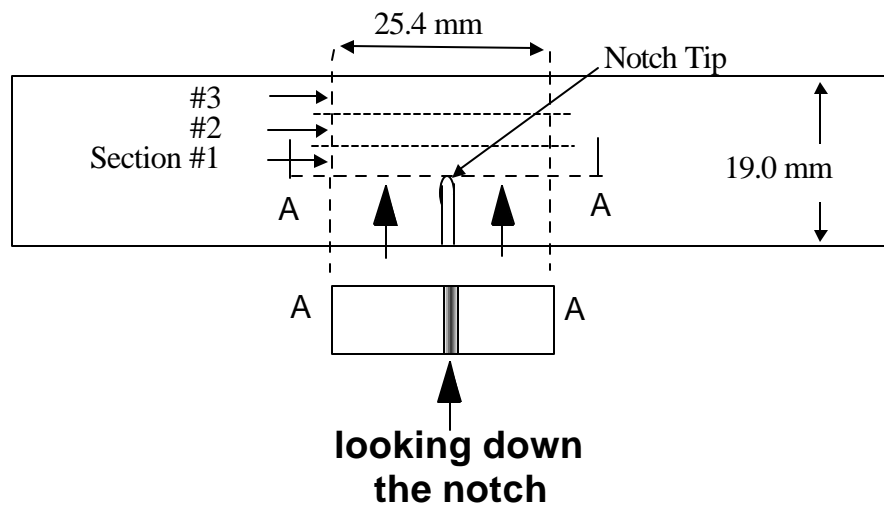


Figure 7.2 Schematic showing the strategy used for sectioning tested specimens.

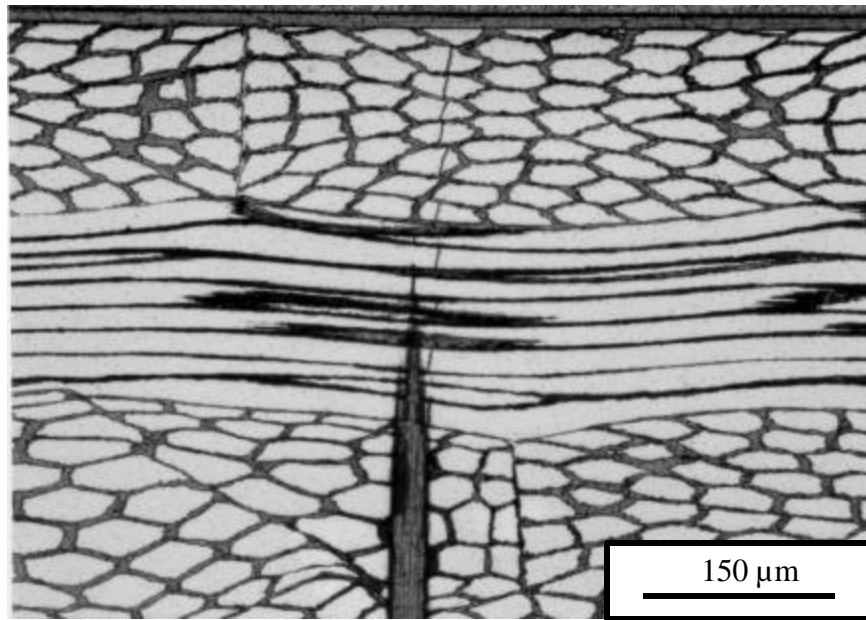


Figure 7.3 (a) Micrograph at 32x of showing an example of the cracks found behind the notch in the case of each single load-unload test.

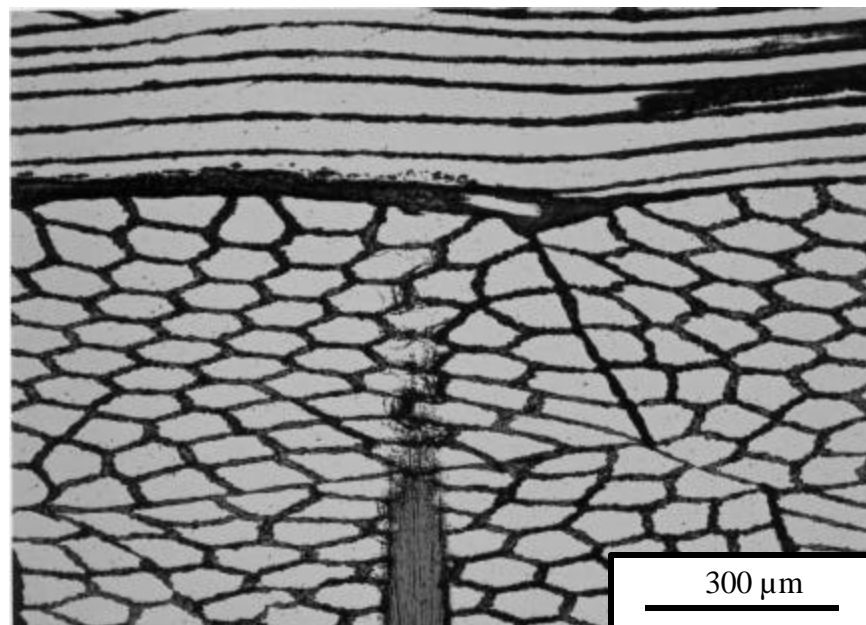
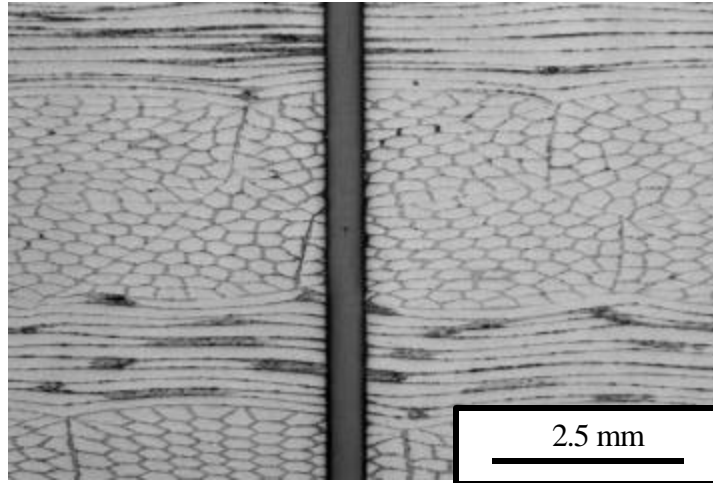
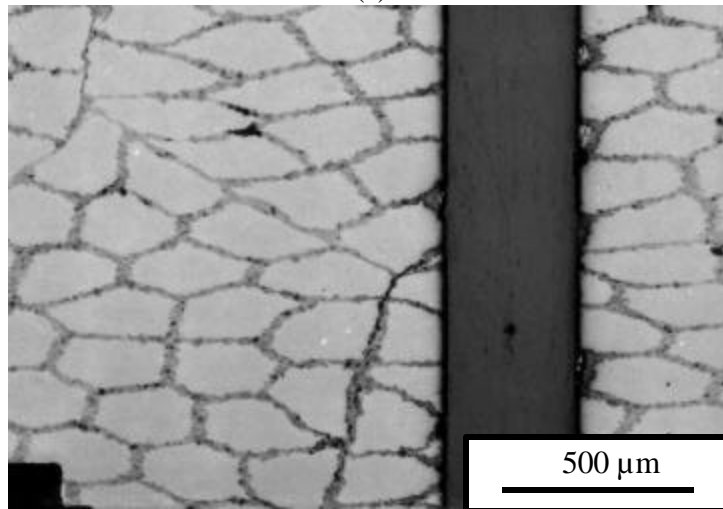


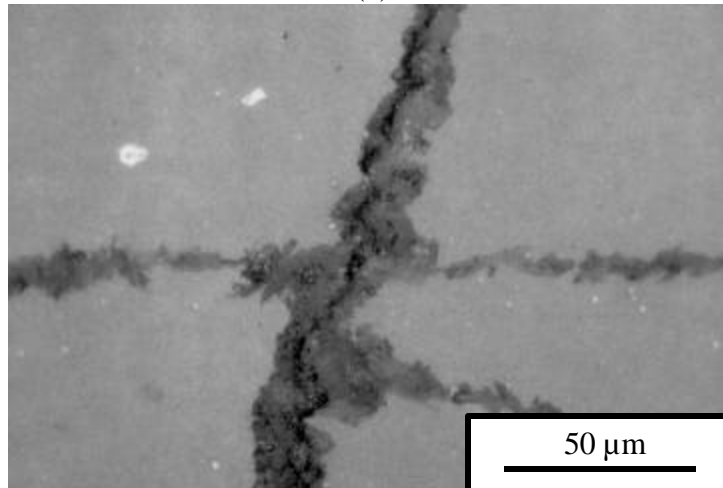
Figure 7.3 (b) Micrograph at 64x of illustrating how no cracks are found in untested notched specimens.



(a)



(b)



(c)

Figure 7.4 (a), (b), and (c) Shows a crack found in the BN around the notch found before polishing down to the notch tip.

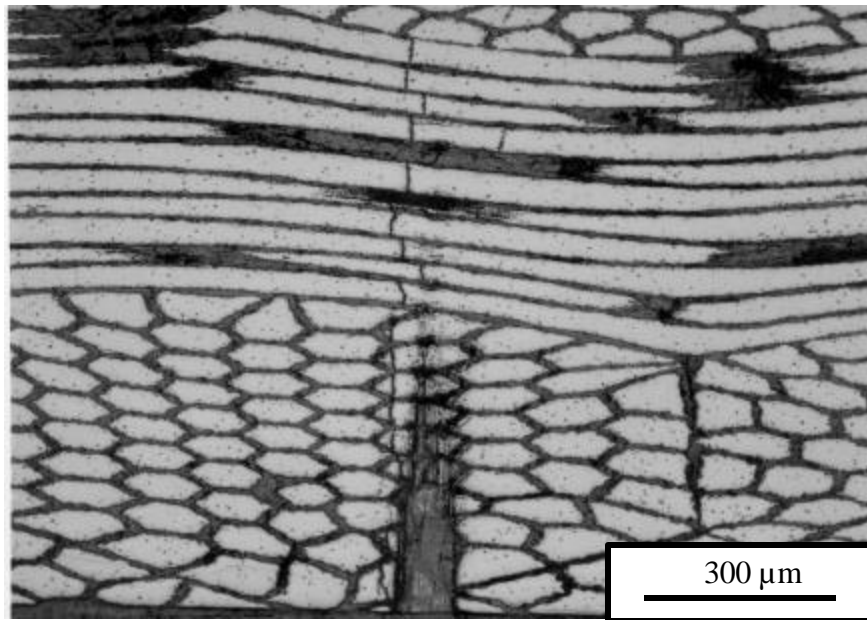


Figure 7.5 Micrograph of 97-B49b section #1 after polishing down through the notch. There is a crack adjacent to the notch.

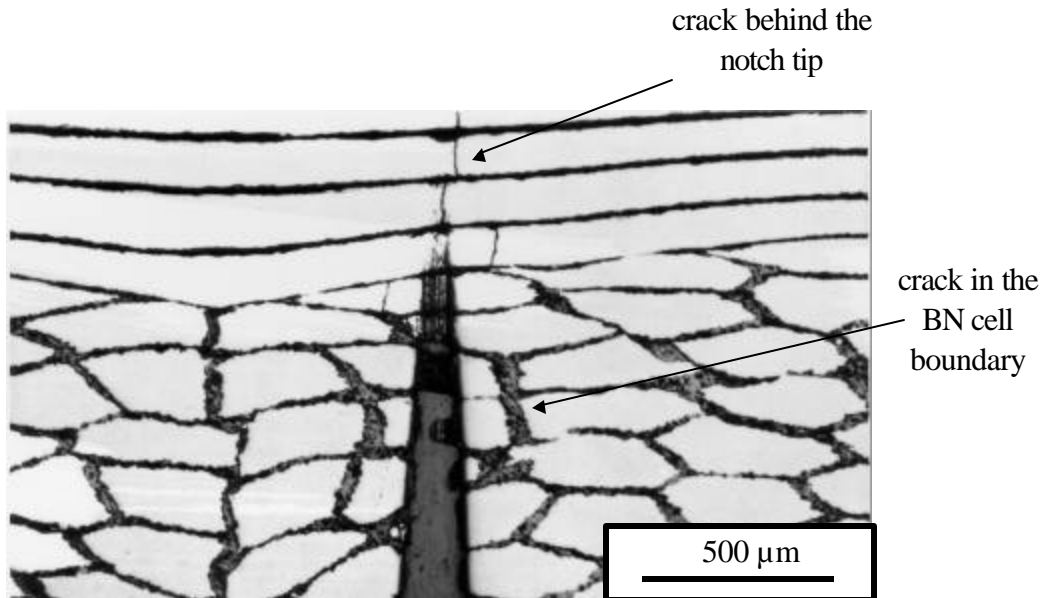


Figure 7.6 Micrograph of 97-B67c section #1 after polishing down through the notch. There is a crack adjacent to the notch and in the BN boundary near the notch.

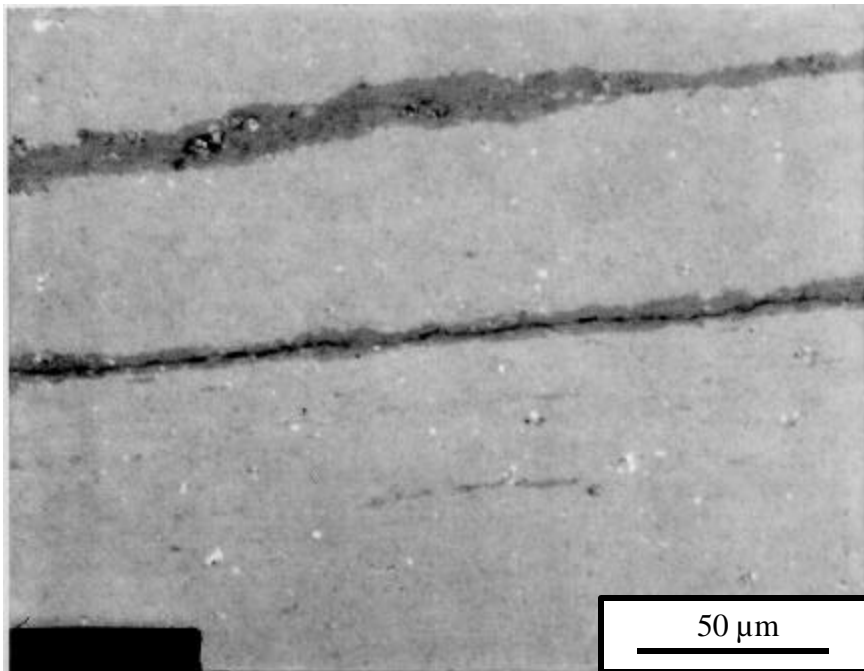
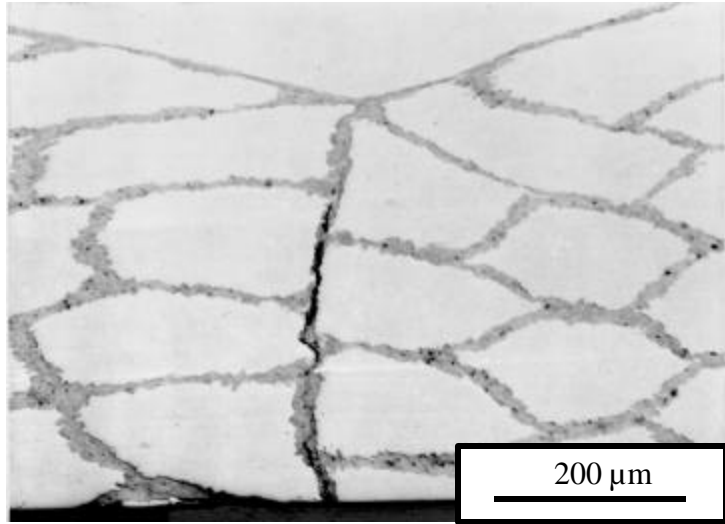
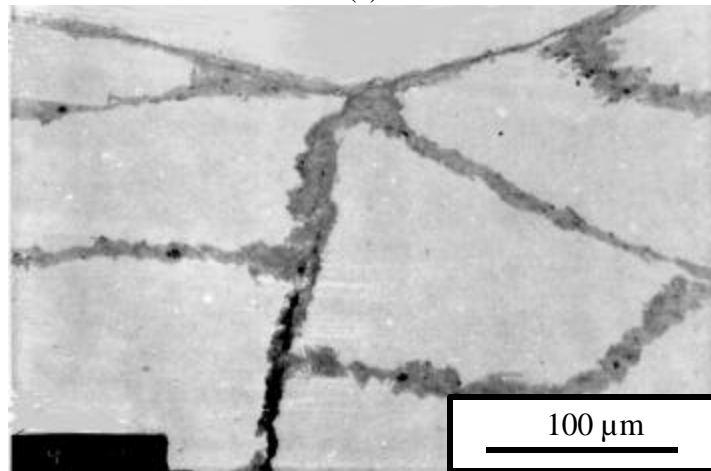


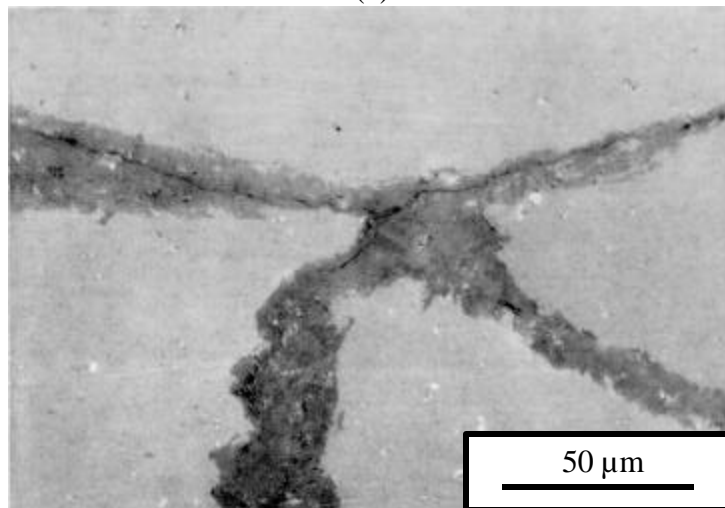
Figure 7.7 Micrograph which demonstrates how fine the cracks in the BN are even when tested near failure.



(a)



(b)



(c)

Figure 7.8 (a), (b), and (c) Shows a crack which appears to have initiated at the surface in the BN and was deflected at the junction with the 0° ply.

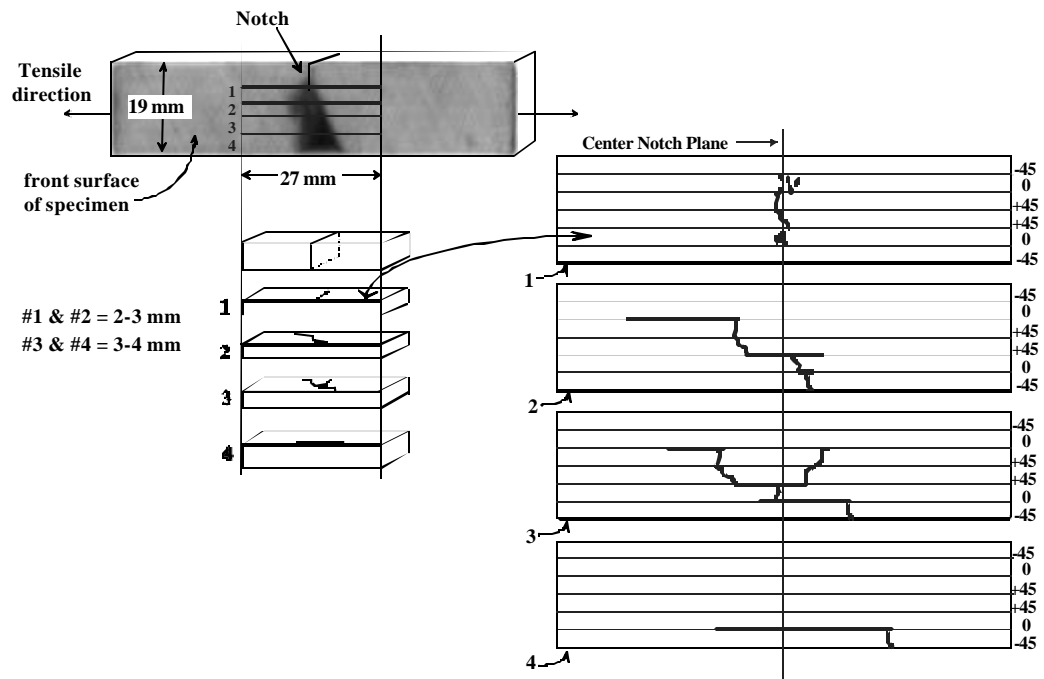


Figure 7.9 Microscopic sections compared to the x-ray radiograph. Sketches from individual specimen sections were drawn from polished sections.

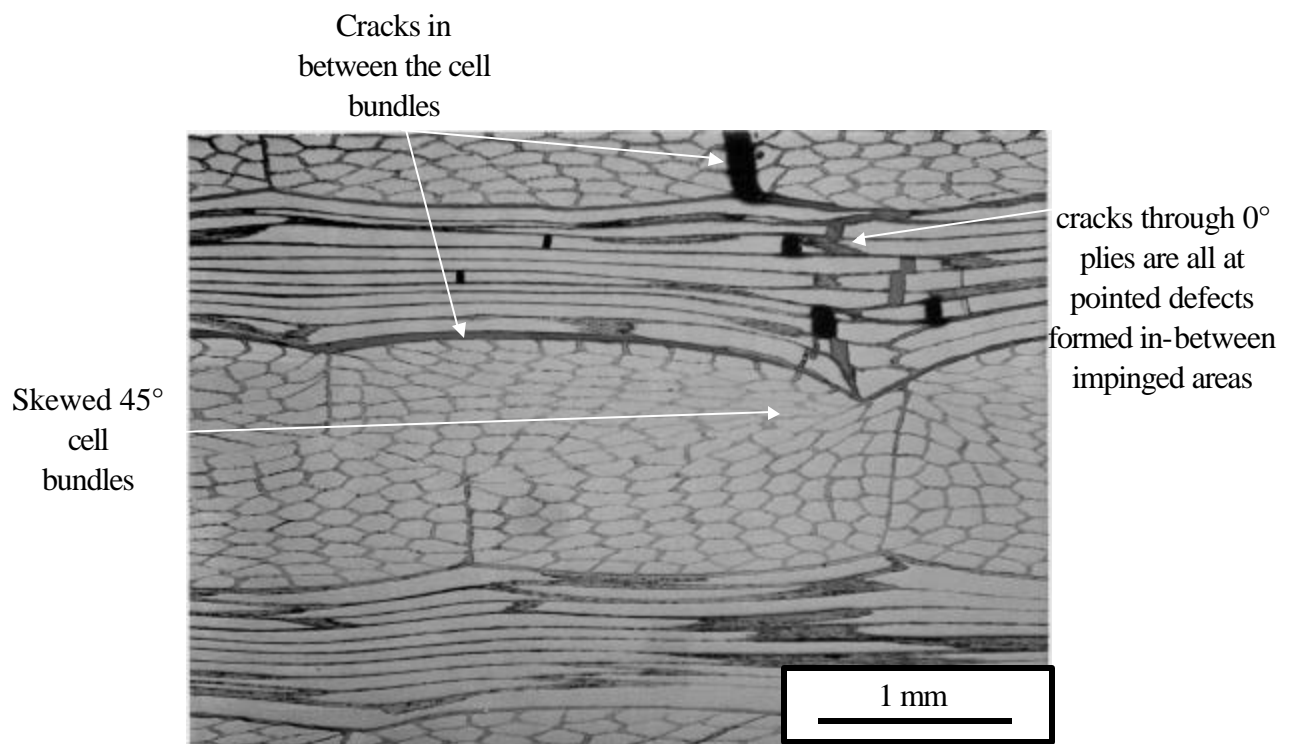


Figure 7.10 Micrograph illustrating that even in the presence of processing defects (skewed cell bundles) the preferred crack path is the cell bundles and at the defects formed presumably due to the impinged 0° cells

CHAPTER 8

SUMMARY AND CONCLUSIONS

8.1 Summary

This investigation has addressed the issues of cell size dependence and notch sensitivity on the fracture behavior of a Si_3N_4 -BN fibrous monolith ceramic through mechanical testing and non-destructive evaluation. Fibrous monoliths (FMs) are fiber-less, textured, ceramics that contain "cells" of a strong phase and "cell boundaries" of a relatively weak phase. Fabrication of fibrous monolith materials consists of traditional powder ceramic processes relying heavily on coextrusion techniques and hot-pressing. The materials considered in this study were fabricated using a multi-filament coextrusion technique where multiple coextruded cells were re-extruded to form cell bundles and the resultant microstructure.

The fracture behavior of two Si_3N_4 -BN fibrous monolith systems, one with a cell size of 125 μm and the other with a cell size of 250 μm , were compared to each other and to monolithic Si_3N_4 . The materials tested were fabricated and provided by Advanced Ceramics Research, Inc. Each fibrous monolith material had a [-45/0/+45]_s cell architecture, a 75% volume fraction of Si_3N_4 , and bulk density of 3.06 g/cm³. The mechanical behavior was evaluated through room temperature fast-fracture tensile testing of straight-sided, dogbone, and modified single-edge notched specimens with various

notch to width ratios. Limited testing was also performed at 1150°C. A number of load-unload and cyclic fracture tests were performed at room temperature in conjunction with several non-destructive evaluation (NDE) techniques including x-ray radiography, thermography, ultrasonic c-scanning, and acoustic emission to determine the critical stages of damage initiation and evolution.

The mean strength values obtained from testing unnotched straight-sided specimens were 113 MPa \pm 13 MPa for the material with the finer cell size, and 126 MPa \pm 4 MPa for the larger cell size material. The mean value of modulus for both materials was found to be approximately 200 GPa with a standard deviation in each case of 15 GPa. Two dogbone specimens from each microstructure were also tested in order to address the effect of geometry on the strength. The mean strengths measured for the material with the 125 μ m cell size were 127 and 98 MPa and the strengths measured for the material with the 250 μ m cell size were 106 and 114 MPa. Modulus values for the materials were approximately 250 GPa and 175 GPa, respectively. The average strength measured for neat Si₃N₄ material was approximately 504 MPa, while the average modulus was 280 GPa.

The damage observed in both fibrous monolith materials included widespread inter-ply delamination, and failure of the 0° plies compared to brittle fracture of the neat Si₃N₄ material. Cracks in the fibrous monolith materials tended to follow a path around and between cell bundles, instead of the more desirable torturous path around single cells within the bundles of the multi-filament coextruded microstructures. The two materials tested herein not only had differing individual cell sizes but also different cell bundle sizes due to the processing technique. A comparison of the results obtained by testing straight-sided specimens of the two different

fibrous monolith materials show that there is statistically no significant difference in the strength. However, a larger variability in strength from plate to plate was observed for the material with the finer microstructural features. It was suggested that the increase variability might be attributed to a higher percentage of processing defects combined with the machine of the tiles and specimens.

Fast-fracture testing of unnotched specimens show that the properties of the fibrous monolith materials are directly related to the amount of reinforcing phase in the uniaxial direction, and that the $[-45/0/+45]_s$ architecture being tested in this study may not provide for optimum fracture resistance compared to neat Si_3N_4 material. Fibrous monolith materials not related to this study were used to address the effect of specimen width on the strength. It was suspected that the tensile results measured were low due to interaction of the interlaminar shear stresses. The outcome of this experiment was inconclusive due to the limited number of data obtained. These data were also used to show that a significant difference in material properties can result with changes in processing, thus pedigree of the fibrous monolith materials should be considered when comparing data.

Fracture behavior of the MSE(T) Si_3N_4 -BN fibrous monolith specimens tested continuously to failure show advantages in both strength and total work of fracture over the neat material in the presence of the various stress concentrations tested. The strength for fibrous monolith specimens with a notch-to-width ratio of 0.3 was shown to be about 9% greater and the WOF_T was as much as 80% greater than the neat material. In general, the two fibrous monolith materials showed nearly the same non-linear behavior for a single notch length while the neat material exhibited behavior that was linear to failure. There were, however, some

differences detected in comparing the two fibrous monolith materials. The material with the larger microstructural features showed slightly larger failure loads, displacements, damage zones, and total work of fractures over the material with the finer microstructure.

When comparing the behavior and fractures for the various notch lengths and materials, it was found that the fibrous monolith materials exhibit behavior which is altered by the length of the notch while the neat materials exhibit behavior which is altered by the stress concentration at the notch. The neat material showed identical fracture morphologies for the various notch lengths and showed behavior which can be modeled by the stress intensity factor using equations from linear elastic fracture mechanics (LEFM). The LEFM relationships do not correctly model the notch size effect in the case of the fibrous monolith materials. Although differences in the fracture morphologies were seen at the various notch lengths, the net-section stress is a more feasible prediction of the behavior.

The mechanical data from single load-unload and cyclic tests on the fibrous monolith materials show hysteresis and permanent offset when tested to loads between 25% and 50% of the average failure load (between 25 MPa and 50 MPa) for the respective microstructures. Damage was also evidenced by acoustic emission detection at loads as low as 2 kN for both fibrous monolith materials. Non-destructive evaluation techniques including x-ray radiography, thermography, and ultrasonics did not show evidence of damage at test loads below about 70% of failure for each material. Only specimens tested to 70% of the failure load or greater showed an indication of damage. Even then, only the c-scans and thermography were able to detect any cracking.

Mechanism of failure in flexure for Si_3N_4 -BN were identified by studies at the University of Michigan as crack deflection, interply delamination, crack kinking, and cell sliding. Recently, it has been postulated that pre-existing microcracks in the cell boundary phase contribute to the damage progression through crack link-up and cleaving. Damage mechanisms associated with microcracking at the lower loads are consistent with relationships seen in the data plots and the fact that no damage was large enough to be identifiable using the NDE techniques.

The plot of work of fracture versus normalized load shows that around 75% of the total energy absorbed occurs after testing to a load which is 90% of the failure load or greater. The WOF's associated with absorbed energy shows that the two materials behave similarly until nearing failure where the dominate energy absorbing mechanisms may be associated with delamination crack area and frictional sliding. At fracture, the material with the larger cell bundles shows a higher work of fracture. Nominally the values of maximum absorbed energy at fracture for the two FM materials were approximately 648 J/m^2 and 885 J/m^2 , respectively. Energy absorption based on these macroscopic mechanisms shows an effect of the microstructure feature size when identical volume fractions are tested.

Microscopic inspection of the single load-unload specimens verifies that the majority of damage due to testing below about 90% of failure may be on the submicroscopic scale, as only isolated cases of damage are detectable optically. Limited through-the-thickness type cracking was evident at the notch tip for the specimens tested to the lowest load levels. Only the specimen from the larger microstructure tested to about 94% of its estimated failure load showed other types of damage, including fine hairline type cracks between the cell bundles

within the 45° plies and between the 0° and 45° plies. In general the interlaminar type cracks seem span the length of a cell bundle and are estimated to be on the order of 1μm wide.

Inspection of the damage on polished sections from failed specimens revealed excellent correlation with the NDE. The radiography shows the most detail of the through-the-thickness type cracks and delaminated zones compared to the other imaging techniques. Detection of interlaminar cracks through the radiography is possible due to the occurrence of large displacements of the plies relative to one another upon failure.

Other observations made from the polished sections show that the damage does not seem to be influenced by some of the processing defects identified in both fibrous monolith materials. Jagged individual cells identified within the cell bundles did not contribute to the damage in either material as the dominant feature in the microstructure was shown to be the cell bundles. Neither the cell bundles which became skewed or kinked from binder burnout and hot-pressing nor the cell bundles which have large differences in individual cell sizes within were associated with preferred crack paths. The defects associated with the macrostructure formed by the multi-filament coextruded cell bundles as a result of the cross-ply architecture did show to be analogous with the damage in both fibrous monolith materials.

8.2 Conclusions

The fracture behavior of the Si_3N_4 -BN materials tested in this study show non-catastrophic behavior compared to monolithic Si_3N_4 -BN when tested in tension. The greatest advantage of the fibrous monoliths tested over the neat materials was shown to be in the presence of a stress concentration. The fibrous monolith materials are insensitive to the stress

concentration at the notch, presumably resulting from the weak BN and the existence of pre-existing microcracks in the cell boundaries. The notch length effect observed was best described by the net-section stress.

The influence of individual cell size on the fracture behavior of the fibrous monolith materials could not be determined by this study since bundle sizes were not held constant. Cell bundle size was shown to have an influence on displacements, extent of damage, and fracture energies. The trend in absorbed energy, the NDE results, and the microscopic inspection indicate that damage evidenced by non-linear load-displacement behavior may be submicroscopic up to relatively high loads. It is presumed the damage incurred initially is consistent with mechanisms of microcracking while macroscopic dissipative mechanisms associated with delamination cracking and frictional sliding dominate near failure. Energy absorption based on the macroscopic mechanisms shows an effect of the microstructural feature size when materials of identical volume fractions are tested.

Future research aimed at better characterizing progressive damage mechanisms in the sub-millimeter structure of the material is needed to correctly model and predict fracture behavior of these materials. Other non-destructive evaluation techniques, such as interferometry, may be better suited for detecting the small displacements presumably caused by the linking of microcracks and the cleaving of BN grains. Better resolution of the ultrasonics and thermography methodologies utilized may be possible as well using variations of the techniques and equipment. Since crack area creation and sliding mechanisms seem to dominate at failure in tension, interfacial energy parameters obtained for tensile loading conditions and specimen geometries are warranted as well. Further testing and analysis, using laminate theory

equations, may be needed to address some of the issues found from tension testing including the relationship between cell architecture, stress state, and specimen width. Further efforts to quantify the material toughness parameters might also consider using larger width specimens and various a_0/W ratios to validate existing fracture mechanics analyses. A more ideal material for future study would include only single cells versus multi-filaments due to the inherent defects formed by the macrostructure.

REFERENCES

1. W. S. Coblenz, "Fibrous Monolithic Ceramic and Method for Production;" U. S. Pat. No. 4,772,524, 1988.
2. J. W. Halloran, "Tough Ceramics from Fibrous Monoliths;" Department of Materials Science and Engineering, University of Michigan Ann Arbor, MI, 1991.
3. J. W. Halloran, J. W. Holmes, A. Mulligan, K. Stuffle, and T. Nielsen, "Advanced Development and Scale-Up of Fibrous Monolithic Ceramics;" University of Michigan, Ann Arbor, 1992.
4. J. W. Halloran, J. W. Holmes, A. Mulligan, K. Stuffle, and T. Nielsen, "Advanced Development and Scale-Up of Fibrous Monolithic Ceramics;" University of Michigan, Ann Arbor, 1994.
5. S. Baskaran, S. D. Nunn, D. Popovic, and J. W. Halloran, "Fibrous Monolithic Ceramics: I, Fabrication, Microstructure, and Indentation Behavior," *Journal of the American Ceramic Society*, **76** [9] 2209-16 (1993).
6. S. Baskaran and J. W. Halloran, "Fibrous Monolithic Ceramics: II, Flexural Strength and Fracture Behavior of the Silicon Carbide/Graphite System," *Journal of the American Ceramic Society*, **76** [9] 2217-24 (1993).
7. S. Baskaran and J. W. Halloran. "SiC-Based Fibrous Monolithic Ceramics." In *Ceramic Engineering Science Proc.*, **14**, 813-823, 1993.
8. S. Baskaran and J. W. Halloran, "Fibrous Monolithic Ceramics: III, Mechanical Properties and Oxidation Behavior of the Silicon Carbide/Boron Nitride System," *Journal of the American Ceramic Society*, **77** [5] 1249-55 (1994).
9. S. Baskaran, S. D. Nunn, and J. W. Halloran, "Fibrous Monolithic Ceramics: IV, Mechanical Properties and Oxidation Behavior of the Alumina/Nickel System," *Journal of the American Ceramic Society*, **77** [5] 1256-62 (1994).
10. G. A. Danko, D. Popovic, K. Stuffle, B. H. King, J. W. Halloran, J. W. Holmes, and D. F. Hasson, "Commercial Development of Fibrous Monolithic Ceramics," Presented at the 19th Annual Conference on Composites, Advanced Ceramics, Materials, and Structures---B, Cocoa Beach, FL, 1995

11. D. Popovic, S. Baskaran, G. Zywicki, C. Arens, and J. W. Halloran. "Silicon Nitride and Silicon Carbide Fibrous Monolithic Ceramics." In *Silicon-Based Structural Ceramics*, edited by B. W. Sheldon and S. C. Danforth, 173-86: American Ceramic Society, 1994.
12. G. E. Hilmas, G. A. Brady, and J. W. Halloran, "SiC and Si₃N₄ Fibrous Monoliths: Non-Brittle Fracture From Powder Processed Ceramics Produced by Coextrusion," Presented at the Ceramic Processing Science and Technology 1995.
13. G. Hilmas, A. Brady, U. Abdali, G. Zywicki, and J. Halloran, "Fibrous Monoliths: Non-Brittle Fracture from Powder-Processed Ceramics," *Materials Science & Engineering A*, **A195** 263-68 (1995).
14. D. Popovich, G. A. Danko, G. E. Hilmas, K. Stuffle, B. H. King, G. A. Brady, R. W. Trice, and J. W. Halloran, "Fibrous Monoliths: Room- and High- Temperature Non-Brittle Fracture from Powder Processed Ceramics," Presented at the Proceedings of the 20th Annual Conference on Composites, Advanced Ceramics, Materials, and Structures---A, Cocoa Beach, FL, 1996.
15. D. Popovic, G. A. Danko, K. Stuffle, B. h. King, and J. W. Halloran, "Relationship Between Architecture, Flexural Strength and Work of Fracture for Fibrous Monolithic Ceramics," Presented at the 19th Annual Conference on Composites and Advanced Ceramic Materials, Cocoa Beach, FL 1995.
16. R. Trice and J. Halloran, "High Temperature Mechanical Behavior of Si₃ N₄ /BN Fibrous Monolithic Ceramics;" Presented at the American Ceramic Society Annual Meeting, Cincinnati, OH, May, 1997.
17. B. H. King, "The Influence of Architecture on the Elasticity and Strength of Si₃N₄/BN Fibrous-Monolithic Ceramic Laminates," Doctor of Philosophy, The University of Michigan, 1997.
18. D. Kovar, B. H. King, R. W. Trice, and J. W. Halloran, "Fibrous Monolithic Ceramics," *Journal of the American Ceramic Society*, **80** [10] 2471-87 (1997).
19. D. Kovar, G. A. Brady, M. D. Thouless, and J. W. Halloran, "Interfacial Fracture Between Boron Nitride and Silicon Nitride and Its Applications to the Failure Behavior of Fibrous Monolithic Ceramics," Presented at the Instability Dynamics, Scaling, and Ductile/Brittle Behavior 1996.
20. J. Cook and J. E. Gordon, "A Mechanism for the Control of Crack Propagation in All-Brittle Systems," *Proceedings of the Royal Society A*, **282** 508-20 (1964).

21. W. J. Clegg, K. Kendall, N. M. Alford, T. W. Button, and J. D. Birchall, "A Simple Way to Make Tough Ceramics," *Letters to Nature*, **347** 455-57 (1990).
22. G. A. Danko, G. E. Hilmas, J. W. Halloran, and B. King, "Fabrication and Properties of Quasi- Isotropic Silicon Nitride-Boron Nitride Fibrous Monoliths," Cocoa Beach, FL 1997.
23. G. A. Brady, G. E. Hilmas, and J. W. Halloran. "Forming Textured Ceramics by Multiple Coextrusion." In *Ceramic Processing Science and Technology*, edited by H. Hausner, G. L. Messing and S. Hirano, 297-301, 1995.
24. C. M. Arens, "The Oxidation of Fibrous Monolithic Ceramics," Masters of Science and Engineering, University of Michigan, 1994.
25. D. Kovar and M. Thouless, "Simple Method for Determining Frictional Sliding Resistance and Frictional Energy Dissipation in Layered Ceramics," *Journal of the American Ceramic Society*, **80** [3] 673-79 (1997).
26. M.-Y. He and J. W. Hutchinson, "Crack Deflection at an Interface Between Dissimilar Elastic Materials," *Int. J. Solids Structure*, **25** [9] 1053-67 (1989).
27. R. W. Trice and J. W. Halloran, "The Influence of Microstructure and Temperature on the Interfacial Fracture Energy of Silicon Nitride/Boron Nitride Fibrous Monolithic Ceramics," *Submitted to the Journal of the American Ceramic Society*, (1998).
28. R. W. Trice and J. W. Halloran, "The Effect of Sintering Aids on Silicon Nitride/Boron Nitride Fibrous Monolithic Ceramics," *Submitted to the Journal of the American Ceramic Society*, (1998).
29. R. W. Trice and J. W. Halloran, "The Elevated Temperature Mechanical Properties of Silicon Nitride/Boron Nitride Fibrous Monolithic Ceramics," *Submitted to the Journal of the American Ceramic Society*, (1998).
30. A. G. Evans and F. W. Zok, "The Physics and Mechanics of Fibre-Reinforced Brittle Matrix Composites;" of 3857-96 in . Chapman & Hall, , 1994.
31. C. A. Folsom, F. W. Zok, and F. F. Lange, "Flexural Properties of Brittle Multilayer Materials: I, Modeling," *Journal of the American Ceramic Society*, **77** [3] 689-96 (1994).
32. C. A. Folsom, F. W. Zok, and F. F. Lange, "Flexural Properties of Brittle Multilayer Materials: II, Experiments," *Journal of the American Ceramic Society*, **77** [8] 2081-87 (1994).

33. W. A. Curtin, "Theory of Mechanical Properties of Ceramic-Matrix Composites," *Journal of the American Ceramic Society*, **74** [11] 2837-45 (1991).
34. J. M. Staehler, "Preliminary Tensile Test Data On a Si₃N₄ -BN Fibrous Monolith;" Wright Laboratory, Materials Directorate, Wright Patterson AFB, OH, 1997.
35. Advanced Ceramics Research, "Unpublished Research;" 1997.
36. R. John and B. Rigling, "Effect of Height to Width Ratio on K and CMOD Solutions for a Single Edge Cracked Geometry with Clamped Ends," *Engineering Fracture Mechanics*, 1-28 (1997).
37. "Methods of Nondestructive Evaluation." In *Nondestructive Evaluation and Quality Control*, edited by A. S. o. Materials, 47-483: ASM International, 1989.
38. J. G. Sun, C. Deemer, W. A. Ellingson, T. E. Easler, A. Szweda, and P. A. Craig, "Thermal Imaging Measurement and Correlation of Thermal Diffusivity in Continuous Fiber Ceramic Composites," Presented at the 22nd Annual Conference of the American Ceramic Society at Cocoa Beach 1998.
39. G. S. Clemons and D. A. Stubbs, "Guidelines for Standardizing the Gain of Ultrasonic Inspection Systems used to Acquire Ultrasonic Reflector Plate C-scans;" NASP Technical Memorandum 1199, Characterization of Titanium Matrix Composites, Vol. VII - Mechanical Behavior and Damage Tolerance of TMCs, 1995.
40. J. Ritter, S. Nair, and W. Dunley, "High Strength Reaction Bonded Silicon Nitride," *Adv. Ceram. Mat.*, **3** [4] 415-417 (1988).
41. Ceramic Source90; American Ceramic Society, Westerville, 1990.
42. J. M. Whitney, I. M. Daniel, and R. B. Pipes, Experimental Mechanics of Fiber Reinforced Composite Materials; 1 ed., The Society for Experimental Stress Analysis, , 1982.
43. K. Friedrich, ed. *Application of Fracture Mechanics to Composite Materials*. Edited by R. B. Pipes. Vol. 6, *Composite Materials Series*. Newark: Elsevier Science Publishers, 1989.
44. R. M. Jones, Mechanics of Composite Materials; Hemisphere Publishing Corporation, Blacksburg, 1975.
45. K. L. Reifsnider, ed. *Damage in Composite Materials: Basic Mechanisms, Accumulation, Tolerance, and Characterization*, *ASTM Special Technical Publication* 775. Bal Harbour, FL: ASTM, 1982.

46. G. P. Sendeckyj. "On Fracture Behavior of Composite Materials." In *Strength and Structure of Solid Materials*, edited by P. D. H. Miyamoto, P. D. T. Kunio, P. D. H. Okamura, P. V. Weiss, P. M. Williams and P. H. Liu, 373-88. Leyden: Noordhoff International Publishing.
47. H. L. Ewalds and R. J. H. Wanhill, Fracture Mechanics; Edward Arnold Delftse Uitgevers Maatschappij, , 1984.
48. N. E. Dowling, Mechanical Behavior of Materials: Engineering Methods for Deformation, Fracture, and Fatigue; Pretice-Hall, Inc, , 1993.
49. D. Kovar, M. D. Thouless, and J. W. Halloran, "Crack Deflection and Propagation in Layered Silicon Nitride/Boron Nitride Ceramics," *Journal of the American Ceramic Society*, **81** [4] 1004-12 (1998).
50. R. V. Hogg and J. Ledolter, pp. 167-77 in Engineering Statistics; Macmillan Publishing Co., New York, 1987.
51. W. Mendenhall and T. Sincich, pp. 328-35 in Statistics for Engineering and the Sciences; Macmillan, Inc., New York, 1992.

APPENDIX A

CALCULATION OF G FOR COMPLIANCE

G (energy release rate) was needed to calculate a theoretical compliance used to find modulus of the MSE(T) specimens. G is dependent on the height-to-width ratio and the notch length-to width ratio for the MSE(T) specimen. Constants used to solve the equation below were developed by John and Rigling³⁶.

$$G = \frac{2.9086 + \sum_{i=1}^6 C_i (a/W)^i}{(1-a/W)^{3/2}}$$

Where

$$C_i = \sum_{j=0}^3 D_{ij} [\log(H/W)]^j$$

And D_{ij} =

i	j=0	j=1	j=2	j=3
1	-6.0503e+00	1.4389e+00	-1.2694e+00	0e+00
2	-1.4413e+00	2.2670e+01	-8.8785e-01	0e+00
3	6.4384e+00	4.7573e+00	-5.2142e+01	0e+00
4	5.7307e+01	-2.0564e+02	2.4435e+02	0e+00
5	-7.7132e+01	3.0193e+02	-3.2597e+02	0e+00
6	3.0795e+01	-1.2485e+02	1.3534e+02	3.8746e-01

APPENDIX B

PREDICTION OF STRENGTH FOR Si_3N_4 -BN FM FROM LITERATURE VALUES

A rough estimate of strength was obtained using a value reported by Staehler³⁴, of WPAFB, OH, for unidirectional [0] Si_3N_4 -BN fibrous monolith material with 85% Si_3N_4 , which was 495 MPa. This value was adjusted to account for the percent of plies in the loading direction in the materials tested in this study which had a ply lay-up of [-45/0/+45]_s by assuming that there was no contribution of the 45° plies to the strength. The reported value was also adjusted for the difference in the volume fraction of the Si_3N_4 phase. The materials tested in this study had a volume fraction of Si_3N_4 of 75%.

The calculation was as follows:

2 plies / 6 plies had a 0° orientation in the material tested in this study → 33%

Since Staehler³⁴ reported a volume fraction of Si_3N_4 of 85%:
volume fraction adjust was → 75% / 85%

Thus the strength prediction using the reported value is:

$$0.33 \times (0.75 / 0.85) \times 495 \text{ MPa} \approx 144 \text{ MPa}$$

The same strategy was used for the reported value of strength in unidirectional material with a 80% volume fraction of Si_3N_4 by ACR., Inc.³⁵

$$0.33 \times (0.75 / 0.80) \times 379 \text{ MPa} \approx 117 \text{ MPa}$$

APPENDIX C

PREDICTION OF STRENGTH FOR Si₃N₄-BN FM FROM NEAT DATA

A rough estimate of strength was obtained using a value reported in the literature for monolithic Si₃N₄⁴¹ by assuming that there is no contribution of the 45° plies and no contribution of the BN to the tensile strength. For the FM materials tested in this study the total fraction of Si₃N₄ was approximately 75%, but only two plies of composite had cells in the uniaxial direction due to the [-45/0/+45]_s lay-up.

$$2 \text{ plies} / 6 \text{ plies} = 33\%$$

Since the total fraction of Si₃N₄ in the composite is 75%:

$$0.33 \times 0.75 = 0.25$$

Therefore the fraction of the Si₃N₄ cells in the loading direction (by volume) is approximately 25%. Therefore, the strength is estimated to be:

$$0.25 \times 504 \text{ MPa} \approx 126 \text{ MPa}$$

APPENDIX D

HYPOTHESIS TEST OF VARIABILITY

To verify that there is no significant difference in the unnotched tensile strength generated for the FM materials with the 125 μm and the 250 μm cells, respectively, a hypothesis test of variance was performed^{50,51}. Assumptions made include that the sample taken is representative of the population and that the population follows a normal distribution.

FM 125 μm cells (1): $s_1 = 113$, std dev. (S_{d1}) = 13, number of samples (n_1) = 4
FM 250 μm cells (2): $s_2 = 126$, std dev. (S_{d2}) = 4, number of samples (n_2) = 4

Null hypothesis: $H_0: \mu_1 = \mu_2$

Alternate Hypothesis: $H_1: \mu_1 < \mu_2$

$$S_p = \text{SQRT} [((n_1-1) * (S_{d1})^2 + (n_2-1) * (S_{d2})^2) / (n_1 + n_2 - 2)] \sim 9.617$$

$$t \text{ statistic : } t_0 = (s_1 - s_2) / S_p * \text{SQRT} [(1/n_1) + (1/n_2)] \sim -1.911$$

$$\text{degrees of freedom: } (n_1 + n_2 - 2) = 6$$

using a 95% confidence interval: $t(0.05, v) = 1.943$ (table look up)

$$t_0 < -t(0.05, v) ? \text{ NO}$$

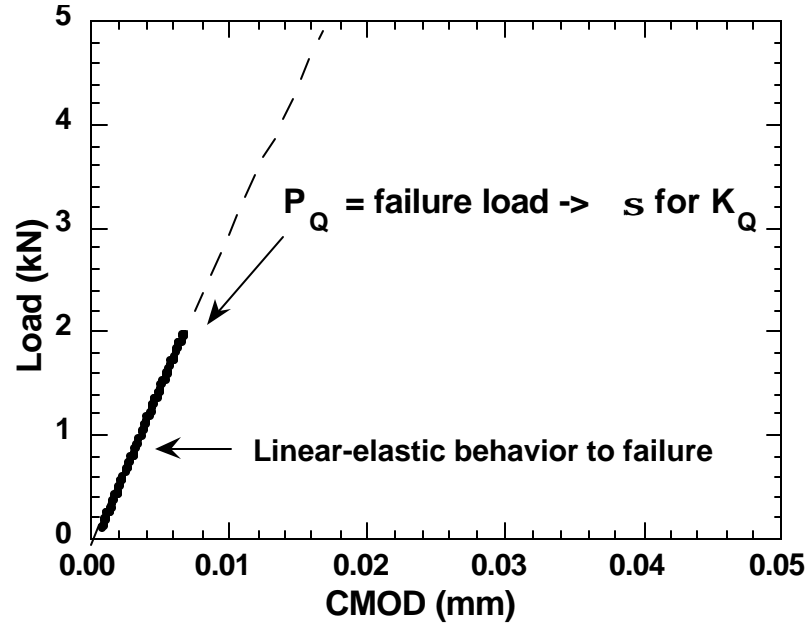
Conclusion: Accept H_0 , reject H_1 . No difference in strength between two materials.

APPENDIX E

NOTCH SIZE EFFECT PREDICTION FOR NEAT Si₃N₄ USING LEFM

$$K_Q = \sigma/\sqrt{a} \bullet F(a_0/W)$$

Where σ is taken at failure and a_0 as the initial notch length



$F(a/W)$ used was found using constants developed by John and Rigling³⁶ for the MSE(T) specimen geometry

$$F = \frac{1.1215 + \sum_{i=1}^6 A_i (a/W)^i}{(1-a/W)^{3/2}}$$

Where

$$A_i = \sum_{j=0}^2 B_{ij} [\log(H/W)]^j$$

APPENDIX E (con't)

And $B_{ij} =$

i	j=0	j=1	j=2
1	-1.6071e+00	-2.5295e-01	1.4856e-01
2	-4.0053e+00	1.9198e+01	-8.7311e+00
3	1.1513e+01	-5.0147e+01	2.1296e+01
4	-5.8413e+00	3.0109e+01	3.8125e+00
5	-4.6316e+00	1.4478e+01	-3.7584e+01
6	3.4420e+00	-1.3352e+01	2.1050e+01

For a_0/W of 0.3 and average failure load of ≈ 2.05 kN, F was found to be ≈ 1.377 and $K_Q \approx 7.9$ MPavm.

For an average $K_Q = 7.9 \sqrt{\text{MPa}}$, the prediction for applied stress versus a_0/W was found by varying a_0 from a_0/W 0.2 to 0.9 through equation:

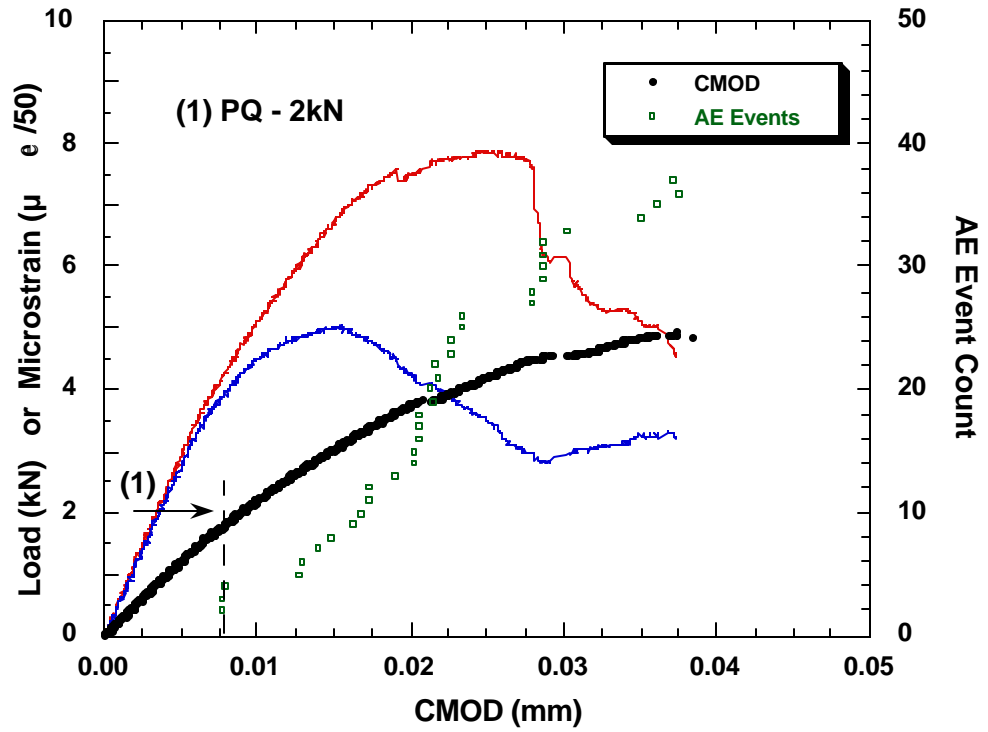
$$\sigma = (7.9) / (1.377 \sqrt{\pi a_0})$$

APPENDIX F

NOTCH SIZE EFFECT PREDICTION FOR Si₃N₄-BN FM USING LEFM

$$K_Q = \sigma_{\sqrt{a}} \bullet F(a/W)$$

Where σ is taken at 1) the onset of non-linearity using a_0 as the initial notch length



$F(a/W)$ used was found using constants developed by John and Rigling³⁶ for the MSE(T) specimen geometry

APPENDIX F (con't)

$$F = \frac{1.1215 + \sum_{i=1}^6 A_i (a/W)^i}{(1-a/W)^{3/2}}$$

Where

$$A_i = \sum_{j=0}^2 B_{ij} [\log(H/W)]^j$$

And $B_{ij} =$

i	j=0	j=1	j=2
1	-1.6071e+00	-2.5295e-01	1.4856e-01
2	-4.0053e+00	1.9198e+01	-8.7311e+00
3	1.1513e+01	-5.0147e+01	2.1296e+01
4	-5.8413e+00	3.0109e+01	3.8125e+00
5	-4.6316e+00	1.4478e+01	-3.7584e+01
6	3.4420e+00	-1.3352e+01	2.1050e+01

- (1) For a_0/W of 0.3 and average load at the onset of non-linearity (at first AE event) of ≈ 2.0 kN, F was found to be ≈ 1.381 and $K_Q \approx 7$ MPavm.

For K_Q and F, the prediction for applied stress versus a_0/W was found by varying a_0 from a_0/W 0.2 to 0.9 through equation:

$$\sigma = (K_Q) / (F\sqrt{\pi a_0})$$

APPENDIX G

CALCULATION OF FRACTURE ENERGY

Equations used by Kovar and Thouless^{18,19, 25, 49} for calculating the energy absorbed in flexure due to crack area formation (W_c) and the absorbed energy due to frictional sliding (W_s) were used to estimate a difference in absorbed energy between the two fibrous monolith materials tested in tension in this study. The equations:

$$(1) \quad W_c = W_L + W_i \\ = \Gamma_L A_L + \Gamma_i A_i$$

$$(2) \quad W_s = n \delta A_i \tau_s$$

$$(3) \quad \text{Total energy} = W_c + W_s$$

W_L = absorbed energy from cracking cells

W_i = absorbed from cracking in the cell boundaries

Γ_L = fracture resistance of the cells

Γ_i = fracture resistance of the cell boundaries

A_L = the cell area

A_i = the interfacial area

W_s = absorbed energy due to frictional sliding

n = the number of cell slipping

δ = the distance slipped

τ_s = the frictional sliding resistance for cracked cell boundaries

Values for Γ_L , Γ_i , δ , and τ_s for Si_3N_4 -BN materials using flexure techniques as found in the literature were used.

APPENDIX G (con't)

$$\Gamma_L = 120 \text{ J/m}^2$$

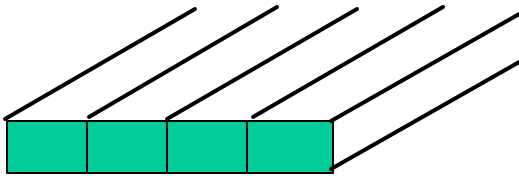
$$\Gamma_i = 30 \text{ J/m}^2$$

$$\delta = 2 \text{ mm}$$

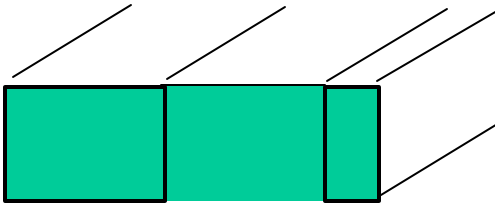
$$\tau_s = 0.3 \text{ MPa.}$$

Values for WC and WS for absorbed energy was made using specimen dimensions tested in this study. Assumptions:

- 1.) energy absorbed is due to cell bundle cracking and sliding
- 2.) energy absorbed is solely due to fracture of the 0° plies
- 3.) cell bundles can effectively be modeled as rectangles where the widths are 1 and 2 mm, respectively, for the two respective materials and the heights are equal to the ply thickness in each case which are all touching.



..... 19 cell bundles (2-1 mm strand FM material)



.....9.5 cell bundles (2-2 mm strand FM material)

Since there are 2 out of 6 plies oriented in the 0° or loading direction, thickness of one ply:
 $= 2.92 \text{ mm} / 6 \text{ plies} = 0.4867 \text{ mm}$ for (2-1 mm material)

$= 4.35 \text{ mm} / 6 \text{ plies} = 0.725 \text{ mm}$ for (2-2 mm material)

Therefore,

$$\text{cell bundle area, } A_L (2-1\text{mm}) = 2 [19 (1\text{mm} * 0.4867\text{mm})] = 18.49 \text{ mm}^2$$

$$\text{cell bundle area, } A_L (2-2\text{mm}) = 2 [9.5 (2\text{mm} * 0.725\text{mm})] = 27.55 \text{ mm}^2$$

APPENDIX G (con't)

Since the area fraction of the BN phase in the material was found to be 25%:

$$\text{cell bundle boundary area, } A_i (2\text{-}1\text{mm}) = 0.25 A_L = 4.62 \text{ mm}^2$$

$$\text{cell bundle boundary area, } A_i (2\text{-}2\text{mm}) = 0.25 A_L = 6.89 \text{ mm}^2$$

$$\begin{aligned} W_C (2\text{-}1\text{mm}) &= [120 \text{ J/m}^2 * (18.49\text{e-}6 \text{ m}^2 - 4.62\text{e-}6 \text{ m}^2)] + [30 \text{ J/m}^2 * (4.62\text{e-}6 \text{ m}^2)] \\ &= 0.001803 \text{ J} \end{aligned}$$

$$\begin{aligned} W_C (2\text{-}2\text{mm}) &= [120 \text{ J/m}^2 * (27.55\text{e-}6 \text{ m}^2 - 6.89\text{e-}6 \text{ m}^2)] + [30 \text{ J/m}^2 * (6.89\text{e-}6 \text{ m}^2)] \\ &= 0.0026859 \text{ J} \end{aligned}$$

The value for W_S was calculated for each material using:

$$n (2\text{-}1\text{mm}) = 2 * 19 = 38$$

and

$$n (2\text{-}2\text{mm}) = 2 * 9.5 = 19$$

and the values given earlier.

$$W_S (2\text{-}1\text{mm}) = 38 * 0.002\text{m} * 0.00462 \text{ m}^2 * 0.30 \text{ MPa} = 0.00010534 \text{ J}$$

$$W_S (2\text{-}2\text{mm}) = 19 * 0.002\text{m} * 0.00689 \text{ m}^2 * 0.30 \text{ MPa} = 0.00007855 \text{ J}$$

$$\begin{aligned} \text{Total absorbed energy (2-1mm)} &= W_C + W_S \\ &= 0.001803 \text{ J} + 0.00010534 \text{ J} \\ &= 0.001908 \text{ J} \end{aligned}$$

$$\begin{aligned} \text{Total absorbed energy (2-2mm)} &= W_C + W_S \\ &= 0.0026859 \text{ J} + 0.00007855 \text{ J} \\ &= 0.002765 \text{ J} \end{aligned}$$

The ratio of the values were found:

$$\frac{W_C + W_S (2\text{-}1 \text{ mm})}{W_C + W_S (2\text{-}2 \text{ mm})} = \frac{0.001908}{0.002765}$$

$$= 0.69 \rightarrow [(0.69*-1) + 1]*100 = 31\%$$

This shows that absorbed energy in the material with the larger cell bundles absorbs approximately 31% more energy using this analysis.